



저작자표시-비영리-변경금지 2.0 대한민국

이용자는 아래의 조건을 따르는 경우에 한하여 자유롭게

- 이 저작물을 복제, 배포, 전송, 전시, 공연 및 방송할 수 있습니다.

다음과 같은 조건을 따라야 합니다:



저작자표시. 귀하는 원저작자를 표시하여야 합니다.



비영리. 귀하는 이 저작물을 영리 목적으로 이용할 수 없습니다.



변경금지. 귀하는 이 저작물을 개작, 변형 또는 가공할 수 없습니다.

- 귀하는, 이 저작물의 재이용이나 배포의 경우, 이 저작물에 적용된 이용허락조건을 명확하게 나타내어야 합니다.
- 저작권자로부터 별도의 허가를 받으면 이러한 조건들은 적용되지 않습니다.

저작권법에 따른 이용자의 권리는 위의 내용에 의하여 영향을 받지 않습니다.

이것은 [이용허락규약\(Legal Code\)](#)을 이해하기 쉽게 요약한 것입니다.

[Disclaimer](#)

Doctoral Thesis

Aligned Silver Nanowire Networks as Transparent
Electrodes for High-Performance Optoelectronics
and Electronic Devices

Saewon Kang

Department of Energy Engineering

Graduate School of UNIST

2018

Aligned Silver Nanowire Networks as Transparent Electrodes for High-Performance Optoelectronics and Electronic Devices

Saewon Kang

Department of Energy Engineering

Graduate School of UNIST

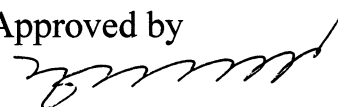
Aligned Silver Nanowire Networks as Transparent Electrodes for High-Performance Optoelectronics and Electronic Devices

A thesis/dissertation
submitted to the Graduate School of UNIST
in partial fulfillment of the
requirements for the degree of
Doctor of Philosophy

Saewon Kang

6. 14. 2018

Approved by



Advisor

Hyunhyub Ko

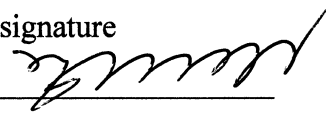
Aligned Silver Nanowire Networks as Transparent Electrodes for High-Performance Optoelectronics and Electronic Devices

Saewon Kang

This certifies that the thesis/dissertation of Saewon Kang is approved.

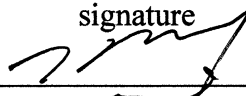
06. 14. 2018

signature



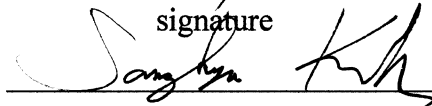
Advisor: Hyunhyub Ko

signature



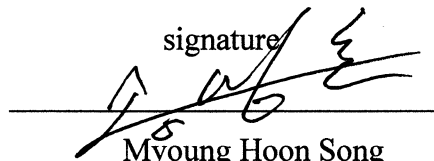
Jin Young Kim

signature



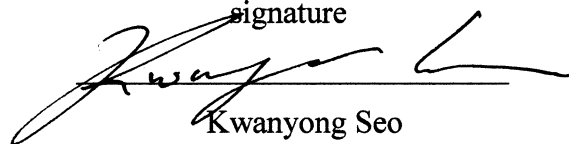
Sang Kyu Kwak

signature



Myoung Hoon Song

signature



Kwanyong Seo

Abstract

Flexible transparent electrode is an essential component for several kinds of electronic and optoelectronic applications, such as organic solar cells (OSCs), perovskite solar cells (PSCs), organic light-emitting diodes (OLEDs), touch sensors, and electronic skins (E-skins). Although conventional indium tin oxide (ITO) has been widely used in commercial transparent electrodes, it still shows a limitation in the fabrication of flexible transparent electrodes for applications in flexible/wearable electronic devices because of their inherent brittleness. Among various alternatives of ITO, silver nanowire (AgNW) network has been considered as promising conductive nano-material due to their high electrical conductivity, excellent transmittance, and mechanical flexibility that can be readily deposited by cost-effective and large-scale solution process. However, random AgNW networks prepared by solution processing have several drawbacks, such as high junction resistance between nanowires (NWs), low transmittance, haze issues, and rough surface morphologies, resulting in a degradation of the device performance. Electrical and optical properties of random AgNW networks can be strongly affected by controlling NW density, electrical current path, and junction resistance related to conductive percolated networks. Therefore, manipulating the assembled structure of AgNW network can provide powerful platforms to realize ideal flexible transparent electrodes with high electrical conductivity, superior transmittance, and smooth surface morphologies for achieving high-performance electronic and optoelectronic device.

In this thesis, we introduce aligned AgNW transparent electrodes and their applications in flexible optoelectronic and functional electronic devices. Firstly, Chapter 1 introduces the research trends in transparent electrodes and several issues of AgNW networks that should be carefully considered in the fabrication for their potential device applications. In chapter 2, we demonstrate the capillary printing technique to make highly aligned AgNW network to fabricate high-performance transparent electrodes for improving device efficiency of optoelectronic devices including OSCs and OLEDs. In Chapter 3, we demonstrate the fabrication of nanoparticle (NP)-enhanced plasmonic AgNW electrode for high-performance optoelectronic devices in which the NP-NW hybrid plasmonic system generates gap plasmonic coupling which induces a large electric field enhancement, resulting in an improvement of the device efficiency in both OSC and OLED devices. In Chapter 4, we demonstrate the fabrication of ultrathin and flexible perovskite solar cell foils with orthogonal AgNW electrodes, which exhibits high power-per-weight performance as well as a conformal contact capability to curvilinear surface. In Chapter 5, we introduce a large-scale assembly technique to uniformly align AgNW arrays for the fabrication of large area transparent electrodes, where cross-aligned AgNW network shows better electrical and optical properties as well as large-scale uniformity than random AgNW network. For the proof of the concept demonstration, we fabricated a flexible force-sensitive touch screen panel

integrated with a mechanochromic polymer film. Finally, we introduce a transparent and conductive nano-membrane (NM) incorporated with orthogonal AgNW arrays in Chapter 6, which exhibits enhanced electrical and mechanical properties than pure polymeric NMs. To show the unique properties of these hybrid NMs for potential device applications, we demonstrate skin-attachable thermoacoustic-based NM loudspeaker and wearable NM microphone, both of which show much improved device performances compared to conventional thin film-based devices.

In this thesis, studies on aligned AgNW transparent electrodes and their device applications could be further expanded for diverse flexible and wearable optoelectronic and electronic applications, such as conformal wearable sensors, healthcare monitoring devices, and wearable plasmonic devices.

Contents

Abstract	1
Contents	4
List of Figures	6
List of Tables	21
Nomenclature	22
Chapter 1. Introduction	24
1.1 Transparent electrodes	25
1.2 Next generation conducting nano-materials	27
1.3 Silver nanowire (AgNW) networks	29
- Synthesis of AgNW	31
- Conductive percolation network	31
- Junction resistance	32
- Surface morphology	34
- Optical property	35
1.4 Other types of transparent electrodes	36
1.5 Device application of transparent AgNW electrode	37
- Solar cells	37
- Displays (OLED)	40
- Touch panel	42
Chapter 2. Aligned AgNW network for high-performance transparent electrode	45
2.1 Introduction	45
2.2 Experimental Details	47
2.3 Results and Discussion	48
2.4 Conclusions	72
Chapter 3. Plasmonic behaviors of aligned AgNW network decorated by Ag nanoparticles for high-performance optoelectronic devices	73
3.1 Introduction	73
3.2 Experimental Details	75
3.3 Results and Discussion	77
3.4 Conclusions	94

Chapter 4. Ultrathin transparent electrodes with orthogonal AgNW arrays for light-weight and flexible perovskite solar cells -----	95
4.1 Introduction -----	95
4.2 Experimental Details -----	97
4.3 Results and Discussion -----	99
4.4 Conclusions -----	114
Chapter 5. Large-area and uniform transparent electrodes with cross-aligned AgNW network for flexible touch screen applications. -----	115
5.1 Introduction -----	115
5.2 Experimental Details -----	117
5.3 Results and Discussion -----	120
5.4 Conclusions -----	148
Chapter 6. Transparent, and conductive nano-membrane (NM) with orthogonal AgNW arrays for wearable acoustic device applications. -----	149
6.1 Introduction -----	149
6.2 Experimental Details -----	151
6.3 Results and Discussion -----	152
6.4 Conclusions -----	178
Chapter 7. Summary and Future perspective -----	179
References -----	183
Appendix A: List of Achievements -----	204
Acknowledgements -----	206

List of Figures

Figure 1.1. Representative images to show recent research trends for flexible/wearable electronic and optoelectronic device applications. (Sekitani et al. *Nat. Mater.* **2009**, 8, 494, Gaynor et al. *Adv. Mater.* **2013**, 25, 4006, Muth et al. *Adv. Mater.* **2014**, 26, 6307, Miyamoto et al. *Nat. Nanotechnol.* **2017**, 12, 907, Lipomi et al. *Nat. Nanotechnol.* **2011**, 6, 788, Liang et al. *Nat. Photonics* **2013**, 7, 817, Lee et al. *Nat. Nanotechnol.* **2016**, 11, 472)

Figure 1.2. The various applications for transparent electrodes with varying the sheet resistance. Such electronic and optoelectronic devices have required different sheet resistance for stable operation and performance of their devices. (Bae et al., *Phys. Scr.*, **2012**, T146, 014024)

Figure 1.3. (a) The sheet resistance vs visible transmittance for various transparent electrodes with different conducting materials including ITO (K. Ellmer, *Nat. Photonics*, **2012**, 6, 809). The various candidates for alternative to ITO, such as (b) silver nanowires (Hu et al. *ACS nano* **2009**, 3, 1767), (c) carbon nanotubes (Wu et al. *Science* **2004**, 305, 1273), (d) graphene (Kim et al. *Nature* 2009, 457, 706), (e) metal mesh (Schneider et al. *Adv. Funct. Mater.* **2016**, 26, 833).

Figure 1.4. (a) The photograph of AgNW ink in ethanol solvent in a vial. (b) Bar-coating method for the fabrication of AgNW network on plastic substrate. (c) Flexible transparent electrode with random AgNW network. (d) The SEM image of random AgNW network. (Hu et al. *ACS Nano* **2010**, 4, 2955)

Figure 1.5. (a) Schematic illustration of the grow mechanism for the AgNW with pentagonal nano-structure. (b) SEM image of AgNWs synthesized by the polyol process (Sun et al. *Nano Lett.* **2003**, 3, 955).

Figure 1.6. Conductive percolated networks for transparent electrode with random AgNW network where green arrow indicates current path due to interconnecting with NWs (Lee et al. *Adv. Mater.* **2012**, 24, 3326).

Figure 1.7. The schematic of random AgNW network in which interconnected NWs generate many contact points (red dot), which cause high junction resistance. (Mutiso et al. *ACS Nano* **2013**, 7, 7654)

Figure 1.8. SEM image of AgNW network with low junction resistance due to (a) mechanical pressing (Tokuno et al. *Nano Res.* **2011**, 4, 1215) (b) soldering with graphene (Liang et al. *ACS Nano* **2014**, 8, 1590). (c) Post-annealing effect at 200°C for lowering junction resistance (Lee et al. *Nano Lett.* **2008**, 8, 689). (d) TEM image of the junction between NWs in which two NWs are well combined by plasmonic welding process (Garnett et al. *Nat. Mater.* **2012**, 11, 241).

Figure 1.9. (a) The SEM image of AgNW network embedded into soft polymeric matrix by using mechanical pressing method. (Gaynor et al. *Adv. Mater.* **2011**, 23, 2905). (b) Cross-sectional SEM image of AgNWs embedded in ITO nanoparticles films (Chung et al. *Nano Res.* **2012**, 5, 805). (c) (Left) The

schematic illustration and (right) a TEM image of random AgNW network embedded in NOA 63 matrix. (Nam et al. *Sci. Rep.* **2014**, 4, 4788)

Figure 1.10. (a-c) Various patterned transparent electrodes fabricated by using different lithographic techniques, such as (a) E-beam lithography (Hsu et al. *Nat. Commun.* **2013**, 4, 2522), (b) grain boundary lithography (Guo et al. *Nat. Commun.* **2014**, 5, 3121), and (c) microsphere lithography (Gao et al. *Nano Lett.* **2014**, 14, 2105). (d-f) Electrospun transparent electrode fabricated by using different methods, such as (d) metal nano-trough (Wu et al. *Nat. Nanotechnol.* **2013**, 8, 421), (e) selective etching (He et al. *ACS Nano* **2014**, 8, 4782), and (f) metal electroless deposition (Hsu et al. *J. Am. Chem. Soc.* **2014**, 136, 10593)

Figure 1.11. (a) Energy-level diagram showing work functions of each component materials. (b) The device structure for the solution-processed OSC with the AgNW electrode as anode (Yang et al. *ACS Appl. Mater. Interfaces* **2011**, 3, 4075).

Figure 1.12. Characteristic J - V curves of OSC solar cell devices based on random AgNW electrodes (Yang et al. *ACS Appl. Mater. Interfaces* **2011**, 3, 4075).

Figure 1.13. A schematic of organic solar cells with AgNW network where the light scattering and trapping effects are induced under the illumination. (Wang et al. *Small* **2015**, 11, 1905)

Figure 1.14. The photograph of white OLEDs with angular color stability incorporated with AgNW-based transparent electrodes. (Gaynor et al. *Adv. Mater.* **2013**, 25, 4006)

Figure 1.15. (a) A schematic illustration of stretchable PLED using random AgNW with graphene oxide fabricated on elastomeric substrate. (b) The characteristics of current density-luminance-driving voltage. (c) Optical photographs of stretchable PLED under applied strain from 0% to 130%. (Liang et al. *ACS Nano* **2014**, 8, 1590)

Figure 1.16. The illustration of commercial touch screen with AgNW-based transparent electrodes. (Cambrios Technologies Corp., <http://www.cambrios.com/>, accessed: May 2018.)

Figure 1.17. (a) The schematic structure of capacitive type touch pad with AgNW electrode fabricated on PDMS substrates. (b) The variation of electrical signal response to finger touch. (c) Touch sensitivity test. (Lee et al. *Adv. Funct. Mater.* **2014**, 24, 3276.)

Figure 1.18. (a) The schematic illustrations of (left) commercial touch panel with ITO/spacer/ITO/glass and (right) flexible touch panel fabricated with AgNW electrodes soldered with conducting polymer. (b) The photographs of touch screen operation by writing a word “KAIST”. (Lee et al. *Adv. Funct. Mater.* **2013**, 23, 4171)

Figure 2.1. (a) Schematic of the procedure for capillary printing using a nano-patterned PDMS stamp for alignment of AgNW array. Optical microscopy (b) and scanning electron microscopy (c) images indicate the nano-patterned PDMS stamp with 400 nm of line width. Scale bars are 10 μm and 1 μm .

Figure 2.2. Solution-printed highly aligned AgNW arrays. (a) Schematic of the capillary printing process using a nano-patterned PDMS stamp to produce highly aligned AgNW arrays. (b) Schematic showing the alignment process during capillary printing of unidirectional AgNW arrays. The solvent-evaporation-induced capillary force produces highly aligned networks by dragging confined AgNWs at the solid-liquid-vapor contact line. (c) Dark-field optical images of differently oriented AgNW structures fabricated with a solution concentration of 0.05 wt% via one-step (unidirectional) and multi-step (45°, 60°, and 90° crossed) capillary alignments. The scale bar is 40 μm. The fast Fourier transform (FFT) analyses of the images, presented in the insets, show the corresponding geometric structures.

Figure 2.3. Dark-field optical micrographs of AgNW networks fabricated with a concentration of 0.1 wt.% by capillary printing using (a,b) nano-patterned, (c,d) micro-patterned and (e) flat PDMS stamps, respectively. The printing conditions include a speed of 1.5 mm/s and a pressure of 1.57 kPa. Alignment using nano-patterned PDMS stamps provides aligned AgNW networks with a characteristic line-shaped FFT pattern, in contrast to the blurred circular FFT pattern produced from networks using a flat PDMS stamp. All scale bars are 40 μm.

Figure 2.4. Effect of the angle of the triangular PDMS stamp on the NW alignment process. Photographic images of AgNW arrays prepared using triangular PDMS stamps with angles of (a) 5°, (b) 10°, (c) 20°, and (d) 30°. (e-h) Close-up images of the menisci formed using triangular PDMS stamps with different angles (5°-30°). (i-l) Dark-field images of aligned AgNW arrays coated using triangular PDMS stamps with different angles on glass treated by O₂ plasma. The scale bar is 40 μm.

Figure 2.5. (a) Schematic illustration showing the measurement of contact pressure between the nano-patterned PDMS stamp and the substrate. (b) Dark-field optical micrographs of aligned AgNW networks fabricated with a concentration of 0.5 wt.% using different contact pressures (0-3.14 kPa). Line-shaped FFT patterns in the insets demonstrate that the alignment degree is increased with increasing contact pressure. The scale bar is 40 μm.

Figure 2.6. Dark-field optical micrographs of aligned AgNWs deposited on substrates chemically modified by (a) hexamethyldisilazane (HMDS), (b) O₂ plasma treatment, (c) (3-Aminopropyl)triethoxysilane (APTES), (d) poly-L-lysine (PLL), and (e) 3-(2-Aminoethylamino)propyltrimethoxysilane (AAPTS). The scale bar is 40 μm. (f) The surface density of aligned AgNWs deposited on differently modified substrates.

Figure 2.7. (a) Photographs of glass, PET, and PDMS substrates deposited with aligned AgNW arrays. (b) Dark-field optical micrographs of highly aligned AgNW arrays using a concentration of 0.05 wt.% measured at three points on the glass substrate with a size of 25 mm × 25 mm. All scale bars are 40 μm.

Figure 2.8. (a) Dark-field optical micrographs of random AgNW network fabricated by spincoating. The scale bar is 40 μm. FFT image provided in inset. (b) Radial summation of pixel intensity distribution between 0° and 360° in the FFT analyses of AgNW networks with aligned and random structures. (c)

Radial summation of pixel intensity distribution between 0° and 360° in the FFT analyses of different geometric (45° , 60° , 90° crossed) AgNW networks fabricated via multi-step capillary printing alignment process.

Figure 2.9. Quantitative FFT analyses of the degree of alignment of capillary-printed AgNW networks. (a) Optical micrographs of aligned AgNW networks fabricated using different coating speeds (0.5 - 10 mm s^{-1}) and solution concentrations (0.1 - 0.5 wt.%) on PLL-coated substrates. FFT images in the insets of the optical micrographs indicate unidirectional structures with anisotropic features. The scale bar is 20 μm . FWHM fitting data, calculated from the radial summation of pixel intensity in the FFT images, indicates the degree of alignment for printed AgNW networks fabricated with (b) different solution concentrations and (c) different coating speeds.

Figure 2.10. Radial summation of pixel intensity between 0° and 180° in FFT analyses of dark-field optical micrographs for aligned AgNW networks coated using (a) different solution concentrations (0.1 - 0.5 wt.%) and (b) different coating speeds (0.5 - 10.0 mm s^{-1}).

Figure 2.11. Electrical percolation behaviors of AgNW networks with different geometries. (a) Comparison of R_s in aligned and random AgNW networks as a function of surface area density. Power-law fits of R_s for (b) aligned and (c) random AgNWs as a function of $(S - S_c)$, where S_c (%) is the critical surface area density for the onset of conductivity

Figure 2.12. Comparison of optical and electrical performances of AgNWs with aligned and randomly oriented networks. (a) SEM images of aligned AgNW and random AgNW networks show good agreement with corresponding geometric structures. Schematics provide a basis for the understanding of the electrical percolation behavior of the networks. All scale bars are $2\mu\text{m}$. (b) Sheet resistance (R_s) for AgNW networks with aligned and randomly oriented geometries as a function of NW linear density. (c) Optical transmittance T (solid lines) and haze factor (dashed lines) over the visible spectrum for aligned (blue) and random (red) AgNWs with similar R_s values. The substrate was used as a reference. (d) Change in the R_s of aligned AgNW networks as a function of the alignment degree, wherein FWHM values are calculated from the radial summation of the pixel intensity in FFT patterns. Comparison of (e) the R_s - T performance and (f) FoM values of different AgNW electrodes.

Figure 2.13. (a) Change in NW linear density and (b) T over the visible light range (400 - 800 nm wavelength) for aligned AgNW networks fabricated with different coating speeds. (c) The comparison of NW density of our work with the NW densities of other assembly techniques estimated from the reported results.

Figure 2.14. Sheet resistances of aligned AgNW networks for different measurement directions as a function of FWHM values. Aligned AgNW networks with various alignment degrees were fabricated with solution concentrations of 0.05 - 0.5 wt.%, coating speed of 1.5 mm s^{-1} , and coating pressure of 1.57 kPa.

Figure 2.15. Mechanical properties of aligned AgNW films on PET substrates. (a) Variations in resistance of aligned AgNW film as a function of bending radius. (b) Resistance change over the course of 1000 bending cycles at the bending radius of 1.25 mm. Resistance was measured after the films were released and had resumed the lengths measured prior to bending.

Figure 2.16. Device structure and characteristics of PLEDs using aligned AgNW electrodes. (a) Schematic PLED structure. (b) Schematic energy level diagrams under the flat-band condition for PLEDs with AgNW electrodes. (c) Current density, (d) luminance, (e) luminous efficiency, and (f) power efficiency with changes in the applied voltage for PLEDs with ITO, random, and aligned AgNW electrodes.

Figure 2.17. AFM images of (a) aligned AgNW networks and (b) random AgNW networks. The surface roughness of aligned AgNWs films is lower than that of random AgNWs films. The scale bars are 2 μm . Optical images for the surface of PEDOT:PSS coated onto (c) aligned and (d) random AgNW films. The scale bars are 100 μm . The surface of random AgNWs films shows the protrusion of NWs through the PEDOT:PSS layer. The scale bars of the magnifications are 20 μm .

Figure 2.18. Transmittance spectra of ITO, random AgNW, and aligned AgNW films on glass substrates.

Figure 2.19. Device structure and characteristics of PSCs using aligned AgNW electrodes. (a) Schematic PSC structure. (b) Schematic energy level diagrams under the flat-band condition. (c) J - V characteristics under AM 1.5 illumination at 100 mW cm^{-2} and (d) IPCE of PSCs with ITO, random, and aligned AgNW electrodes.

Figure 2.20. Light-emitting characteristics. Variations in (a) current density, (b) luminance, (c) EL efficiency, and (d) power efficiency with applied voltage using ITO-coated and random or aligned AgNW-based electrodes on flexible substrates.

Figure 2.21. J - V characteristics under AM 1.5 illumination at 100 mW cm^{-2} with ITO and aligned AgNWs for flexible PSCs.

Figure 2.22. Performances of flexible PLEDs and PSCs. (a) Normalized luminance of flexible PLEDs and (b) power conversion efficiency (η) of PSCs using ITO and aligned AgNW on PET substrates over the course of 1000 bending cycles at 5 V with a bending radius of 5 mm. The insets show photographs of the flexible aligned AgNW-based PLED and PSC.

Figure 3.1. Hybrid NP-enhanced plasmonic AgNW network. (a) Representative illustration of a NP-enhanced plasmonic AgNW network. (b) Schematic illustration of plasmon coupling in a NW-NP hybrid plasmonic system showing the interaction between LSP of a metal NP and propagating SPP on a metal NW. (c) Transmission electron microscopy (TEM) image of core-shell Ag@SiO₂NPs. The scale bar indicates 20 nm. (d,e) SEM images of an aligned AgNW network decorated with core-shell Ag@SiO₂NPs. Scale bars indicate 500 nm and 100 nm, respectively. (f) Optical transmittance of an aligned AgNW decorated with Ag@SiO₂NPs film in the visible region. (g) Optical absorption spectra

of (top) aligned AgNW networks decorated with different densities of Ag@SiO₂NPs, (bottom) AgNP and Ag@SiO₂NPs in the range of 300–800 nm. (h) Polarization dependent optical absorption spectra of aligned AgNW networks decorated with Ag@SiO₂NPs. Polarization angles are defined as parallel (0° of polarization) and perpendicular (90° of polarization) to the axis of the NWs.

Figure 3.2. (a) TEM image of core-shell Ag@SiO₂ NPs, which comprise of core AgNP and SiO₂ shells (b) The size distribution of core-shell Ag@SiO₂ NPs, obtained from an image analysis of 60 core-shell Ag@SiO₂ NPs in TEM images.

Figure 3.3. Schematic of fabrication process for NP-enhanced plasmonic AgNW electrodes on glass substrates.

Figure 3.4. SEM images of aligned AgNW network. All scale bars indicate 1 μm.

Figure 3.5. Optical absorption spectra of (a) aligned AgNW and (b) random AgNW with different polarization of incident light.

Figure 3.6. Simulated extinction spectra of a single AgNW and an AgNW-Ag@SiO₂NP junction.

Figure 3.7. Enhancement in extinction spectrum of NP-enhanced plasmonic AgNWs.

Figure 3.8. Plasmonic behavior of NP-enhanced plasmonic AgNW electrodes. E-field distribution of (a) an AgNW and (b) an AgNW decorated with an Ag@SiO₂NP. Incident light of 416 nm wavelength is polarized perpendicular to the long axis of the NW. (c) Schematic of plasmonic behavior of an AgNW decorated with an Ag@SiO₂NP. The AgNP on the AgNW acts as nano-antenna to couple incident light into SPPs propagating along the NW (top). Calculated electric field intensity for NW and NP-NW along the NW length (bottom). (d,e) Raman analysis of a NP-NW system with different polarization angles of incident light. (d) SEM image of a single AgNW decorated with an AgNP for Raman analysis. The arrows indicate incident light with perpendicular (purple) and parallel (red) polarization along the NW direction, respectively. The scale bar is 100 nm. (e) Raman spectra of poly-L-lysine (PLL) adsorbed on NP-NW junction using an incident laser with 532 nm wavelength, polarized perpendicular (purple) and parallel (red) along the NW direction. (f) Raman spectra of PLL adsorbed onto NW and NP-NW junction networks. (g-i) Surface-enhanced Raman spectroscopy (SERS) images. Raman mapping images of PLL adsorbed on (g) AgNW, (h) Ag@SiO₂NPs-AgNWs and (i) Ag@SiO₂NPs on glass substrates.

Figure 3.9. E-field distribution for single AgNW and AgNW decorated with Ag@SiO₂NP when the incident light at 416 nm, polarized in parallel direction to NW.

Figure 3.10. (a-c) SEM images for three different structures of (a) AgNW, (b) AgNW-Ag@SiO₂NPs, and (c) Ag@SiO₂NPs. All scale bars indicate 1 μm.

Figure 3.11. Photoluminescence behavior of fluorescent SY films on NP-enhanced plasmonic AgNW electrodes. Confocal images of (a) an aligned AgNW network and (b) an aligned AgNW network decorated by Ag@SiO₂NPs coated by SY. The scale bars indicate 5 μm. (c) High-resolution confocal

image of a single AgNW decorated by an Ag@SiO₂NP, coated by SY where significant enhancement of fluorescence emission is observed at the NW-NP junction. The scale bar is 4 μm. (d) Steady-state photoluminescence spectra of SY films with an aligned AgNW network and an aligned AgNW network decorated by Ag@SiO₂NPs.

Figure 3.12. Device structure and characteristics of OLEDs using NP-enhanced plasmonic AgNW electrodes. (a) Schematic device structure of OLEDs with NP-enhanced plasmonic AgNW electrodes. (b) Schematic energy level diagram under the flat-band condition. (c) Current density, (d) luminance, (e) luminous efficiency and (f) power efficiency versus applied voltage for OLEDs with ITO, aligned AgNW, and NP-enhanced plasmonic AgNW electrodes.

Figure 3.13. Device structure and characteristics of OSCs using NP-enhanced plasmonic AgNW electrodes. (a) Schematic device structure of OSCs with NP-enhanced plasmonic AgNW electrodes. (b) Schematic energy level diagram under the flat-band condition. (c) *J-V* characteristics of under AM 1.5G illumination at 100 mWcm⁻². (d) IPCE spectra of OSCs using ITO, aligned AgNW and NP-enhanced plasmonic AgNW electrodes.

Figure 3.14. Comparison of EQE enhancement with absorption changes caused by AgNW-Ag@SiO₂NPs.

Figure 3.15. Photocurrent density versus effective voltage for devices with AgNW and Ag@SiO₂NPs-AgNW electrodes.

Figure 4.1. (a) Schematic illustrations of the fabrication procedure for ultrathin orthogonal AgNW transparent electrodes produced on 1.3 μm-thick PEN foil. (b) Dark-field optical microscope image of the orthogonal AgNW arrays with corresponding fast Fourier transform (FFT) pattern of inset image. The scale bar indicates 40 μm. (c) The ultrathin orthogonal AgNW transparent electrode foil, crumpled by a person's finger. (d) An ultrathin and lightweight PSC device mounted on a surface of the leaf. (e) Cross-sectional SEM image of device structure for PSC with orthogonal AgNW array. The scale bar is 100 nm. (f-h) Mechanical properties of the orthogonal AgNW transparent electrode foils. Variation in resistance of orthogonal AgNW electrode foil as a function of (f) bending cycles at a bending radius of 2 mm, (g) crumpling cycles, and (h) twisting angles. The inset images show corresponding deformation (twisting, crumpling, bending) of orthogonal AgNW electrode foil, adhered to PDMS thin film.

Figure 4.2. Dark-field optical micrograph of random AgNW network. The fast Fourier transform (FFT) image of the optical micrograph in the inset exhibits a blurred circular pattern, indicating corresponding surface geometric structure.

Figure 4.3. The optical transmittance of orthogonal AgNW and random AgNW electrodes, deposited on glass substrates, in visible range of 350-800 nm wavelength with corresponding sheet resistance. The glass substrate was used as reference.

Figure 4.4. The energy band diagram for the PSC with orthogonal AgNW electrode.

Figure 4.5. (a) A schematic illustration of silver-halide formation in PSCs fabricated on random and orthogonal AgNW electrodes. (b,c) Tilted SEM images of the surface of PEDOT:PSS coated on (b) PH1000/orthogonal AgNW electrode and (c) PH1000/random AgNW electrode, respectively. (d,e) AFM images of the surface of PEDOT:PSS coated on (d) PH1000/orthogonal AgNW electrode and (e) PH1000/random AgNW electrode, respectively. (f) The variation in the resistance of both the random and orthogonal AgNW electrodes as a function of the SVA time. (g,h) The distribution of the Ag originated from XPS-depth profiles of PSCs with (g) orthogonal AgNW and (h) random AgNW electrodes, respectively.

Figure 4.6. The SEM images for the surface of perovskite active layers, deposited on PEDOT:PSS/PH1000/AgNW, as a function of the SVA time.

Figure 4.7. (a) J - V characteristic and (b) IPCE of PSC devices with ITO, orthogonal AgNW, and random AgNW electrodes. (c) Long-term stability of PSCs in controlled atmosphere (N_2 -filled glove box). (d) The quantitative PCE values of PSCs with ITO, orthogonal AgNW, and random AgNW electrodes.

Figure 4.8. J - V hysteresis characteristic of PSC with orthogonal AgNW electrode measured with forward and reverse bias.

Figure 4.9. (a) J - V characteristic of flexible PSC and ultralight PSC with orthogonal AgNW foil electrode. (b) Ultralight PSC adhered to a toy robot in which two copper wires are connected to anode and cathode of PSC, respectively. (c) Ultralight PSC suspended in bubbles. (d) The power-per-weight performance of ultralight PSC compared to other types of light solar cells.

Figure 4.10. (a) A photograph of flexible PSC fabricated on the orthogonal AgNW electrode. (b) The variation in normalized device efficiency of PSCs with ITO and orthogonal AgNW electrodes under repeated 1000 times bending cycles.

Figure 4.11. A photograph of ultralight PSC device attached to a miniaturized toy robot to demonstrate wearable feature. Such ultralight PSC device was connected with two copper wires and 91Ω load, which produced 7.8 mW with an open circuit voltage of 0.84V on a sunny spring.

Figure 4.12. A photograph of ultralight PSC device put on an electric scale, indicating extremely light weight.

Figure 5.1. (a) Photographs of various kinds of Meyer rods (#2, #3, #6, #10, and #15) and (b) corresponding optical microscope images. The scale bar is 200 μm . (c) Schematic illustration of the specifications of various Meyer rods. The rod number determines the diameter of wrapped wires and the open area.

Figure 5.2. Large-scale bar-coating alignment of unidirectional and cross-aligned AgNW arrays. (a) A photograph of the solution-processed bar-coating alignment of the AgNWs on a $20 \times 20 \text{ cm}^2$ PET substrate and (b) a schematic showing the alignment process of AgNWs during the bar-coating assembly

of the AgNW solution. The combined interaction between shear stress alignment and the electrostatic pinning produced highly aligned and uniform AgNW arrays during the dragging of a confined meniscus between the rod and substrate. (c) Dark-field optical microscope images of the unidirectionally aligned and (d) cross-aligned AgNW arrays. Insets are the fast Fourier transform (FFT) analyses of the optical micrographs indicating the direction and uniformity of the aligned AgNW structures. The scale bars are 40 μm . (e) Distribution of the alignment degrees of 150 NWs in Fig. 1c with a full width at half maximum (FWHM) value of 21.4. (f) Mapping image showing the highly uniform distribution of FWHM values of each pixel in a 4×4 array over a large-area ($20 \times 20 \text{ cm}^2$) of aligned AgNWs. The FWHM values were calculated by fitting the radial summation of the pixel intensities of the FFT analysis.

Figure 5.3. Schematic of an overall procedure for the solution-processed bar-coating assembly to fabricate unidirectionally and cross-aligned AgNW arrays. Before the bar-coating assembly, poly-L-lysine (PLL) solution is coated on O_2 plasma-treated target substrate to form amine groups on the surface. Consecutively, the meniscus dragging produces highly aligned AgNW arrays. The cross-aligned AgNW array is formed by repeating the bar-coating assembly in a perpendicular direction to that of the pre-aligned AgNW arrays.

Figure 5.4. Dark-field optical micrographs of the unidirectionally aligned AgNWs coated with AgNW ink dispersed in different kinds of solvents; (a) isopropyl alcohol (IPA), (b) water, and (c) ethanol. During the bar-coating assembly, #2 bar, 3 μl of volume, and 10 mm s^{-1} of coating speed were used in all experiments. The scale bar is 40 μm .

Figure 5.5. Dark-field optical micrographs of the aligned AgNW networks coated on substrates modified with different types of functional groups; (a) PLL ($-\text{NH}_2$), (b) hexamethyldisilazane (HMDS) ($-\text{CH}_3$), and (c) O_2 plasma ($-\text{OH}$). During the bar-coating assembly, #2 bar, 3 μl of volume, and 10 mm s^{-1} of coating speed were used in all experiments. The scale bar is 40 μm .

Figure 5.6. X-ray photoelectron spectroscopy (XPS) survey to investigate the interactions between AgNWs and the substrate surface pretreated with different functional groups with PLL, HMDS, and O_2 plasma. (a) High resolution N 1s spectra of the pristine AgNW, PLL, PLL/AgNW, HMDS/AgNW, and O_2 plasma/AgNW. (b) High resolution C 1s spectra of the pristine AgNW, HMDS/AgNW, and O_2 plasma/AgNW. (c) High resolution Ag 3d spectra of the pristine AgNW, PLL/AgNW, HMDS/AgNW, and O_2 plasma/AgNW.

Figure 5.7. The radial summations of the pixel intensities of the fast Fourier transform (FFT) analysis data as a function of radial angle (0 - 180°) of the unidirectional AgNW array, cross-aligned AgNW arrays, and random AgNW network. Contrary to aligned and cross-aligned AgNWs networks which show clear Gaussian peaks, random AgNW network shows uncertain spectra of radial summations due to the lack of directionality.

Figure 5.8. Dark-field optical micrograph of the random AgNW networks fabricated by conventional bar-coating process. Inset shows the corresponding FFT analysis data. The scale bar is 40 μm .

Figure 5.9. Large-area ($20 \times 20 \text{ cm}^2$) alignment of the AgNWs by bar-coating assembly. 16 dark-field optical micrographs of the aligned large-area AgNW arrays in a large-area ($20 \times 20 \text{ cm}^2$) PET film and the corresponding FFT analysis images in the insets. For the bar-coating assembly, #2 bar, 100 μl of volume, and 10 mm s^{-1} of coating speed were used in the experiment. The FWHM values of 16 AgNW arrays confirm the high uniformity and the scalability of the bar-coating assembly process as shown in Figure 5.2f. The scale bar is 40 μm .

Figure 5.10. Unidirectional bar-coating alignment of the AgNW arrays and the anisotropic optical properties. (a-c) FWHM values according to the variation in the bar-coating parameters, including the amount of solution (2-40 μl), coating speed (10-70 mm s^{-1}), and substrate temperature (23-60 $^{\circ}\text{C}$). (d-f) Anisotropic optical properties of the unidirectional AgNW arrays. (d) Schematic showing the polarized absorption test as a function of the angle θ between the direction of the polarized incident light and the NW alignment. (e) Polarized UV-vis absorption spectra of unidirectionally aligned AgNW arrays as a function of polarization angle (0-90 $^{\circ}$). (f) Optical dichroic property of unidirectionally aligned AgNW array. Polarized optical microscope images of “UNIST” patterns with different AgNW alignment directions exhibits invisible AgNW arrays when the light was polarized parallel to the direction of AgNW alignment ($\theta = 0^{\circ}$) and clearly visible AgNW array when the light was polarized perpendicular to the direction of AgNW alignment ($\theta = 90^{\circ}$). The scale bar is 100 μm .

Figure 5.11. Dark-field optical micrographs of the aligned AgNW networks fabricated by the bar-coating assembly with different coating conditions; (a) volume of solution (2-40 μl), (b) coating speed (10-70 mm s^{-1}), and (c) substrate temperature (23-60 $^{\circ}\text{C}$). All insets show the corresponding FFT analysis images. The scale bar is 40 μm .

Figure 5.12. The effect of the amount of AgNW dispersion on the formation of contact area between the meniscus and the substrate. Schematics and close-up photographs show the meniscus between the rod and substrate with a different volume of dispersion (2-40 μl). As the volume of dispersion increases, the contact area becomes broader. The scale bars are 500 μm (top) and 1000 μm (bottom).

Figure 5.13. Schematic showing the intensity distribution of shear force according to the variation of the height (δ) of meniscus. In the meniscus dragging process, the shear force gradient is generated as a function of the height of the meniscus in a Couette flow. Therefore, the AgNWs located far from the dragging bar have a high probability of misalignment due to a reduced shear force. In thick meniscus film, many of AgNWs are located far from the dragging bar and thus have a high probability of misalignment. In thin meniscus film, most of AgNWs are near the dragging bar, which results in the high probability of alignment.

Figure 5.14. The effect of spacer thickness for the alignment of AgNWs. (a) Schematics showing the different height of the meniscus between the rod and the substrate depending on the thickness of spacer. As the thickness of spacer increases, the height of meniscus increases. (b) Dark-field optical micrographs showing the alignment of AgNWs depending on the variation of spacer thickness (20-120 μm). During the bar-coating assembly, #2 bar and 10 mm s^{-1} of coating speed were used in all experiments. The scale bar is $40 \mu\text{m}$.

Figure 5.15. Polarized UV-Vis absorption spectra of the random AgNW networks as a function of polarization angle (θ) from 0 to 90° . As compared to aligned AgNW arrays, random AgNW networks without any anisotropic optical properties do not show any noticeable change in their absorption peaks as the polarization angle increases.

Figure 5.16. Schematics showing the polarized optical microscope modes according to the direction between the polarizing filter and the AgNW alignment direction; (a) $\theta = 0^\circ$, (b) $\theta = 90^\circ$. When the polarizing filter and the aligned AgNW array have the same vertical polarization direction ($\theta = 0^\circ$), vertically polarized light passes through the aligned AgNW film. However, when the polarizing filter and aligned AgNW array have the perpendicular polarization direction ($\theta = 90^\circ$), polarized light cannot penetrate the aligned AgNW film.

Figure 5.17. Dark-field optical micrographs of cross-aligned AgNW arrays by varying the number of cross-coatings for bar-coating conditions of (a) #2 bar and $3 \mu\text{l}$, (b) #3 bar and $4 \mu\text{l}$, and (c) #6 bar and $8 \mu\text{l}$. All of the cross-aligned AgNW arrays were fabricated at the coating speed of 10 mm s^{-1} . The scale bar is $40 \mu\text{m}$.

Figure 5.18. Optical and electrical performance of the large-area transparent conductive electrodes (TCEs) using the cross-aligned AgNW networks. (a) UV-vis spectra and corresponding sheet resistance, R_s , of cross-aligned AgNW arrays with different numbers of cross-coatings. The substrate was used as a reference in all UV-vis experiments. (b) R_s versus optical transmittance, T , at 550 nm for the cross-aligned and random AgNW networks fitted by percolative regime. (c) R_s versus T performance of various AgNW TCEs. (d) A photograph of large-scale ($20 \times 20 \text{ cm}^2$) TCE coated with uniform cross-aligned AgNW arrays (top), and schematic showing its 4×4 pixels for analysis (bottom). (e) 4×4 pixels mapping images showing the R_s distribution of cross-aligned and (f) random AgNW networks over a large substrate area ($20 \times 20 \text{ cm}^2$). The average R_s was set so as to be similar in both films. (g) 4×4 pixels mapping images showing the T distribution of cross-aligned and (h) random AgNW networks over a large substrate area ($20 \times 20 \text{ cm}^2$).

Figure 5.19. Mechanical stability of cross-aligned AgNW based TCEs on PET substrate. (a) Variation in resistance of cross-aligned AgNW TCEs as a function of bending radius. (b) Resistance change of cross-aligned AgNW TCEs during 1000 bending cycles at the bending radius of 1.5 mm .

Figure 5.20. Large-scale, flexible, and transparent touch screens using cross-aligned AgNW TCEs. (a) Schematic showing the structure of the large-scale, flexible, and transparent touch screen using the cross-aligned AgNW arrays on a PET substrate connected to a laptop computer through a controller board. (b) A photograph of the large-scale, flexible, and transparent touch screen ($20 \times 20 \text{ cm}^2$) using cross-aligned AgNW TCEs. (c) Demonstration of writing alphabet letters on the transparent touch screen, which have been recorded on the computer monitor. (d) Demonstration of tracing a picture of a butterfly placed under the transparent touch screen.

Figure 5.21. (a-f) Output images of touch signal and (g) normalized gap distance between adjacent touch signals, generated by two touch points pressed with different gap distance of (a) $0 \mu\text{m}$, (b) $50 \mu\text{m}$, (c) $100 \mu\text{m}$, (d) $200 \mu\text{m}$, (e) $500 \mu\text{m}$, and (f) $1000 \mu\text{m}$ on touch screen based on cross-aligned AgNW TCEs. Our touch screen can detect touch location with the resolution of $100 \mu\text{m}$, which corresponds to the resolution of touch controller board. L_0 is defined as minimum gap distance between two touch signals that can be distinguished by touch screen.

Figure 5.22. Demonstration of large scale, flexible touch screen fabricated by cross-aligned AgNW based TCEs. Handwritten letters “FNL” was precisely written on top of curved surface.

Figure 5.23. Flexible, transparent, and force-sensitive touch screens. (a) Schematic illustration of the device structure of a force-sensitive touch screen showing simultaneous force and touch sensing in response to dynamic writings. (b) Schematic illustration of the mechanochromic touch screen system with the color analysis using a spectroradiometer. (c) Normalized luminance at 448 nm wavelength as a function of the writing force. A fitted line shows a linear relationship between the normalized luminance and the writing force. (d) Photographs of mechanochromic color changes on the touch screen as a function of different dynamic writing force. The blue color intensity of the written letters “FNL” on the touch screen increases with the writing force. The scale bar is 1 cm . (e) Normalized luminance spectra of blue color letters “FNL” in visible range ($380\text{-}520 \text{ nm}$). Based on the linear curve in Figure 5c, the applied forces can be determined to be from $F_1 = 4.3 \pm 0.2 \text{ N}$ to $F_5 = 14.9 \pm 3.4 \text{ N}$. (f) Representation of the color coordinates on the CIE 1931 color space according to the different writing force. The X-Y coordinates move to the deep blue region with the increase of applied force. (g) A photograph of the written letter “A” on the mechanochromic touch screen (left) and its 10×10 pixels array of applied force mapping data showing the local force distribution (right). The scale bar is 1 cm .

Figure 5.24. The investigation of the relationship between the color intensity and the applied writing force using a spectroradiometer. (a) The photographs of the different lines on the mechanochromic touch screen as a function of writing force and (b) its normalized luminance spectra in visible range ($380\text{-}520 \text{ nm}$). The horizontal lines are drawn by a stylus as a function of dynamic writing force.

Figure 5.25. The resolution of line width drawn by using different tip size of stylus on mechanochromic SP-PDMS film. (a,b) The stylus with small size of tip can generate very thin blue line with the thickness of $\sim 79 \mu\text{m}$. (c,d) Stylus with large size of tip generates blue line with the thickness of $\sim 147 \mu\text{m}$.

Figure 5.26. Real time monitoring images of mechanochromic colors on the touch screen (a) and its touch signals on the laptop monitor (b). The red dotted squares show the alphabet “A” written by the smallest force during the writing on the mechanochromic touch screen. The scale bar is 2 cm.

Figure 6.1. Fabrication of free-standing hybrid NMs with orthogonal AgNW array. (a) Schematic of fabrication procedure for free-standing hybrid NMs with orthogonal AgNW array embedded in polymer matrix. (b) Free-standing AgNW composite NMs floating on a surface of water. The scale bar indicates 1 cm. (c) Dark-field optical microscope image of orthogonal AgNW arrays. The inset shows a fast Fourier transform (FFT) image of the optical micrograph, corresponding to its surface geometric structure. The scale bar indicates $40 \mu\text{m}$. (d) Cross-sectional SEM image of hybrid NM as-fabricated on a ZnO/Si substrate. The scale bar indicates 100 nm. (e) Optical transmittance of polymer NMs, hybrid NM, bare PET, and bare glass in visible range of 400–800 nm. The glass is used as a reference. (f) Photograph of hybrid NM on surface of water under compressive force applied by a glass rod. The scale bar indicates 3 mm. (g) Free-standing hybrid NM supported by a wire loop. Inset shows the high transparency of the hybrid NM. The scale bar indicates 1 cm. (h) Hybrid NMs transferred onto curvilinear surface and (i) onto human skin.

Figure 6.2. Fabrication of free-standing hybrid NM with orthogonal AgNW array by removing the sacrificial layer.

Figure 6.3. Total thickness of hybrid NMs measured by atomic force microscopy.

Figure 6.4. Transmittance in visible range of 400–800 nm and corresponding sheet resistance, R_s , of the orthogonal AgNW array with different numbers of orthogonal coatings.

Figure 6.5. The structural design of the hybrid NM for the calculation of the bending stiffness with geometrical parameters illustrated.

Figure 6.6. SEM images of the hybrid NM folded in half.

Figure 6.7. Conformal contact of AgNW composite hybrid NMs on 3D microstructures. (a) Schematic of conformal contact of NMs on the skin surface. (b) Hybrid NMs attached to a thumb. The inset shows a micrograph of a hybrid NM on the skin of a fingertip. The scale bar indicates 1 mm. (c) and (d) SEM images of the hybrid NMs transferred on line-patterned 3D PDMS microstructures with a line width of (c) 20 and (d) 120 μm . The scale bars indicate 10 and 20 μm , respectively. The insets show a magnification images with the scale bars indicating (c) 10 and (D) 50 μm . SEM images of the hybrid NMs with different thickness of (e) 40, (f) 100, and (g) 200 nm transferred on micropyramid-patterned 3D PDMS microstructures with diameter of 10 μm and height of 7 μm . All scale bars indicate 5 μm .

Figure 6.8. High magnitude SEM images of the hybrid NM transferred on the line-patterned PDMS with a line width of 20 μm .

Figure 6.9. Estimated step surface coverage of the hybrid NMs with different thickness placed on a micropylramid-patterned PDMS substrate.

Figure 6.10. Mechanical properties of hybrid NMs with orthogonal AgNW array. (a) Free-standing hybrid NMs with different densities of orthogonal AgNW arrays floating on the water surface. NMs are wrinkled by a water droplet of radius $a \approx 0.3$ mm. The number of wrinkles decreases as the density of AgNWs increases. All scale bars indicate 200 μm . (b) Young's modulus (E) of NMs as calculated from the wrinkle tests. (c) Comparison of calculated and experimental bending stiffness of hybrid NMs with different density of orthogonal AgNW arrays. Measured bending stiffness was calculated by using Young's modulus experimentally obtained from capillary wrinkling method. (d) Applied indentation load versus displacement of free-standing hybrid NMs as a function of density of orthogonal AgNW array. (e) Maximum indentation load versus displacement of hybrid NMs as a function of orthogonal AgNW arrays.

Figure 6.11. Number of wrinkles generated from a pure parylene NM and hybrid NMs.

Figure 6.12. Variation in the number of wrinkles N as a function of $N \sim a^{1/2}h^{-3/4}$.

Figure 6.13. Indentation test for measuring the mechanical properties of NMs.

Figure 6.14. Loading-unloading indentation test.

Figure 6.15. Skin-attachable NM loudspeaker. (a) Schematic of skin-attachable NM loudspeaker with orthogonal AgNW array. Sound is generated by temperature oscillation produced by applying an AC voltage. (b) Acoustic measurement system where sound emitted from NM loudspeaker is collected by a commercial microphone with a dynamic signal analyzer. (c) Variation in sound pressure (SP) generated from NM loudspeaker and thick film loudspeaker as a function of the input power at 10 kHz. (d) Experimental and theoretical values of sound pressure level (SPL) versus sound frequency for NM and thick PET film loudspeakers. (e) Skin-attachable NM loudspeaker mounted on the back of a hand. The scale bar indicates 1 cm.

Figure 6.16. Infrared (IR) images of the orthogonal AgNW array with AC 10 V applied at a frequency of 10 kHz.

Figure 6.17. SPL versus distance between the commercial microphone and thermoacoustic loudspeaker using an orthogonal AgNW array on a PET substrate.

Figure 6.18. Theoretical values of SPL as a function of sound frequency for (a) 100 nm-thick and (b) 220 μm -thick loudspeakers with different substrates.

Figure 6.19. Wearable and transparent NM microphone. (a) Schematic of wearable NM microphone device. (b) Transparent NM microphone placed over "UNIST" logo, illustrating its transparent and unobtrusive appearance. The scale bar indicates 1 cm. (c) Sensing measurement system for NM

microphone. Variation in the output voltages as a function of (d) sound frequency and (e) SPL for NM microphone and thin-film microphone. (f) Waveform and short-time Fourier transform (STFT) signals of original sound (“There’s plenty of room at the bottom”, left) extracted by the sound wave analyzer, the signal read from the NM-based microphone (middle), and thin-film microphone (right)

Figure 6.20. Comparison of adhesion force of various micro-patterned PDMS films.

Figure 6.21. Schematic of (a) NM and (b) thin-film microphone devices. In the NM microphone, NMs are mounted to the “holey” PDMS film as a free-standing geometry. In the thin-film microphone, a hybrid NM mounted to a planar PDMS film without a hole is fully laminated with the surface of PDMS film, where NMs cannot be free-standing.

Figure 6.22. Waveform and short-time Fourier transform (STFT) signals of original sound (“There’s plenty of room at the bottom”, left) extracted by the sound wave analyzer, where the signal was read from a commercial microphone.

Figure 6.23. Personal voice-based security system. (a) Schematic of voice security system (left) and photograph of authorization process using free-standing NM microphone (right). (b) Sound waveforms and (c) voiceprints collected from registrant, authorized user, and denied user using NM microphone. (d) Matching probability of voiceprint for authorized user using NM microphone and commercial microphone. (e) Matching probability of voiceprints obtained from different users including registrant, man, and two women.

Figure 6.24. FFTs extracted from the sound wave of the word “Nanomembrane” obtained from voices of different subjects including the registrant, authorized user and denied users.

Figure 6.25. FFTs extracted from the sound wave, obtained from the voice of a registrant by using (upper) NM microphone and (bottom) commercial microphone (40PH, G.R.A.S.).

Figure 6.26. FFTs for repeated test of 10 times, extracted from the sound wave of the word “hello” obtained from various voices of different subjects including the registrant, a man, and two women.

List of Tables

Table 2.1. Device Characteristics of PTB7-Th/PC₇₁BM PSCs and SY PLEDs with ITO or random and aligned AgNW Electrodes.

Table 3.1. Device characteristics of SY-based OLEDs and PTB7-Th:PC₇₁BM based OSCs using ITO, aligned AgNW and NP-enhanced plasmonic AgNW electrodes

Table 4.1. (a) J - V characteristics of PSC devices with ITO, orthogonal AgNW, and random AgNW electrodes fabricated on glass substrates.

Table 4.2. (a) J - V characteristics of flexible PSC and ultralight PSC fabricated on thin-PEN film and 1.3 μm -thick PEN foil with orthogonal AgNW arrays, respectively.

Nomenclature

AgNW	Silver nanowire
ITO	Indium tin oxide
TCE	Transparent conductive electrode
PEDOT:PSS	Poly(3,4-ethylenedioxythiophene) and poly(styrene sulfonate)
CNT	Carbon nanotube
E-skin	Electronic skin
IoT	Internet of Thing
PVP	Polyvinylpyrrolidone
PET	Polyethylene terephthalate
OLED	Organic light-emitting diode
OSC	Organic solar cell
FFT	Fast Fourier transform
PLL	Poly-L-lysine
PDMS	Polydimethylsiloxane
FoM	Figure of merit
LSPR	Localized surface plasmon resonance
SPP	Surface plasmon polariton
AgNP	Silver nanoparticle
E-field	Electric field
HTL	Hole transport layer
Ag@SiO₂P	Core-shell silver-silica nanoparticle
SEM	Scanning electron microscopy
TEM	Transmission electron microscope
SERS	Surface-enhanced Raman scattering
UV-vis	Ultraviolet-visible
AFM	Atomic force microscope
OOD	Organic optoelectronic device
DDA	Discrete dipole approximation
CLSM	Confocal laser scanning microscopy
XPS	X-ray photoelectron spectroscopy
PL	Photoluminescence
SY	Super Yellow

EQE	External quantum efficiency
TEOS	Tetraethyl orthosilicate
PCE	Power conversion efficiency
PSC	Perovskite solar cell
PEN	Polyethylene naphthalate
SVA	Solvent vapor annealing
SP-PDMS	Spiropyran-polydimethylsiloxane
HMDS	Hexamethyldisilazane
FWHM	Full width at half maximum
NM	Nanomembrane
ZnO	Zinc oxide
CVD	Chemical vapor deposition
AAO	Anodic aluminum oxide
EI	Bending stiffness
SPL	Sound pressure level
EL	Electroluminescence

Chapter 1. Introduction.

In recent advances with miniaturized, portable, and light-weight personal devices, academic and industrial researchers are now seeking for the fabrication of more convenient and comfortable electronic devices that are highly flexible, foldable, and even wearable. Figure 1.1 represents the research trends for the rapid progress of electronic and optoelectronic devices in last decade. Here, a number of research groups have actively developed conformal, flexible, or even stretchable electronic devices for potential applications, such as flexible/wearable power source, electronic skin (E-skin), healthcare monitoring devices, stretchable organic light emitting diodes (OLEDs), and flexible touch sensor.¹⁻⁷ Recently, Someya research group has developed skin-attachable e-skin for monitoring bio-signal of human body with metal nano-mesh electrodes that provides ultrathin, gas-permeable, and light-weight features, enabling conformal integration of the devices to the skin.⁴

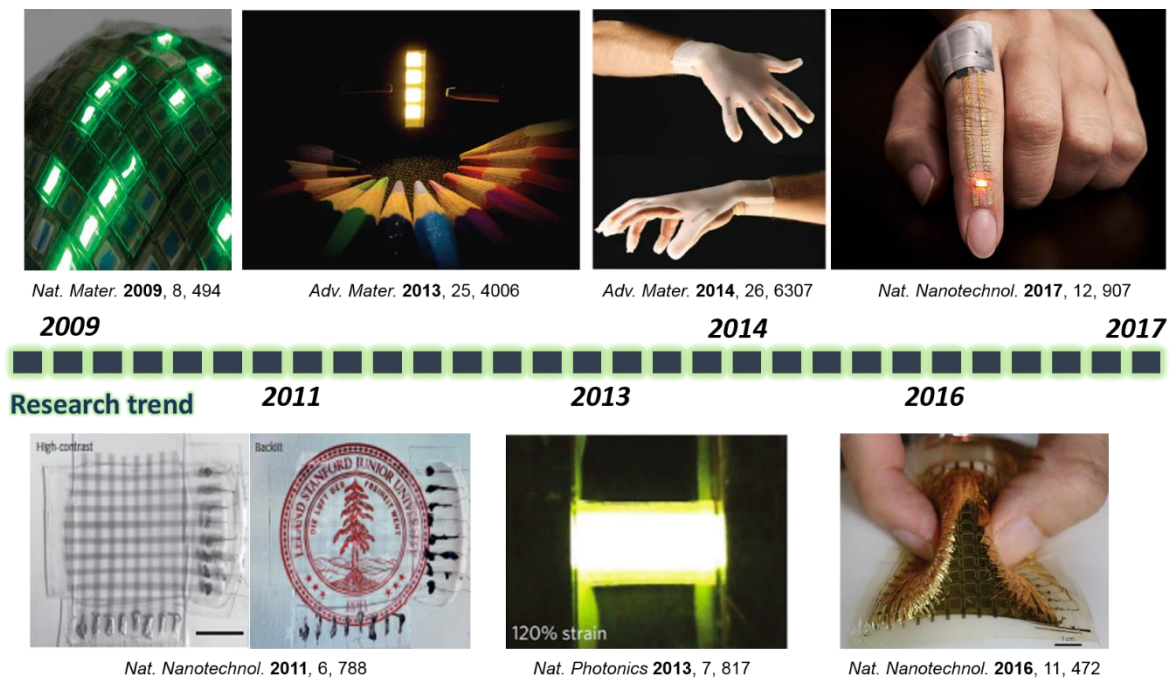


Figure 1.1. Representative images to show recent research trends for flexible/wearable electronic and optoelectronic device applications. (Sekitani et al. *Nat. Mater.* **2009**, 8, 494, W. Gaynor et al. *Adv. Mater.* **2013**, 25, 4006, Muth et al. *Adv. Mater.* **2014**, 26, 6307, Miyamoto et al. *Nat. Nanotechnol.* **2017**, 12, 907, D. J. Lipomi et al. *Nat. Nanotechnol.* **2011**, 6, 788, Liang et al. *Nat. Photonics* **2013**, 7, 817, Lee et al. *Nat. Nanotechnol.* **2016**, 11, 472)¹⁻⁷

With these impressive advances in wearable electronics, the research paradigm of electronics has rapidly changed conventional technology-oriented devices to user-oriented devices with increasing the

demand of Internet of Thing (IoT) that interconnects with human and machine. In particular, with significant progress in these flexible/wearable electronic devices, the integration with flexible transparent conductors in designing soft electronics have been intensively studied as key components that should be electrically conductive as well as mechanically durable even under repeated deformation induced by applied force to realize stable operation of such devices.⁸ Despite continuous development in the nanotechnology, it still remains challenging to achieve high-performance flexible electrode that has high electrical conductivity, optical transparency, an excellent mechanical stability, and even conformability, simultaneously.

Recently, random silver nanowire (AgNW) networks have been considered as promising flexible transparent electrodes due to low sheet resistance, high transmittance, and mechanical flexibility, which can be used in various flexible electrical and optoelectronic applications, such as solar cell, organic light-emitting, touch screen panel, e-skin, transparent heater, and smart window.⁹ However, there are still several challenges that should be overcome, such as rough surface, junction resistance, haze, and transmittance for successful device integration.

To address those issues, this thesis introduces aligned AgNW network transparent electrodes fabricated by novel, facile, and solution-based alignment techniques, which provide several unique features including outstanding electrical and optical properties as well as mechanical stability to realize high-performance flexible/wearable electronic and optoelectronic devices. Thus, we believe that our novel strategies will be powerful platform to open a new route to future soft and wearable electronic devices.

1.1 Transparent electrodes

Transparent electrode is an electrically conductive and optically transparent thin film, which is an essential component for various optoelectronic and electronic devices, such as solar cells, organic light-emitting diodes (OLEDs), transparent heater, touch sensor, and e-papers.¹⁰ In specific, transparent electrodes should have low electrical sheet resistance below 1000 ohm sq⁻¹ and high optical transmittance more than 80% in visible light range from 300 nm to 800 nm, simultaneously.¹¹ In particular, the combination of both low sheet resistance and high transmittance in transparent electrodes are essential and desirable to ensure the device performance in their device applications because they suffer from the trade-off between an electrical conductivity and an optical transmittance. Figure 1.2 shows various electronic and optoelectronic applications for different transparent electrodes with corresponding sheet resistance. For example, solar cells and OLEDs have required low sheet resistance less than ~100 ohm sq⁻¹ while higher sheet resistance over ~300 ohm sq⁻¹ is acceptable for the application of touch screen or smart window.

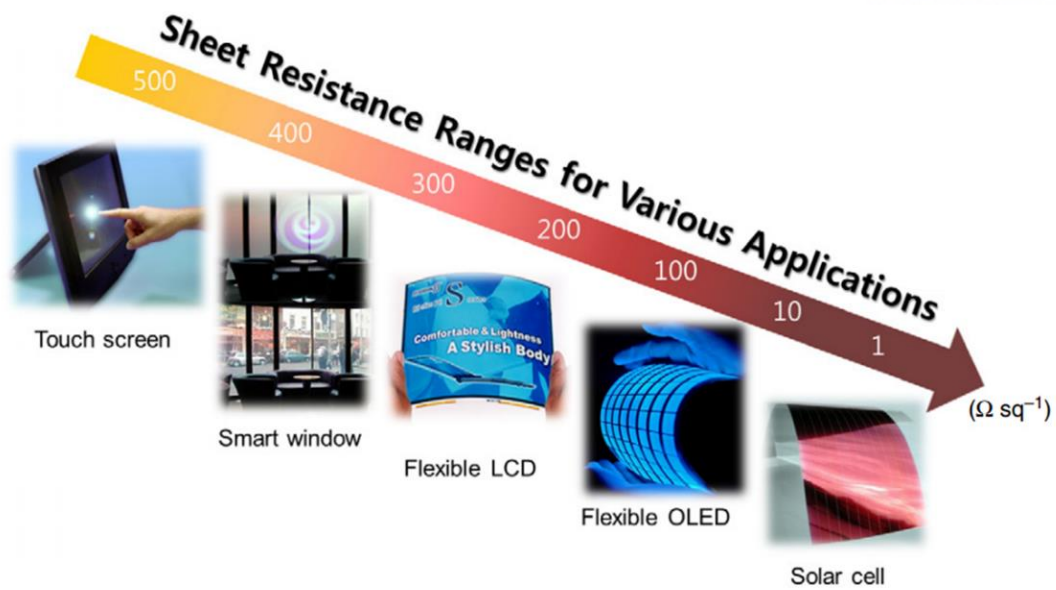


Figure 1.2. The various applications for transparent electrodes with varying the sheet resistance. Such electronic and optoelectronic devices have required different sheet resistance for stable operation and performance of their devices. (Bae et al., *Phys. Scr.*, **2012**, T146, 014024)¹²

For several decades, conventional indium tin oxide (ITO) coated glass substrates have been mostly used as transparent conducting electrode due to low sheet resistance and high transparency to visible light. However, ITO cannot meet several requirements for the next generation electronic device that has required simple fabrication process, mechanical flexibility, and low-cost materials. Firstly, ITO has inherent brittleness. The brittle nature of ITO causes the crack formation of the electrode under a repeating bending deformation, which leads to the degradation in their electrical conductivity, resulting in a deteriorated device performance for the device integration.¹³ Secondly, the price of indium as rare element is skyrocketing because of the limitation in the supply of the indium. Thirdly, the deposition process of ITO is also costly because of the fabrication process under high temperature and high vacuum.¹¹ Therefore, the fabrication of ideal flexible transparent electrode with an excellent electrical conductivity, optical transmittance, and outstanding mechanical stability is the critical challenge for the development of potential flexible electronic devices.

1.2 Next generation conducting nano-materials

To address these issues, various conductive materials have been widely studied in many research efforts to substitute conventional ITO, such as silver nanowires (AgNWs),¹⁴ carbon nanotubes (CNTs),¹⁵ graphene,¹⁶ and metal mesh,¹⁷ due to outstanding electrical and optical properties (Figure 1.3). Although these alternatives show good electrical and optical properties, they still suffer from the classic trade-off between an electrical conductivity and optical transparency (Figure 1.3(a)). Moreover, there have been several issues for each conducting nano-materials due to performance limits and costly production, which should be carefully considered for practical utilization. Firstly, conducting polymer including the combination of poly(3,4-ethylenedioxythiophene) and poly(styrene sulfonate) (PEDOT:PSS) have been interested as promising alternative of ITO¹⁸, due to high flexibility, light weight, and low cost. However, they have some problems because of complicated process for synthesis, low transmittance in blue ranges, chemical instability, and solubility, which limits their processibility. For another alternative of ITO, CNTs were firstly synthesized in 1990,¹⁹ which show unique electrical, optical, and mechanical properties including an excellent electron mobility more than $100,000 \text{ cm}^2/\text{V}\cdot\text{s}$ (Figure 1.3(d)).²⁰ After that, random CNT networks have been intensively studied as promising alternative to ITO by many research groups due to its low sheet resistance and superior mechanical stability.²¹ However, it is still being in challenges to separate metallic CNT from semiconducting CNTs, which do not contribute to their electrical conductivity. In addition, the electrical conductivity of CNT films shows much lower than ITO because of high junction resistance induced by aggregated nanotubes in the random network.²⁰ In Figure 1.3(c), graphene, synthesized by chemical vapor deposition (CVD), has been considered for replacing ITO due to good electrical and optical properties. Especially, graphene sheets have a few nanometer thicknesses, enabling to have an excellent transparency in visible light region. However, the major limitation of using graphene is the complexity of the fabrication for a single graphene sheet in large area. In addition, they are facing the challenge in the oxidation of graphene, high cost, and mass production. Recently, metal mesh has been introduced with an excellent electrical conductivity by various deposition methods, such as metallized electrospinning,²² self-forming,²³ or patterned metal grid²⁴ (Figure 1.3(e)). However, there still remain some issues for low transmittance and the problem of pattern visibility.

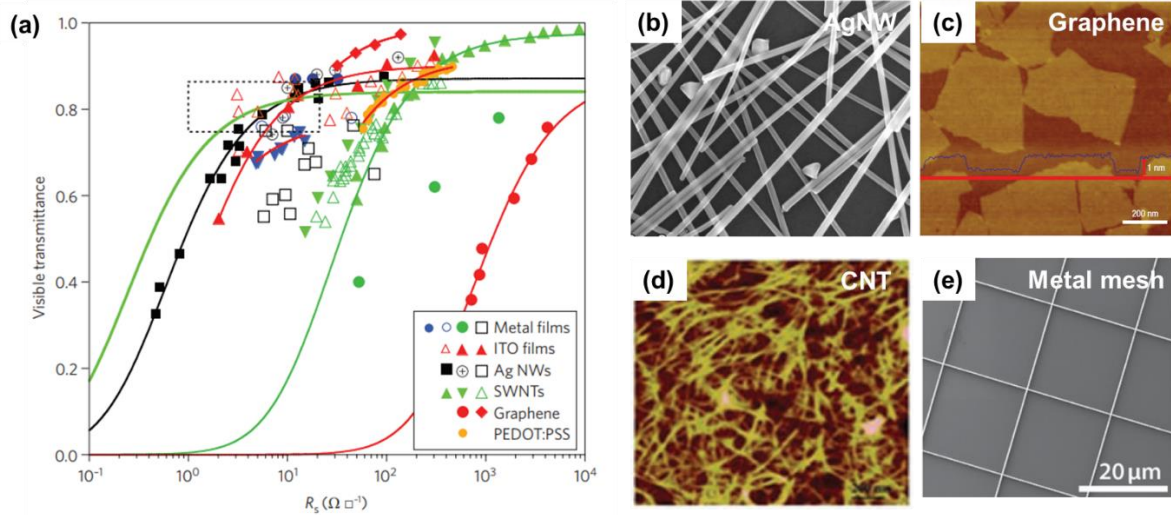


Figure 1.3. (a) The sheet resistance vs visible transmittance for various transparent electrodes with different conducting materials including ITO (Ellmer, *Nat. Photonics*, **2012**, 6, 809).¹⁰ The various candidates for alternative to ITO, such as (b) silver nanowires (De et al. *ACS nano* **2009**, 3, 1767),¹⁴ (c) carbon nanotubes (Wu et al. *Science* **2004**, 305, 1273),¹⁵ (d) graphene (Kim et al. *Nature* 2009, 457, 706),¹⁶ (e) metal mesh (Schneider et al. *Adv. Funct. Mater.* **2016**, 26, 833).¹⁷

1.3 Silver nanowire (AgNW) networks

Silver nanowire (AgNW) network have been considered as promising flexible transparent electrodes due to their excellent electrical conductivity, high optical transmittance, and good mechanical flexibility. Figure 1.4 presents several advantages of AgNWs in practical use. Firstly, such AgNWs can be made by a solution-based synthesis process with small diameter less than 100 nm and length of more than 1 μm .²⁵ Although the silver is one of expensive elements as novel metal, the cost of them used in the synthesis of AgNWs is lower than ITO. In addition, AgNW networks can be readily deposited by low-cost solution-based processes, such as spin-coating,²⁶ drop-casting,²⁷ bar-coating,²⁸ spray-coating,²⁹ brush-painting,³⁰ and blade-coating³¹ that are scalable and low temperature deposition processes, enabling them compatible with plastic substrates for the fabrication of flexible electrodes. In these deposition processes, AgNW networks are made of randomly interconnected NWs, which provide electrical percolating current paths, resulting in low sheet resistance.³² The desired sheet resistance and transmittance of AgNW networks can be easily tailored by assembling such conductive percolated network with controlling the NW density and the aspect-ratio of NWs.

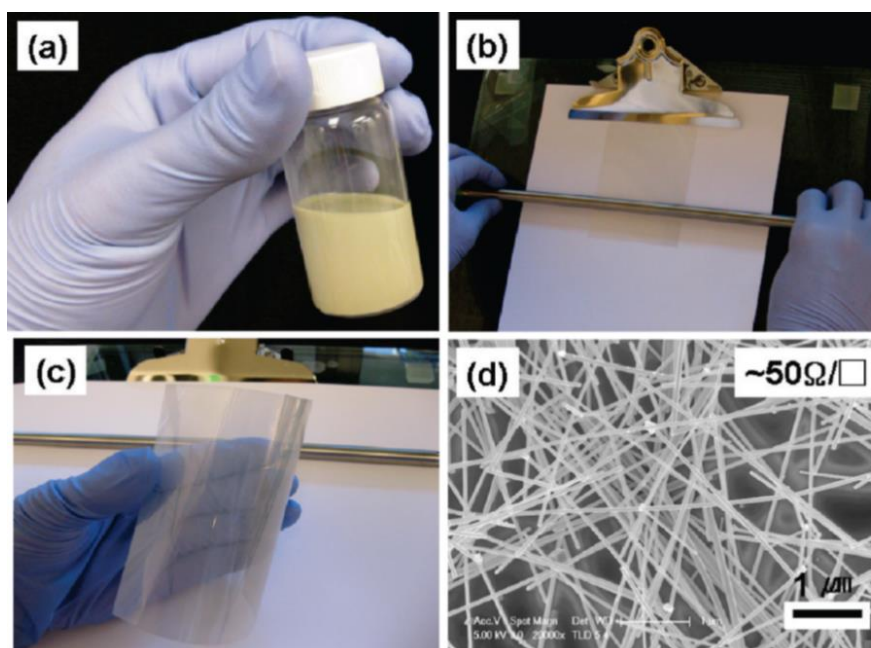


Figure 1.4. (a) The photograph of AgNW ink in ethanol solvent in a vial. (b) Bar-coating method for the fabrication of AgNW network on plastic substrate. (c) Flexible transparent electrode with random AgNW network. (d) The SEM image of random AgNW network. (Hu et al. *ACS Nano* **2010**, 4, 2955)²⁵

1.3.1 Synthesis of AgNW

AgNWs possess one-dimensional metal nanostructure with pentagonal structure. In addition, AgNWs have attracted great interest as promising conductive nano-materials due to superior intrinsic properties of bulk Ag. They are usually synthesized by the polyol process that is solution processing with the scalability and reproducibility. In the polyol process,³³ AgNWs are mainly synthesized by the reduction of the silver nitrate (AgNO_3) in the presence of polyvinylpyrrolidone (PVP) in ethylene glycol as capping agent. A pentagonal nano-structure in 5-fold twinned decahedron is formed with homogenous nucleation of Ag as shown in Figure 1.5. Here, NW growth and their dimension are controlled by the PVP, responsible for the passivation of anisotropic surface by preferential adsorption along the (100) surfaces of the AgNWs while the (111) surfaces are free to grow. In addition, the degree of nucleation and growth could be manipulated by controlling reaction conditions including temperature, the concentration of reagent, and the presence of trace ions. Finally, AgNWs synthesized by polyol process can be dispersed in diverse solvent, such as water, ethanol, and isopropyl alcohol (IPA).

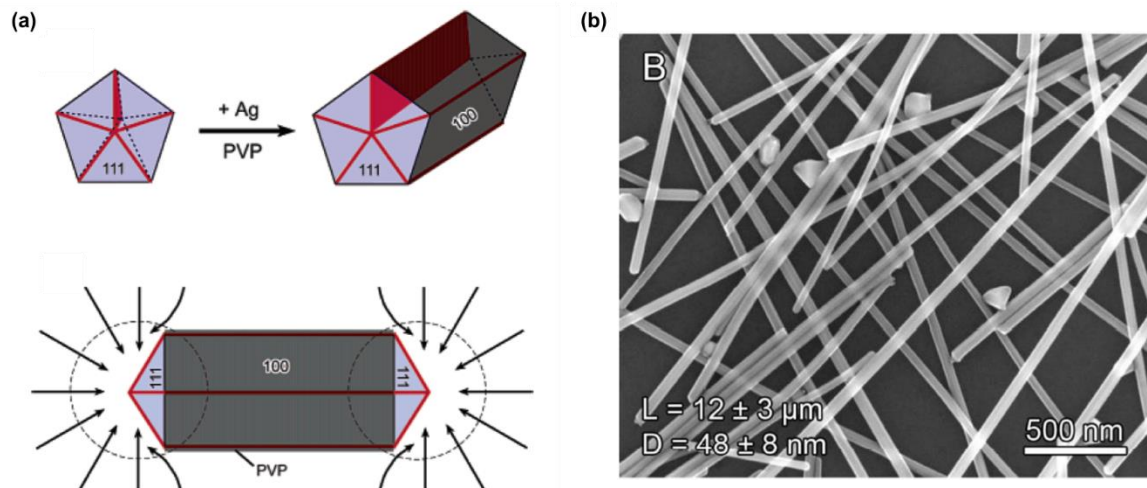


Figure 1.5. (a) Schematic illustration of the grow mechanism for the AgNW with pentagonal nano-structure. (b) SEM image of AgNWs synthesized by the polyol process (Sun et al. *Nano Lett.* **2003**, 3, 955).³³

1.3.2 Conductive percolation network

The electrical current path across AgNW network is an important parameter to determine their electrical conductivity in the transparent electrode. Here, charge carriers can move along the NW and can change their path at NW-NW junction (Figure 1.6). Therefore, high electrical conductivity of the film needs high connectivity between AgNWs that can be manipulated with controlling the NW density and the aspect ratio of NWs in conductive percolated network. In this respect, long AgNWs are beneficial to enable to reach the electrical percolation with a lower NW density.

In percolation theory, the critical density (percolation threshold) of conductive network, defined as N_c , can be determined by using the relation, $\sigma \propto (N - N_c)^\alpha$, where N is the concentration of AgNW, N_c is the threshold concentration of NWs and α is the critical exponent which relates to the spatial geometry of AgNW in ranging from 1.33 for 2D network to 1.94 for 3D network.³⁴ Therefore, controlling the diameter and the length of NWs plays key role to allow high electrical conductivity by reducing the junction resistance between NWs due to decreasing critical density of AgNWs involved in conductive percolation network.

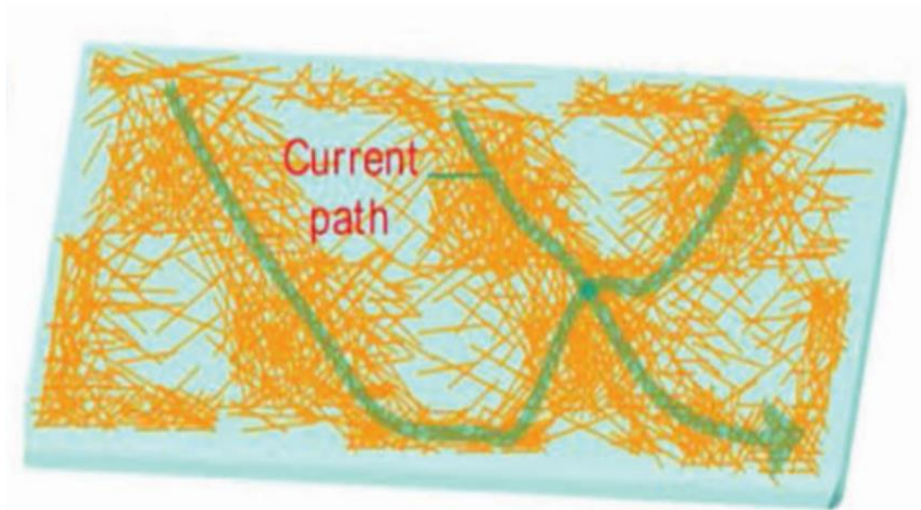


Figure 1.6. Conductive percolated networks for transparent electrode with random AgNW network where green arrow indicates current path due to interconnecting with NWs (Lee et al. *Adv. Mater.* **2012**, 24, 3326).³²

1.3.3 Junction resistance

In conductive percolated network of AgNWs, the charge carriers are mainly moved along two components with individual NWs and NW-NW junctions. Previously, Liangbing Hu et al. have demonstrated the junction resistance between NWs originated from insulating PVP capping agents that is measured larger than $1\text{G}\Omega$ while the resistance of individual AgNWs is measured few hundred ohms (around $200 - 300\ \Omega$).²⁵ As shown in Figure 1.7, it has been reported that the junction resistance is a dominant to determine overall electrical properties of AgNW network although the electrical conductivity of individual NWs depend on their geometric structure including the diameter and the length³⁵. Especially, the resistance of as-coated AgNW network is often high because of a lot of contact points caused by many interconnected NWs. Therefore, there remains in a challenge to reduce the junction resistance between interconnected NWs, resulting in a degradation of the electrical conductivity in AgNW network.

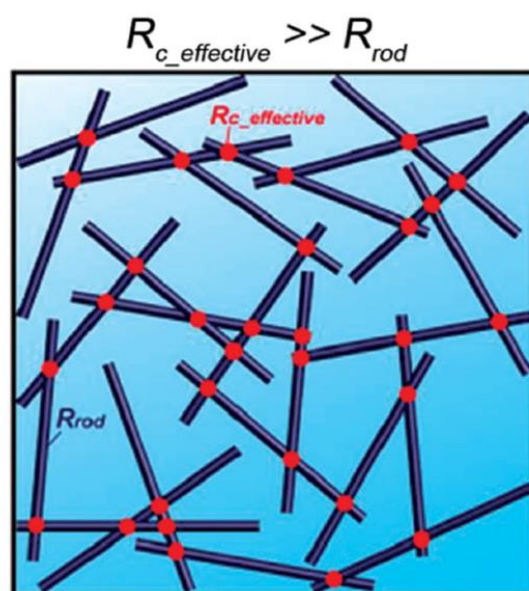


Figure 1.7. The schematic of random AgNW network in which interconnected NWs generate many contact points (red dot), which cause high junction resistance. (Mutiso et al. *ACS Nano* **2013**, 7, 7654)³⁵

To address these issues, many research groups have attempted various approaches to clearly remove the PVP residues surrounding the surface of NWs after the deposition of AgNW network. In Figure 1.8, the junction resistance in AgNW network can be effectively decreased by various post-treatment methods, such as thermal annealing, plasmonic welding, high pressure, optical sintering, and Joule heating. For simple post-annealing process, moderate annealing temperature ($< 200\ ^\circ\text{C}$) makes the fusion of AgNWs at the junctions, resulting in a decrease of sheet resistance as shown in Figure 1.8(c). In another approach,

junction resistances of crossed AgNWs with the resistance of $8\text{k}\Omega$ and $0.5\text{k}\Omega$ have been reported by plasmonically welded junctions and over-coated with gold, respectively.

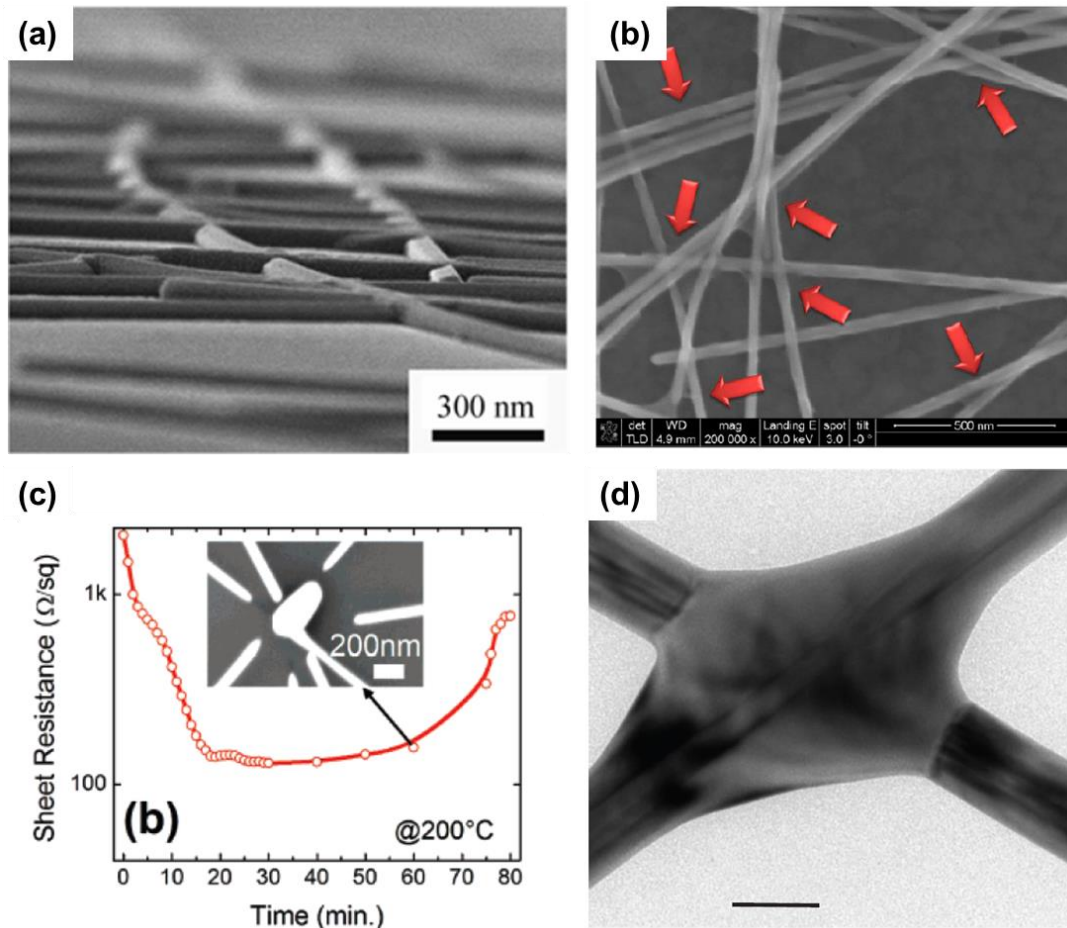


Figure 1.8. SEM image of AgNW network with low junction resistance due to (a) mechanical pressing (Tokuno et al. *Nano Res.* **2011**, 4, 1215)³⁶ (b) soldering with graphene (Liang et al. *ACS Nano* **2014**, 8, 1590).³⁷ (c) Post-annealing effect at 200°C for lowering junction resistance (Lee et al. *Nano Lett.* **2008**, 8, 689).²⁷ (d) TEM image of the junction between NWs in which two NWs are well combined by plasmonic welding process (Garnett et al. *Nat. Mater.* **2012**, 11, 241).³⁸

1.3.4 Surface morphology

Although AgNW networks represent an excellent electrical and optical properties, the surface morphology of AgNW networks is one of most important issues to be addressed for a device integration. In general, most optoelectronic devices need a smooth surface of the electrode to avoid direct contacts between active layer and the electrode, which cause an electrical shortage or a leakage current in multilayered device structure. In wet-coating process including bar coating or spin-coating, AgNW networks commonly have high surface roughness with peaks ranging from tens of nanometer to hundreds of nanometer that is mainly affected by the diameter and length of NWs, coating techniques, and substrate types.³⁹ After coating AgNW network, some of NWs lie on the surface of the film each other and other NWs can protrude from the surface. Thus, as-deposited AgNW networks typically have surface roughness as high as at least two nanowire diameters because of such protruding NWs. In addition, high surface roughness of AgNW networks often causes short circuits in device integration for optoelectronic applications, such as OLED and OSC. Many research groups have addressed these issues for the surface morphology of AgNW-based transparent electrodes. Thus, various efforts have been attempted to reduce the surface roughness and peaks of AgNW network, such as embedding AgNW into a soft polymer matrix,⁴⁰ lamination with polymers by mechanical pressing, over-coating with metal oxide or graphene sheets (Figure 1.9).

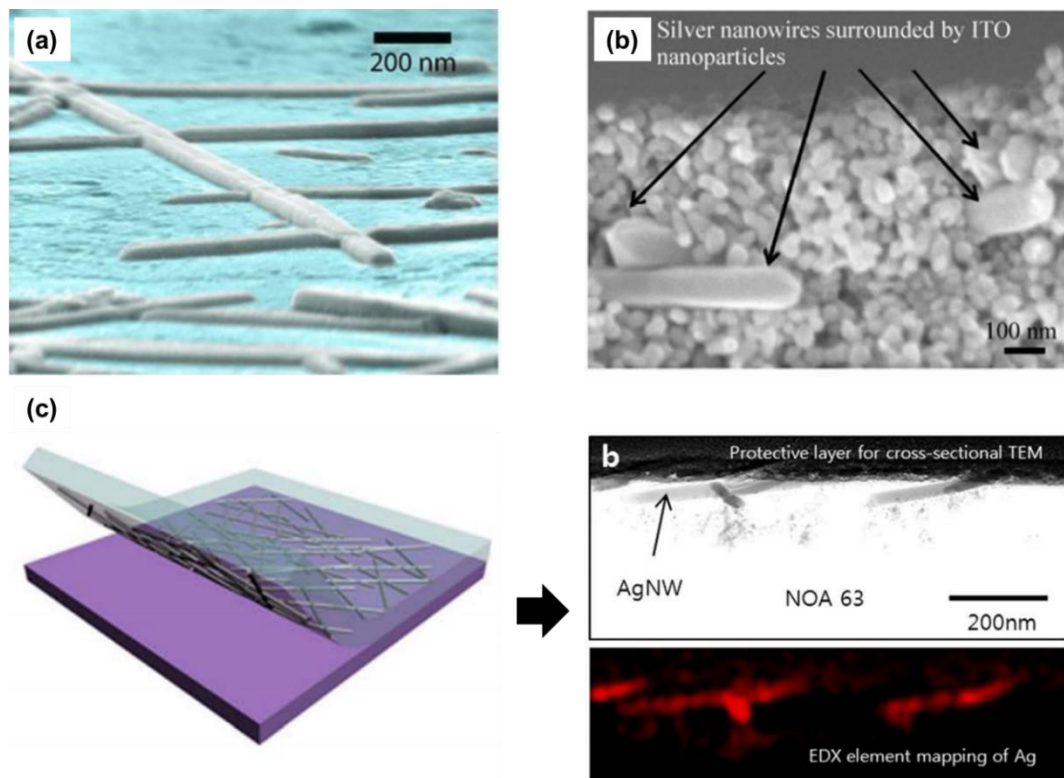


Figure 1.9. (a) The SEM image of AgNW network embedded into soft polymeric matrix by using mechanical pressing method. (Gaynor et al. *Adv. Mater.* **2011**, 23, 2905).⁴⁰ (b) Cross-sectional SEM

image of AgNWs embedded in ITO nanoparticles films (Chung et al. *Nano Res.* **2012**, 5, 805).⁴¹ (c) (Left) The schematic illustration and (right) a TEM image of random AgNW network embedded in NOA 63 matrix. (Nam et al. *Sci. Rep.* **2014**, 4, 4788)⁴²

1.3.5 Optical property.

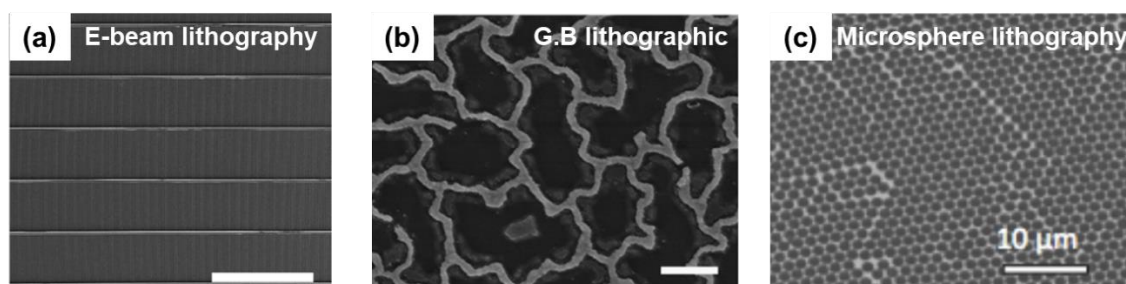
When AgNW networks are under the irradiation of incident light, the light can be absorbed, transmitted, or reflected. Optical transmittance and light absorption over a broad wavelength range is critical parameters to understand optical behavior of AgNW-based transparent electrodes. In general, the transmittance of AgNW networks is strongly affected by different NW densities.²⁵ Here, the total transmittance can be divided by two parts that is specular and diffusive transmittance. The specular transmittance means the transmitted light with same direction of incident light. On the other hand, diffusive transmittance represents the transmitted light that is scattered by individual NWs or NW junctions, which mainly determines the optical behavior of AgNW network while these of ITO is negligible with little scattered light. In the study on AgNW-based transparent electrode, the haze factor, defined as the ratio of diffusive transmittance to total transmittance, is one of important issues that needs to be considered in the fabrication of AgNW networks, which may blur pixels or reduce the resolution and visibility in display device applications.^{43, 44}

To avoid the haze issues, the aspect ratio of NWs should be carefully designed in the deposition of AgNW networks. In addition, very long AgNWs facilitate to achieve high transmittance as well as low haze, attributed by a decrease of NW density due to lower percolation threshold. In particular, the small diameter of AgNWs are strong benefits to increase the transmittance due to a decrease of the scattered light by individual NWs. However, although these light scattering by NWs should be reduced for achieving high transparency in electronic display applications, manipulating light scattering can provide significant benefits for the fabrication of optoelectronic devices, such as OSC and OLED. Recently, random AgNW networks have been considered as promising plasmonic electrodes with strong light scattering and trapping because Ag nanostructures are an important plasmonic materials that can support localized surface plasmon resonance (LSPR) in ranging from visible spectrum to near-IR region.⁴⁵ In previous studies, these light scattering and trapping effects of AgNWs have been suggested to generate an increase of the optical path length and near-field excitation of LSPR, which enhance the light absorption efficiency of the photo active layer for various solar cell applications.⁴⁶ Moreover, the light extraction efficiency could be also improved due to light scattering by NWs, resulting in higher efficiency of AgNW-based LED devices compared than ITO-based LED devices.⁴⁷

1.4 Other types of transparent electrodes

In addition to using conducting-nanomaterials to overcome these challenges, various flexible transparent electrodes have been widely reported by different approaches including lithographical patterning or electrospinning processes as shown in Figure 1.10. Wu et al. have developed high-performance transparent electrodes based on metal-nanotrough network, fabricated by the combined method involving electrospinning and metal deposition, which exhibited low sheet resistance of less than $10 \Omega \text{ sq}^{-1}$ at 90% transmission.²² For another methods, Guo et al. have demonstrated transparent nano-metal mesh electrodes on elastomer made by grain boundary lithographic technique that show high stretchability as well as outstanding electrical and optical properties ($\sim 20 \Omega \text{ sq}^{-1}$ at 82.5% transmittance). Although these methods can offer new opportunities for the fabrication of novel flexible/wearable electronic devices, most of them includes complex and time-consume fabrication process, limiting their scalability and applicability in practical use.

Lithographic transparent electrodes



Electrospun transparent electrodes

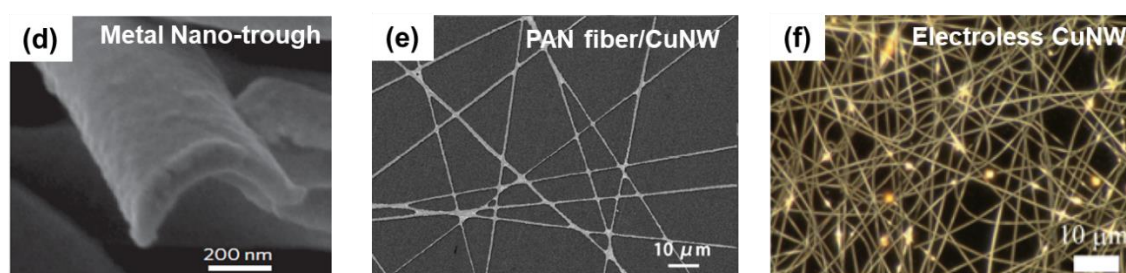


Figure 1.10. (a-c) Various patterned transparent electrodes fabricated by using different lithographic techniques, such as (a) E-beam lithography (Hsu et al. *Nat. Commun.* **2013**, 4, 2522),⁴⁸ (b) grain boundary lithography (Guo et al. *Nat. Commun.* **2014**, 5, 3121),⁴⁹ and (c) microsphere lithography (Gao et al. *Nano Lett.* **2014**, 14, 2105).⁵⁰ (d-f) Electrospun transparent electrode fabricated by using different methods, such as (d) metal nano-trough (Wu et al. *Nat. Nanotechnol.* **2013**, 8, 421)²², (e) selective etching (He et al. *ACS Nano* **2014**, 8, 4782),⁵¹ and (f) metal electroless deposition. (Hsu et al. *J. Am. Chem. Soc.* **2014**, 136, 10593)⁵²

1.5 Device application of transparent AgNW electrode

With rapid progress in flexible electronic devices, AgNW-based transparent electrodes have been widely used for a device integration in various device applications, such as photovoltaic devices, touch panel, light-emitting display, transparent heater, and e-skin sensors due to low sheet resistance and high optical transmittance. In addition, outstanding mechanical properties of AgNW networks allow them to be integrated in emerging flexible electronic devices without significant degradation in their device performance. However, there are still some drawbacks that should be overcome for successful device fabrication, such as stable operation, long-term stability, and interface engineering. Therefore, the major challenges in the device integration with AgNW-based transparent electrode in terms of several device applications should be addressed.

1.5.1 Solar cells

The solar cells are photovoltaic device that is considered one of most attractive renewable power source, which converts the sunlight to the electricity through absorbing incident light by active layer in which electron-hole pair is generated under the irradiation of photon energy. For example, in OSCs, common operating mechanism of the device, composed of photovoltaic active layer, anode and cathode electrodes, includes five stages, such as i) light absorption by active layer, ii) the exciton generation by absorbed photon, iii) exciton diffusion, vi) exciton dissociation and charge transport, and v) charge collection by electrodes.⁵³ Thus, overall device efficiency (PCE) is determined by those parameters. Here, transparent electrodes can be either the anode or cathode in the solar cell that allow the incident light enters inside the device as shown in Figure 1.11.

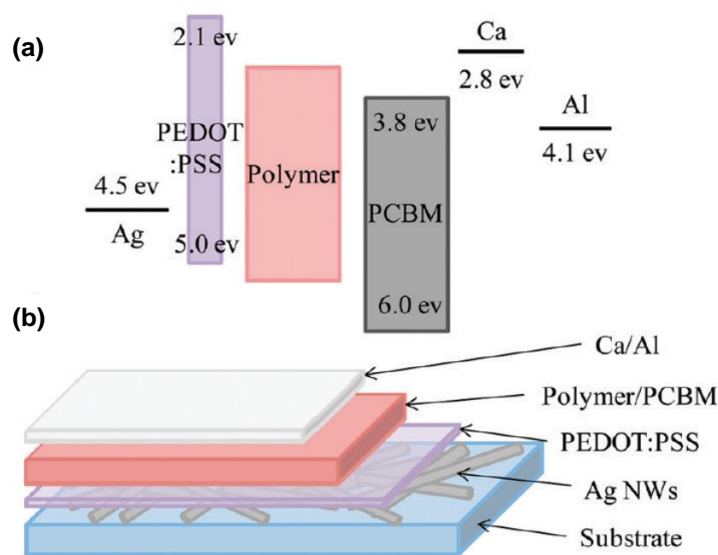


Figure 1.11. a) Energy-level diagram showing work functions of each component materials. b) The device structure for the solution-processed OSC with the AgNW electrode as anode (Yang et al. *ACS Appl. Mater. Interfaces* **2011**, 3, 4075).⁵⁴

The most conventional materials as transparent electrode for solar cell are ITO due to high electrical conductivity and an excellent optical transmittance as mentioned in previous sections. Recently, with increasing demands in optoelectronic device that should be lightweight, cost-effective, and flexible, many research groups have focused on the fabrication of flexible solar cells integrated with various alternatives of ITO, such as graphene, metal NWs, CNTs, conducting polymer, and metal mesh. Among them, AgNW-based transparent electrode is good candidate to be integrated in flexible solar cells due to comparable electrical and optical properties with conventional ITO. Initial attempts to incorporate random AgNW networks recorded relatively low power conversion efficiency up to 2.8% while that with ITO as reference cell showed PCE of 5.8% (Figure 1.12). Afterward, many researchers have started to incorporate AgNW-based transparent electrode for the fabrication of several type of solar cells.^{46, 55-}

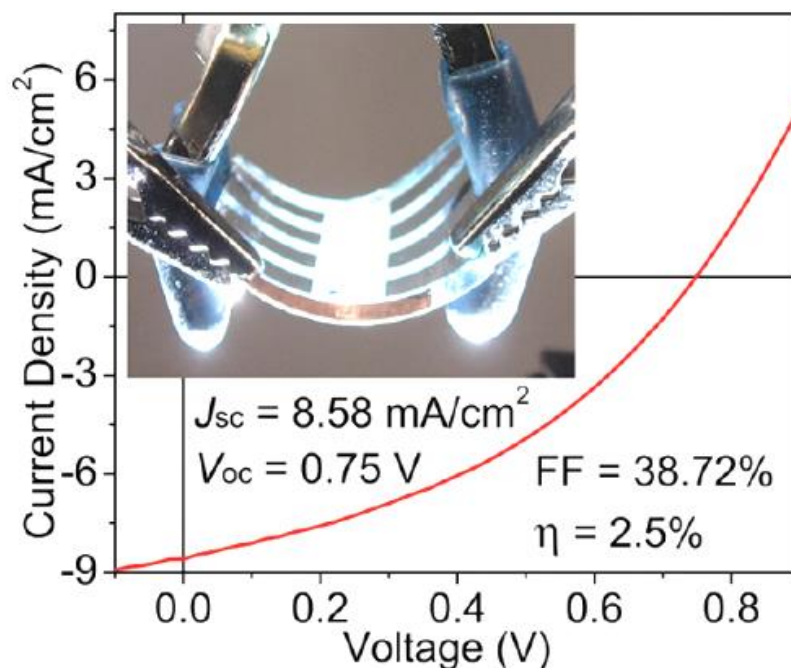


Figure 1.12. Characteristic J - V curves of OSC solar cell devices based on random AgNW electrodes (Yang et al. *ACS Appl. Mater. Interfaces* **2011**, 3, 4075).⁵⁴

One of important benefits of using AgNW electrodes is that solution-based flexible AgNW network facilitates the solar cell to be flexible and be fabricated under low temperature process and roll-to-roll process on flexible polymer substrates. In addition, unique optical behaviors of AgNW networks including LSPR and light scattering effect can provide an increase of light absorption efficiency of

active layer, which leads to an increase of exciton generation, resulting in improved device efficiency. Previously, B. Y. Wang et al. have demonstrated the effect of light scattering and trapping by random AgNW electrodes on flexible OSC devices, which provides an enhancement of light absorption in active layer, resulting in enhance PCE of 7.58 % of the device (Figure 1.13).

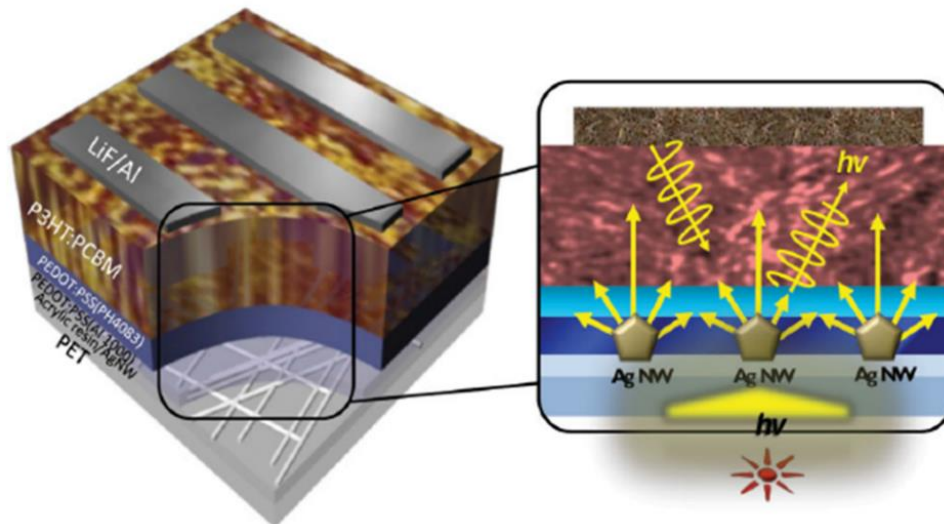


Figure 1.13. A schematic of organic solar cells with AgNW network where the light scattering and trapping effects are induced under the illumination. (Wang et al. *Small* **2015**, 11, 1905)⁴⁶

In rapid advances of such flexible solar cells, manipulating surface roughness of AgNW network has been one of important challenge that should be addressed for realizing high device efficiency of AgNW-based flexible solar cells. The protruding NW caused by the entanglement of AgNWs leads to high surface roughness in order of hundreds nanometer, resulting in an electrical shortage or leakage current in multilayered configuration of devices. To address these issues, various approaches to reduce the surface roughness of AgNW networks have been developed by mechanical pressing, thermal annealing, embedding polymer, surface peeling, and transfer processes. It has been shown that the reduction of surface roughness by flattening the network not only reduces the risk of short circuit but also decreases sheet resistance. For example, the use of metal oxide buffered AgNW network have been previously reported, which improved fill factors and open-circuit voltage, resulting in high PCEs of up to 3.5%, which is comparable with that of ITO with PCE of 3.52%.⁵⁹ In another approaches, J. H. Seo et al. have reported random AgNW network with low surface roughness produced by cold isostatic pressing, which achieved high device efficiency of inverted flexible OSCs with a PCE of 8.75%.⁵⁸

1.5.2 Displays (OLED)

Organic light emitting diodes (OLEDs) have attracted much interests as next generation flexible lighting devices due to several advantages, such as light-weight, flexibility, and solution processing, enabling to fabrication low area and flexible display. In OLED, the electrical current flow into emissive active layers to emitting the light induced by the combination of hole-electron pairs. In these charge carrier transport, the interface between the electrode and neighboring layers plays important role to efficiently operate such devices. Here, AgNW-based transparent electrodes can be an essential component for OLED devices due to outstanding electrical, optical, and mechanical properties. In particular, the transparent electrodes should have the low sheet resistance and high optical transmittance to ensure low operating voltage, uniform light emission, stable external quantum efficiency in the fabrication of large-area OLED display.⁹ Previously, Gaynor et al has reported white OLEDs with random AgNW network that recorded highest luminous efficacy for an ITO-free white OLED with stable angular color stability² (Figure 1.14). These first studies open the way towards large-scale integration of AgNW-based electrodes in emerging flexible display devices.



Figure. 1.14. The photograph of white OLEDs with angular color stability incorporated with AgNW-based transparent electrodes. (Gaynor et al. *Adv. Mater.* **2013**, *25*, 4006)²

After that, there have been many studies on OLED devices integrated with AgNW-based electrodes in which they demonstrated the light scattering of AgNWs to enhance the light extraction efficiencies in OLEDs.⁶⁰⁻⁶² For example, L. Li et al. reported flexible phosphorescent polymer light-emitting diode (PLED) with AgNW-polymer composite electrodes, which exhibited higher electroluminescent performance than that with ITO.⁶² In addition, recently, fully stretchable PLEDs have been reported with random AgNW network soldered with graphene oxide as shown in Figure. 1.15. Here, the PLED showed stable device operation under large strain due to an excellent mechanical compliance of modified AgNW electrode, which represent one of major challenges for the fabrication of

flexible/stretchable optoelectronic devices. Although significant advances have been made in OLEDs with AgNW-based transparent electrodes, some issues in low out-coupling efficiency and stable device operation are still in challenges, which limits further development to realize high-performance OLED devices.

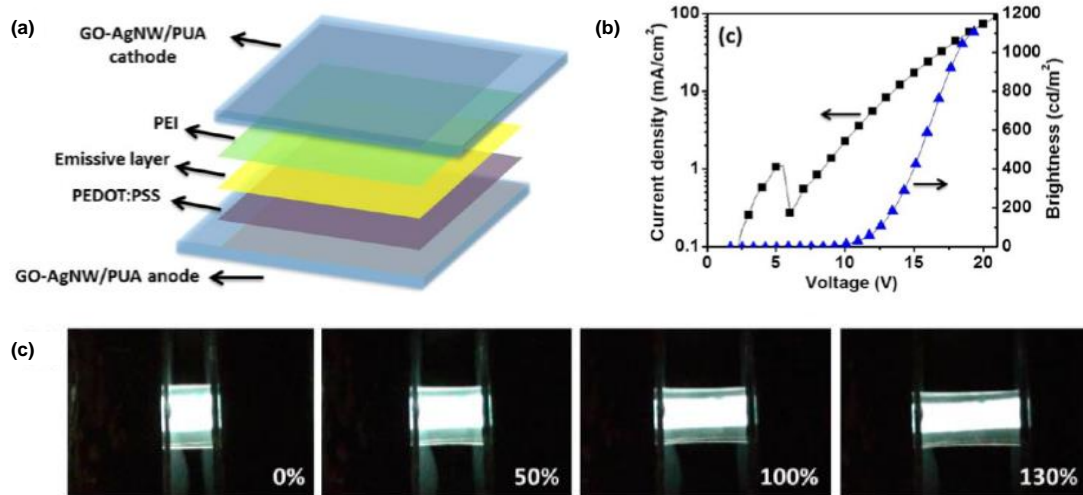


Figure 1.15. (a) A schematic illustration of stretchable PLED using random AgNW with graphene oxide fabricated on elastomeric substrate. (b) The characteristics of current density-luminance-driving voltage. (c) Optical photographs of stretchable PLED under applied strain from 0% to 130%. (Liang et al. *ACS Nano* **2014**, 8, 1590)³⁷

1.5.3 Touch panels

Touch screen panel has been a necessary component in recent many kinds of electronic products, such as smartphones, smart TV, tablet PCs, and other various technologies. In general, the most common touch panel formats are based on capacitive type or resistive type touch sensing both of which require the transparent electrodes like conventional ITO. As basic design structure of touch screen, resistive-type touch panel uses two continuous transparent electrodes separated by air gap. When two opposing electrodes contact each other, the current flow originated from the contact of two electrodes makes the computer to identify the touch position. Resistive sensing is benefits for lost cost and high resolution while capacitive sensing can provide multi-touch capability and durability of devices. In both types of touch panels, the sheet resistance of sensing electrodes is important for device performance, such as response time, touch sensing accuracy, and activation force. With increasing flexible touch screen marketing, however, another issue for mechanical durability has been focused on a research field in a replacement for ITO for flexible transparent electrodes. Deformation of touch electrode under repeated compressive force leads to microcracks of touch electrode, resulting in the degradation in an electrical conductivity of the electrode. With respect to these issues, AgNW-based touch sensors can offer good performance for future flexible touch panel technology (Figure 1.16).



Figure 1.16. The illustration of commercial touch screen with AgNW-based transparent electrodes. (Cambrios Technologies Corp., <http://www.cambrios.com/>, accessed: May 2018.)

Recently, some of papers demonstrated that the AgNW-based electrodes can be promising candidates for the fabrication of resistive-type or capacitive-types touch sensors. Lee et al. has demonstrated capacitive AgNW-based touch pad integrated with insulating GO film as separator, which directly detect the touch signal by a human finger with a high ON/OFF ratio⁶³ (Figure 1.17).

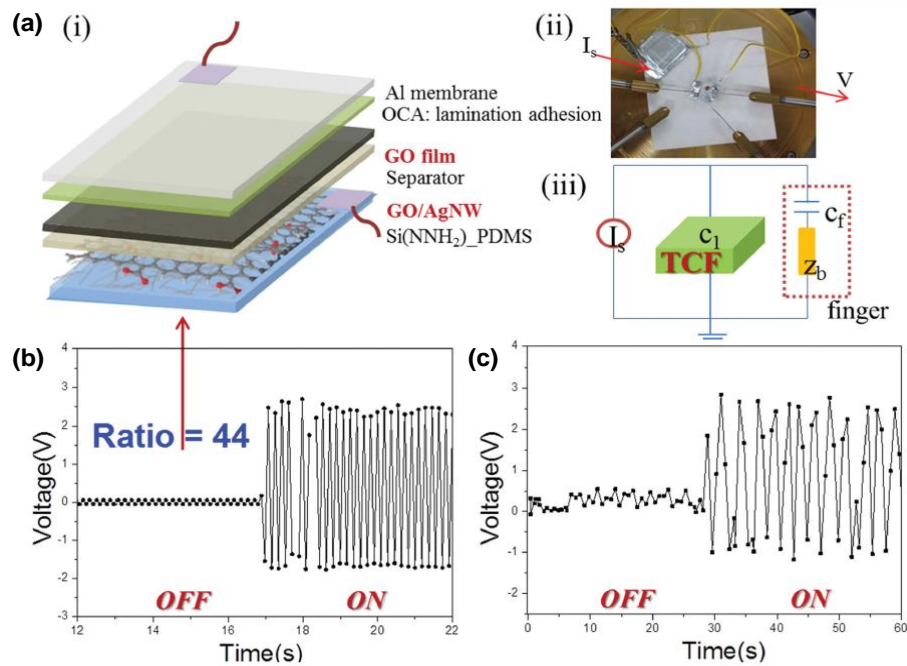


Figure 1.17. (a) The schematic structure of capacitive type touch pad with AgNW electrode fabricated on PDMS substrates. (b) The variation of electrical signal response to finger touch. (c) Touch sensitivity test. (Lee et al. *Adv. Funct. Mater.* **2014**, *24*, 3276)⁶³

Moreover, for resistive sensing, flexible and large-scale touch panel with very long AgNW network soldered with conducting polymer has been developed,⁶⁴ which can accurately detect the human writing on the surface of touch panel mounted on even curved object (Figure. 1.18).

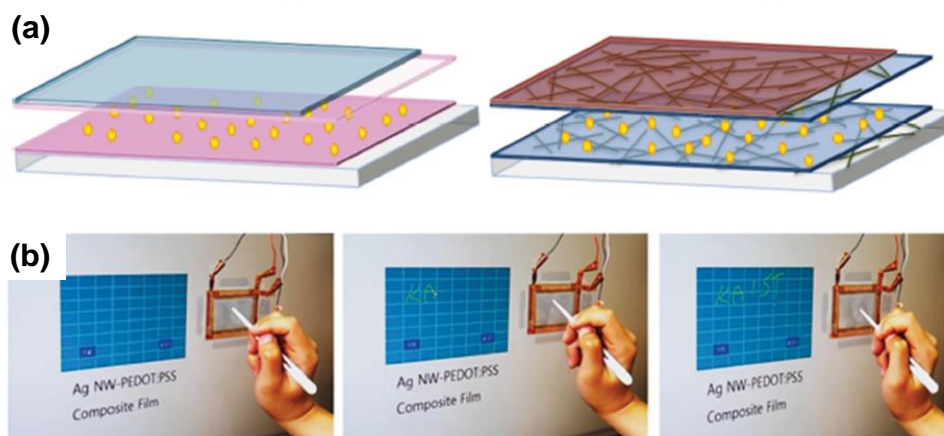


Figure 1.18. (a) The schematic illustrations of (left) commercial touch panel with ITO/spacer/ITO/glass and (right) flexible touch panel fabricated with AgNW electrodes soldered with conducting polymer. (b) The photographs of touch screen operation by writing a word "KAIST" (Lee et al. *Adv. Funct. Mater.* **2013**, *23*, 4171).⁶⁴

Recently, Pei et al. have reported healable touch screens with random AgNW network integrated with healable polymeric matrix.⁶⁵ It was also recently demonstrated that flexible transparent capacitive sensors can be used for the detection of deformation and pressure in which capacitive sensor sheets fabricated by employing AgNW networks embedded in the surface layer of a polyurethane matrix exhibit good stretchability and transparency. These advances in touch panel applications could open the possibility of a new platform for realizing human-machine interacting devices in flexible/wearable electronic applications.

Chapter 2. Aligned AgNW network for high-performance transparent electrode

2.1 Introduction

Transparent conductive electrodes (TCEs) are essential components in many optoelectronic devices such as solar cells, touch panels and organic light-emitting diodes (OLEDs).^{10, 11, 66-68} While indium tin oxide (ITO) has been widely used in commercial transparent electrodes, the further development and application of ITO has been limited by the cost and inherent brittleness of the material.^{10, 67, 69} One promising alternative to ITO as a TCE material includes random networks of Ag nanowires (AgNWs),^{14, 38, 70, 71} which can provide lower sheet resistance (R_s) and higher optical transmittance (T) than other TCE candidates such as carbon nanotubes (CNTs),^{11, 15, 72} graphene^{16, 73-76} CuNWs,⁷⁷ and conducting polymer.¹⁸ Moreover, AgNW networks can be readily prepared by low-cost solution-based processes, such as spin coating,²⁶ drop casting,²⁷ rod-coating^{25, 28} and spray coating.^{44, 78, 79}

However, for the use of random AgNW networks in high-performance solar cells and OLEDs, the junction resistance between nanowires and the large surface roughness are two critical issues that need to be addressed. Junction resistance prevents NW networks from achieving low R_s , while high density of NWs lower the optical transmittance of the electrodes.⁴¹ The protruding NWs of overlapping random NW network structures can cause electrical short-circuits and leakages in multilayered device configurations.^{40, 80} In addition, the optical haze, defined as the ratio of diffusive transmittance to total transmittance, of random NW networks may blur pixels or reduce the resolution in touch-screen and OLED devices.^{25, 43, 44} To overcome the issue of junction resistance between NWs, several approaches including thermal annealing²⁷, hybridization with metal oxides and graphenes,^{37, 78} mechanical pressing³⁶ and plasmonic weldings³⁸ have been introduced. The surface roughness issue has been addressed by the addition of coatings and laminations with polymers,^{40, 60} metal oxides,⁴¹ and graphene sheets.⁸¹ However, these additional processes complicate the fabrication process or are incompatible with large-scale solution processing.

To overcome the trade-off between electrical conductivity and optical transmittance in a one-step solution process, conductive percolation networks within NW structures must be precisely controlled.^{35, 82-84} The percolation-limited performances of random NW networks in applications as TCEs have been addressed by several approaches.^{23, 48, 50-52, 85, 86} One such approach utilizes high-aspect-ratio metallic NWs, generating conductive pathways with low NW densities.⁸⁵ Another approach uses lithographic^{23, 48, 50, 86} or electrospinning techniques^{51, 52} to design ordered conductive networks; very low R_s values have been obtained via the formation of junction-free conductive networks using these methods. However, these fabrication processes are complicated and unsuitable for the cost-effective and scalable

production of TCEs.

Here, we introduce a simple and high-throughput fabrication strategy for the assembly of aligned AgNWs using a capillary printing technique for the fabrication of highly conductive and transparent electrodes with low surface roughness. In this approach, AgNW solutions are dragged and deposited by polydimethylsiloxane (PDMS) nanochannels, in which AgNWs are partially aligned prior to unidirectional alignment by meniscus surface tensions. Previously, various techniques including Lagmuir-Blodgett,⁸⁷ contact printing,⁸⁸ post-alignment shrinkage,⁸⁹ nanocombing,⁹⁰ nanotrench-assisted capillary force,⁹¹ and fluid flow⁹² have been employed for the alignment of semiconducting or metallic NWs. Although significant progress has been made to improve the alignment degree and density of assembled NWs, many of previous techniques require essential necessities such as pre-grown vertical NW arrays, additional transfer process, and substrate pre-patterning, which limit the cost-effective and scalable assembly of high-density NWs with a controllable NW alignment degree. Our capillary printing method can overcome these limitations and has several advantages in the fabrication of TCEs based on AgNW networks. First, the alignment technique provides large areas of highly aligned AgNWs via a one-step solution-based process that is both cost-effective and compatible with rapid roll-to-roll processes. Second, the aligned AgNWs overcome the trade-off between the electrical conductivity and optical transmittance that occurs in random NW networks, because the alignment of the AgNW networks significantly decreases the NW density; the electrical percolation threshold is lower in the aligned networks than in random NW networks. Third, the aligned AgNW networks exhibit lower surface roughness than random networks without the need for additional smoothing processes, thus providing good device compatibility in optoelectronic applications.

2.2 Experimental Details

Preparation of patterned PDMS stamp: Polydimethylsiloxane (PDMS) base and curing agent (Sylgard 184, Dow-corning) were completely mixed in a 10:1 weight ratio. The air-bubble in PDMS mixture during the mixing process was subsequently removed in a vacuum desiccator for 20 min. For the fabrication of the line patterned PDMS stamp, the PDMS mixture was cast onto a silicon micromold with periodic line pattern with 400 nm line width and 800 nm periodicity. Then, the PDMS mixture were thermally cured at 80°C for 4 hr on a hot-plate.

Preparation of the functionalized substrates: Glass substrates were cleaned with IPA and D.I water by sonication for 10 min. After blown-drying with N₂ gas, the substrate was treated with O₂ plasma for 5 min to increase the wettability of glass substrates. To further increase the AgNW adhesion on the substrate, poly-L-lysine (PLL) layers with amine functional groups were coated on the substrates by spin-coating the PLL solution (0.1% concentration in H₂O) at 4000 rpm for 60 sec.

Alignment of AgNW by capillary printing process: For the formation of triangular-shaped PDMS stamp, nano-patterned PDMS stamp was attached on a trigonal prism-shaped aluminum frame. The aluminum frame was subsequently installed onto the micro-stage, where the PDMS stamp can be freely moved back and forward with a controlled constant speed. When the PDMS stamp was put into contact with the target substrate, the contact pressure was controlled by using an electronic scale supporting the substrate. Next, AgNW dispersion (L= 35 μm, D= 30 nm, purchased from Nanopyxis Corporation) was dropped on the target substrate, which was subsequently sucked into PDMS line-patterns. Then, the sliding of the PDMS stamp with constant speed produced highly aligned AgNW arrays along the coating direction (Figure 2.1). Finally, the aligned AgNWs are dried in ambient environment conditions and treated by O₂ plasma for 1 min to remove organic impurities and enhance electrical conductivity.

Characterization: The sheet resistance of aligned AgNW networks was measured by using four-point probe measurement (Kiethley 2400 equipment). The optical transmittance of aligned AgNW networks was measured by UV-visible spectrophotometer (Jasco V-670). The haze factor was calculated using the diffusive and total transmittances over visible light range. To investigate the mechanical robustness of aligned AgNW films, the change in sheet resistance of aligned AgNWs on PET under various bending radius and cycles was measured using a two-probe method, in which copper tapes were attached to each side of aligned AgNWs with silver paste.

2.3 Results and Discussion

The alignment of AgNWs by capillary printing was performed by dragging nano-patterned PDMS stamps over AgNW solutions on target substrates under constant velocity and pressure. Figure 2.1a shows a schematic of the preparation of the aligned AgNW assemblies using this capillary printing technique. In this work, we utilized a nano-patterned PDMS stamp with a line pattern spacing of 400 nm to create the nanochannels inducing the alignment of the AgNWs in the printing direction (Figure 2.1b,c). The nano-patterned PDMS stamp was attached to a trigonal prismatic frame that placed the sharp peak of the PDMS stamp in contact with the substrate during the dragging of the AgNW solutions (Figure 2.2a). This facilitated the uniform formation of air-liquid-solid meniscus lines behind the contact points between the stamp and substrate. The capillary force induced by solvent evaporation further facilitated the unidirectional alignment of the AgNWs. Figure 2.2b illustrates the principle of AgNW alignment via capillary forces. First, droplets of the AgNW solution are deposited on the target substrate and soaked into the line-patterned PDMS stamp. Next, the dragging of the AgNW solution, confined between the PDMS line-pattern and the target substrate, induces the partial pre-alignment of AgNWs in the dragging direction. This nanochannel-confined pre-alignment step is followed by the pinning of AgNWs by the evaporating air-liquid-solid meniscus line. The continued evaporation and movement of the meniscus contact line induces the further alignment of AgNWs in the dragging direction by the influence of the meniscus surface tension.

In this capillary printing technique, the PDMS nanochannels are crucial in the pre-alignment of AgNWs and the uniform formation of the meniscus line. We observed that the alignment of the AgNWs was not achieved when a flat PDMS stamp without nanochannels was used (Figure 2.3). When the PDMS channel width (10, 20 μm) is comparable to the NW length (20-30 μm), the weak physical confinement of NWs within the PDMS channels results in the increase of misaligned NWs (Figure 2.3). The smaller PDMS channel width (150 nm) than the 400 nm width results in a similar NW alignment degree (Figure 2.3), indicating that the 400 nm channel width is sufficient to physically confine long NWs (20-30 μm) and induce NW alignments in the channel direction. Because the nanochannel-confined pre-alignment step was followed by the alignment of AgNWs by the meniscus line, the distance between the nanochannel contact area and the meniscus contact line affected the degree of AgNW alignment. When the meniscus contact line was located too far from the nanochannel contact area, the pre-aligned AgNWs had a higher probability of random re-orientation within the solution before further alignment could be induced by the meniscus contact line. We varied the peak angle of the PDMS stamp, which affected the distance between the nanochannel contact area and the meniscus line. When the peak angle of the stamp was increased from 5° to 30° which resulted in a decreased distance, the degree of AgNW alignment increased (Figure 2.4). The contact pressure of the PDMS stamp also affected the degree of nanochannel confinement and thus the NW alignment. When the

contact pressure between the stamp and the target substrate was increased from 0 to 3.14 kPa, we observed an increased degree of alignment with sharper and clearer fast Fourier transform (FFT) spectral line shapes (Figure 2.5).

The inset in Figure 2.2b illustrates the principle of the capillary alignment of AgNWs at the meniscus contact line. Here, AgNWs are aligned perpendicular to the receding meniscus contact line by capillary forces, which can be defined as $F_s \approx 2\pi r\gamma$ where γ is the liquid surface tension and r is the radius of the NWs.⁵³ An estimation using $r = 16$ nm for the AgNWs and $\gamma = 22.39$ mN/m for the ethanol solvent provides $F_s \approx 2.2$ nN. When the AgNW is not perfectly aligned in the dragging direction by the solvent evaporation, as in the left-hand inset of Figure 2.2b, the slanted AgNW deforms the meniscus, resulting in the different dynamic contact angles of θ_1 and θ_2 on each side of the slanted AgNW. When θ_1 is larger than θ_2 for the slanted NW, the vertical component of the surface tension on one side is larger than that on the other ($\gamma^v \sin\theta_1 > \gamma^v \sin\theta_2$). This results in the rotation of the slanted AgNW toward the $\gamma^v \sin\theta_1$ direction, thus correcting the slant of the NW. When $\theta_1 = \theta_2$ after this rotation of the NW, the surface tensions are balanced ($\gamma^v \sin\theta_1 = \gamma^v \sin\theta_2$), which maintains the perpendicularity of the NW with respect to the meniscus line. The alignment of the AgNW can also be partially attributed to a hydrodynamic force, $F_{\text{hydrodynamic}} \approx \eta lV$, where η is the liquid viscosity, l is the length of the NW, and V is the printing velocity.⁹³ The estimated hydrodynamic dragging force is ~ 13 pN, using $\eta = 1.074$ mPa·s, $l = 25$ μm , and $V = 0.5$ mm s⁻¹, which is negligible compared to the capillary forces.

The friction force between the NWs and the substrate surface can also disrupt the movement of the AgNWs during the alignment process. Because the friction force strongly depends on the surface chemistry,⁹⁴ we investigated the influences of surface chemical modifications on the NW alignment (Figure 2.6). On CH₃-terminated surfaces, which are known to have low friction and adhesion forces,⁹⁴ the AgNWs were highly aligned along the dragging direction because of the low friction force, but the density of the assembled NWs was very low as a result of the low adhesion force between the AgNWs and the surface. In contrast, the stronger friction and adhesion forces on surfaces modified with amine monolayers led to poor NW alignment but larger NW density. Among the various surface treatments, modification with poly-L-lysine (PLL) produced the best conditions with good alignment, high NW density, and uniform NW assembly over a large area. The PLL modification can be employed on various substrate materials for the uniform alignment of AgNWs over large areas (Figure 2.7). The capillary printing technique not only generates uniformly aligned AgNWs, but also enables the formation of diverse morphologies of crossed AgNW arrays via multi-step printing processes without interference by the pre-aligned AgNW array. Figure 2.2c shows dark-field optical micrographs of differently oriented structures, including unidirectional, 45°-crossed, 60°-crossed, and rectangular AgNW networks. The FFT image of the unidirectional AgNWs exhibits a pattern of sharp lines, while those of crossed AgNWs at various angles of 45°, 60°, and 90° show crossed line patterns. By contrast, FFT

imaging of random AgNWs exhibit blurry circular patterns, indicating isotropic surface structures (Figure 2.8a).

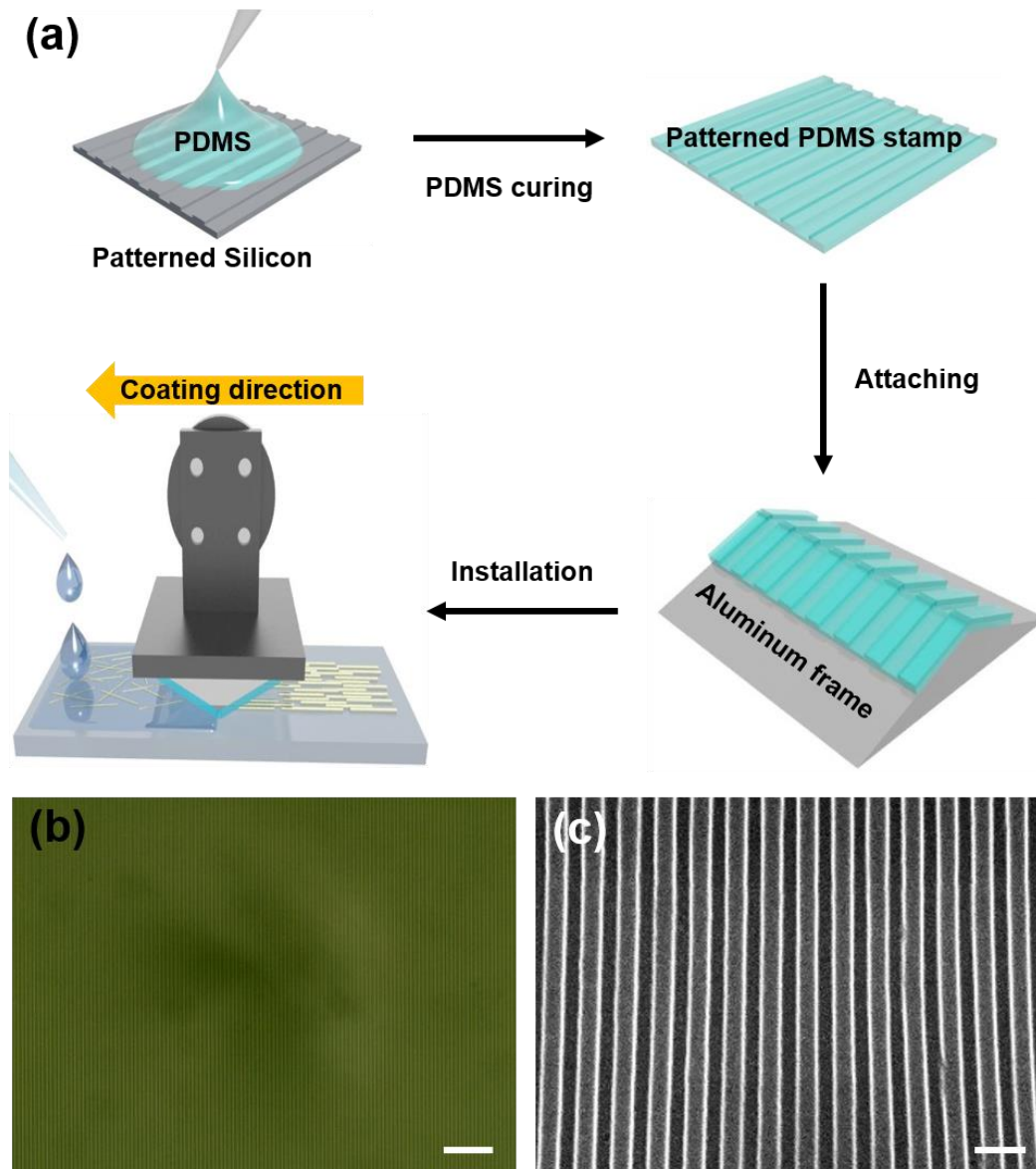


Figure 2.1. (a) Schematic of the procedure for capillary printing using a nano-patterned PDMS stamp for alignment of AgNW array. Optical microscopy (b) and scanning electron microscopy (c) images indicate the nano-patterned PDMS stamp with 400 nm of line width. Scale bars are 10 μm and 1 μm .

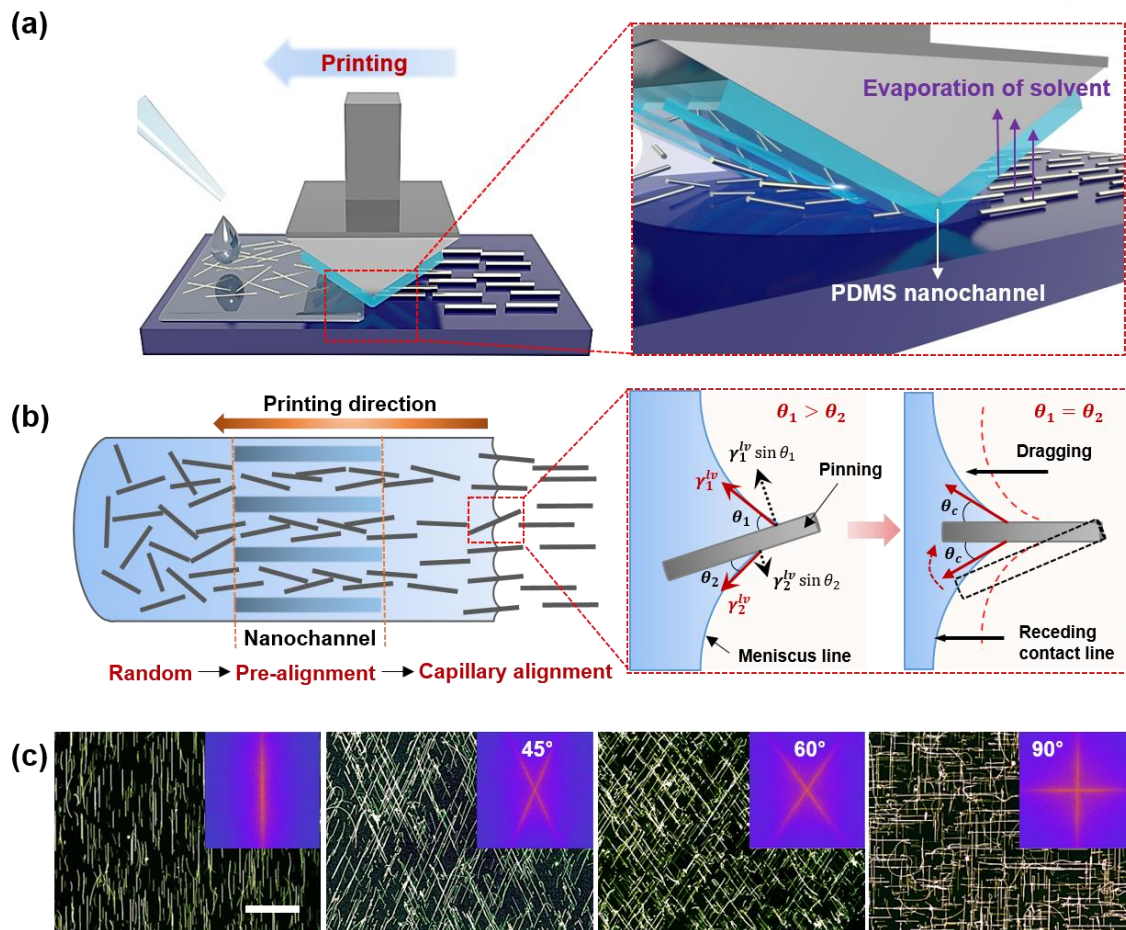


Figure 2.2 Solution-printed highly aligned AgNW arrays. (a) Schematic of the capillary printing process using a nano-patterned PDMS stamp to produce highly aligned AgNW arrays. (b) Schematic showing the alignment process during capillary printing of unidirectional AgNW arrays. The solvent-evaporation-induced capillary force produces highly aligned networks by dragging confined AgNWs at the solid-liquid-vapor contact line. (c) Dark-field optical images of differently oriented AgNW structures fabricated with a solution concentration of 0.05 wt.% via one-step (unidirectional) and multi-step (45°, 60°, and 90° crossed) capillary alignments. The scale bar is 40 μm . The fast Fourier transform (FFT) analyses of the images, presented in the insets, show the corresponding geometric structures.

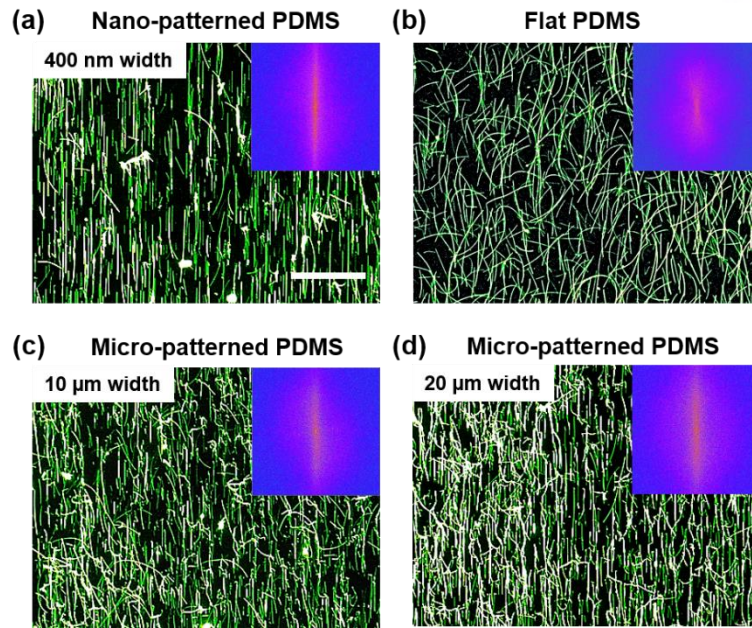


Figure 2.3. Dark-field optical micrographs of AgNW networks fabricated with a concentration of 0.1 wt.% by capillary printing using (a,b) nano-patterned, (c,d) micro-patterned and (e) flat PDMS stamps, respectively. The printing conditions include a speed of 1.5 mm/s and a pressure of 1.57 kPa. Alignment using nano-patterned PDMS stamps provides aligned AgNW networks with a characteristic line-shaped FFT pattern, in contrast to the blurred circular FFT pattern produced from networks using a flat PDMS stamp. All scale bars are 40 μm .

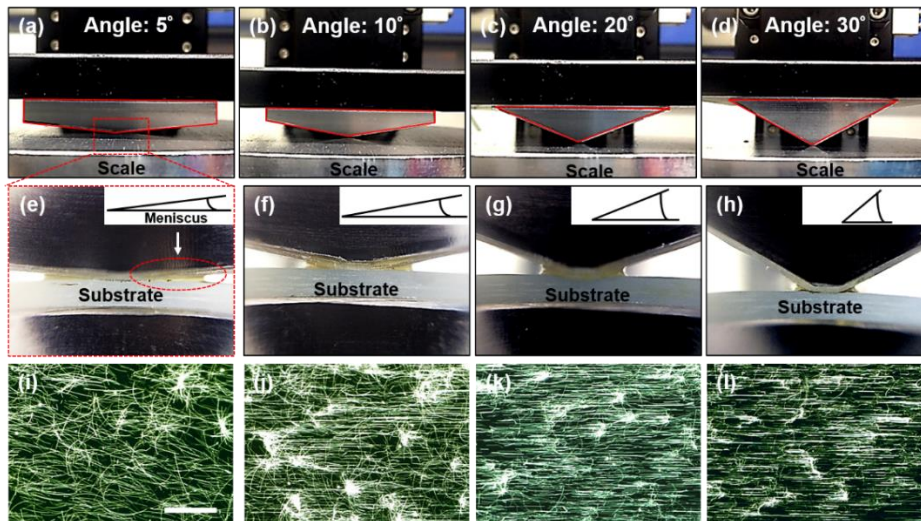


Figure 2.4. Effect of the angle of the triangular PDMS stamp on the NW alignment process. Photographic images of AgNW arrays prepared using triangular PDMS stamps with angles of (a) 5°, (b) 10°, (c) 20°, and (d) 30°. (e-h) Close-up images of the menisci formed using triangular PDMS stamps with different angles (5°-30°). (i-l) Dark-field images of aligned AgNW arrays coated using triangular PDMS stamps with different angles on glass treated by O_2 plasma. The scale bar is 40 μm .

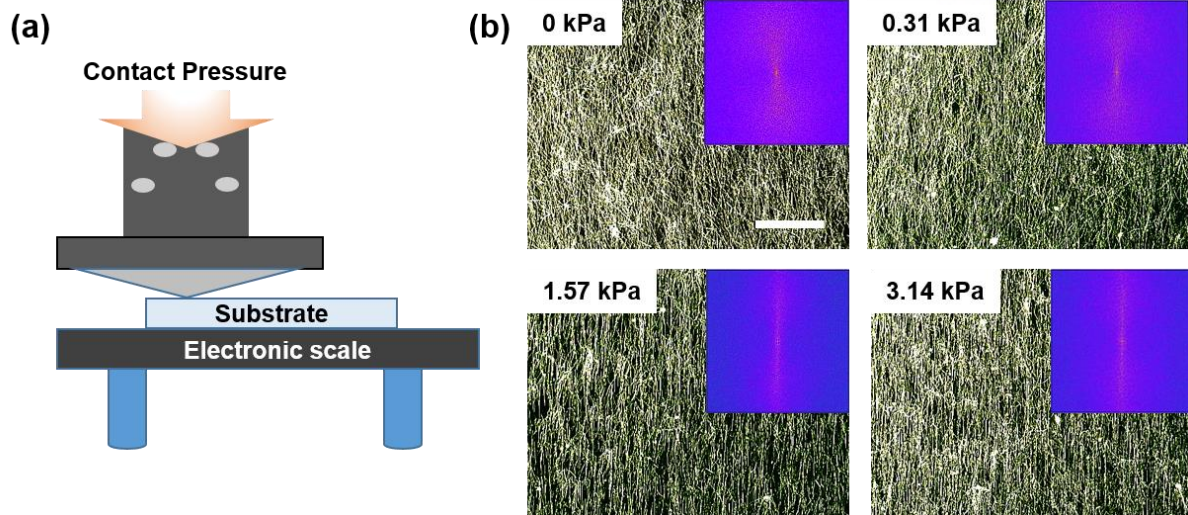


Figure 2.5. (a) Schematic illustration showing the measurement of contact pressure between the nano-patterned PDMS stamp and the substrate. (b) Dark-field optical micrographs of aligned AgNW networks fabricated with a concentration of 0.5 wt.% using different contact pressures (0-3.14 kPa). Line-shaped FFT patterns in the insets demonstrate that the alignment degree is increased with increasing contact pressure. The scale bar is 40 μm .

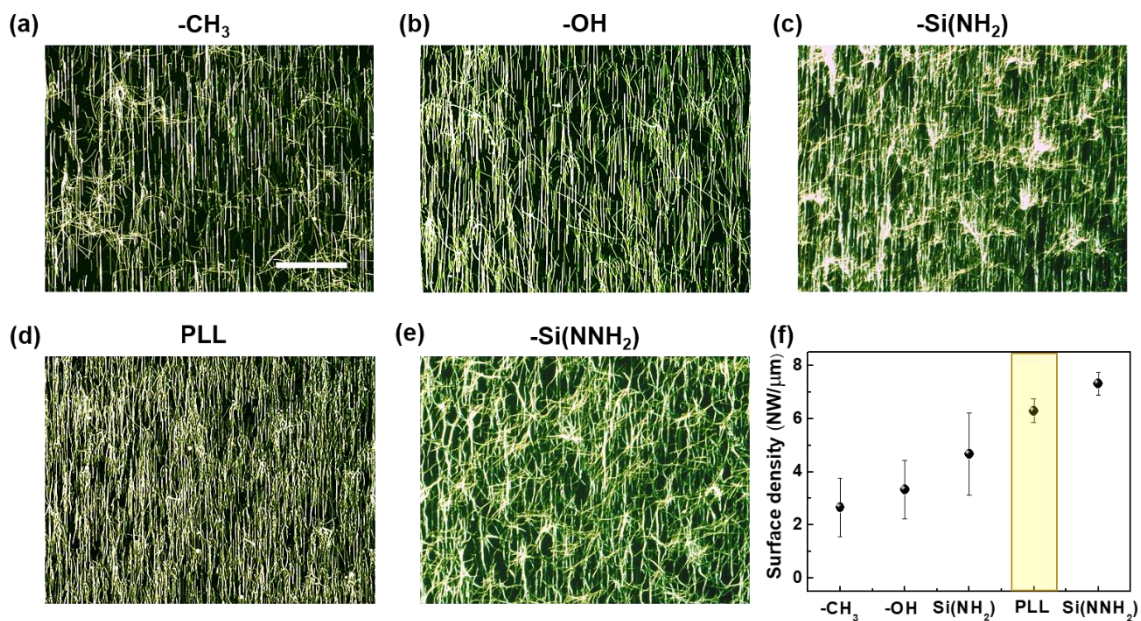


Figure 2.6 Dark-field optical micrographs of aligned AgNWs deposited on substrates chemically modified by (a) hexamethyldisilazane (HDMS), (b) O_2 plasma treatment, (c) (3-Aminopropyl)triethoxysilane (APTES), (d) poly-L-lysine (PLL), and (e) 3-(2-Aminoethylamino)propyltrimethoxysilane (AAPTMS). The scale bar is 40 μm . (f) The surface density of aligned AgNWs deposited on differently modified substrates.

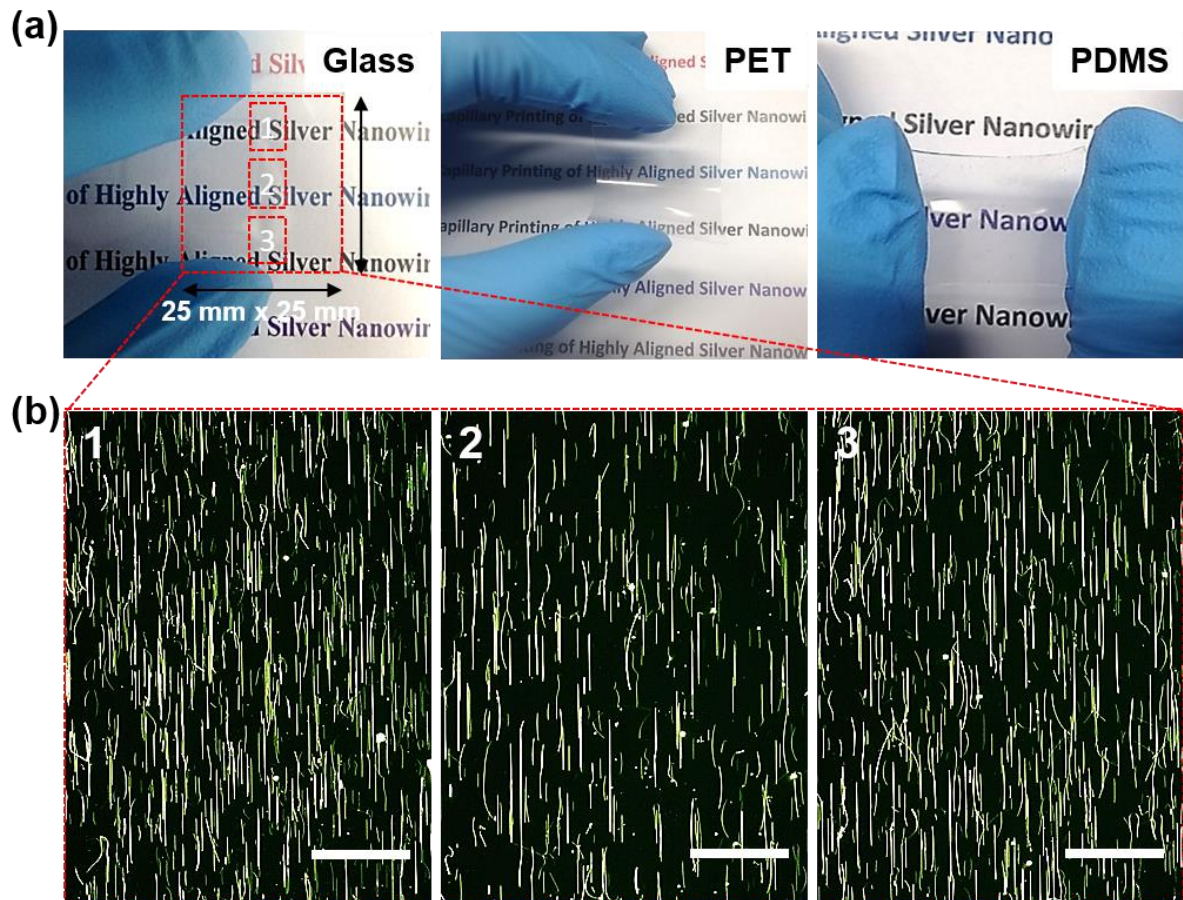


Figure 2.7. (a) Photographs of glass, PET, and PDMS substrates deposited with aligned AgNW arrays. (b) Dark-field optical micrographs of highly aligned AgNW arrays using a concentration of 0.05 wt.% measured at three points on the glass substrate with a size of 25 mm × 25 mm. All scale bars are 40 μm.

To further corroborate the quantitative analysis of the degree of alignment, a radial summation of the pixel intensity of the FFT data was plotted as a function of the radial angle (0-360°). As shown in Figure 2.8b, the unidirectional AgNW array shows clear peaks at 90° and 270°, indicating AgNW orientation in one direction. In contrast, random AgNWs shows no clear peak, resulting from the absence of any particular orientation of the AgNWs. Likewise, 45°-crossed, 60°-crossed, and rectangular AgNW arrays show four peaks centered at each corresponding radial angle, indicating that, in each case, the AgNWs are aligned in two discrete directions (Figure 2.8c).

To quantitatively characterize the AgNW alignment in the capillary printing process, the degree of AgNW alignment was monitored as a function of AgNW concentration and printing speed. Figure 2.9a shows that the degree of alignment increases as the NW density and coating speed decrease. In order to quantitatively compare the degree of alignment, the full width at half maximum (FWHM) of the FFT spectra were plotted as functions of NW density and printing speed (Figure 2.9b,c). The FFT spectra were acquired by plotting the pixel intensities as a function of radial summation from the 2D FFT patterns and fitting this plot by a Gauss function (Figure 2.10), in which the FWHM value quantified the degree of AgNW alignment by an inverse relationship. The FWHM value increases with the increase of NW concentration, indicating the decrease of the degree of alignment. This behavior can be attributed to the increased entanglement and cohesion between AgNWs at higher concentrations, which would prevent the pre-alignment of AgNWs in the nanochannels during the printing process. The increase of printing speed results in the increase of the FWHM value, correlating to the decrease of the alignment degree. This can be attributed to the disturbance of the uniform formation of meniscus contact lines when the movement of the receding meniscus contact line is impeded by the movement of the line-patterned stamp. This indicates that the alignment degree of the AgNW network can be decisively modulated by controlling the printing speed and NW concentration, enabling the precise control of the electrical properties of conductive percolation networks.

The aligned AgNW network showed a lower electrical percolation threshold than the random AgNW network. This is beneficial for the achievement of higher T at similar R_s or that of lower R_s at similar T . According to percolation theory, the electrical percolation threshold of AgNW networks can be determined by using the relation, $R_s \propto (m - m_c)^{-\alpha}$, where m_c is the threshold concentration of NWs and α is the critical exponent. The critical exponent reflects the dimensionality of the conductive network, with approximate values of 1.3 and 2.0 for 2D and 3D percolation networks, respectively.^{34, 95} The analysis of R_s as a function of NW areal density (S) reveals conductive percolation thresholds at $S = 6.05\%$ and 9.04% for aligned and random AgNWs, respectively (Figure 2.11a). The best fit to R_s as a function of $(S - S_c)$, where S_c is the critical percolation threshold, was obtained using $\alpha = 1.27$ and 1.30 for aligned and random AgNWs, respectively, both of which are close to the 2D theoretical values (Figure 2.11b,c)

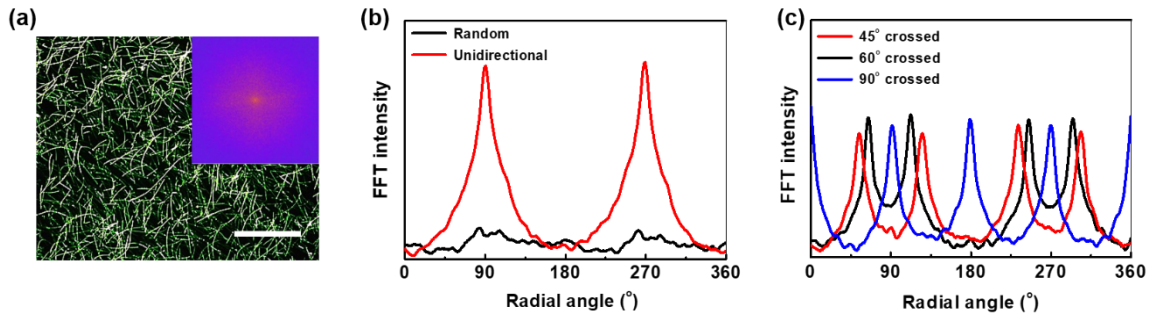


Figure 2.8. (a) Dark-field optical micrographs of random AgNW network fabricated by spincoating. The scale bar is 40 μm . FFT image provided in inset. (b) Radial summation of pixel intensity distribution between 0° and 360° in the FFT analyses of AgNW networks with aligned and random structures. (c) Radial summation of pixel intensity distribution between 0° and 360° in the FFT analyses of different geometric (45° , 60° , 90° crossed) AgNW networks fabricated via multi-step capillary printing alignment process.

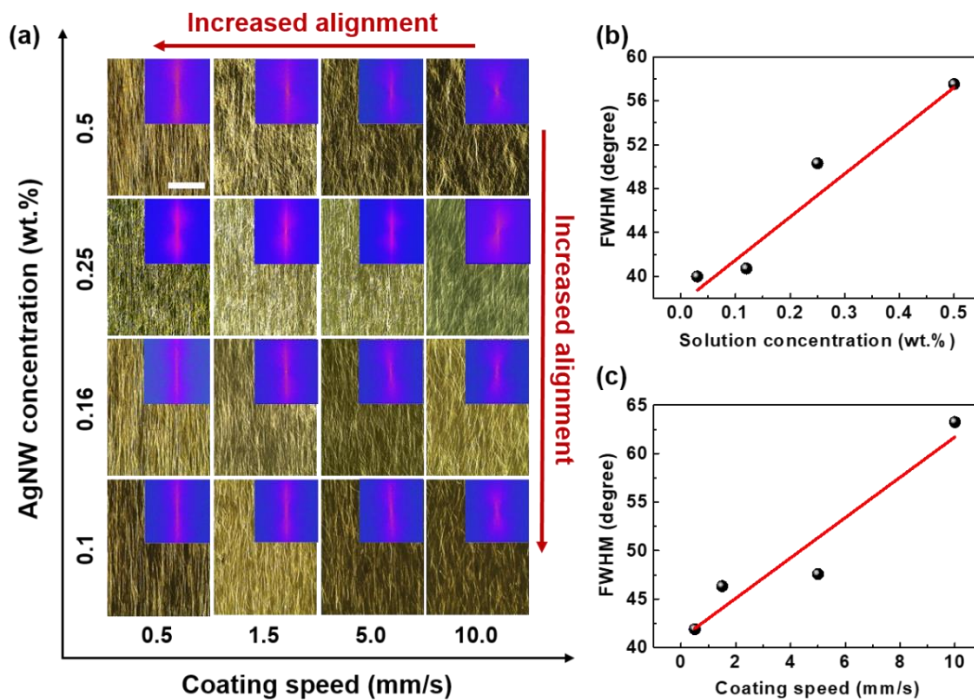


Figure 2.9. Quantitative FFT analyses of the degree of alignment of capillary-printed AgNW networks. (a) Optical micrographs of aligned AgNW networks fabricated using different coating speeds (0.5 - 10 mm s^{-1}) and solution concentrations (0.1 - 0.5 wt.%) on PLL-coated substrates. FFT images in the insets of the optical micrographs indicate unidirectional structures with anisotropic features. The scale bar is 20 μm . FWHM fitting data, calculated from the radial summation of pixel intensity in the FFT images, indicates the degree of alignment for printed AgNW networks fabricated with (b) different solution concentrations and (c) different coating speeds.

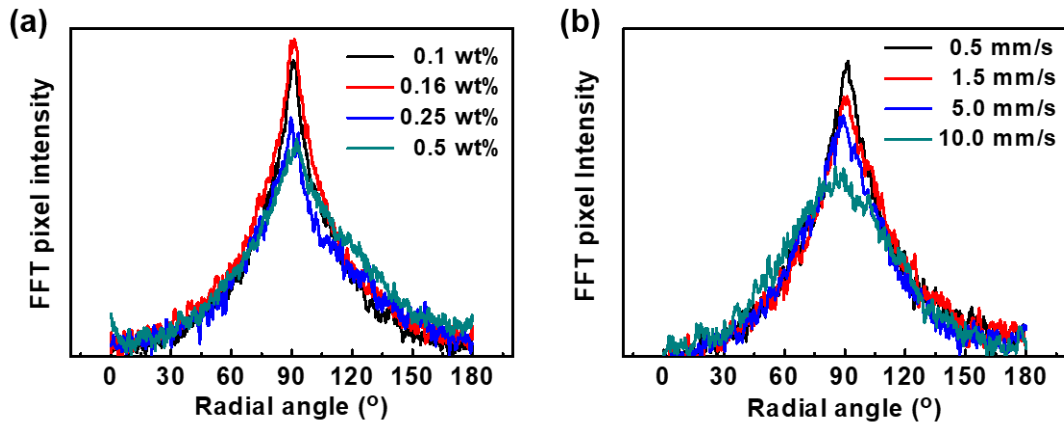


Figure 2.10. Radial summation of pixel intensity between 0° and 180° in FFT analyses of dark-field optical micrographs for aligned AgNW networks coated using (a) different solution concentrations (0.1-0.5 wt.%) and (b) different coating speeds (0.5-10.0 mm s⁻¹).

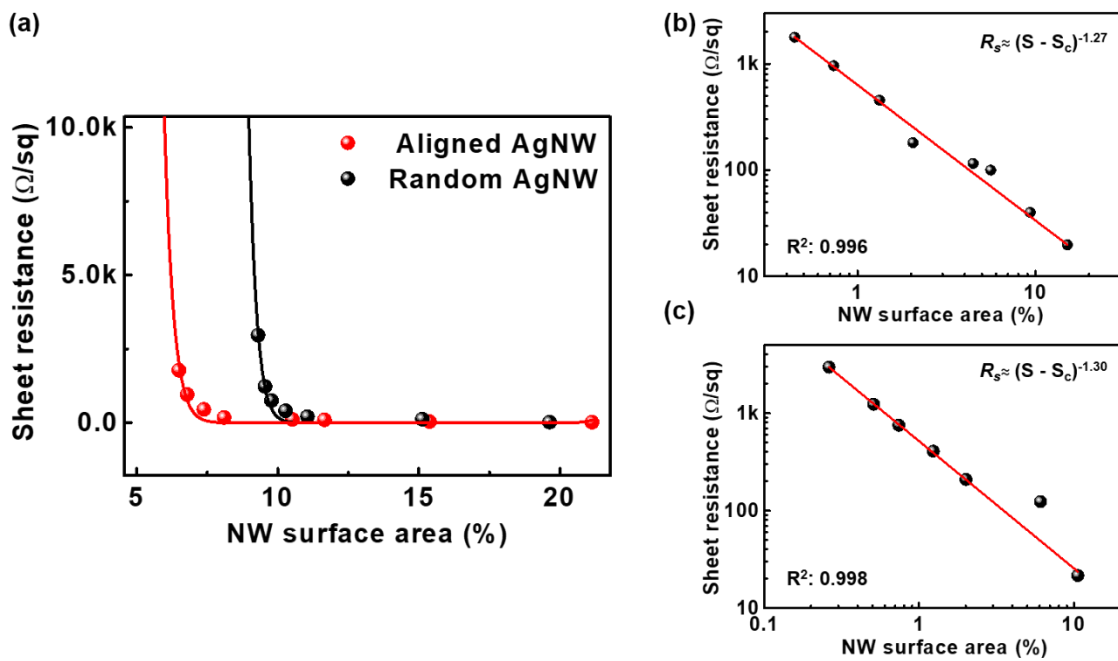


Figure 2.11. Electrical percolation behaviors of AgNW networks with different geometries. (a) Comparison of R_s in aligned and random AgNW networks as a function of surface area density. Power-law fits of R_s for (b) aligned and (c) random AgNWs as a function of $(S - S_c)$, where S_c (%) is the critical surface area density for the onset of conductivity.

Figure 2.12a shows SEM images of different morphologies of NW networks with similar electrical conductivities ($\sim 22 \text{ } \Omega \text{ sq}^{-1}$) and corresponding schematic representations of the electrical percolation networks for the aligned and random AgNW networks. For similar R_s , the aligned AgNW network displays a lower NW density compared to the random AgNW network because of the lower percolation threshold. To compare the electrical performances of aligned and random AgNW structures, R_s values of the AgNW networks have been plotted as a function of NW surface densities (Figure 2.12b). Here, the surface densities of the aligned AgNW networks were controlled by the coating speed (Figure 2.13a,b). One major advantage of our alignment technique is the production of high density NW assembly via a one-step solution-based process. At a coating speed of 0.5 mm/s, the NW density is $\sim 14 \text{ NWs}/\mu\text{m}$, which is higher than those of most previous NW assembly techniques (Figure 2.13c). The aligned AgNW films showed significantly lower R_s by a factor of $\sim 1.7\text{--}3.4$ at the same NW surface density, or significantly lower NW surface density by a factor of $\sim 1.4\text{--}1.8$ at the same R_s in comparison with those of random AgNW films (Figure 2.12b). The lower percolation thresholds of the aligned AgNW networks allow higher T values than those of random AgNW films at similar R_s . Figure 2.12c shows T , as well as the haze factor, of aligned and random AgNW networks with similar R_s values of $22.4 \text{ } \Omega/\text{sq}$ and $22 \text{ } \Omega/\text{sq}$, respectively. The aligned AgNW networks exhibit $\sim 3\%$ higher T and 2.4 times lower haze values at 550 nm wavelength compared to the random AgNW networks. These enhanced optical properties of the aligned AgNW networks can be attributed to the decreased light scattering resulting from the reduced percolation threshold and thus the lower NW surface density.

The R_s values of the aligned AgNW networks depend on the degree of alignment. Figure 2.12d shows the variation of R_s and T of the aligned AgNWs as a function of the FWHM value, as acquired from FFT analysis of optical images. The R_s decreases with the decrease of the FWHM value from 62° to 45° , indicating that the increase of alignment degree lowers R_s . However, T remains constant with the increase of alignment. The R_s value of the aligned AgNW networks is the lowest at $19.5 \text{ } \Omega/\text{sq}$ at the FWHM value of 50.6° . Further increase in the degree of alignment, with a FWHM of 45° , does not lead to the further decrease of R_s . The existence of this critical FWHM value, corresponding to a critical degree of alignment, indicates that the probability of contact between AgNWs decreases and therefore the percolation networks are disturbed when the degree of alignment in the AgNW network is greater than a critical point. Similar behaviors have been observed for aligned CNTs, where partially aligned networks provide lower percolation thresholds and higher conductivities than either randomly or perfectly aligned networks.⁹⁶⁻⁹⁸ We also note that R_s values of the aligned AgNW networks do not depend on the measurement directions (parallel and orthogonal directions) for aligned AgNW networks when the alignment degree is below the critical FWHM value (50.6°) (Figure 2.14). When the alignment degree further increases over the critical FWHM value, the aligned AgNW networks exhibit an increasing discrepancy of R_s values in the parallel and orthogonal directions.

Figure 2.12e compares the R_s to T performance of various AgNW TCEs, including the aligned and random AgNW networks fabricated in this study. The aligned AgNW networks exhibit superior transparencies of 95.0-96.7% and R_s values of 15.6-25.2 Ω/sq compared to other TCEs based on random AgNW networks. The best value of R_s - T performance of 19.5 Ω/sq at 96.7% transmittance for the aligned AgNW film compares favorably to the performances of previously reported AgNW TCEs, such as graphene-AgNWs hybrid film (33 Ω/sq , 94%)⁹⁹, very long AgNWs (9-23 Ω/sq , 89-95%),⁸⁵ spray-coated AgNWs (20 Ω/sq , 92.1%),⁴⁴ dry-transferred AgNWs (10 Ω/sq , 85%),⁸⁴ graphene oxide-soldered AgNWs (12-26 Ω/sq , 86-92.1%),³⁷ and polymer-soldered AgNWs (25 Ω/sq , 85%).⁶⁴

In order to evaluate the trade-off in performance between R_s and T for TCEs, the electrical to optical conductivity ratio (σ_{dc}/σ_{opt}) is used as a figure of merit (FoM), defined as¹⁴

$$T = \left(1 + \frac{188.5}{R_s} \times \frac{\sigma_{opt}}{\sigma_{dc}} \right)^{-2}$$

where the values of R_s and T at 550 nm wavelength are used. The aligned AgNWs with $T = 95.0$ - 96.7% and $R_s = 15.6$ - $25.2 \Omega/\text{sq}$ exhibited a FoM of $\sigma_{dc}/\sigma_{opt} = 360$ - 571.3 with an average value of 444.1. The FoM of the aligned AgNW films is significantly higher than that (218.6) of the random AgNW films as well as those of other solution-processed TCEs based on various NWs ($\sigma_{dc}/\sigma_{opt} = 89$ - 349) (Figure. 2.12f). The TCEs based on the aligned AgNWs also possess high flexibility. The aligned AgNW TCEs exhibit small variations in resistance (below 10%) under bending radii as small as 1.25 mm, whereas the resistance of ITO films sharply increases because of the brittle nature of ITO (Figure 2.15a). Moreover, the aligned AgNW films show high mechanical stabilities without significant changes in resistance, even after 1,000 bending cycles at the bending radius of 1.25 mm (Figure 2.15b).

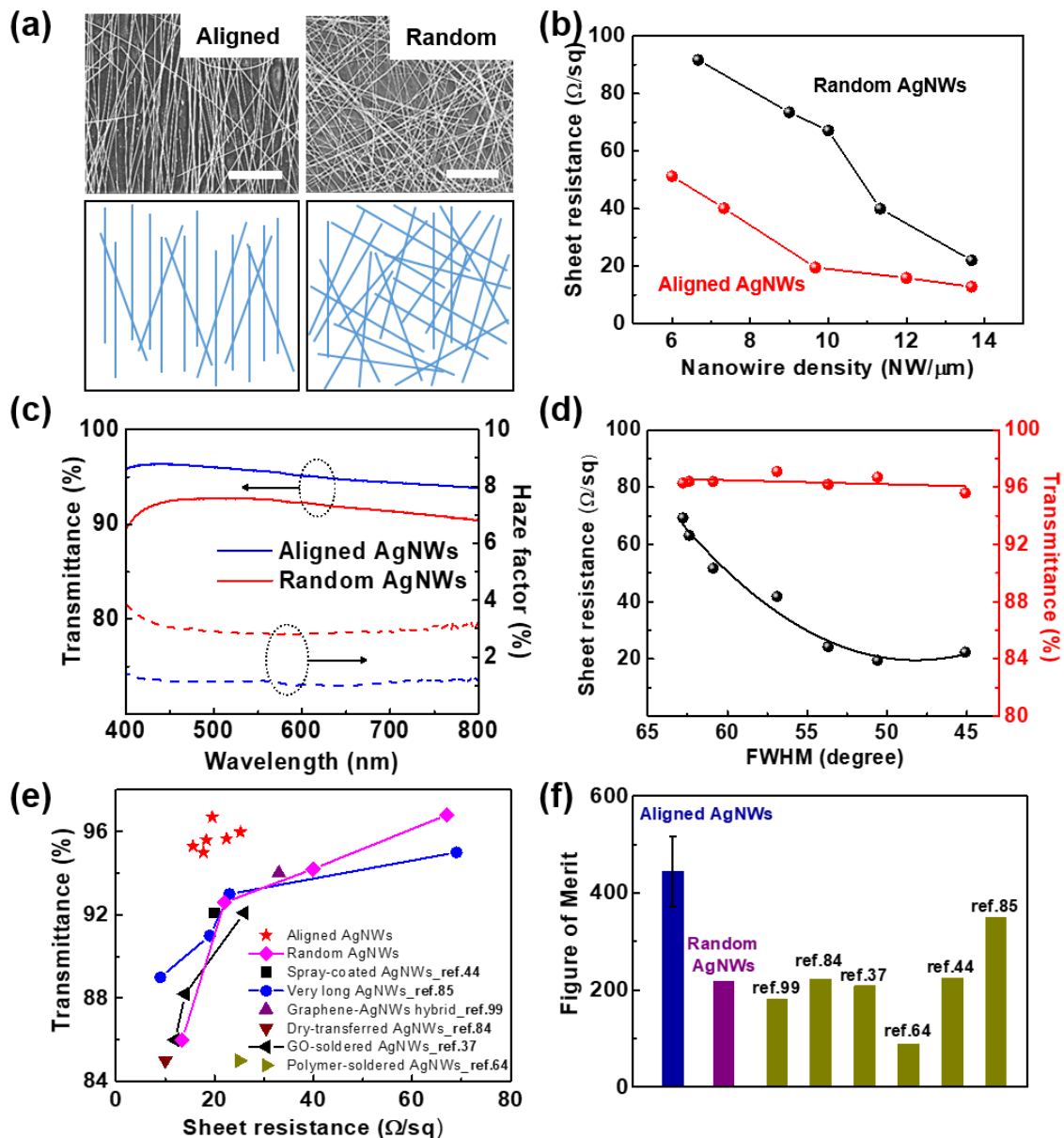


Figure 2.12. Comparison of optical and electrical performances of AgNWs with aligned and randomly oriented networks. (a) SEM images of aligned AgNW and random AgNW networks show good agreement with corresponding geometric structures. Schematics provide a basis for the understanding of the electrical percolation behavior of the networks. All scale bars are 2 μm . (b) Sheet resistance (R_s) for AgNW networks with aligned and randomly oriented geometries as a function of NW linear density. (c) Optical transmittance T (solid lines) and haze factor (dashed lines) over the visible spectrum for aligned (blue) and random (red) AgNWs with similar R_s values. The substrate was used as a reference. (d) Change in the R_s of aligned AgNW networks as a function of the alignment degree, wherein FWHM values are calculated from the radial summation of the pixel intensity in FFT patterns. Comparison of (e) the R_s - T performance and (f) FoM values of different AgNW electrodes.

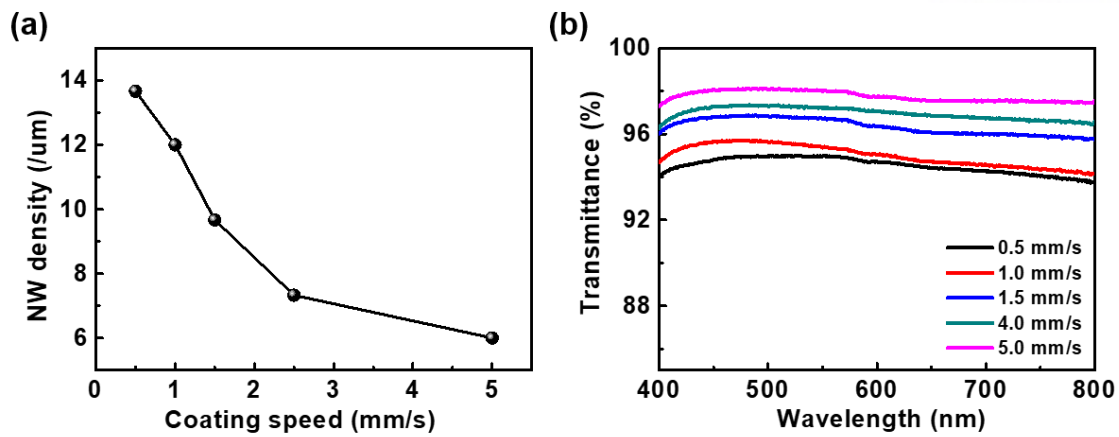


Figure 2.13. (a) Change in NW linear density and (b) T over the visible light range (400-800 nm wavelength) for aligned AgNW networks fabricated with different coating speeds. (c) The comparison of NW density of our work with the NW densities of other assembly techniques estimated from the reported results.

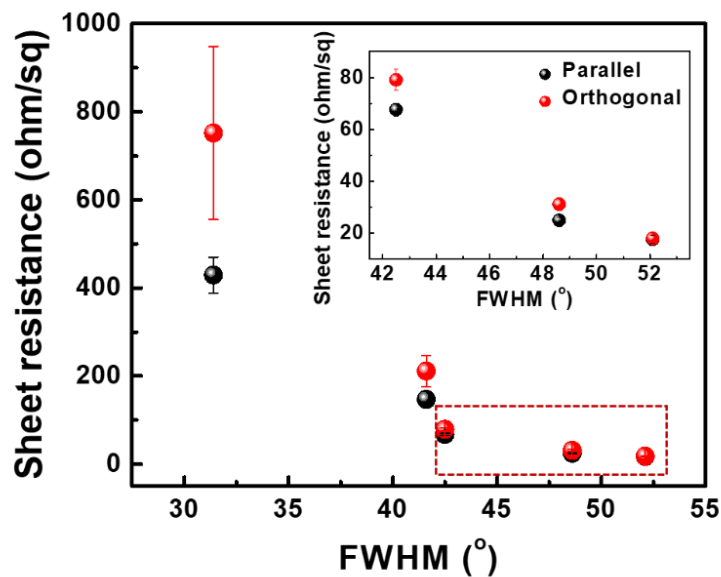


Figure 2.14. Sheet resistances of aligned AgNW networks for different measurement directions as a function of FWHM values. Aligned AgNW networks with various alignment degrees were fabricated with solution concentrations of 0.05-0.5 wt.%, coating speed of 1.5 mm/s, and coating pressure of 1.57 kPa.

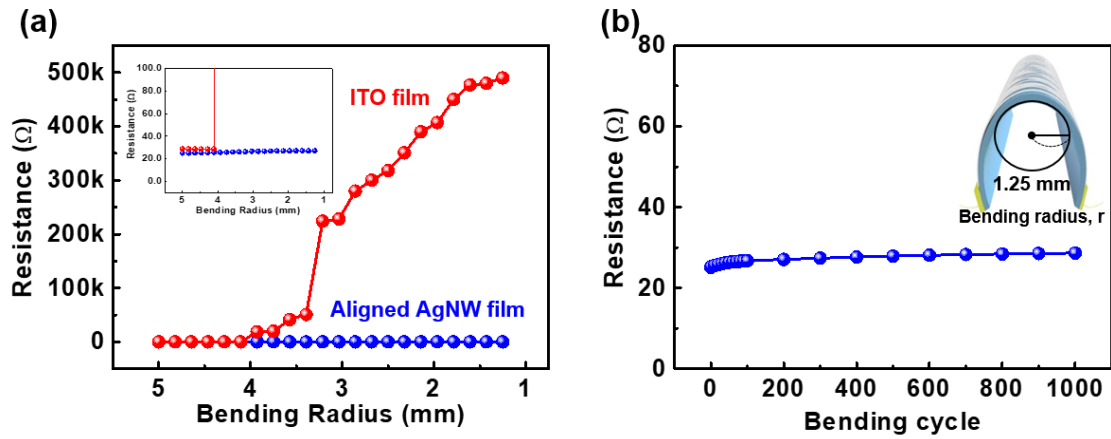


Figure 2.15. Mechanical properties of aligned AgNW films on PET substrates. (a) Variations in resistance of aligned AgNW film as a function of bending radius. (b) Resistance change over the course of 1000 bending cycles at the bending radius of 1.25 mm. Resistance was measured after the films were released and had resumed the lengths measured prior to bending.

In order to further evaluate the performances and compatibilities of the aligned AgNW TCEs for optoelectronic devices, we fabricated PLEDs using a device architecture of glass/AgNWs/poly(3,4-ethylenedioxythiophene) polystyrene sulfonate (PEDOT:PSS)/emitting layer/LiF/Al (Figure 2.16a). Super Yellow (SY-PPV) was used as the emitting layer material to create high-performance PLEDs.¹⁰⁰ Figure 2.16b shows the energy level diagram of the device. Figures 2.16c-f show the comparisons of current density, luminance, electroluminescence (EL), and power efficiencies of PLED devices based on ITO, random AgNW ($R_s = 20 \Omega/\text{sq}$, $T = 92.9\%$), and aligned AgNW electrodes ($R_s = 21.4 \Omega/\text{sq}$, $T = 95.8\%$), the results of which are summarized in Table 2.1. In traditional PLEDs with random AgNW networks, it has been reported that electrical charges were irregularly injected because of the protruding features and poor surface coverage of the AgNWs. This led to high leakage currents and irregular charge recombination inside the emissive layer, which caused unstable and low device efficiency.^{80, 101} Meanwhile, as can be seen in Figure 2.16c, the device with an aligned AgNW network shows a lower leakage current with a turn-on voltage of 2.0 V than that of the device with a random AgNW network, which can be attributed to the smoother surface morphology of the aligned AgNW network (Figure 2.17). In addition, the devices with aligned AgNW networks show enhanced light-emitting performances including maximum luminance, EL efficiency, and power efficiency of 33068 cd/m^2 (at 8.0V), 14.25 cd/A (at 5.8V), and 10.62 lm/W (3.6V), compared to devices with random AgNWs with performances of 25223 cd/m^2 (at 8.6V), 12.23 cd/A (at 7.0V), and 7.16 lm/W (4.8V), respectively (Table 2.1). The control devices with ITO electrodes exhibit the EL efficiency of 11.61 cd/A and power efficiency of 7.54 lm/W . In particular, the device with aligned AgNWs exhibits a 30% enhancement in maximum luminance compared to that with random AgNWs and also shows a high EL efficiency (14.25 cd/A), which is among the highest values reported so far using ITO-free TCEs for fluorescent PLEDs.^{57, 61, 80, 100-102}

The improved device performance with the aligned AgNW TCE can be attributed to the reduction in the optical loss of emitted light by the high T (Figure 2.18), low leakage current, and uniform charge injection by the smooth surface morphologies of the aligned AgNWs, resulting in the enhanced out-coupling efficiency. The low leakage current for the aligned AgNWs is beneficial in enhancing the stability and efficiency of the PLEDs. Atomic force microscope (AFM) and optical microscope images show that the aligned AgNW networks possesses a smoother surface (root mean square (RMS) roughness, $R_q = 15.6 \text{ nm}$) with no aggregated NWs, as compared to the random AgNW network with a large roughness ($R_q = 33.9 \text{ nm}$) and clumps of NWs, which can cause irregular charge injection as well as high leakage currents and short circuits from the AgNWs protruding through the emissive layer (Figure 2.17). Although random AgNW networks have been known to enhance the light extraction efficiency of LED due to the light scattering effect,^{47, 62} this effect is not significant in our study because our random AgNWs have a relatively low haze factor ($\sim 2.8\%$ at 550 nm wavelength) compared to the

previous studies.

As another application in optoelectronic devices, we evaluated the device performance of PSCs using aligned AgNW TCEs. The device structure and energy level diagram are presented in Figure 2.19a,b. Blended poly[4,8-bis(5-(2-ethylhexyl) thiophen-2-yl)benzo[1,2-b:4,5-b']dithiophene-co-3-fluorothieno[3,4-b]thiophene-2-carboxylate] (PTB7-Th):[6,6]-phenyl-C₇₁ butyric acid methyl ester (PC₇₁BM) electron donor:electron acceptor was used as the active layer to ensure high-performance PSCs.¹⁰³ Figure 2.19c shows the current density–voltage (*J*-*V*) characteristics of the devices with ITO, random, and aligned AgNW TCEs. Detailed characteristics of the PSCs are reported in Table 2.1. Notably, an enhanced short-circuit current (*J*_{SC}) of 17.83 mA/cm is observed for the case of aligned AgNWs. Meanwhile, random AgNW and ITO TCEs exhibited *J*_{SC} values of 16.37 mA/cm and 17.17 mA/cm, respectively. The high *J*_{SC} value using aligned AgNW-based PSCs can be attributed to the effective charge-carrier collection from the smooth surface of the electrodes, as well as the high *T* of 95.8% at 550 nm wavelength of the aligned AgNWs.

The increase in *J*_{SC} using the aligned AgNW TCEs is evident in the incident photon-to-current efficiency (IPCE) data. Figure 2.19d compares the IPCE in the wavelength range of 300–900 nm for PSCs with different TCE materials. In particular, in the range of 350 to 500 nm, PSCs with aligned AgNWs show quantum efficiencies several percent higher than those with random AgNWs, as a result of the higher *T* of the aligned AgNWs (Figure 2.18). In addition, the series resistance of the aligned AgNW-based devices, measured at 5 Ω cm² was lower than those with random AgNW (8.20 Ω cm²) and ITO (6.67 Ω cm²) electrodes, which resulted in a higher fill factor of 0.64 for the PSCs with aligned AgNWs than for those with random AgNW (0.61) and ITO (0.61) electrodes. As the results of these features, the PSCs with aligned AgNWs yielded power conversion efficiency (PCE, η) of 8.57% which is superior to that of PSCs with random AgNWs (7.62%) and comparable to that of the control devices with ITO (8.56%) (Table 2.1). Notably, the obtained $\eta = 8.57\%$ is the highest reported to date for PSCs using AgNW electrodes.

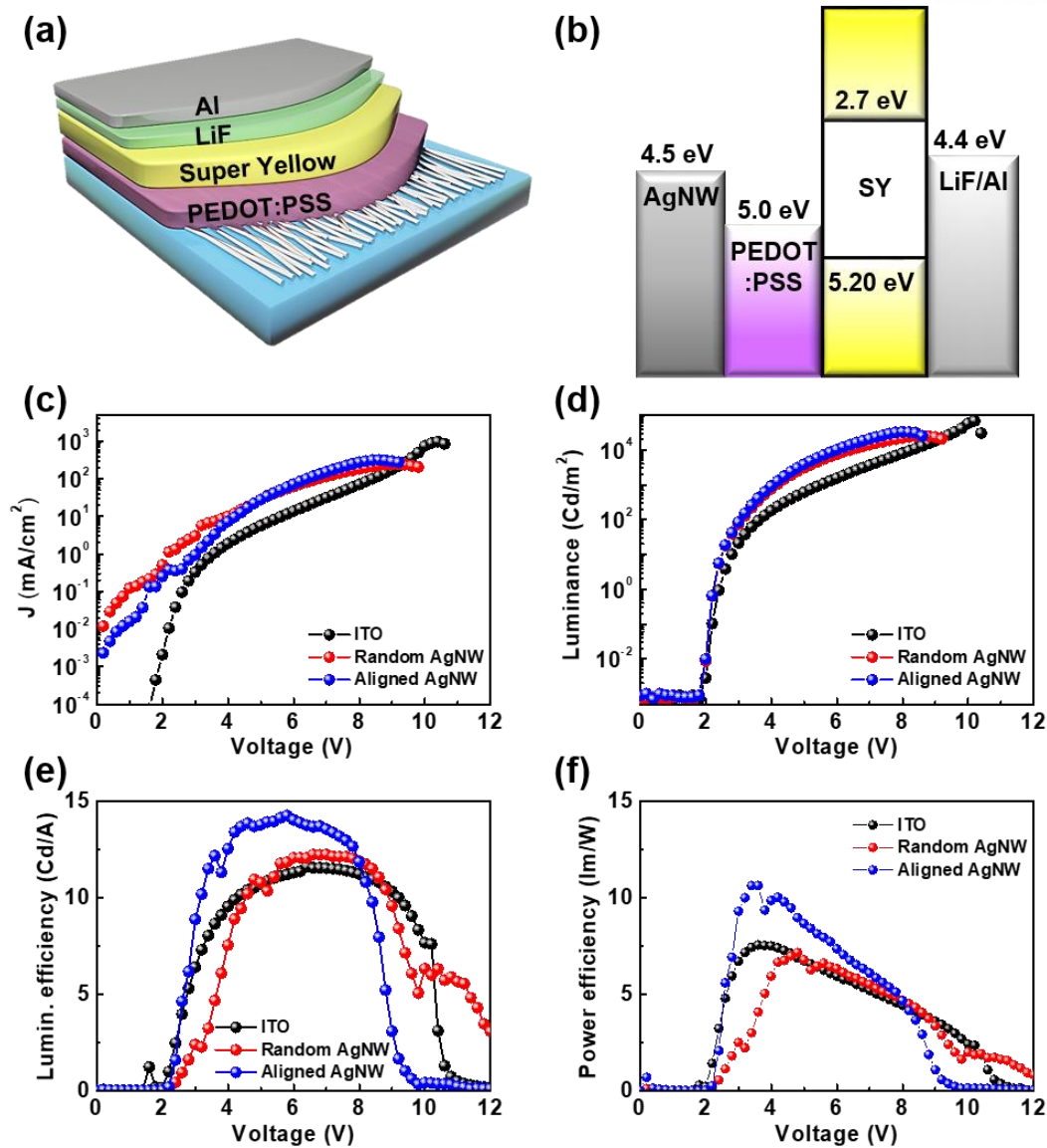


Figure 2.16. Device structure and characteristics of PLEDs using aligned AgNW electrodes. (a) Schematic PLED structure. (b) Schematic energy level diagrams under the flat-band condition for PLEDs with AgNW electrodes. (c) Current density, (d) luminance, (e) luminous efficiency, and (f) power efficiency with changes in the applied voltage for PLEDs with ITO, random, and aligned AgNW electrodes.

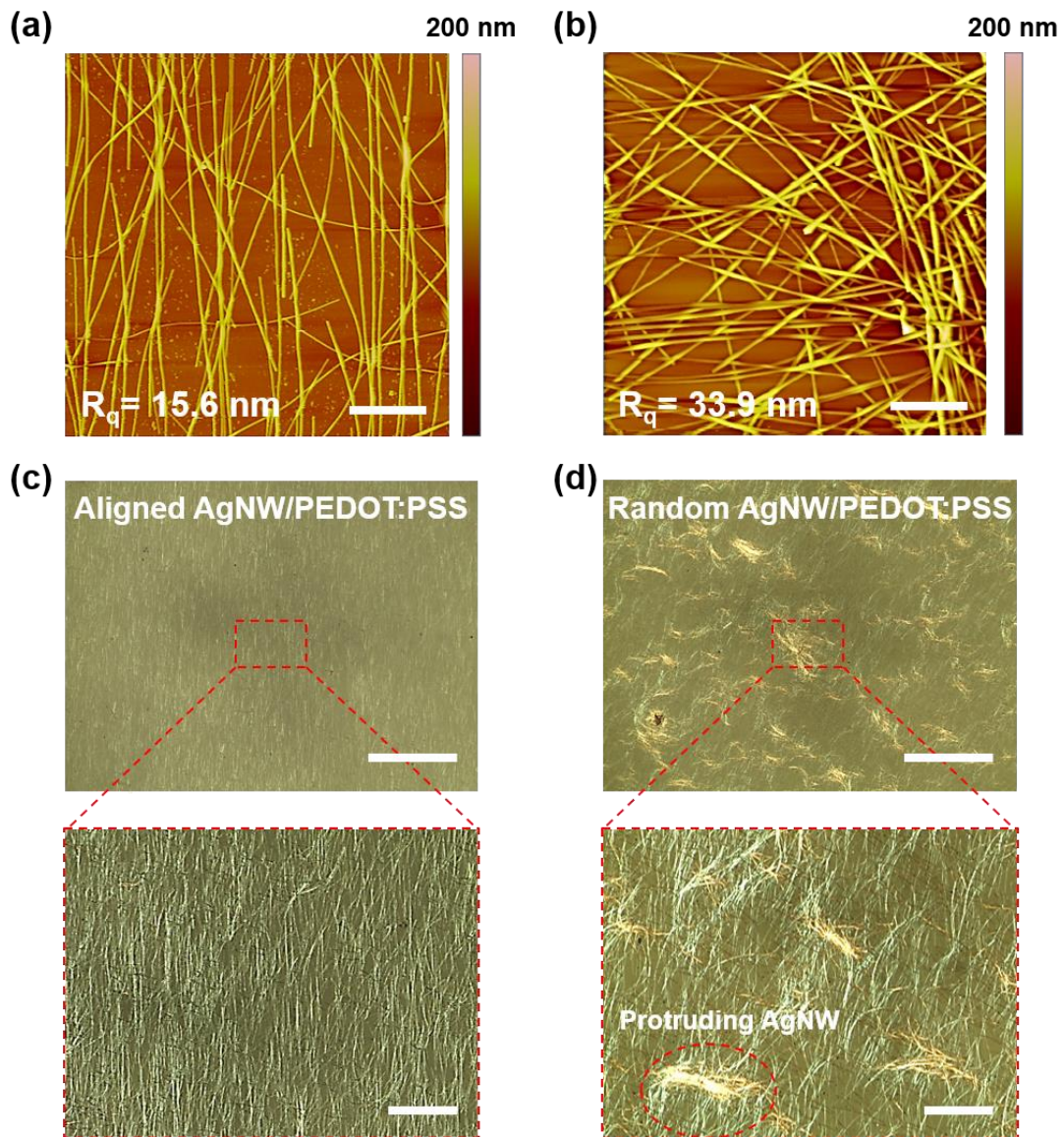


Figure 2.17. AFM images of (a) aligned AgNW networks and (b) random AgNW networks. The surface roughness of aligned AgNWs films is lower than that of random AgNWs films. The scale bars are 2 μm . Optical images for the surface of PEDOT:PSS coated onto (c) aligned and (d) random AgNW films. The scale bars are 100 μm . The surface of random AgNWs films shows the protrusion of NWs through the PEDOT:PSS layer. The scale bars of the magnifications are 20 μm .

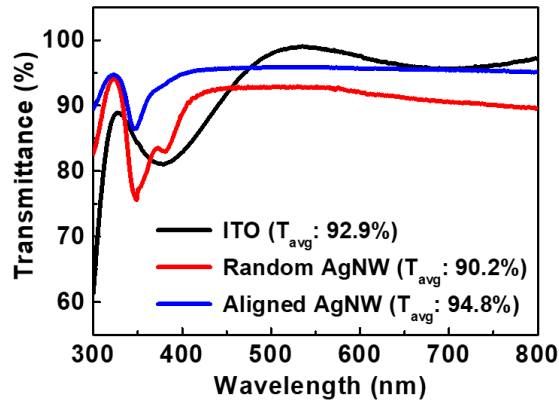


Figure 2.18. Transmittance spectra of ITO, random AgNW, and aligned AgNW films on glass substrates.

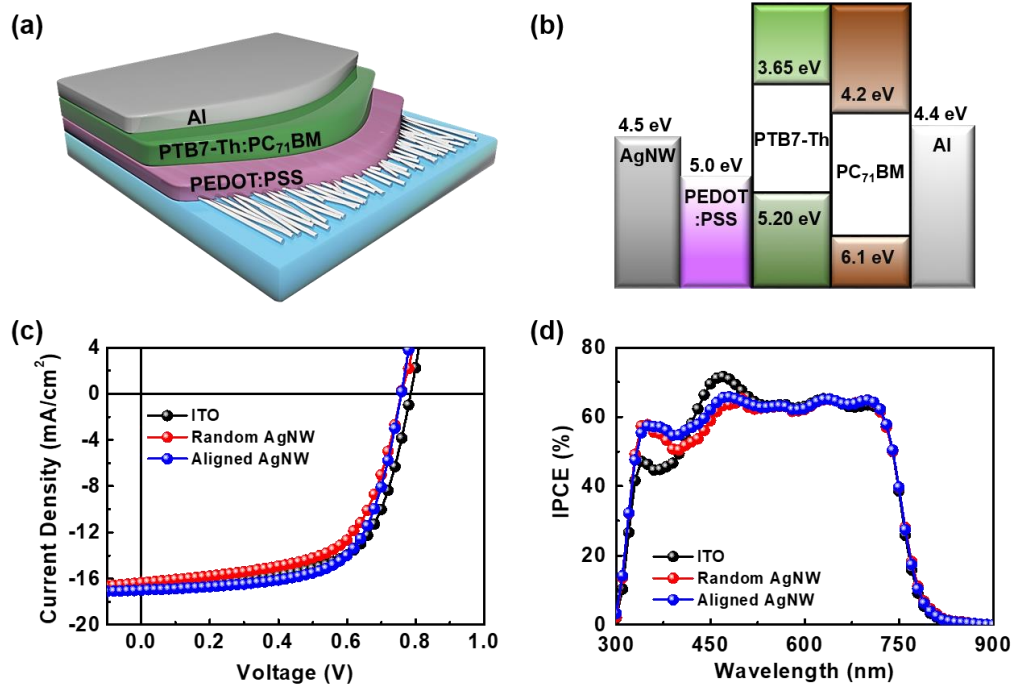


Figure 2.19. Device structure and characteristics of PSCs using aligned AgNW electrodes. (a) Schematic PSC structure. (b) Schematic energy level diagrams under the flat-band condition. (c) J - V characteristics under AM 1.5 illumination at 100 mW cm^{-2} and (d) IPCE of PSCs with ITO, random, and aligned AgNW electrodes.

Table 2.1. Device Characteristics of PTB7-Th/PC₇₁BM PSCs and SY PLEDs with ITO or random and aligned AgNW Electrodes.

PLED configuration	Maximum luminance [cd m ⁻²]	Maximum EL efficiency [cd A ⁻¹]	Maximum power efficiency [lm W ⁻¹]	Turn-on Voltage
ITO / PEDOT:PSS / SY / LiF / Al (<i>n</i> =4)	62301 ± 5952 (68253) ^a	10.16 ± 1.45 (11.61) ^a	8.37 ± 0.83 (7.54) ^a	2.0 V
Random AgNW / PEDOT:PSS / SY / LiF / Al (<i>n</i> =4)	22740 ± 2483 (25223) ^a	11.89 ± 0.34 (12.23) ^a	7.83 ± 0.67 (7.16) ^a	2.0 V
Aligned AgNW / PEDOT:PSS / SY / LiF / Al (<i>n</i> =4)	30523 ± 2545 (33068) ^a	12.49 ± 1.76 (14.25) ^a	9.51 ± 1.11 (10.62) ^a	2.0 V
PSC configuration	J _{sc} [mA cm ⁻²]	V _{oc} [V]	FF	PCE [%]
ITO / PEDOT:PSS / PTB7-Th:PC ₇₁ BM / Al (<i>n</i> =10)	16.57 ± 0.59 (17.17) ^a	0.79 ± 0.08 (0.80) ^a	0.63 ± 0.02 (0.61) ^a	8.26 ± 0.30 (8.56) ^a
Random AgNW / PEDOT:PSS / PTB7-Th:PC ₇₁ BM / Al (<i>n</i> =10)	16.29 ± 0.09 (16.37) ^a	0.76 ± 0.01 (0.76) ^a	0.61 ± 0.01 (0.61) ^a	7.46 ± 0.01 (7.62) ^a
Aligned AgNW / PEDOT:PSS / PTB7-Th:PC ₇₁ BM / Al (<i>n</i> =10)	17.20 ± 0.62 (17.83) ^a	0.76 ± 0.01 (0.76) ^a	0.64 ± 0.01 (0.64) ^a	8.39 ± 0.19 (8.57) ^a

To further evaluate the potential use of aligned AgNW networks in flexible devices, flexible PLEDs and PSCs based on aligned AgNWs were prepared using flexible substrates. The characteristics of the flexible PLEDs and PSCs using aligned AgNW and ITO electrodes are shown in Figure 2.20 and 2.21, respectively. The performances of the flexible PLEDs and PSCs with aligned AgNW TCEs were comparable to those of the devices with ITO films. In particular, a PCE of 8% was achieved for flexible PSCs with aligned AgNWs, which constitutes the highest PCE to date among flexible PSCs based on AgNW TCEs.^{46, 54, 55, 104} To investigate the mechanical stability of the flexible devices with aligned AgNWs, Figure 2.22a shows the change in luminance of flexible PLEDs using ITO and aligned AgNW TCEs over the course of 1,000 bending cycles at a bending radius of 5 mm. The flexible PLEDs using aligned AgNW TCEs retain 80% of the initial luminance over 300 bending cycles, whereas the ITO-based flexible PLEDs show rapid decreases in luminance. Likewise, the flexible PSCs using aligned AgNW TCEs retain over 80% of the original PCE value even after 1000 bending cycles, whereas the PCEs of devices using ITO rapidly decrease after only 100 cycles (Figure 2.22b). These results demonstrate the viability of using aligned AgNWs in flexible devices including OLEDs, PSCs and other optoelectronic devices.

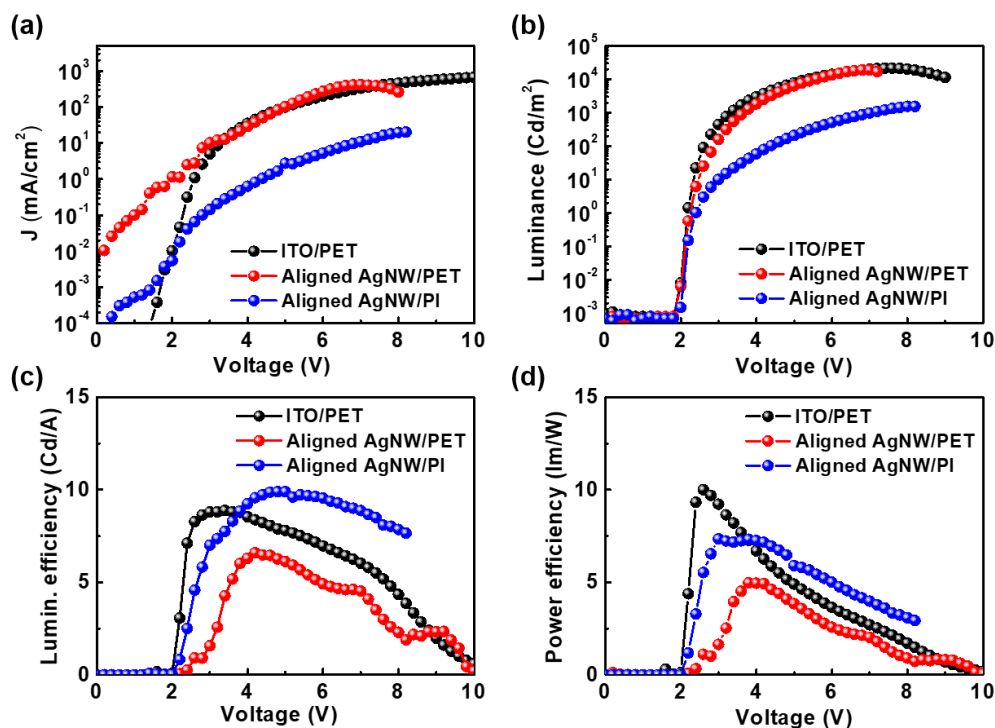


Figure 2.20. Light-emitting characteristics. Variations in (a) current density, (b) luminance, (c) EL efficiency, and (d) power efficiency with applied voltage using ITO-coated and random or aligned AgNW-based electrodes on flexible substrates.

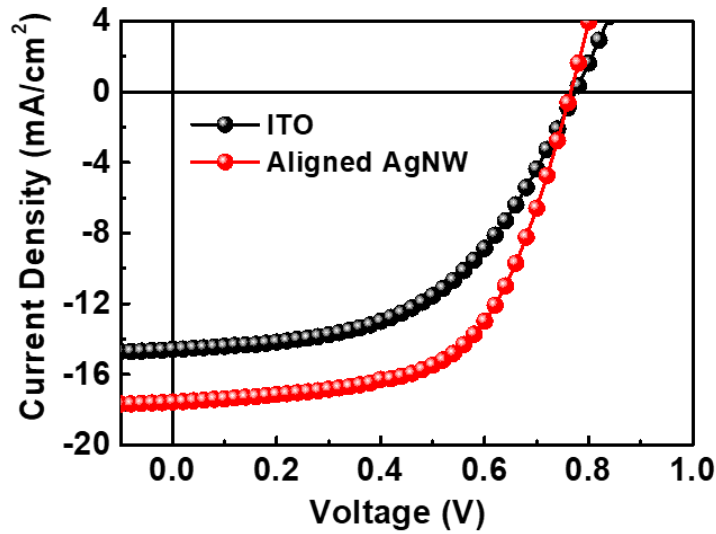


Figure 2.21. J - V characteristics under AM 1.5 illumination at 100 mW cm^{-2} with ITO and aligned AgNWs for flexible PSCs.

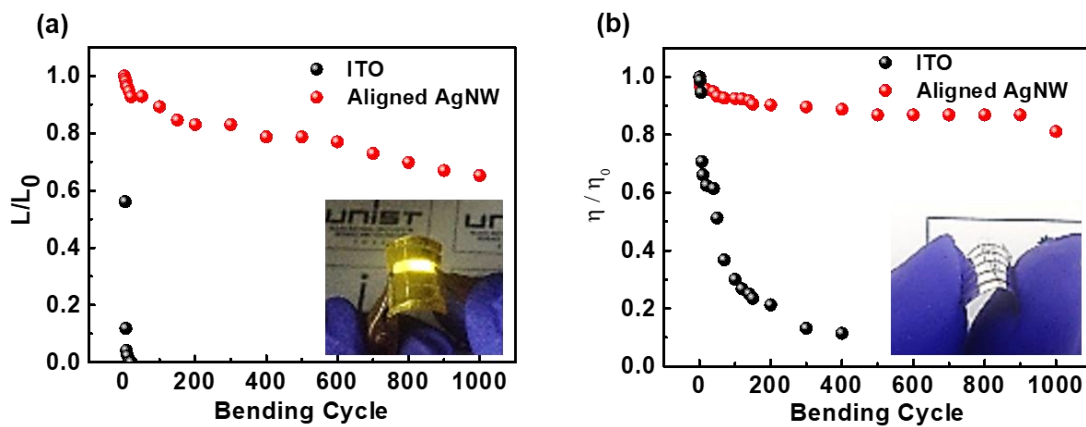


Figure 2.22. Performances of flexible PLEDs and PSCs. (a) Normalized luminance of flexible PLEDs and (b) power conversion efficiency (η) of PSCs using ITO and aligned AgNW on PET substrates over the course of 1000 bending cycles at 5 V with a bending radius of 5 mm. The insets show photographs of the flexible aligned AgNW-based PLED and PSC.

2.4 Conclusions

In conclusion, we have developed a high-throughput, one-step capillary printing strategy for the fabrication of TCEs based on aligned AgNWs. In the capillary printing process, the unidirectional dragging of AgNW solutions by a trigonal prismatic PDMS stamp with nano-patterned channels produced highly aligned AgNW arrays. The key technologies essential to the success of the capillary printing strategy include the pre-alignment of AgNWs in the PDMS nanochannels by physical confinement and the subsequent alignment of NW by the uniform meniscus line, which exerts solvent-evaporation-induced capillary forces on the meniscus-trapped AgNWs. The aligned AgNW networks showed lower electrical percolation thresholds than random AgNW networks, which led to higher T at similar R_s or lower R_s at similar T . Notably, partially misaligned NWs are necessary for the formation of the electrical percolation network. By tuning the degree of NW alignment, we demonstrated that the degree of NW alignment could be optimized for the fabrication of high-performance TCEs.

The TCEs based on aligned AgNW networks exhibited outstanding performances of 19.5 Ω/sq at 96.7% transmittance and a high FoM value of 571.3, which can be favorably compared to the performances of other NW-based TCEs. For the potential applications of aligned AgNW TCEs in optoelectronic devices, we demonstrated highly efficient, flexible PSCs and PLEDs. The observed PCE of 8.57% in PSCs, as well as the luminance efficiency of 14.25 cd/A and power efficiency of 10.62 lm/W in PLEDs, currently represent the highest efficiencies reported for AgNW-based devices. Moreover, the flexible PSC fabricated using aligned AgNWs had a PCE of 8.00%, 80% of which was maintained after 1,000 bending cycles. This work demonstrates that aligned Ag NW networks are excellent candidates for low-cost ITO-free TCEs used in optoelectronic devices and future flexible electronics. While the AgNW entanglement issue for high aspect ratio AgNWs needs to be addressed in the future, this capillary printing strategy for the preparation of aligned AgNW films may be further explored and applied to the alignment and assembly of other NW types, and may be of great utility in the development and mass production of next-generation optoelectronic devices.

Chapter 3. Plasmonic behaviors of an aligned AgNW network decorated by Ag nanoparticles for high-performance optoelectronic devices

3.1 Introduction

Organic optoelectronic devices (OODs) such as organic light-emitting diodes (OLEDs) and organic solar cells (OSCs) have attracted great attention due to their advantages such as cost-effective, light-weight, large scale solution processing and mechanical flexibility.¹⁰⁵⁻¹⁰⁷ Although significant progress has been made to enhance their device performance through the continued development of new materials and device configurations, further improvement of device efficiency is still necessary for their commercialization.¹⁰⁸⁻¹¹¹ One strategy to maximize device efficiency is to increase the active layer thickness to improving light absorption. However, the thickness of active layer is severely limited by the low carrier mobilities of most organic materials.^{112, 113} Therefore, it is necessary to find strategies to maximize light absorption within thin active layers.

Plasmonic metal nanostructures such as nanoparticles (NPs), nanorods (NRs), and nanowires (NWs) have been introduced as an efficient way to improve device efficiency via scattering or trapping of light.¹¹⁴⁻¹²⁶ Among various metal nanostructures, silver nanowires (AgNWs) are considered promising plasmonic materials with strong surface plasmon resonance (SPR) spanning the visible spectrum and near-IR region. AgNW networks offer the unique advantage of simultaneously serving as an excellent transparent electrode as well as a plasmonic nanostructure for high performance OODs.⁴⁵ Recently, plasmonic OSCs and OLEDs have been reported using random AgNW networks to enhance light scattering and trapping effects.^{101, 127} However, these devices based on random AgNW networks still contain several drawbacks including rough surface morphology and NW aggregation, which results in electrical short-circuits or deteriorated device efficiency.⁸⁰ In addition, despite their enormous potential for improving the efficiency of OSCs and OLEDs, the plasmonic effects of AgNW networks are still not fully understood and remain topics of intense investigation.

NW and NP-NW gap structures can be considered as efficient nano-antennas and nano-resonators. Both structures are rather efficient in resonantly enhancing the scattered light and local electromagnetic fields. NP-NW plasmon coupling has been known to provide large E-field enhancements via the gap-plasmon effect.¹²⁸⁻¹³⁰ In particular, NP-NW junctions can act as efficient nano-antenna for the efficient coupling of incident light into propagating surface plasmon polaritons (SPPs) on metal NWs surface.^{128, 130} The NP-NW plasmon systems constitutes a powerful platform for the design of new hybrid, plasmonic optoelectronic devices. However, there have not yet been concerted attempts to utilize NP-NW plasmon system to implement and improve device performance in OLEDs and OSCs.

Here, we demonstrate plasmonic transparent electrodes based on aligned AgNW networks decorated with core-shell Ag@SiO₂NPs (NP-enhanced plasmonic AgNW electrodes) for enhanced OOD

performance. Ag@SiO₂NP-AgNW electrodes provide strong plasmon coupling of incident light, resulting in outstanding E-field enhancement at NP-NW interface due to the NP-NW gap-plasmon effect. Furthermore, compared to plasmonic OSCs and OLEDs based on random AgNW networks, the aligned AgNW networks in our devices provide excellent figures of merit (electrical to optical conductivity ratio) and smooth surface morphologies, providing good contact with the active area for efficient carrier injection and reduced series resistance.¹³¹ Therefore, NP-enhanced plasmonic AgNW network serves as high-performance transparent electrode, which can be synergistically combined with plasmon properties with largely enhanced electromagnetic near-field coupling at NW-NP interface via gap plasmon effect to improve OOD device performance.

3.2 Experimental Details

Synthesis of core-shell Ag@SiO₂NP: For the preparation of core-shell Ag@SiO₂NPs, AgNPs were first synthesized by the polyol method. In detail, 0.1 g of silver nitrate was dissolved in a solution consisting of polyvinylpyrrolidone (PVP) (1.5 g) and ethylene glycol (6 mL). The PVP-capped Ag nanoparticles were collected after reaction at 120°C for 1 hr. Next, silica shells were formed onto the surfaces of AgNPs in the following way: A homogeneous AgNP solution in ethanol (140 mL) was mixed with ammonium hydroxide (4 mL) with stirring, and then 0.75 mL of tetraethyl orthosilicate (TEOS) was injected. Another aliquot of TEOS (0.75 mL) was added in the resulting solution after 30 min. Finally, Ag@SiO₂ NPs were collected after several centrifugations with ethanol.

Fabrication of aligned AgNW decorated by core-shell Ag@SiO₂NPs film: To prepare AgNP enhanced plasmonic AgNW electrodes, glass substrates were cleaned with acetone, isopropyl alcohol (IPA) and deionized (D.I.) water by sonication for 15 min each. Substrates were functionalized with amine groups using PLL layers, which were spin-coated onto substrates using 0.1% solutions of PLL in H₂O at 4000 rpm for 60 s. Next, aligned AgNW networks were fabricated onto amine functional group terminated substrates by solution based capillary printing, where 0.5 wt% AgNW dispersions in ethanol were used. AgNWs with an average length of 25 ± 5 μm and diameter of 32 ± 5 nm (Nanopyxis Corp.) were used. To fabricate hybrid NW-NP structures, aligned AgNW films were immersed in an 1.0 wt.% Ag@SiO₂NPs dispersion in ethanol for 10 min.

Fabrication and characterization of OSCs using NP-enhanced plasmonic AgNW: OSCs were fabricated using AgNWs and Ag@SiO₂NP-AgNW films on top of cleaned glass substrates. A poly[4,8-bis(5-(2-ethylhexyl) thiophen-2-yl)benzo[1,2-b:4,5-b']dithiophene-co-3-fluorothieno[3,4-b]thiophene-2-carboxylate] (PTB7-Th, 1-Material) and [6,6]-phenyl-C₇₁ butyric acid methyl ester (PC₇₁BM, Rieke Metal) blend system was used for the active layer of the PSCs. The device configurations used for the PSCs was AgNWs or Ag@SiO₂NP-AgNW/PEDOT:PSS/active layer/Al. A PEDOT:PSS(A14083) solution was spin-cast on top of the Ag NWs and ITO films after UV-treatment for 15 min., then dried at 120 °C to remove moisture. The resulting substrates were transferred to a nitrogen-filled globe box and a PTB7-Th:PC₇₁BM (12 mg:15 mg) mixture in chlorobenzene (1 mL) with 3% of diphenyl ether (DPE) as an additive was spin coated. Subsequently, the devices were transferred to a vacuum chamber (<10⁻⁶ torr) and Al electrodes (ca. 100 nm thick) were deposited by thermal evaporation. The area of the Al electrodes was 13 mm². Photovoltaic characteristics were measured inside a nitrogen filled glove box using a high quality optical fiber to guide light from a solar simulator. The current-voltage characteristics were measured using a Keithley 2635A source measurement unit under AM 1.5G illumination at 100 mW cm⁻². The devices were measured using a shadow mask to define the photoactive area (0.13 cm²). The external quantum efficiency was measured using an EQE system (Model QEX7) by PV measurement Inc (Boulder, Colorado).

Characterization: Core-shell Ag@SiO₂NPs were characterized using UV-visible spectrometry (Jasco V-670) and transmission electron microscopy (TEM, JEOL). Optical properties of Ag@SiO₂NP-AgNW networks were measured using UV-visible spectrometry (Jasco V-670) equipped with a linear polarizer. The sheet resistance of hybrid Ag@SiO₂NP-AgNW films was obtained using the four-point probe technique (Kiethley 2400 equipment). For Raman mapping analysis, the Raman intensity was investigated using a confocal Raman microscope (Alpha 300, WITec) with 532 nm laser excitation. Confocal images were obtained by the CLSM technique (FV1000, OLYMPUS Corp.) using an incident laser with the wavelength of 473 nm. Fluorimetry (Cary Eclipse, Varian Corp.) was used without an integrating sphere to measure solid-state PL spectra.

3.3 Results and Discussion

A schematic illustration of the NP-enhanced plasmonic AgNW electrode design is shown in Figure 3.1a, consisting of aligned AgNW networks decorated with core-shell Ag@SiO₂NPs where AgNPs are separated from the surface of AgNW by nanometer-scale gaps due to their SiO₂ shells. Here, we employed core-shell Ag@SiO₂NPs to provide dielectric gaps between NPs and NWs, thus preventing direct contact between AgNPs and AgNWs and generating gap plasmon coupling. These gaps at the NP-NW interfaces can induce giant localized E-field enhancements by mediating the coupling of light to plasmonic near-field excitations and guided modes such as SPPs with in the plane.

Specifically, AgNPs on the AgNWs can function as nano-antenna to couple the incident light into delocalized SPPs on the NW surfaces. This type of E-field enhancement is schematically shown in Figure 3.1b.¹²⁸ Figure 3.1c shows a transmission electron microscopy (TEM) image of core-shell Ag@SiO₂NPs, which comprise of the Ag@SiO₂NPs separated from the NWs by a nanoscale dielectric gap of ~ 5 nm provided by the SiO₂ shells. The size of core-shell nanoparticles was controlled to prevent electric short-circuits through the active layer and to ensure a smooth surface morphology. The optical absorption spectra of Ag@SiO₂NP films exhibit a broader and slightly red-shifted absorption band around 420 nm wavelength compared to AgNP films without shells (Figure 3.2), which is attributed to the dielectric environment change from air to SiO₂ which modulates the localized surface plasmon resonance (LSPR) frequency of AgNPs. The fabrication procedure of NP-enhanced plasmonic AgNW film is schematically illustrated in Figure 3.3. The aligned AgNW networks are directly coated onto a glass substrate using a capillary printing technique after the modification of glass surface by amine-terminated poly-L-lysine (PLL) (Figure 3.4).¹³¹ Next, core-shell Ag@SiO₂NPs are uniformly coated onto the aligned AgNW networks using a dip coating method. Figure 3.1d shows a scanning electron microscope (SEM) image of the surface geometry of an NP-enhanced plasmonic AgNW film. It can be seen that Ag@SiO₂NPs are uniformly assembled onto and between the aligned AgNW networks. AgNPs adhered onto AgNWs provide NW-NP junctions which generate gap plasmon effects (Figure 3.1e). Moreover, the aligned AgNW networks have been demonstrated to exhibit a lower percolation threshold, resulting in significantly improved optical transmittance at a similar sheet resistance and smoother surface roughness compared to random AgNW networks.¹³¹ Therefore, NP-enhanced plasmonic AgNW electrodes yield low sheet resistance (20.5 Ω/sq) and high transmittance (94.3% at 550 nm wavelength), allowing them to function as high performance transparent electrodes (Figure 3.1f).

The optical absorption spectra were collected with different densities of Ag@SiO₂NPs. NP-enhanced plasmonic AgNW films showed several absorption maxima, where 350 and 380 nm extinction peaks arise from the transverse SPR modes of AgNWs and the 420 nm extinction peak represents LSPR of AgNPs, respectively (Figure 3.1g).⁴⁵ The spectral intensities at 380 nm and 420 nm gradually increase

with increasing surface density of Ag@SiO₂NPs, which can be attributed to a combination of absorption produced by plasmon excitations from the nano-antenna as well as the resonance couplings between SPRs of AgNPs and AgNWs.¹³² To further investigate the plasmon coupling of NP-enhanced plasmonic AgNW films, we collected absorption spectra of aligned AgNW networks without AgNPs using light with different polarization directions. As shown in Figure 3.5, the aligned AgNW networks clearly show polarization dependent absorption spectra according to the polarization direction of incident light relative to the NW orientation. In contrast, random AgNW networks do not show polarization dependence. For the aligned AgNW networks, the intensities of two absorption maxima at ~350 and ~380 nm are strongly enhanced for incident light polarized perpendicular to the NWs due to two distinct transverse SPR modes. In contrast, the broad absorption at longer wavelengths (500 – 800 nm), arising from the longitudinal SPR modes of AgNWs, is enhanced when the incident light is polarized parallel to the NWs. This polarization dependent optical behavior is mainly attributed to optical anisotropy of the aligned AgNW networks.¹³³ Plasmonic behavior of NP-enhanced plasmonic AgNW films differs somewhat from aligned AgNW films. Previously, it has been reported that SPPs can be excited by incident light through the NP antenna on NWs and propagate along the NWs over tens of microns (with gradual energy loss by Ohmic damping) and can be scattered back into free-space photons by the NP antennas on the NWs.^{128, 134, 135} Figure 3.1h shows polarized absorption spectra of NP-enhanced aligned plasmonic AgNW films with different polarization directions of incident light. Interestingly, when the incident light is polarized perpendicular to the NW axis, the intensities of transverse SPR peaks (350 and 380 nm peaks) of AgNWs are higher than those of parallel polarization, indicating the higher probability of excitation of transverse SPR modes of AgNWs at perpendicular polarization. In the meantime, the intensity of the LSPR peak (420 nm) of AgNPs for perpendicular polarization is lower than that of parallel polarization, suggesting that the LSPR mode of AgNPs is partially deactivated through the hybridization between LSPs of AgNPs and propagating SPPs on AgNWs. This result indicates that the coupling efficiency of NP-NW gap plasmons is higher at perpendicular than parallel polarization, in agreement with previous reports.¹³⁶ We also observe that the broad absorption at long wavelengths (500 to 800 nm) is higher for parallel polarization than for perpendicular polarization, implying that the longitudinal SPP modes on AgNWs are highly excited by parallel polarization (Figure 3.1h).

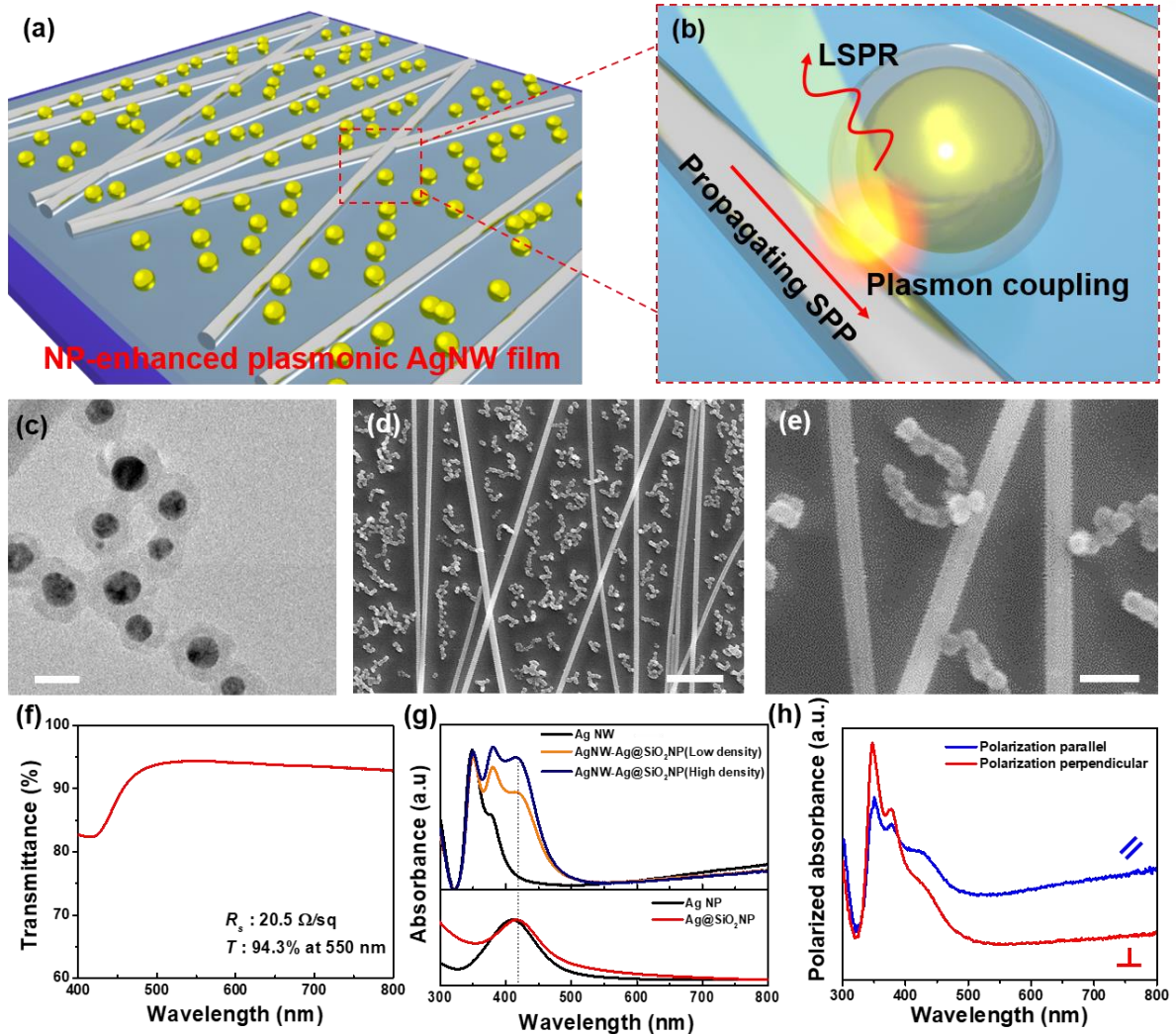


Figure 3.1. Hybrid NP-enhanced plasmonic AgNW network. (a) Representative illustration of a NP-enhanced plasmonic AgNW network. (b) Schematic illustration of plasmon coupling in a NW-NP hybrid plasmonic system showing the interaction between LSP of a metal NP and propagating SPP on a metal NW. (c) Transmission electron microscopy (TEM) image of core-shell Ag@SiO₂NPs. The scale bar indicates 20 nm. (d,e) SEM images of an aligned AgNW network decorated with core-shell Ag@SiO₂NPs. Scale bars indicate 500 nm and 100 nm, respectively. (f) Optical transmittance of an aligned AgNW decorated with Ag@SiO₂NPs film in the visible region. (g) Optical absorption spectra of (top) aligned AgNW networks decorated with different densities of Ag@SiO₂NPs, (bottom) AgNP and Ag@SiO₂NPs in the range of 300–800 nm. (h) Polarization dependent optical absorption spectra of aligned AgNW networks decorated with Ag@SiO₂NPs. Polarization angles are defined as parallel (0° of polarization) and perpendicular (90° of polarization) to the axis of the NWs.

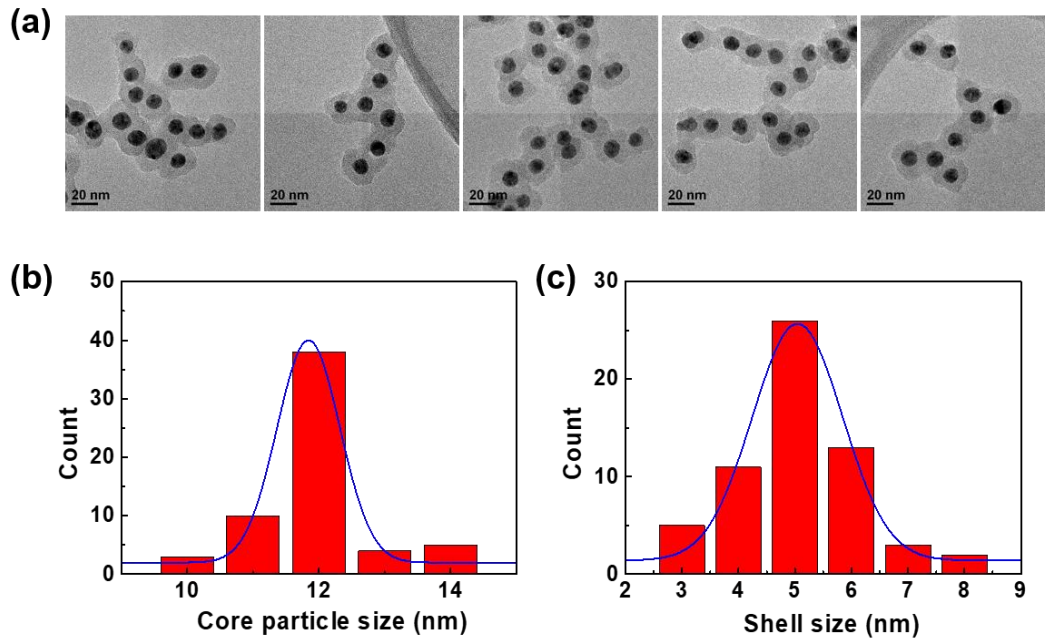


Figure 3.2. (a) TEM image of core-shell Ag@SiO₂ NPs, which comprise of core AgNP and SiO₂ shells (b) The size distribution of core-shell Ag@SiO₂ NPs, obtained from an image analysis of 60 core-shell Ag@SiO₂ NPs in TEM images.

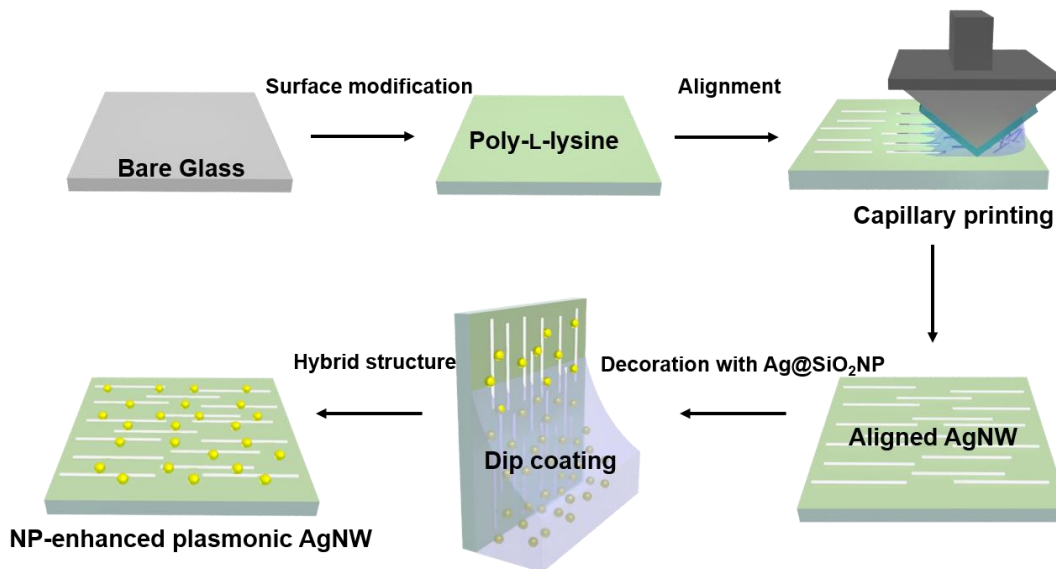


Figure 3.3. Schematic of fabrication process for NP-enhanced plasmonic AgNW electrodes on glass substrates.

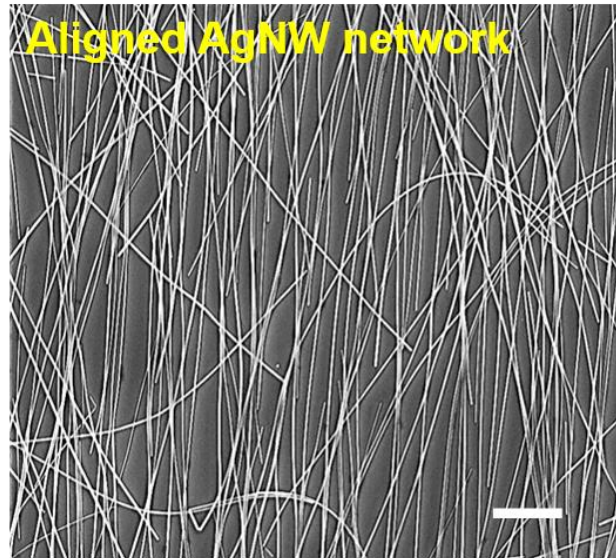


Figure 3.4. SEM images of the aligned AgNW network. The scale bar indicates 1 μm .

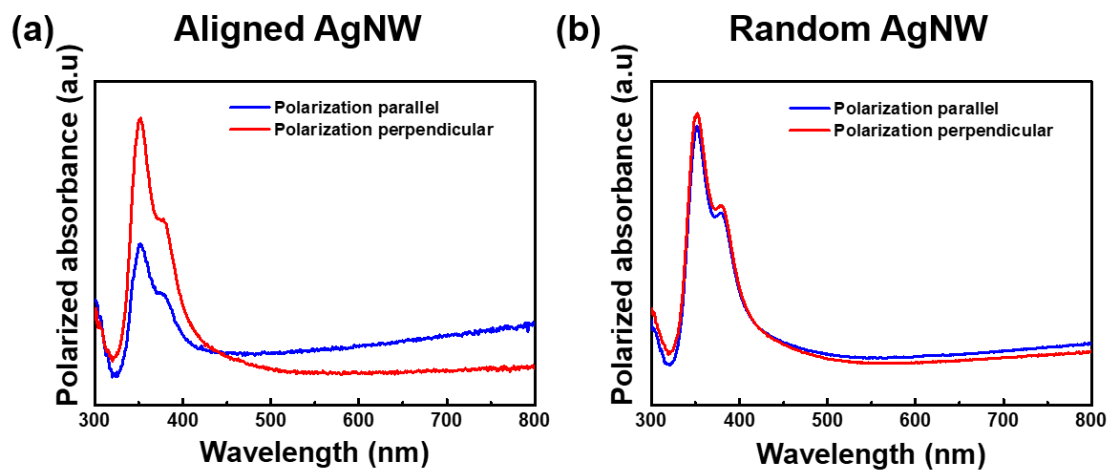


Figure 3.5. Optical absorption spectra of (a) aligned AgNW and (b) random AgNW with different polarization of incident light

To elucidate NP-NW plasmon couplings, extinction spectra of NP-enhanced plasmonic AgNWs were simulated by the discrete dipole approximation (DDA) algorithm to calculate the E-field enhancement by NP-NW plasmon couplings. Simulated extinction spectra of both AgNW and Ag@SiO₂NP-AgNW systems were obtained where two distinct peaks at 372 and 402 nm are commonly observed due to transverse SPRs of AgNWs (Figure 3.6). One weak excitation mode at 466 nm was also observed due to the longitudinal SPR excitation along the axis parallel to the wire.¹³⁷ In addition, a significant extinction enhancement was observed at 416 nm with the addition of Ag@SiO₂NP in the NP-NW plasmonic system (Figure 3.7). Figures 3.8a, b show local electric-field enhancement images of NW and NP-NW systems, respectively, under 416 nm excitation for polarization perpendicular to the nanowire. E-field enhancement images for the NP-NW system show a giant enhancement of localized E-field at the NP-NW junction due to the strong gap plasmon couplings at the nanoscale gap of the NP-NW interface. Figure 3.8c shows normalized E-field intensities for NW and NP-NW systems along the NW length. In the NP-NW system, the gap plasmon effect between NW and NP provides significant E-field enhancement at NP-NW junction as well as additional E-field enhancement at both ends of the AgNW. The modeled E-field enhancements provide a conceptual basis to confirm the mechanism by which AgNPs adhered on AgNWs can act as nano-antenna which couple incident light into SPP modes in the AgNWs which propagate to both ends of the NW.¹³⁵ In addition, it has been reported that NP-NW coupling strongly depends on polarization direction where E-field enhancements are much larger for polarization perpendicular to NWs than for polarization parallel to NWs.^{128, 136} In our simulation, for light polarization parallel to the NW, E-field enhancement at the NP-NW interface is relatively low compared to polarization perpendicular to the NW which demonstrates the existence of polarization dependent plasmon coupling (Figure 3.8a,b and 3.9). To verify the plasmon coupling at NP-NW junctions, surface-enhanced Raman scattering (SERS) spectra of NP-NW junctions absorbed on PLL were investigated under different polarizations in single NP-NW system as shown in Figure 3.8d. The Raman spectra of PLL at NP-NW junctions exhibit higher intensity when the incident light is polarized perpendicular to the NWs, which shows good agreement with the simulation results (Figure 3.8e). In addition, the Raman intensity for NP-NW junctions is considerably larger than that for the NWs alone, indicating a giant enhancement due to the NP-NW plasmon coupling effect (Figure 3.8f). To compare plasmonic behavior of three different plasmonic systems including AgNW films, NP-enhanced plasmonic AgNW films, and Ag@SiO₂NP films, Raman mapping analysis images were obtained as shown in Figures 3.8g-i. SEM images of the three different systems showing their surface geometries are shown in Figure 3.10. Notably, NP-enhanced plasmonic AgNW films showed the brightest regions with many intense spots, indicating that the strong NP-NW plasmon couplings resulted in overall increases in Raman intensity. On the other hand, AgNW films without NPs exhibited only local bright spots due to strong plasmon couplings at the junctions between AgNWs. In contrast, the Raman

mapping image of an Ag@SiO₂NP film shows an entirely dark region with extremely low Raman signals, suggesting that NP-NP plasmon interactions in Ag@SiO₂NP assemblies are not the main factor in our NP-NW plasmonic system due to the larger gap distance formed by two SiO₂ shells at NP-NP contacts, which reduces the SERS intensities. The large improvement of Raman intensity distribution for NP-enhanced plasmonic AgNW films can be attributed to giant E-field enhancement due to NP-NW gap plasmon couplings.

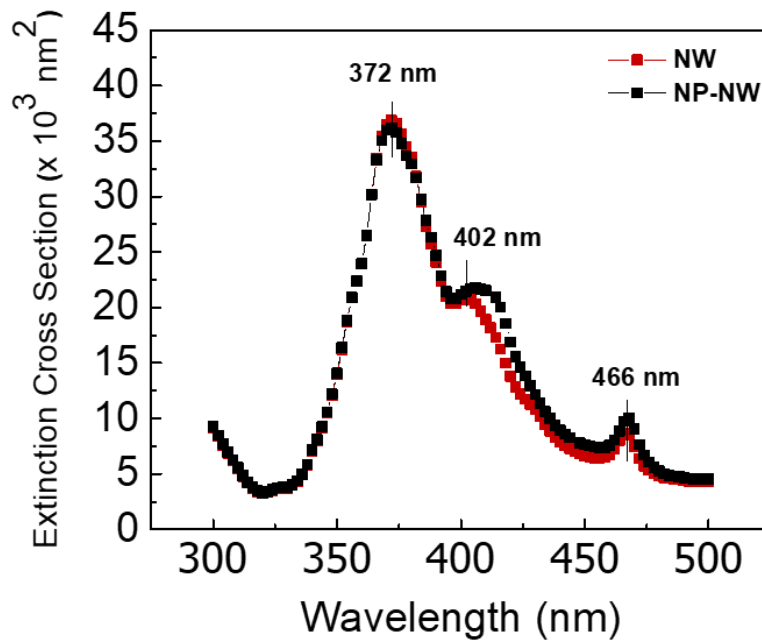


Figure 3.6. Simulated extinction spectra of a single AgNW and an AgNW-Ag@SiO₂NP junction.

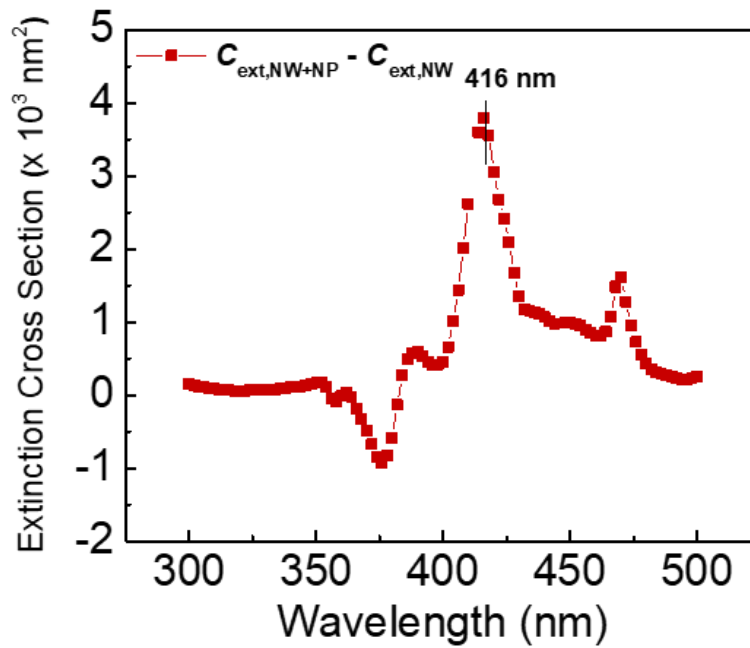


Figure 3.7. Enhancement in extinction spectrum of NP-enhanced plasmonic AgNWs.

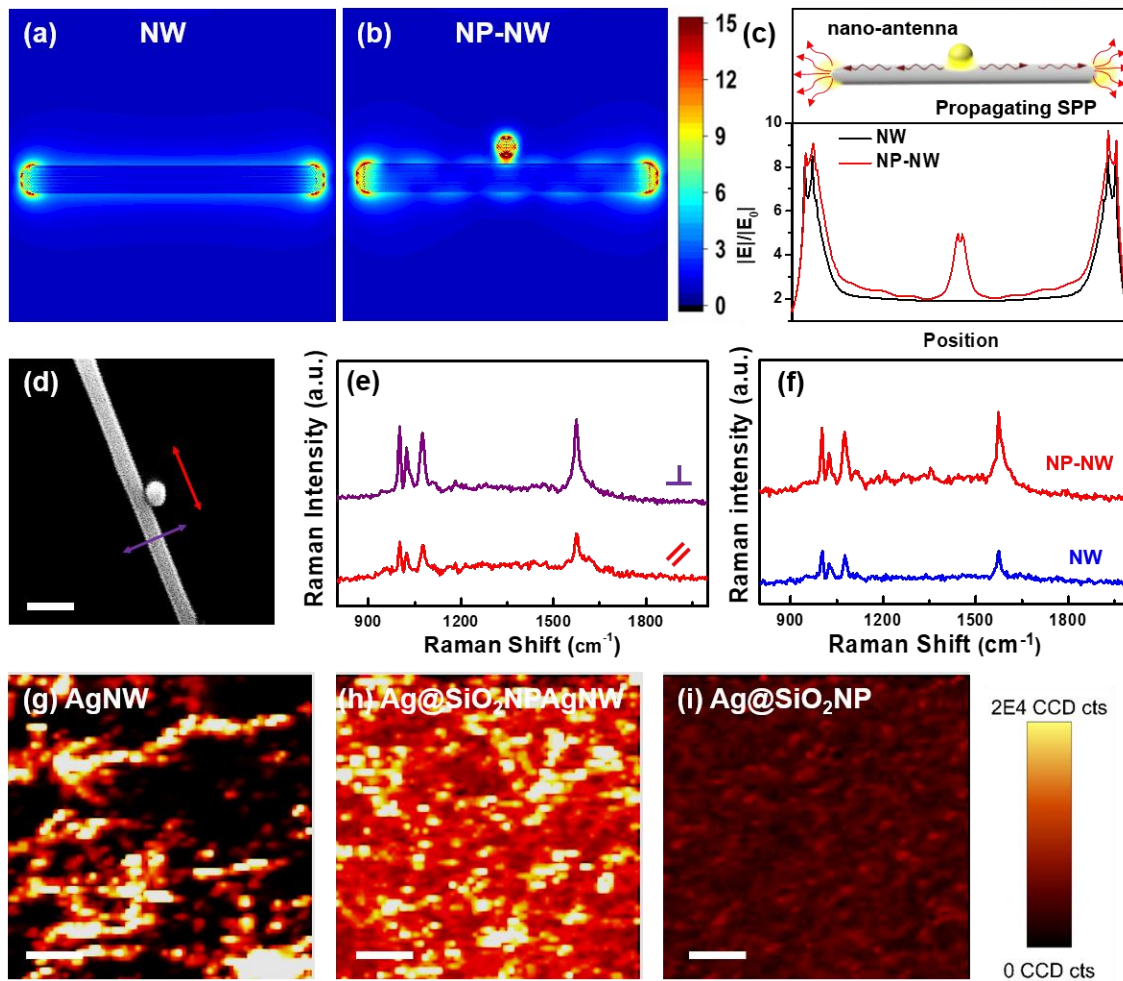


Figure 3.8. Plasmonic behavior of NP-enhanced plasmonic AgNW electrodes. E-field distribution of (a) an AgNW and (b) an AgNW decorated with an Ag@SiO₂NP. Incident light of 416 nm wavelength is polarized perpendicular to the long axis of the NW. (c) Schematic of plasmonic behavior of an AgNW decorated with an Ag@SiO₂NP. The AgNP on the AgNW acts as nano-antenna to couple incident light into SPPs propagating along the NW (top). Calculated electric field intensity for NW and NP-NW along the NW length (bottom). (d,e) Raman analysis of a NP-NW system with different polarization angles of incident light. (d) SEM image of a single AgNW decorated with an AgNP for Raman analysis. The arrows indicate incident light with perpendicular (purple) and parallel (red) polarization along the NW direction, respectively. The scale bar is 100 nm. (e) Raman spectra of poly-L-lysine (PLL) adsorbed on NP-NW junction using an incident laser with 532 nm wavelength, polarized perpendicular (purple) and parallel (red) along the NW direction. (f) Raman spectra of PLL adsorbed onto NW and NP-NW junction networks. (g-i) Surface-enhanced Raman spectroscopy (SERS) images. Raman mapping images of PLL adsorbed on (g) AgNW, (h) Ag@SiO₂NPs-AgNWs and (i) Ag@SiO₂NPs on glass substrates.

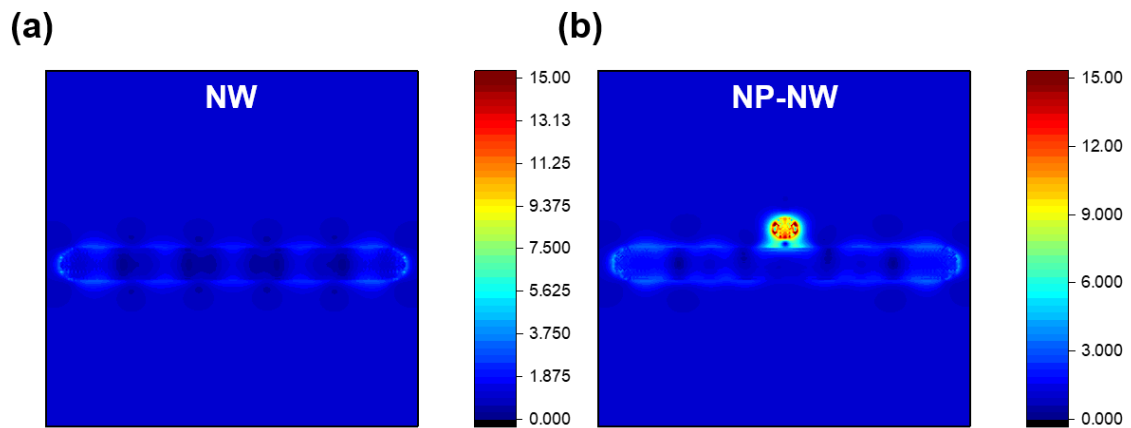


Figure 3.9. E-field distribution for single AgNW and AgNW decorated with Ag@SiO₂NP when the incident light at 416 nm, polarized in parallel direction to NW.

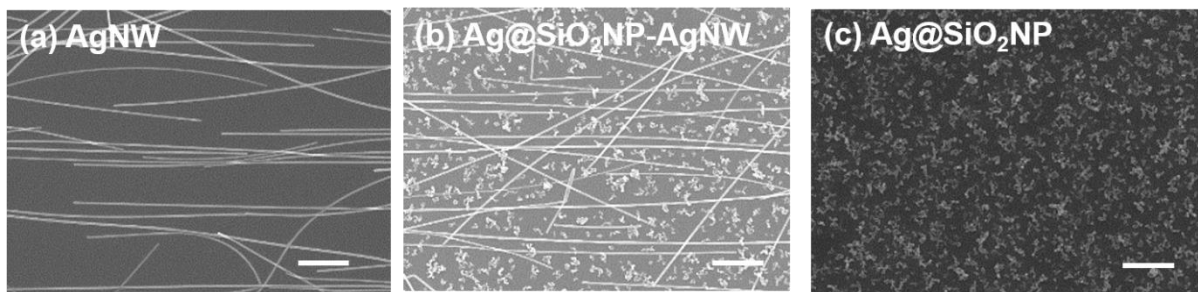


Figure 3.10. (a-c) SEM images for three different structures of (a) AgNW, (b) AgNW-Ag@SiO₂NPs, and (c) Ag@SiO₂NPs. All scale bars indicate 1 μ m.

To elucidate the effect of NP-NW plasmon coupling on OPV devices, we performed confocal laser scanning microscopy (CLSM) using Super Yellow (SY) as the fluorescence emissive layer coated on AgNWs and NP-enhanced plasmonic AgNW films, respectively (Figures 3.11a,b). For NP-enhanced plasmonic AgNW films, emission enhancement is clearly observed with a significant number of bright spots, corresponding points where Ag@SiO₂NPs couple to AgNWs, while weaker fluorescence emission is observed in the Ag NW only films, caused by a few NW-NW junctions. These results are consistent with enhanced fluorescence generated by SY within the near-field of NP-NW plasmon coupling points. To further investigate emission enhancement due to NP-NW plasmon coupling, confocal image with high resolution was obtained for a single Ag@SiO₂NP decorated AgNW system as shown in Figure 3.11c. We observed photoluminescence (PL) enhancement for all three plasmonic systems including NW, NP, and NP-NW junction. Notably, NP-NW junctions show significantly enhanced emission compared to NWs or NPs alone, due to the giant near-field effect of the NP-NW plasmonic system, which is in good agreement with theoretical DDA simulations of the near-field enhancement.

Steady-state PL spectra of SY films are plotted in Figure 3d, using different substrates including poly(3,4-ethylenedioxythiophene):polystyrene sulphonic acid (PEDOT:PSS/SY), AgNW/PEDOT:PSS/SY, AgNP/PEDOT:PSS/SY and Ag@SiO₂NP-AgNW/PEDOT:PSS/SY films coated on quartz substrates. As a control, we tested SY films on PEDOT:PSS, which showed the lowest photoluminescence intensity due to exciton quenching at the PEDOT:PSS/SY interface. Ag@SiO₂NP-AgNW/PEDOT:PSS/SY films showed the highest PL intensity, which we attribute to significant electromagnetic field enhancement induced by strong resonant coupling between excitons in SY and the NP-NW plasmons, resulting in an overall increase in the number of photogenerated excitons compared to films with AgNPs or AgNWs alone. The PL spectra of the films are consistent with confocal microscopy results, which both support fluorescence emission enhancement due to NP-enhanced plasmonic AgNW networks.

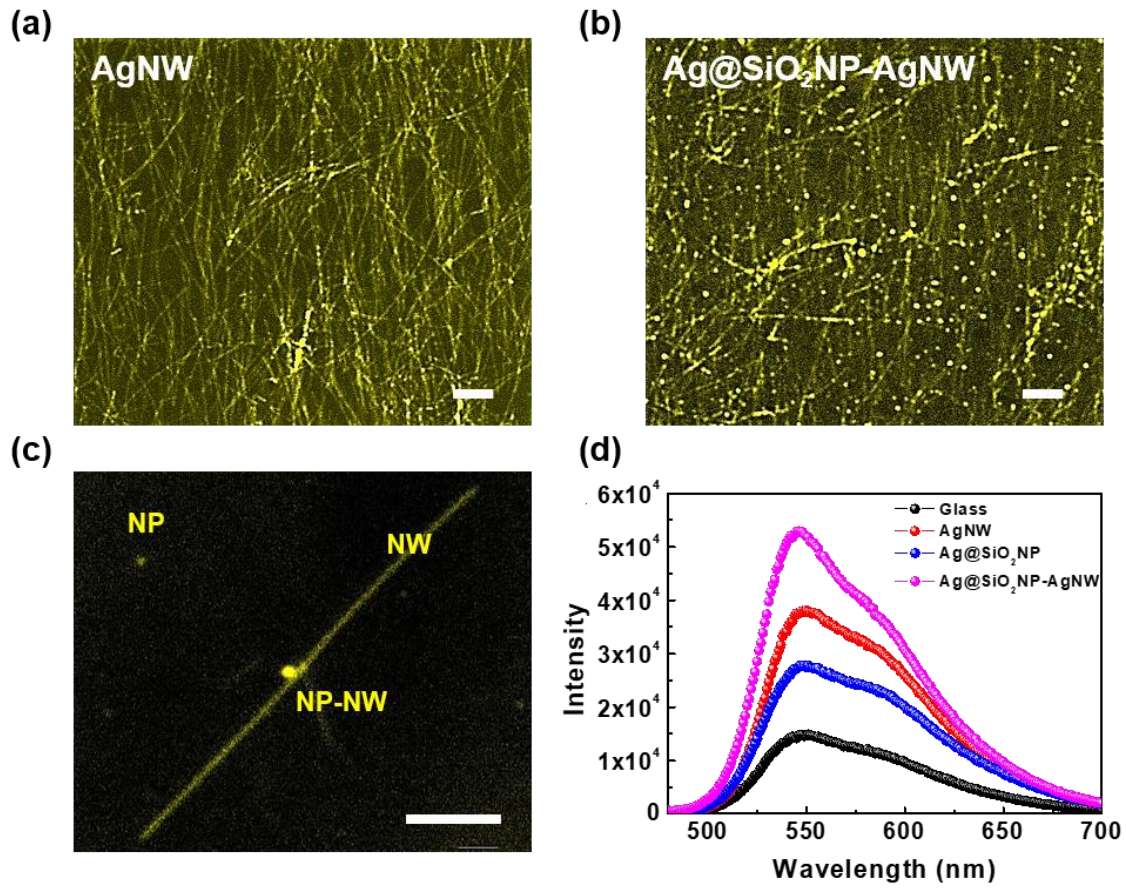


Figure 3.11. Photoluminescence behavior of fluorescent SY films on NP-enhanced plasmonic AgNW electrodes. Confocal images of (a) an aligned AgNW network and (b) an aligned AgNW network decorated by Ag@SiO₂NPs coated by SY. The scale bars indicate 5 μm. (c) High-resolution confocal image of a single AgNW decorated by an Ag@SiO₂NP, coated by SY where significant enhancement of fluorescence emission is observed at the NW-NP junction. The scale bar is 4 μm. (d) Steady-state photoluminescence spectra of SY films with an aligned AgNW network and an aligned AgNW network decorated by Ag@SiO₂NPs.

To investigate the effect of plasmon coupling on the improvement of device performance in OSCs and OLEDs, we fabricated fluorescent OLEDs with NP-enhanced plasmonic AgNW electrodes to improve the light emitting properties of the OLEDs. The device structure and energy diagram are schematically illustrated in Figures 3.12a,b. SY was used as the emissive layer to ensure high-performance OLEDs.^{118, 138} Figures 3.12c-f show OLED characteristics of devices using ITO, aligned AgNWs and NP-enhanced plasmonic AgNW electrodes. In our previous work, we reported an improvement of device performance in OSCs and OLEDs using aligned AgNWs due to coverage of protruding features and poor surface coverage.¹³¹ As shown in Figure 3.12c, both devices with NP-enhanced plasmonic AgNW and aligned AgNW electrodes showed low leakage currents with a turn on voltage of 2.0 V due to the smooth surface morphology of aligned AgNW networks. The devices with NP-enhanced plasmonic AgNW electrodes showed similar current density and reduced voltage for maximum luminance compared to devices with aligned AgNW electrodes. The device with NP-enhanced plasmonic AgNW electrodes showed substantially improved light-emitting properties with the highest luminance (29991 cd/m² at 7.2 V for the device with NP-enhanced plasmonic AgNW electrode and 20436 cd/m² at 7.4 V for the device with aligned AgNW electrode) as shown in Figure 3.12d. In particular, the EL efficiency and power efficiency were found to be 25.33 cd/A, and 25.14 lm/W, respectively, for the device with NP-enhanced plasmonic AgNW electrodes, which are more than twice as large compared to aligned AgNW only electrodes (EL efficiency and power efficiency is 10.57 cd/A, and 10.98 lm/W). Control devices with ITO electrodes exhibited an EL efficiency of 10.28 cd/A and power efficiency of 9.31 lm/W. In particular, the device with NP-enhanced plasmonic AgNW electrodes exhibited by far the highest power efficiency of 25.14 lm/W. These values of EL efficiency and power efficiency are the highest values reported so far using ITO-free TCEs for fluorescent OLEDs.^{80,57} The improved device performance with NP-enhanced plasmonic AgNW electrodes can be attributed to strong plasmon coupling of light resulting in outstanding E-field enhancement at NP-NW interfaces due to the NP-NW gap plasmon effect. Fluorescence emission enhancement of the SY film with NP-enhanced plasmonic AgNW electrodes also supports the improved device performance in OLEDs, which was further confirmed by solid state PL measurements and CLSM.

To investigate OSC characteristics with NP-enhanced plasmonic AgNW electrodes, we employed various approaches to demonstrate the effect of plasmon coupling. The device structure and energy diagram are schematically illustrated in Figure 3.13a,b. Blended poly[4,8-bis(5-(2-ethylhexyl)thiophen-2-yl)benzo[1,2-b:4,5-b']dithiophene-co-3-fluorothieno[3,4-b]thiophene-2-carboxylate] (PTB7-Th):[6,6]-phenyl-C₇₁ butyric acid methyl ester (PC₇₁BM) electron donor/electron acceptor bulk heterojunctions were used as the active layers to ensure high-performance OSCs.

Figure 3.13c shows the *J-V* characteristics of OSC devices using ITO, aligned AgNW and NP-enhanced plasmonic AgNW electrodes. Both OSCs using two different electrodes showed higher fill

factors of 0.70 and 0.71 due to the smooth surface morphology of aligned AgNW networks¹³³. The J_{sc} value of 16.25 mA/cm² for the device with NP-enhanced AgNW electrode was improved compared to the J_{sc} values of 14.58 mA/cm² and 15.20 mA/cm² observed for aligned AgNW and ITO electrodes, respectively, whereas values of V_{oc} and FF remained similar. The increase in J_{sc} with NP-enhanced plasmonic AgNW electrode was verified by external quantum efficiency (EQE) enhancement in the range of 300-800 nm, as shown in Figure 3.13d and 3.14. To clarify the plasmon coupling effect of NP-enhanced plasmonic AgNW electrodes on the photogeneration of charge carriers, we calculated the changes in absorption (Δ absorbance) and EQE (Δ EQE) of the NP-enhanced plasmonic AgNW devices. The enhancement of EQE is consistent with increases in absorption, showing similar enhancement peaks at wavelengths of 400 nm and 700 nm (Figure 3.14). As a result of these features, we achieved excellent PCEs of up to 9.19% for the OSCs with NP-enhanced plasmonic AgNW electrodes, constituting a ~10% enhancement compared to 8.28% observed for aligned AgNW electrodes (Table 3.1). Note that the PCE value of 9.19% represents the highest device efficiency reported for OSC devices using AgNW electrodes.^{46, 54-56, 58}

To investigate the charge generation and extraction processes using NP-enhanced plasmonic AgNW electrodes, photocurrent (J_{ph}) versus effective voltage (V_{eff}) is plotted for OSCs under illuminated and in the dark (Figure 3.15). J_{ph} is given by $J_{ph} = J_L - J_D$, where J_L is illuminated current density and J_D is dark current density. V_{eff} is given by $V_{eff} = V_0 - V$, where V_0 is the compensation voltage at $J_{ph} = 0$ and V is the applied bias voltage. Log-log plots of $J_{ph} - V_{eff}$ show a transition to saturation regime at a certain V_{eff} , where it becomes limited by the field and G as described by equation (1);

$$J_{sat} = qLG_{max} \quad (1)$$

where q is the elementary charge, L is the thickness of the active layer, and G_{max} is the maximum photo-induced carrier generation rate per unit volume. Even though both devices showed good exciton generation rate and exciton dissociation probability, the device with NP-enhanced plasmonic AgNW electrodes reached saturation region at slightly lower fields, compared to devices with AgNW-only electrodes. This result confirms that the excitation of LSP modes generated excitons which dissociated to free charge carriers. Additionally, it can be inferred from this result that the gap-plasmon effect not only improved the exciton generation rate but also exciton dissociation efficiency.¹³⁹

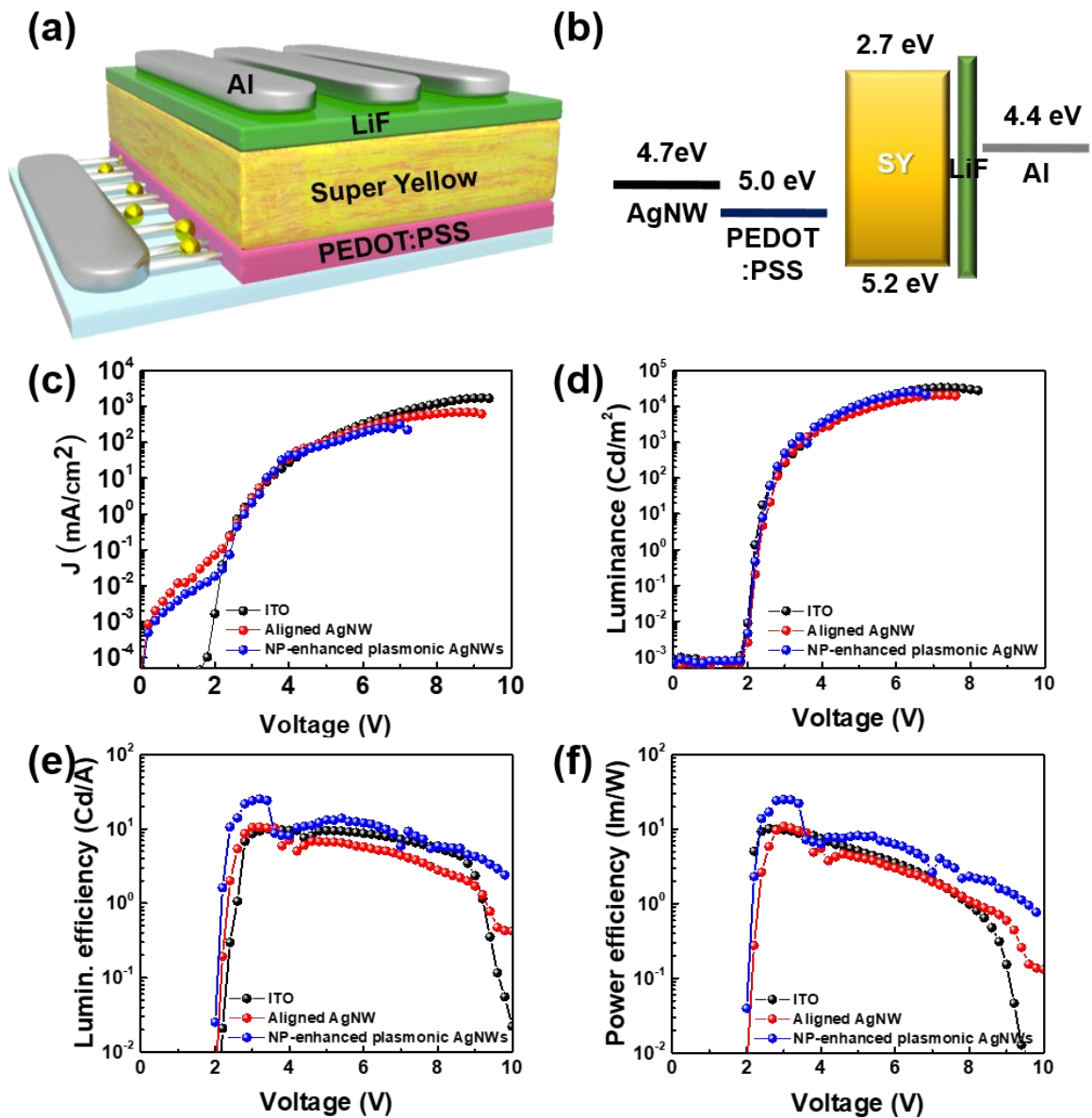


Figure 3.12. Device structure and characteristics of OLEDs using NP-enhanced plasmonic AgNW electrodes. (a) Schematic device structure of OLEDs with NP-enhanced plasmonic AgNW electrodes. (b) Schematic energy level diagram under the flat-band condition. (c) Current density, (d) luminance, (e) luminous efficiency and (f) power efficiency versus applied voltage for OLEDs with ITO, aligned AgNW, and NP-enhanced plasmonic AgNW electrodes.

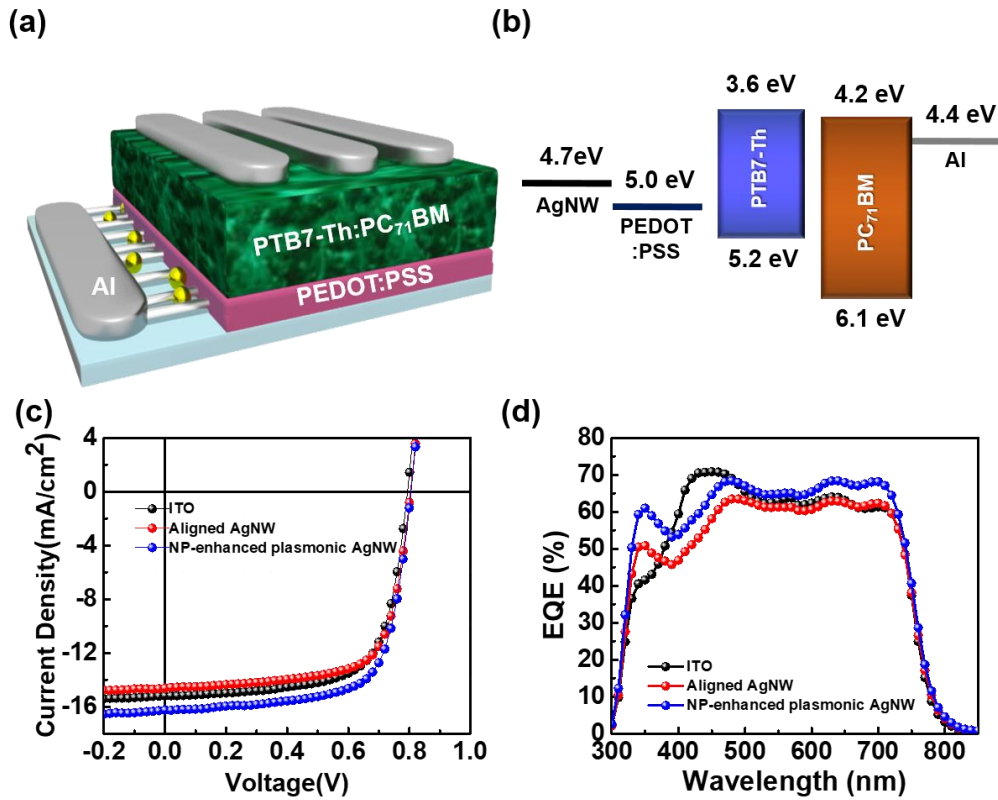


Figure 3.13. Device structure and characteristics of OSCs using NP-enhanced plasmonic AgNW electrodes. (a) Schematic device structure of OSCs with NP-enhanced plasmonic AgNW electrodes. (b) Schematic energy level diagram under the flat-band condition. (c) J - V characteristics of under AM 1.5G illumination at 100 mWcm^{-2} . (d) IPCE spectra of OSCs using ITO, aligned AgNW and NP-enhanced plasmonic AgNW electrodes.

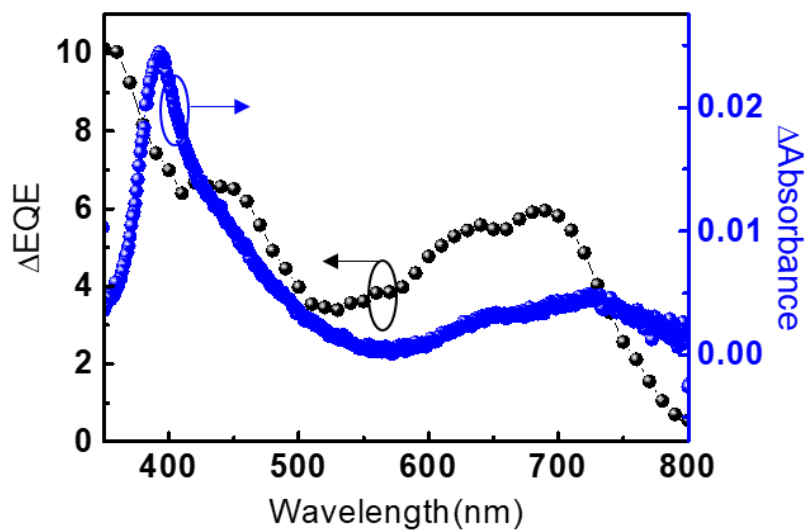


Figure 3.14. Comparison of EQE enhancement with absorption changes caused by AgNW-Ag@SiO₂NPs.

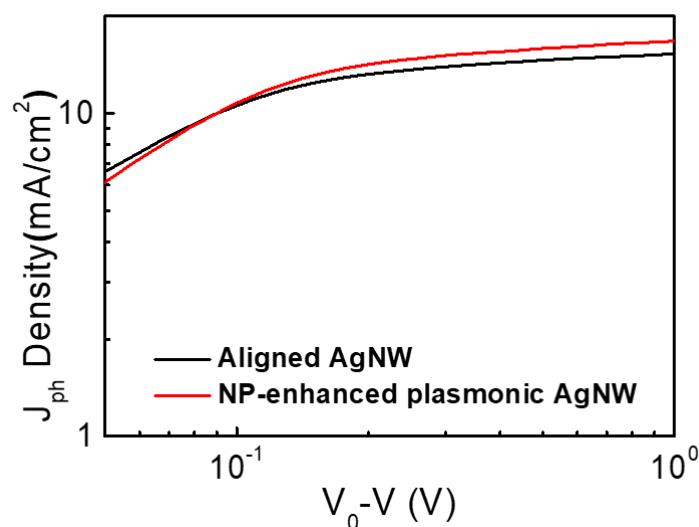


Figure 3.15. Photocurrent density versus effective voltage for devices with AgNW and Ag@SiO₂NPs-AgNW electrodes.

Table 3.1. Device characteristics of SY-based OLEDs and PTB7-Th:PC₇₁BM based OSCs using ITO, aligned AgNW and NP-enhanced plasmonic AgNW electrodes

PLED configuration		Maximum luminance [cd m ⁻²] (at listed voltage)	Maximum EL efficiency [cd A ⁻¹] (at listed voltage)	Maximum power efficiency [lm W ⁻¹] (at listed voltage)	Turn-on Voltage
ITO		56792 (8.4V)	10.28 (3.6 V)	9.31 (3.4 V)	2.0 V
Aligned AgNW		20436 (7.4V)	10.57 (3.2 V)	10.98 (3.2 V)	2.0 V
NP-enhanced plasmonic AgNW		29991 (7.2V)	25.33 (3.2V)	25.14 (3.0 V)	2.0 V
PSC configuration	J_{sc} (mA/cm ²)	Cal. J_{sc}	V_{oc} (V)	FF	η (%)
ITO	15.20	15.25	0.79	0.69	8.31
Aligned AgNW	14.58	13.66	0.80	0.71	8.28
NP-enhanced plasmonic AgNW	16.25	15.98	0.81	0.70	9.19

3.4 Conclusions

In conclusion, we have demonstrated that NP-enhanced plasmonic AgNW electrodes, consisting of aligned AgNW networks decorated by core-shell Ag@SiO₂NPs, provide an effective means to improve the efficiency of both OLED and OSC devices via plasmonic and gap-plasmonic effects. Such NP-enhanced plasmonic AgNW electrodes functioned both as outstanding transparent electrodes as well as functioning as plasmonic structures. In the NP-NW hybrid plasmonic system, Ag@SiO₂NPs played an important role as nanoantenna, serving to couple incoming light into NW plasmons propagating along NWs. This resulted in large near-field enhancement, which improved light absorption efficiency in OSCs. Simulated near-field distributions of the NP-NW system indicated a giant local E-field enhancement at NP-NW junctions due to strong gap-plasmon coupling between LSPs of AgNPs and propagating SPPs of AgNWs. Raman mapping results confirmed that strong plasmon coupling in the NW-NP system provides large E-field enhancement at NP-NW junctions. Finally, we achieve outstanding EL efficiencies of up to 25.33 cd/A (at 3.2 V) and power efficiency of 25.14 lm/W (3.0 V) in OLEDs as well as high PCEs of up to 9.19% in OSCs using Ag@SiO₂NP-AgNW electrodes. These results represent the highest efficiencies reported to date for OLEDs and OSCs based on AgNW electrodes. Furthermore, this work demonstrates that NP-enhanced plasmonic AgNW films constitute a multifunctional platform which may provide great utility in a wide variety of optoelectronic devices and other plasmonic applications.

Chapter 4. Ultrathin transparent electrodes with orthogonal AgNW arrays for light-weight and flexible perovskite solar cells

4.1 Introduction

With rapid progress in energy harvesting devices, flexible and wearable photovoltaic devices have attracted great interest to provide portable and wearable power sources in potential applications, such as smart window, wearable personal electronic devices, and wearable textiles.¹⁴⁰⁻¹⁴² In particular, lightweight and ultrathin solar cells have been one of major challenges to minimize the energy consumption with increasing the power-per-weight, which provides primary benefits in specific applications for future power source such as miniaturized drones or blimps, aerospace electronics, and weather balloons.¹⁴⁰ To address these issues, various lightweight solar cells have been reported to increase a power-per-weight across an overall solar cell technologies including silicon (Si) solar cells, organic and perovskite solar cells.^{140, 143-146} Among them, perovskite solar cells (PSCs) with solution processing and high light absorption capabilities have been considered as promising flexible and lightweight power sources with rapid progress in both device efficiency and stability.¹⁴⁷⁻¹⁴⁹ The development in planar-heterojunction perovskite materials facilitates the construction of flexible PSCs on polymer substrates due to low temperature solution processing.^{150, 151} High absorption coefficient of perovskite material facilitates the active layer of the device to be very thin below 1 μ m, enabling large flexibility of PSCs.¹⁴⁸ Recently, Martin et al. suggested flexible perovskite solar cells (PSCs) fabricated on ultrathin polymer foils, achieving the highest power-per-weight of 23 Wg⁻¹, which open the possibility of lightweight PSC device.¹⁴⁰

To further improve a device performance and mechanical stability for flexible PSCs, the fabrication of ideal flexible transparent electrodes with low conductivity and excellent mechanical robustness is essential to replace conventional indium tin oxide (ITO), whose brittle nature has limited their use in flexible applications.⁶⁷ To date, several approaches have been reported to fabricate high-performance flexible PSCs using various alternative to ITO, such as metal nanowire,¹⁵²⁻¹⁵⁴ carbon nanotube (CNT),^{155, 156} graphene,^{143, 157} and metal mesh.^{146, 158} Among these conducting nano-materials, silver nanowire (AgNW) networks have been known as attractive flexible transparent electrode in various photovoltaic devices owing to their excellent electrical and optical properties as well as outstanding mechanical flexibility.¹⁴ In addition, AgNW networks can be readily deposited to fabricate NW transparent electrodes by using solution processing, such as spin-coating,²⁷ bar-coating,^{25, 159} spray-coating,²⁹ and vacuum filtration.¹⁶⁰ However, such conventional solution-based processes cause the formation of random AgNW networks, which lead to several limitations for the fabrication of high-performance flexible PSCs, such as NW aggregation, low transmittance, surface roughness. In particular, for perovskite solar cell applications, AgNWs are severely damaged in the presence of halogen ions in the

perovskite active layer, resulting in the formation of a silver-halide phase, which causes the loss of electrical conductivity of AgNWs.¹⁴⁶ Previously, there have been few attempts to prevent the diffusion of halogen ions by using passivation layers deposited on random AgNW networks.^{153, 154} Lee et al. demonstrated AgNW-based flexible PSC devices with amorphous metal oxide protection, which achieved power conversion efficiency (PCE) of 11.23 %.¹⁵⁴ For another methods, Kim et al. has reported all-solution-based transparent electrode with random AgNW network embedded in both sol-gel ITO and zinc oxide layers, which can effectively prevent the silver-halide formations in the fabrication of perovskite solar cells. However, such approaches need the complex fabrication process for the formation of oxide/metal NW/oxide structure and thick-buffer layer to fully cover protruding NWs in random AgNW networks. In addition, further improvement of device performance is still in a challenge in flexible applicatons. Thus, fundamental solution is that manipulating surface morphology of AgNW network has to be preceded to efficiently prevent silver-halide formation and to improve device efficiency, simultaneously.

Herein, we demonstrated the fabrication of PSC devices with orthogonal AgNW electrodes, which enable to effectively prevent silver-halide formation during device fabrication, resulting in higher device efficiency of 15.1% for PSC with orthogonal AgNW electrode on glass substrates, compared to that with random AgNW electrode of 10.3%. In addition, we fabricated ultrathin and lightweight PSC devices with orthogonal AgNW electrodes on very thin polymer foils, which show a capability to be attached to an arbitrary surface due to low device thickness and lightness in addition to achieve an outstanding power-per-weight of 34.4Wg^{-1} with a PCE of 11.3 %.

4.2 Experimental Details

Fabrication of ultrathin transparent electrode with orthogonal AgNW arrays: To support ultrathin PEN foil as the substrate, planar PDMS films were prepared by mixing silicone elastomer base (Sylgard 184, Dow Corning) and a curing agent in the ratio of 10:1. The mixture of liquid PDMS prepolymer was poured onto petri dishes and stored in a vacuum desiccator for 30 min to eliminate air bubbles. Next, the liquid PDMS prepolymer was solidified at 90°C for 3 hours.

The 1.3 µm-thick PEN foil was physically adhered on planar PDMS film. The PEN foil on PDMS film was treated by O₂ plasma for 5 min to provide hydrophilicity and surface wettability. Then, as-treated PEN foil was functionalized with amine groups using PLL layers, which were spin-coated onto substrates using 0.1% solutions of PLL in H₂O at 4000 rpm for 60 s. Next, orthogonal AgNW networks were fabricated onto amine functional group terminated substrates by second step capillary printing. Here, 0.5 wt% AgNW dispersions (an average length of 25 ± 5 µm and a diameter of 32 ± 5 nm.) in an ethanol (Nanopyxis Corp.) were used.

Materials and preparation of perovskite: 2-Propanol (IPA) and anhydrous *N,N*-dimethylformamide (DMF) were purchased from Sigma-Aldrich and were used without purification. Lead Iodide (PbI₂, 99.999%) were purchased from Alfa Aesar. Methylammonium iodide (MAI) was reported previous literature. To prepare perovskite precursor solutions, 1.3 mM of PbI₂ was dissolved in 1ml DMF and MAI precursor was varied from 50 mg/ml to 65 mg/ml in IPA. A 25 mg/ml solution of PC₆₁BM in 1:1 mixture of chlorobenzene and chloroform. The obtained solution was stirred at room temperature for 30 min.

Device fabrication and characterization: ITO-coated glass substrates were cleaned by ultrasonication in deionized water, acetone and isopropyl alcohol for 10 min each. For glass/ITO devices, A poly(3,4-ethylenedioxythiophene):polystyrene sulfonic acid (PEDOT:PSS) layer was deposited on cleaned ITO substrates by spin-casting at 4000 rpm for 30s, followed by annealing at 140 °C for 10 min. For glass/AgNW and flexible AgNW substrates, a PEDOT:PSS was spin-casted for 2000rpm for 40s and annealed 140 °C for 15 min. A PH1000 layer was deposited on PEDOT:PSS layer by spin-casting at 1500 rpm for 30s, followed by annealing at 140 °C for 10 min. On top of PEDOT:PSS layer or PH1000, MAI precursor solutions were spin-cast at 3000 rpm for 30s and PbI₂ were spin-coated at 5000 rpm for 30s. The films were dried on a hot-plate at 100 °C for 2 min in air atmosphere. After cooling the substrates, solvent vapor annealing was treated using 40ul DMSO solvent for 2min at 100 °C. On top of the perovskite layer, PC₆₁BM was spin-cast at 1500 rpm. Subsequently, an Al electrode with a thickness of 100 nm was deposited on the PC₆₁BM layer under vacuum (<10⁻⁶ Torr) by thermal evaporation. The current density-voltage (*J-V*) characteristics of the solar cells were measured using a Keithley 2635A Source Measure Unit. Solar cell performance was carried out under illumination by an Air Mass 1.5 Global (AM 1.5 G) solar simulator with an irradiation intensity of 100 mW cm⁻².

Apertures (13.0 mm^2) made of thin metal were attached to each cell before measurement for J - V characteristics. External quantum efficiency (EQE) measurements were obtained with a PV measurements QE system under ambient conditions, with monochromated light from a xenon arc lamp. The monochromatic light intensity was calibrated with a Si photodiode and chopped at 100 Hz.

4.3 Results and Discussion

Figure 4.1a shows the schematic of fabrication procedures for ultralight PSC with orthogonal AgNW transparent electrodes deposited on ultrathin 1.3 μm -thick PEN foil. Firstly, we prepared polydimethylsiloxane (PDMS) films, which are subsequently laminated to glass substrate. This preparation step is followed by the lamination step of ultrathin 1.3 μm -thick PEN foils to the PDMS film in which thin PEN foils are physically attached to the surface of PDMS for easy handling during the device fabrication. And, orthogonal AgNW electrodes were fabricated using capillary printing technique via second-step process. Next, PH1000 and AI4083 layers are over-coated for a passivation layer and hole transporting layers (HTLs) on orthogonal AgNW electrodes, respectively. The perovskite active layers were deposited by a standard two-step method in regular succession.¹⁶¹ After the deposition of top electrodes, as-fabricated the PSC device on ultrathin PEN foil are physically released and free-standing. Here, orthogonal AgNW electrodes provide several advantages as high-performance flexible transparent electrodes, such as uniform electrical current path, smooth surface morphologies, and superior transmittance, which are significant merits for a device integration with AgNW electrodes. Dark-field optical micrograph of orthogonal AgNW arrays shows highly oriented NW surface morphology with the inset of fast furrier transform (FFT) image, which indicates crossed line patterns, corresponding to its surface geometry (Figure 4.1b) In the contrary, random AgNW network showed disordered surface structures with blurry circular patterns of FFT image (Figure 4.2). Optical transmittance in the visible wavelength of 350 – 800 nm was measured for orthogonal and random AgNW networks. We confirmed that orthogonal AgNW electrodes provide higher transmittance (92.3% at 550 nm wavelength) than random AgNW electrodes with similar sheet resistance (90.8% at 550 nm wavelength) due to lower percolation threshold (Figure 4.3).¹⁵⁹ Figure 4.1c shows ultrathin conductive foil with orthogonal AgNW networks, indicating highly flexible and transparent appearance. Figure 4.1d displays a photograph of ultralight and flexible PSC with orthogonal AgNW electrode foils adhered to a surface of a leaf, indicating adhesive capability due to very small thickness and lightness of the device. Figure 4.1e shows the cross-sectional scanning electron microscopy (SEM) of our PSC with orthogonal AgNW electrodes. We designed a p-i-n device structure for the fabrication of PSC devices, that is polyethylene naphthalate (PEN)/orthogonal AgNW electrode/PH1000/poly(3,4-ethylenedioxythiophene): poly(styrenesulfonate) (PEDOT:PSS)/ $\text{CH}_3\text{NH}_3\text{PbI}_3$ (MAPbI_3)/phenyl-C61-butyric acid methyl ester (PCBM)/Aluminum (Al). The energy bend diagram of our PSC devices have been drawn as shown in Figure 4.4.

To investigate the mechanical properties of orthogonal AgNW electrode foils, the electrical resistance of orthogonal AgNW electrode foils, attached to PDMS thin film, was monitored under various mechanical deformations, such as bending, twisting, and crumpling. We conformed that the orthogonal AgNW electrode foil sustains its electrical conductivity under repeated 1000 bending cycles at a

bending radius of 2 mm (Figure 4.1f). Moreover, we observed that the electrical resistance of orthogonal AgNW electrodes foils remains without significant variation for twisting angles (0° - 900°) (Figure 4.1g). In addition, our orthogonal AgNW electrode remains its electrical resistance with small variation below 10% under even crumpling deformation with 500 repeating cycles (Figure 4.1h). These outstanding mechanical durabilities of orthogonal AgNW electrode foils could be attributed by uniform percolated networks.¹⁵⁹

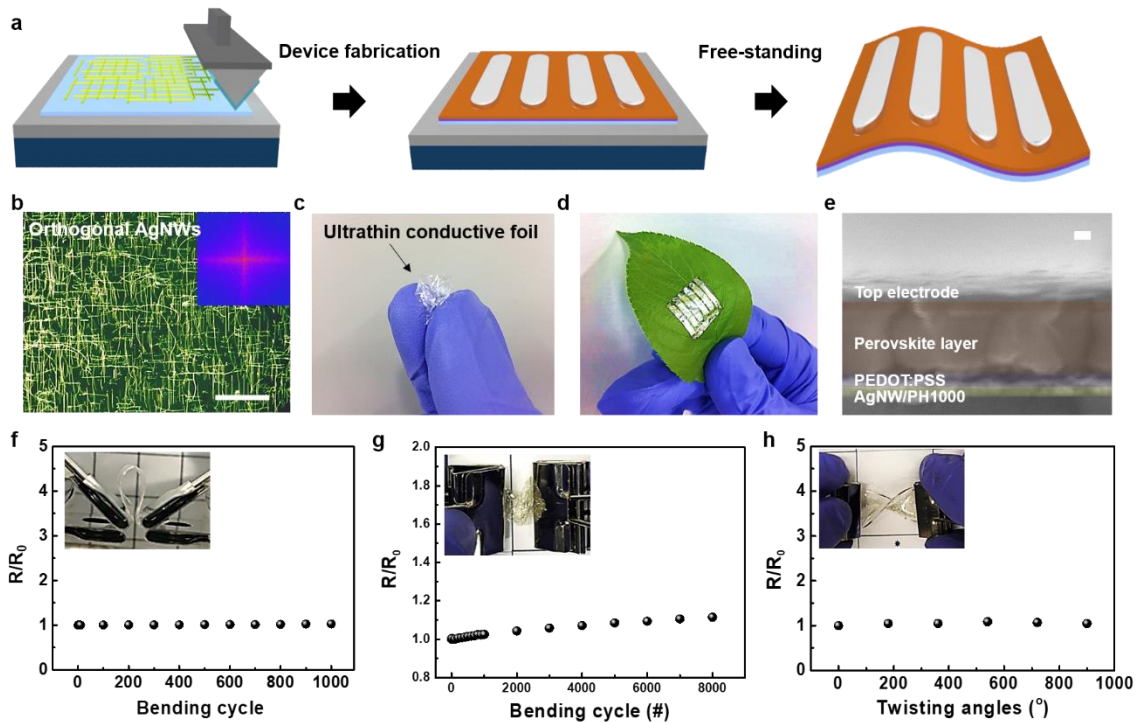


Figure 4.1. (a) Schematic illustrations of the fabrication procedure for ultrathin orthogonal AgNW transparent electrodes produced on 1.3 μm -thick PEN foil. (b) Dark-field optical microscope image of the orthogonal AgNW arrays with corresponding fast Fourier transform (FFT) pattern of inset image. The scale bar indicates 40 μm . (c) The ultrathin orthogonal AgNW transparent electrode foil, crumpled by a person's finger. (d) An ultrathin and lightweight PSC device mounted on a surface of the leaf. (e) Cross-sectional SEM image of device structure for PSC with orthogonal AgNW array. The scale bar is 100 nm. (f-h) Mechanical properties of the orthogonal AgNW transparent electrode foils. Variation in resistance of orthogonal AgNW electrode foil as a function of (f) bending cycles at a bending radius of 2 mm, (g) crumpling cycles, and (h) twisting angles. The inset images show corresponding deformation (twisting, crumpling, and bending) of orthogonal AgNW electrode foil, adhered to PDMS thin film.

Random AgNW network

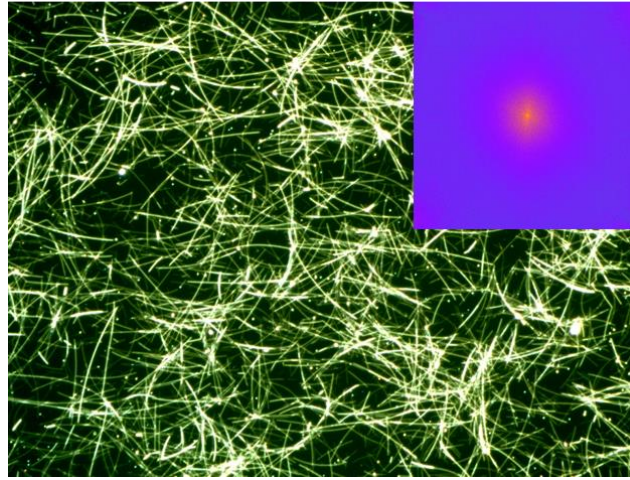


Figure 4.2. Dark-field optical micrograph of random AgNW network. The fast Fourier transform (FFT) image of the optical micrograph in the inset exhibits a blurred circular pattern, indicating corresponding surface geometric structure.

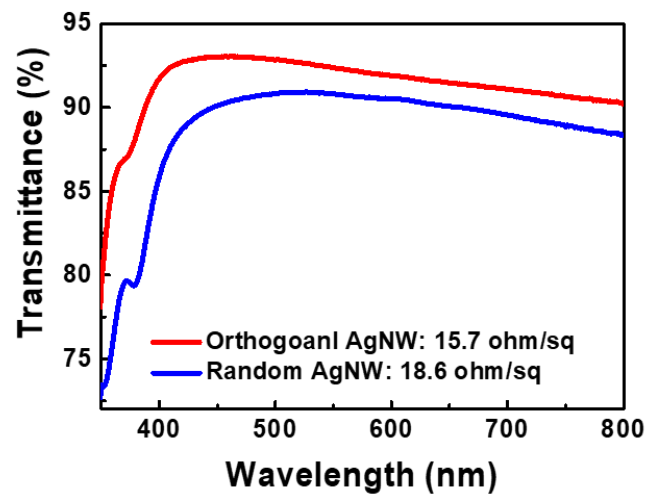


Figure 4.3. The optical transmittance of orthogonal AgNW and random AgNW electrodes, deposited on glass substrates, in visible range of 350-800 nm wavelength with corresponding sheet resistance. The glass substrate was used as reference.

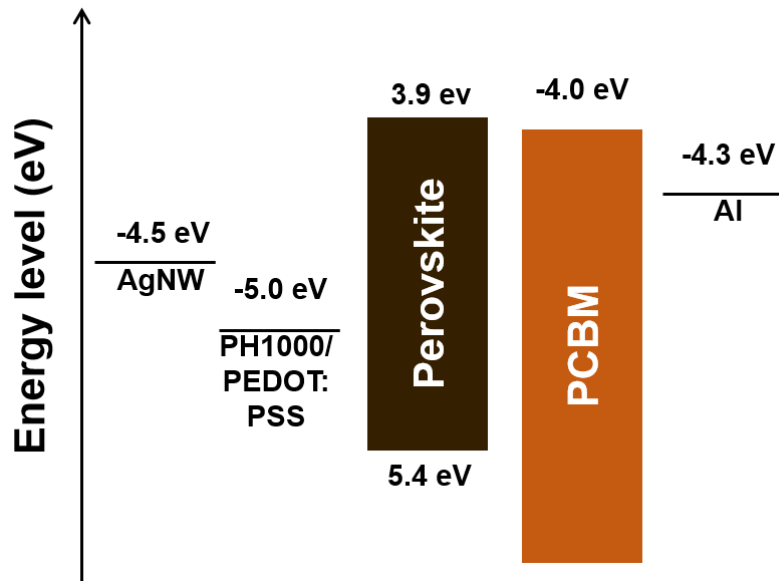


Figure 4.4. The energy band diagram for the PSC with orthogonal AgNW electrode.

In this study, the formation of non-conducting metal-halide is crucial issue for the fabrication of AgNW-based PSC devices, which induces significant loss in an electrical conductivity of AgNW electrodes. To address this issue, recently, Lee et al. have reported that the presence of iodine ions in perovskite active solution (PbI_2 and $\text{CH}_3\text{NH}_3\text{PbI}$) cause the chemical reaction between AgNW and iodine species with the formation of AgI, resulting in the diffusion and vanishing of Ag out of AgNW through the defect sites of stacked layer. To address these issues, they have demonstrated flexible PSCs with random AgNW network/aluminum doped zinc oxide (AZO) electrodes laminated with amorphous AZO protection layer to avoid non-conducting a silver-halide formation.¹⁵⁴ In this manner, we employed the PH1000 layer as a passivation layer to minimize the formation of AgI in the fabrication of AgNW-based PSC devices.¹⁴⁶ Smooth surface morphologies of orthogonal AgNW electrodes laminated with PH1000 layer can effectively prevent reacting between AgNW and iodine ions while protruding NWs induced by an aggregation of random AgNW network cannot fully covered by PH1000 layers through which iodine ions easily diffuse into AgNW, resulting in a decrease of electrical conductivity in overall electrodes as shown in a schematic of Figure 4.5a. To certify smooth surface morphologies of orthogonal AgNW electrodes, we observed the surface of PEDOT:PSS (AI 4083) layer deposited on PH1000/orthogonal and random AgNW electrodes using scanning electron microscope (SEM), respectively (Figures 4.5b,c). In SEM images, we conformed that the AI4083/PH1000 layer does not efficiently cover whole area of random AgNW network because of aggregated AgNWs, which show poor surface morphologies while orthogonal AgNW/PH1000 electrode provides uniform and smooth surface morphology without uncovered NWs. To further investigate the smooth morphologies for orthogonal AgNW electrodes, we measured the surface roughness of both PEDOT:PSS surface deposited on orthogonal and random AgNW/PH1000 electrodes using atomic force microscope (AFM) (Figure 4.5d,e). The surface of PEDOT:PSS with orthogonal AgNW electrodes showed much smoother surface (root-mean-square (RMS) roughness, $R_q = 1.47$ nm) compared to that with random AgNW electrodes ($R_q = 4.8$ nm), which are well corresponded with the surface morphologies observed by SEM images.

To certify the capability of orthogonal AgNW electrode to prevent the AgI formation in the fabrication of PSC device, we monitored the variation in the sheet resistance of orthogonal and random AgNW/PH1000/AI4083 films during the device fabrication in which the deposition of perovskite films was followed by solvent vapor annealing (SVA) process with dimethyl sulfoxide (DMSO) solution. Here, it is widely known that DMSO vapor provide a wet environment condition so that MAI and PbI_2 precursor molecules and ions can diffuse a long distance, resulting in an increase of grain size from 200 nm to over 1 μm as a function of SVA time for improving device efficiency (Figure 4.6).¹⁶² However, the diffusion of iodine species into AgNW electrode during SVA can promote the AgI formation, leading to further degradation in electrical conductivity. As a result, orthogonal AgNW electrodes maintain

initial electrical resistance without significant loss of electrical conductivity during an entire fabrication process while random AgNW networks show severe damage in an electrical resistance with a rapid increase of the sheet resistance (Figure 4.5f). Note that thicker PH1000 layer does not guarantee high device performance, which results in a decrease of charge collection efficiency and series resistance, although they fully cover the protruding NWs of random AgNW network.¹⁶³ These topological results indicate that orthogonal AgNW/PH1000 electrodes can effectively prevent the formation of AgI than random AgNW electrodes. To further validate the capability of orthogonal AgNW electrode to prevent the AgI formation for the fabrication of PSCs, we measured X-ray photoelectron spectroscopy (XPS) depth profile analysis in which orthogonal AgNW/HTL/perovskite and random AgNW/HTL/perovskite films were prepared for comparison, respectively. Binding energy of Ag ion for both samples were measured using X-ray photoelectron spectroscopy (XPS) after aging process for 10 days in controlled atmosphere (N₂-filled globe box at room temperature) (Figures 4.5g,h). Random AgNW electrode sample was obtained Ag⁺ and Ag metal peaks at 367.9 eV and 368.2 eV which indicate the presence of Ag⁺ ion was founded in the top regime of the cell stack by reacting with iodine of perovskite layer, whereas in the case of the orthogonal AgNW electrode showed only Ag metal peak at 368.2 eV after 250 sec etching times past, implying that orthogonal AgNW system effectively prevents the perovskite photoactive layer from contacting AgNW electrode.¹⁶⁴

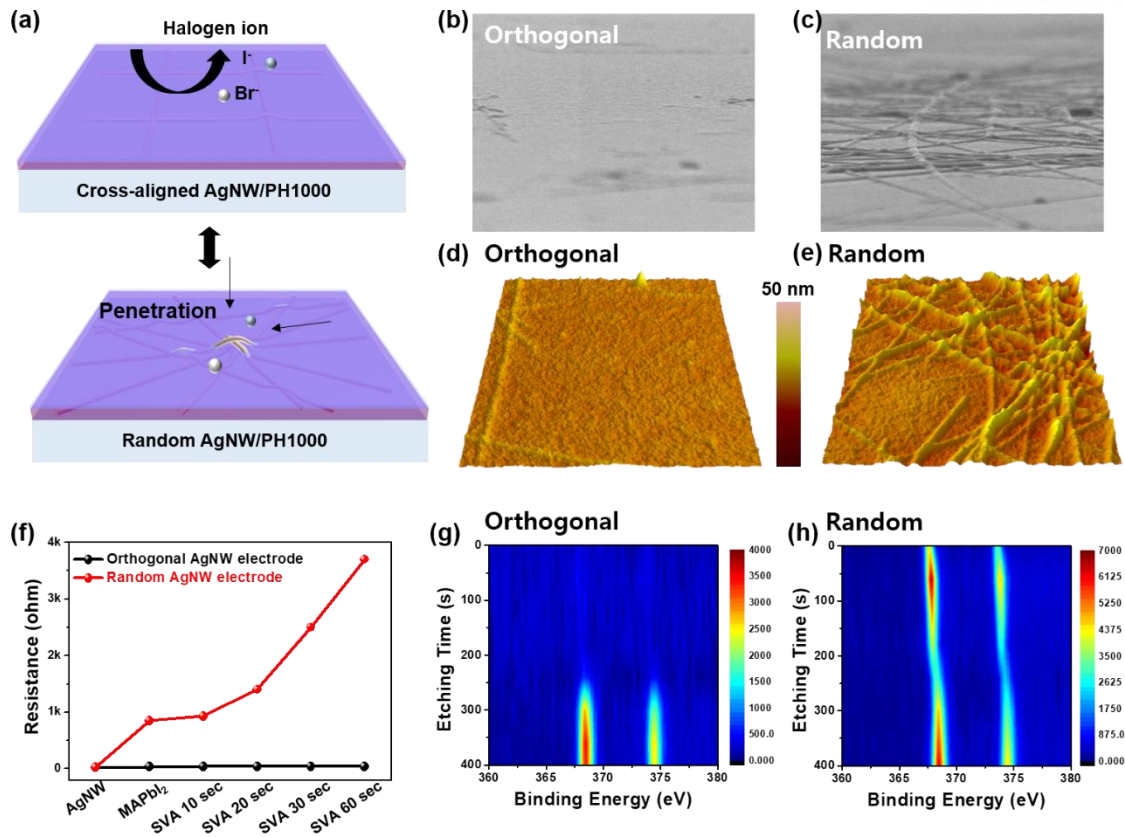


Figure 4.5. (a) A schematic illustration of silver-halide formation in PSCs fabricated on random and orthogonal AgNW electrodes. (b,c) Tilted SEM images of the surface of PEDOT:PSS coated on (b) PH1000/orthogonal AgNW electrode and (c) PH1000/random AgNW electrode, respectively. (d,e) AFM images of the surface of PEDOT:PSS coated on (d) PH1000/orthogonal AgNW electrode and (e) PH1000/random AgNW electrode, respectively. (f) The variation in the resistance of both the random and orthogonal AgNW electrodes as a function of the SVA time. (g,h) The distribution of the Ag originated from XPS-depth profiles of PSCs with (g) orthogonal AgNW and (h) random AgNW electrodes, respectively.

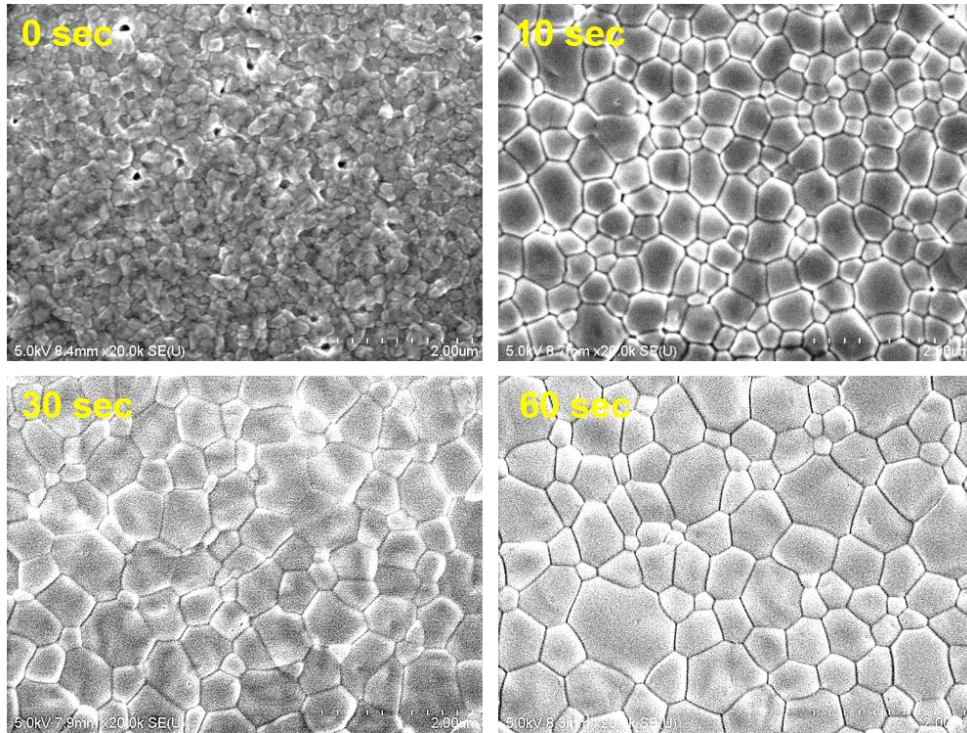


Figure 4.6. The SEM images for the surface of perovskite active layers, deposited on PEDOT:PSS/PH1000/AgNW, as a function of the SVA time.

To investigate the effect of the orthogonal AgNW electrode on a device performance in AgNW-based PSCs, the current density-voltage (J - V) characteristics for PSC devices with ITO, orthogonal and random AgNW electrodes were measured under the AM 1.5G 100 mW cm⁻² illumination for a comparison (Figure 4.7a). The PSC with ITO electrode exhibits a short-circuit current density (J_{SC}) of 20.09 mA cm⁻², open circuit voltage (V_{OC}) of 1.00 V, fill factor (FF) of 0.79% and overall power conversion efficiencies (PCEs) of 16.25% which is suitable value for control p-i-n structure perovskite.¹⁶⁵ Note that the PSC with orthogonal AgNW electrode achieved outstanding PCEs of 15.19% with a J_{SC} of 18.04 mA cm⁻², V_{OC} of 1.05 V, and FF of 80% while that with random AgNW electrode relatively yielded lower PCEs of 10.30% with a J_{SC} of 16.04 mA cm⁻², V_{OC} of 0.98 V, and FF of 65% (Table 4.1). This result could be attributed to uniform and homogenous perovskite photoactive layer on the flat hole transport layer which can increase charge collection efficiency and reduce the recombination by smooth surface of orthogonal AgNW electrodes without an influence of the AgI formation. In the forward scan direction, in addition, the PSC with orthogonal AgNW electrode was achieved PCE of 14.80% with a J_{SC} of 17.87 mA cm⁻², a V_{OC} of 1.05 V and a FF of 79%, indicating that our PSC devices show reliable device performance with negligible photocurrent hysteresis (Figure 4.8).¹⁶⁶ Figure 4.7b shows an external quantum efficiency (EQE). The PSC devices with ITO, orthogonal and random AgNW electrodes show broad spectral response in the range of 300-780 nm and calculated current density is 19.79 mA cm⁻², 16.49 mA cm⁻², and 15.69 mA cm⁻², respectively. The integrated photocurrent of both devices shows only 10% mismatch with obtained value from J - V curve which implies well agreement and substantiates the observed J_{SC} . To characterize the stability of PSCs with orthogonal AgNW electrode, the device performance was continuously monitored with aging time for 500 hours in the N₂-filled globe box. The PSC with orthogonal AgNW electrode showed an improvement in long-term stability compared to the PSC with random AgNW electrode as shown in Figure 4.7c. For PSC devices with orthogonal AgNW electrode, 85% of the initial PCE was retained after 500 hours while PSC devices with random AgNW electrode rapidly decreased less than 50% after 500 hours. This improved stability of device with orthogonal AgNW electrode could be attributed to preventing the reaction Ag⁺ with I⁻ ions due to the smooth surface, which shows good agreement with XPS depth profile. Figure 4.7d presents the statistical analyses of device performance obtained from PSCs with ITO, orthogonal and random AgNW electrodes, respectively. Both devices with ITO and orthogonal AgNW electrodes showed high reproducibility with small variation in device efficiency, whereas PSCs with random AgNW electrodes have large variation in device performance.

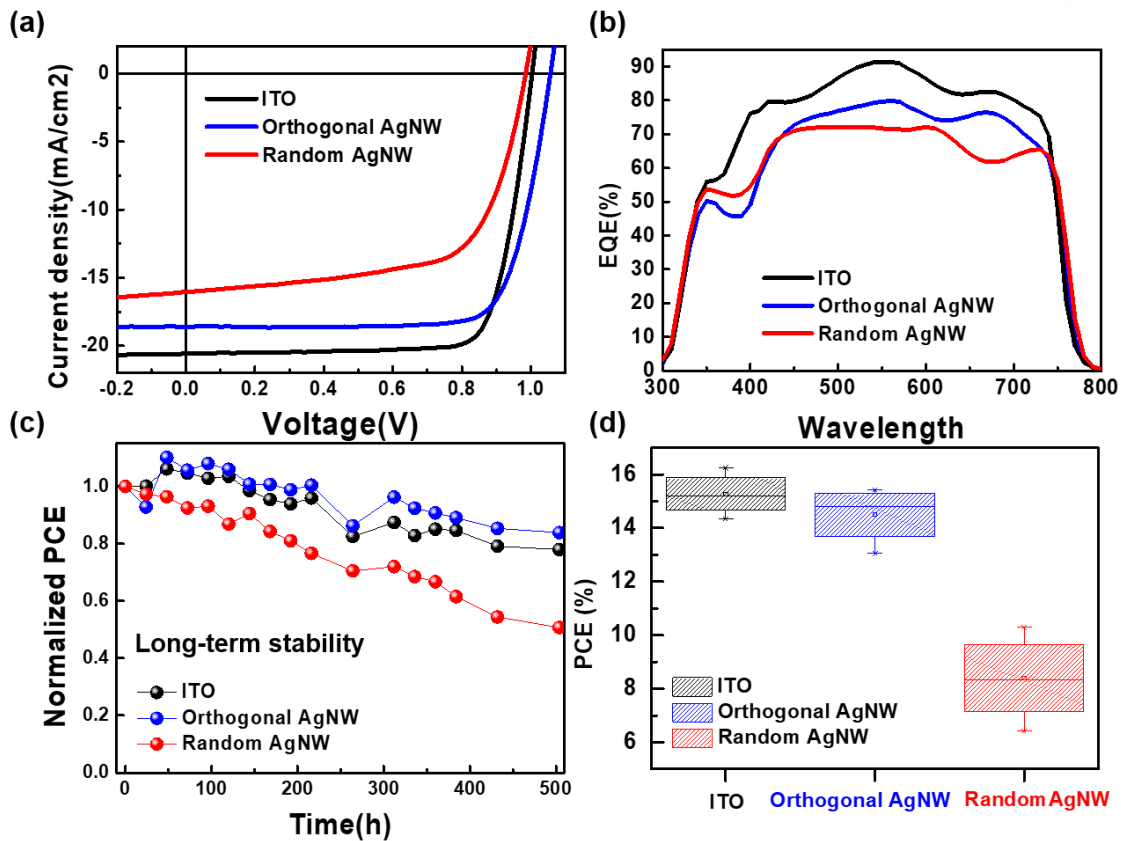


Figure 4.7. (a) $J-V$ characteristic and (b) IPCE of PSC devices with ITO, orthogonal AgNW, and random AgNW electrodes. (c) Long-term stability of PSCs in controlled atmosphere (N_2 -filled glove box). (d) The quantitative PCE values of PSCs with ITO, orthogonal AgNW, and random AgNW electrodes.

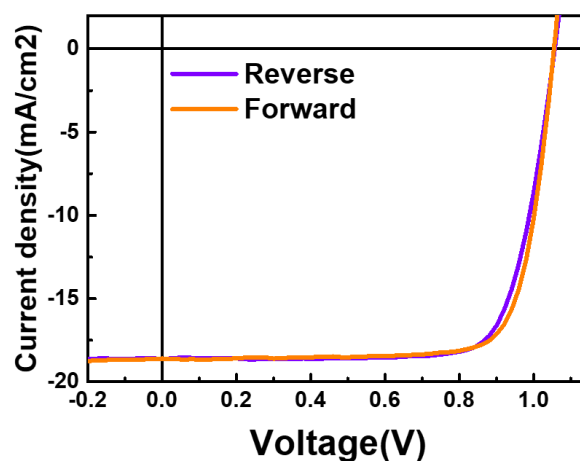


Figure 4.8. $J-V$ hysteresis characteristic of PSC with orthogonal AgNW electrode measured with forward and reverse bias.

Table 4.1. (a) J - V characteristics of PSC devices with ITO, orthogonal AgNW, and random AgNW electrodes fabricated on glass substrates.

Electrode	$J_{sc}(mAcm^{-2})$	$V_{oc}(V)$	FF	$PCE(\%)$	$Cal. J_{sc}$
ITO	20.09	1.00	0.79	16.25	19.79
Orthogonal AgNW	18.63	1.06	0.77	15.18	17.51
Random AgNW	16.04	0.98	0.65	10.30	16.49

To realize ultrathin and lightness, we fabricated flexible PSCs with orthogonal AgNW electrodes on ultrathin 1.3 μm thick PEN foils and 120 μm -thick PEN films. Figure 4.9a shows the J - V characteristics of ultrathin PSCs with orthogonal AgNW electrodes with different-thick PEN substrates for comparison. The device efficiencies of 13.05% and 12.85% were achieved for flexible PSC and ultrathin PSC devices with orthogonal AgNW electrodes, respectively (Table 4.2), which constitutes the highest PCE reported so far in flexible PSC with AgNW electrodes.^{153, 167-171}

To evaluate the mechanical stability for flexible PSC with orthogonal AgNW electrode, the variation of device performance of flexible PSCs was measured under 1000 bending cycles at 5 mm of bending radius (Figure 4.10). The device performance for flexible PSC remains 80% of the initial PCE over 1000 bending cycles without significant degradation of PCE value.

One of important advantages in our PSC devices is adhesive capability, enabling to be mounted on arbitrary objects due to small thickness and lightness of the device, which means that our device can be utilized for wearable power source in specific potential applications including military robots and wearable electronics. For a proof-of-concept demonstration, we mounted the devices on miniaturized toy robot and connected the electrode using copper wires to measure the device performance under the illumination of the sun as shown in Figure 4.9b. We confirmed that the V_{oc} of 0.84 was obtained for PSC device attached to the toy robot, indicating it can generate 7.8 mW power connecting to 91 Ω load on a sunny day (Figure 4.11).

Another advantage of our devices is as light as our device floats onto even the surface of bubbles without a burst, which can be strong benefits in terms of power-per-weight in the field of aerospace electronics or miniaturized blimp (Figure 4.9c). We calculated the power-per-weight of our devices whose weight of 0.74mg was measured using electronic scale (Figure 4.12). It is noteworthy that conformal PSC foils exhibited an excellent power-per-weight of 34.4 W g^{-1} while flexible PSCs showed a power-per-weight of 0.07 W g^{-1} , which records the highest value reported in various lightweight solar cells (Figure 4.9d).^{140, 143-145}

Table 4.2. (a) J - V characteristics of flexible PSC and ultralight PSC fabricated on thin-PEN film and 1.3 μm -thick PEN foil with orthogonal AgNW arrays, respectively.

Electrode	$J_{sc}(\text{mAcm}^{-2})$	$V_{oc}(\text{V})$	FF	$PCE(\%)$
Flexible substrate	17.99	1.00	0.72	13.05
Ultrathin foil	18.88	0.95	0.69	12.85

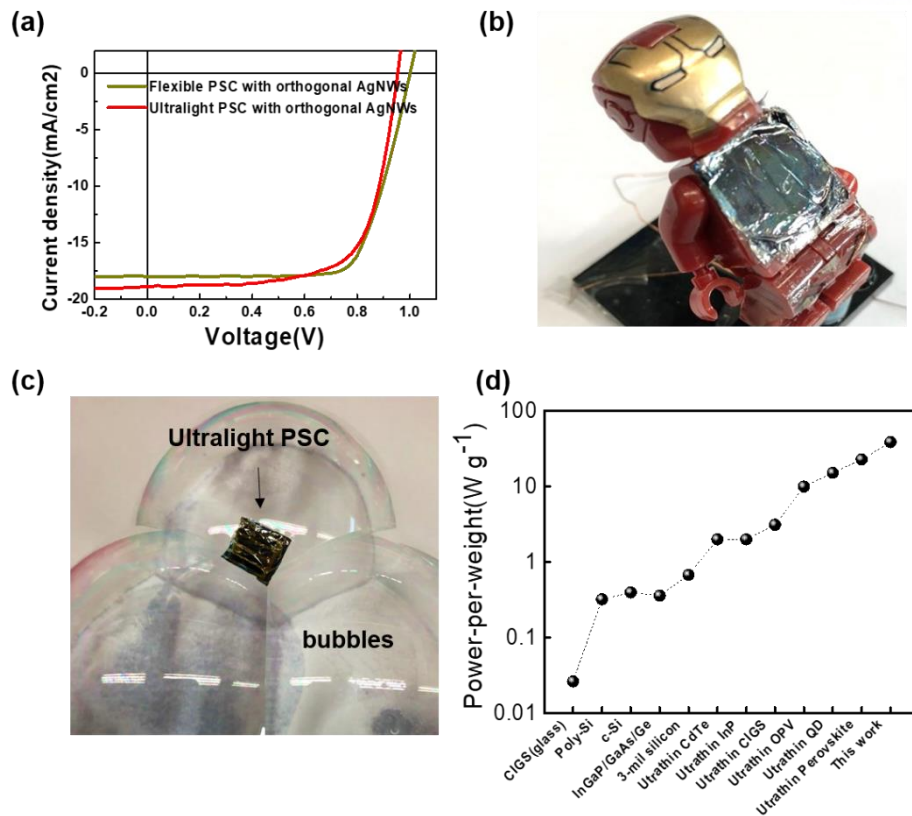


Figure 4.9. (a) J - V characteristic of flexible PSC and ultralight PSC with orthogonal AgNW foil electrode. (b) Ultralight PSC adhered to a toy robot in which two copper wires are connected to anode and cathode of PSC, respectively. (c) Ultralight PSC suspended in bubbles. (d) The power-per-weight performance of ultralight PSC compared to other types of light solar cells.

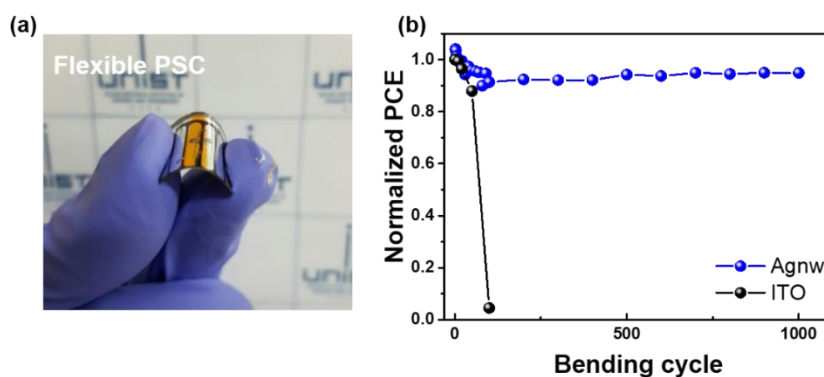


Figure 4.10. (a) A photograph of flexible PSC fabricated on the orthogonal AgNW electrode. (b) The variation in normalized device efficiency of PSCs with ITO and orthogonal AgNW electrodes under repeated 1000 times bending cycles.

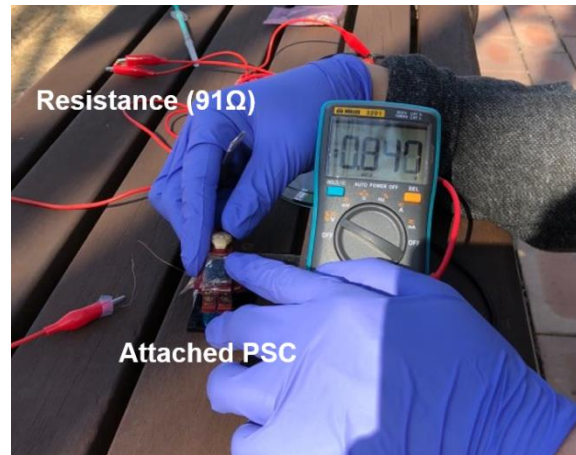


Figure 4.11. A photograph of ultralight PSC device attached to a miniaturized toy robot to demonstrate wearable feature. Such ultralight PSC device was connected with two copper wires and 91 Ω load, which produced 7.8 mW with an open circuit voltage of 0.84V on a sunny spring.



Figure 4.12. A photograph of ultralight PSC device put on an electric scale, indicating extremely light weight.

4.4 Conclusions

In conclusion, we demonstrate ultrathin, lightweight and flexible PSC devices with orthogonal AgNW electrodes foils. Orthogonal AgNW electrodes provide a smooth surface morphology as well as outstanding electrical and optical properties to effectively prevent non-conducting silver-halide formation, resulting in an improved device efficiency than that with random AgNW electrodes. The PCE value of 13.05% for flexible PSC with orthogonal AgNW electrodes was achieved, which is the highest device efficiency reported to date in AgNW-based flexible PSC devices. Furthermore, we present ultrathin and lightweight PSC device with orthogonal AgNW electrode on 1.3 μm polymer foils with the weight of 0.7 mg, achieving the PCE of 12.85% with excellent power-per-weight of 34.4 Wg^{-1} .

Chapter 5. Large-area and uniform transparent electrodes with cross-aligned AgNW network for flexible touch screen applications.

5.1 Introduction

Flexible and transparent conductive electrodes (TCEs) have attracted great attention in a variety of flexible optoelectronic devices, such as touch screen panels, organic solar cells, and organic light emitting diodes.^{172, 173} High mechanical flexibility, optical transparency, and electrical conductivity are the critical properties that TCEs should possess for the realization of high-performance flexible optoelectronics. In addition, the development of scalable and cost-effective fabrication of large-area and uniform TCEs still remains a great challenge. In accordance with these demands, TCEs based on metallic nanowires (NWs) have attracted considerable attention as an essential component for a variety of next-generation optoelectronic applications due to their excellent conductivity, transmittance, and flexibility.^{9, 174} Various solution-based processes, such as spin-coating,^{56, 175} spray-coating,^{175, 176} vacuum filtration,¹⁶⁰ and bar-coating⁵⁷ have been widely used for fabricating NW TCEs. In such conventional solution-making processes, NWs are assembled into random networks; this generates several drawbacks for optoelectronic applications, such as nonuniform networks, NW-NW junction resistance, entanglement between NWs, and surface roughness.¹⁷⁷⁻¹⁸⁰ Manipulating percolating conductive networks to overcome the trade-off between electrical conductivity and optical transmittance has been a key hurdle for random NW network.¹⁸¹ To address these issues, aligned NW networks have been proposed. While the alignment of various types of NWs has been carried out through various solution processes, such as Langmuir-Blodgett,⁸⁷ nanocombing,⁹⁰ contact printing,⁸⁸ capillary force,⁹¹ and flow-enabled self-assembly,¹⁸² these methods still have drawbacks such as the requirement of additional processes (substrate pre-patterning, post-transfer, pre-growing NWs), a slow evaporation rate, a slow coating speed, and incompatibility with large-scale development. To the best of our knowledge, a large-scale and high-throughput assembly of aligned NW networks with high uniformity has not yet been reported.

Here, we report a simple, fast, and large-scale NW assembly strategy for the fabrication of flexible TCEs based on cross-aligned silver nanowire (AgNW) networks. To achieve this, we adopt and modify a conventional bar-coating, or Meyer rod coating technique, that has been used extensively in large-scale solution-based coating applications. Numerous research groups have previously proposed various techniques for aligning AgNWs,¹⁸²⁻¹⁸⁷ but they had limitations in terms of scalability, controllability of NW density, degree of NW alignment, and large-scale uniformity needed for practical optoelectronic applications. Our NW alignment technique, however, can address all these limitations and enables flexible TCEs to be produced with remarkable figures-of-merits (FoMs). As a proof of concept, we

fabricate the large-area ($20 \times 20 \text{ cm}^2$), flexible, and transparent touch screen based on cross-aligned AgNW TCEs as the top and bottom transparent electrodes. In addition, force-sensitive response can be added to touch screens by integrating mechanochromic spiropyran-polydimethylsiloxane (SP-PDMS) composite film into the devices. Unlike conventional touch screens which can only perceive the location of writing, our touch screens enable the monitoring of handwriting patterns with locally different writing forces.

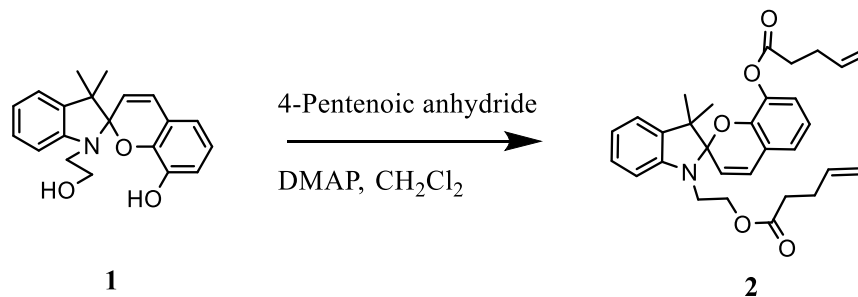
5.2 Experimental Details

Preparation of surface-modified substrates. Before surface modifications, all of the substrates were thoroughly cleaned by sonication for 10 min in the order of deionized (D.I.) water, acetone, and isopropyl alcohol (IPA). For generating –OH-terminated surfaces, cleaned substrates were treated with O₂ plasma for 10 min with a RF power of 18 W. Surface modification with –NH₂ group was prepared by spin-coating a 0.1% poly-L-lysine (PLL) solution in H₂O at 4,000 rpm for 60 s onto an O₂ plasma-treated substrate. The surface terminated with –CH₃ group was prepared by spin-coating hexamethyldisilazane (HMDS) at 4,000 rpm for 60 s.

Fabrication of large-area aligned AgNW arrays by bar-coating assembly. First, a Meyer rod (RD Specialties, Inc.) was mounted onto a bar coater, in which the coating speed and temperature can be precisely controlled. The target substrate was fixed onto the bar coater by using 3M scotch tapes on both edges. The thickness of scotch tape was used as a spacer between the Meyer rod and the substrate during the bar-coating assembly. AgNW ink (Nanopyxis Corporation) containing 0.15 wt.% AgNWs with an average length of 20 μm and diameter of 35 nm was injected into the empty space between the Meyer rod and the substrate, which resulted in the formation of meniscus by a capillary force. Subsequently, the meniscus dragging due to the moving of the Meyer rod at a constant speed resulted in the formation of highly uniform and aligned AgNW arrays along the coating direction. In order to fabricate cross-aligned AgNW arrays, right after complete drying of solvent, an additional bar-coating assembly was carried out on the aligned AgNW substrate in a direction that was perpendicular to that of the pre-aligned AgNWs. In the second bar-coating process, it is not necessary to repeat the chemical surface treatment by PLL on the first aligned AgNW substrate because AgNWs can be attached at the empty surface area between AgNWs. All of the fabricated AgNW TCEs were used in characterizations and applications without any post-treatments to increase the conductivity.

Fabrication of flexible and transparent touch screen. The transparent touch screen was operated by connecting a 4-wire resistive touch screen controller (ER-DBTP-USB04W-1, Eastrising Technology Co Ltd.) to a laptop computer. For the fabrication of the transparent touch screen based on a four-wire resistive-type touch sensor, cross-aligned AgNW TCEs were used as the top and bottom transparent electrodes of resistive touch sensor without any protective layers or dot spacers. The cross-aligned AgNW networks were fabricated by a bar-coating assembly on a 20 × 20 cm² PET substrate. In this bar-coating assembly, a #6 rod was used to align AgNWs at a coating speed of 10 mm s⁻¹ at room temperature. Then, two cross-aligned AgNW TCEs were assembled with AgNW-coated sides facing each other. Here, the top and bottom TCEs were separated by an air gap (thickness of ~1 mm) that had been developed by attaching 3M scotch tapes around the substrate edges. Finally, the prepared touch screen was connected to a laptop computer through a four-wire resistive controller board.

Synthesis of active spiropyran mechanophore. 1'-(2-hydroxyethyl)-3,3'-dimethyl-spiro[chromene-2,2'-indolin]-8-ol (**1**) and 3,3'-dimethyl-1'-(2-(pent-4-enoyloxy)ethyl)spiro[chromene-2,2'-indolin]-8-yl-pent-4-enoate (SP-2-H-bisPentenoate) (**2**).



In this study, SP-2-H-bisPentenoate was used as an active spiropyran mechanophore. For the synthesis of the SP-2-H-bisPentenoate, in a flame dried round bottom flask, dried under N₂, 1'-(2-hydroxyethyl)-3,3'-dimethyl-spiro[chromene-2,2'-indolin]-8-ol (12.7 g, 39.3 mmols, 1.0 equiv) and 4-dimethylaminopyridine (DMAP) (0.48 g, 3.93 mmols, 0.1 equiv) were added in 200 ml anhydrous CH₂Cl₂. Suspension was stirred at ambient for 10 min and 4-pentenoic anhydride (15 g, 82.5 mmols, 2.1 equiv) were added in 3 aliquots, 20 min apart. After the addition of first aliquot, solution became homogeneous, honey colored and a mild exotherm was detected. Stirring was continued for 1.5 h after last aliquot. Product solution was extracted with satd. NaHCO₃ (3x, 100 ml each), 1 M HCl (100 ml), D.I. water (2x, 100 ml each), dried over Na₂SO₄ and solvent removed to obtain 19 g (99 %) of pale honey colored oil.

The NMR spectra (¹H and ¹³C) were obtained on 600 MHz Bruker NMR Spectrometer (B600). Chemical shifts were recorded as parts per million (ppm) referenced to the residual ¹H or ¹³C peak at 5.32 ppm in CD₂Cl₂ or 53.84 in CD₂Cl₂, respectively. ¹H multiplicity was reported as: s (singlet), d (doublet), dd (doublet of doublets), dt (doublet of triplets), ddd (doublet of doublet of doublets), ddt (doublet of doublet of triplets), t (triplet), td (triplet of doublets), q (quartet), mp (multiplet), and b (broad). Coupling constants (J) were reported in Hertz. High-resolution mass spectrometry was performed on an Agilent LCMS-TOF-DART at Duke University's Mass Spectrometry Facility.

¹HNMR (600 MHz, CD₂Cl₂) δ 7.15-7.11 (dt, J = 7.6, 1.2 Hz, 1H), 7.09-7.05 (dd, J = 7.2, 0.9 Hz, 1H), 7.01-6.98 (dd, J = 7.5, 1.5 Hz, 1H), 6.94-6.91 (d, J = 10 Hz, 1H), 6.90-6.86 (dd, J = 7.9, 1.5 Hz, 1H), 6.85-6.75 (m, 2H), 6.65-6.62 (d, J = 7.6 Hz, 1H), 5.85-5.77 (m, 2H), 5.64-5.54 (m, 1H), 5.06-5.00 (qd, J = 16.9, 1.5 Hz, 1H), 4.99-4.95 (br qd, J = 10.2 Hz, 1H), 4.92-4.89 (br qd, J = 7.4 Hz, 1H), 4.89-4.87 (t, J = 1.5 Hz, 1H), 4.22-4.13 (m, 2H), 3.40-3.33 (m, 1H), 3.33-3.26 (m, 1H), 2.40-2.28 (m, 4H), 2.22-2.09 (m, 2H), 1.90-1.79 (m, 2H), 1.26 (s, 3H), 1.16 (s, 3H).

¹³CNMR (150.9 MHz, CD₂Cl₂) δ 173.05, 171.28, 147.45, 145.36, 138.23, 137.27, 137.23, 136.78, 129.63, 127.78, 124.48, 123.05, 121.79, 120.35, 119.98, 119.79, 119.76, 115.48, 115.08, 107.04, 105.45, 63.01, 51.97, 42.74, 32.73, 33.35, 29.10, 28.85, 25.93, 19.52.

HRMS-ESI (m/z): $[M + H]^+$ calcd for $C_{30}H_{33}NO_5$, 488.2431; found, 488.2433.

Fabrication of force-sensitive mechanochromic touch screen. For the fabrication of mechanochromic composite films on top of the touch screen, spiropyran mechanophore was completely mixed with a PDMS base (Sylgard 184, Dow Corning) and PDMS curing agent (10:1 ratio for base to curing agent). The SP-PDMS composite was stored in a vacuum desiccator for 30 min to remove the bubbles. Then, the mechanochromic composite film was evenly deposited on top of the transparent touch screen by a bar-coating of the SP-PDMS composite solution using the #15 rod at a coating speed of 10 mm s^{-1} and thermal-curing at $60 \text{ }^\circ\text{C}$ for 6 h.

Characterizations. The chemical bonding and functional groups were investigated by the X-ray photoelectron spectrometry (XPS, K-alpha, Thermo Fisher, Waltham, MA, USA). The sheet resistances of the cross-aligned and random AgNW networks were measured using a four-point probe measurement device (Kiethley 2400 equipment). Optical transmittance and absorption spectra of unidirectional, cross-aligned, and random AgNW networks were measured by a UV-vis-NIR spectrophotometer (Jasco V-670). For the measurement of polarized absorption, a polarizer accessory (WP25M-UB, Thorlabs, Inc.) was equipped to the UV-vis-NIR spectrophotometer. The surface alignment structure of AgNW arrays was examined by an optical microscope (PSM-1000, Olympus). The mechanochromic colors were investigated by a spectroradiometer (PR-655, Photo Research, Inc.).

5.3 Results and Discussion

A Meyer rod is composed of a metal bar wrapped in wires, where the diameter of the wrapped wires determines the slit width (51–381 μm) and the amount of solution required to achieve the desired density of AgNWs (Figure 5.1). In this study, the alignment of AgNWs by bar-coating assembly is carried out by dragging a Meyer rod at a constant velocity and predefined rod-substrate gap distance over an AgNW solution on a surface-modified target substrate. Figure 5.2a shows a photograph of the bar-coating assembly process on a large polyethylene terephthalate (PET) substrate ($20 \times 20 \text{ cm}^2$). We pretreat the PET target substrate with poly-L-lysine (PLL) to enhance the AgNW adhesion to the substrate *via* an electrostatic force from amine-functional groups. By placing the AgNW solution into an empty space between the gap of the moving rod and the target substrate, thin uniform layer of AgNW solution film can be produced due to the confinement between the dense grooves of the Meyer rod and the target substrate. Dragging the trapped AgNW solution results in shear-induced hydrodynamic force on the trapped liquid film, which enables the alignment of AgNWs.

In the one-step bar-coating assembly, the interaction between shear-induced hydrodynamic and electrostatic forces enables the fabrication of highly aligned AgNW arrays (Figure 5.2b and 5.3). Unlike typical convective assembly processes, where NWs are aligned in an evaporation regime at a particularly slow coating speed (10–100 $\mu\text{m s}^{-1}$), the alignment of AgNW in the bar-coating assembly is dominated by the Landau-Levich regime which has a fast meniscus dragging speed ($> 1 \text{ mm s}^{-1}$), where the viscous forces caused by shearing of the meniscus are predominant.¹⁸⁸ During the alignment process, the hydrodynamic force can be calculated¹⁸⁹ as $F = \frac{4\pi\mu Ua}{\ln(2a/b)-0.72} = 3.26 \text{ nN}$, where μ is the viscosity of the fluid ($\sim 9.12 \times 10^{-3} \text{ Pa s}$, at 298.15 K for AgNW ink dispersed in ethanol), U is the velocity of capillary flow at the bottom of the moving bar (which is close to the moving speed of the bar, which is 10 mm s^{-1}), and a and b are the length ($\sim 20 \mu\text{m}$) and radius ($\sim 17.5 \text{ nm}$) of the NWs, respectively. This estimated drag force is comparable to the force ranges to align AgNWs by capillary forces and carbon nanotubes by hydrodynamic forces.¹⁹⁰

The AgNWs can be aligned during bar-coating assembly regardless of the solvent used, as long as the AgNW ink is viscous enough for generating the hydrodynamic force (Figure 5.4). The hydrodynamic drag force of the AgNW ink is estimated for various solvents, such as isopropyl alcohol (IPA) ($\mu = 9.37 \times 10^{-3} \text{ Pa s}$) and water ($\mu = 9.52 \times 10^{-3} \text{ Pa s}$), and the corresponding hydrodynamic force for the IPA and water are 3.35 nN and 3.4 nN, respectively.

The surface chemistry of the target substrate is a critical factor affecting the alignment of AgNWs capped with slightly negatively charged polyvinylpyrrolidone (PVP), which acts as a capping layer.¹⁹¹ ¹⁹² To investigate this effect, the target silicon (Si) substrates are pretreated with different functional groups, including amine ($-\text{NH}_2$), methyl ($-\text{CH}_3$), and hydroxyl groups ($-\text{OH}$) (Figure 5.5). The amine group ($-\text{NH}_2$)-terminated PLL treatment provides the best aligned AgNW arrays because of the strong

electrostatic interaction between the negatively charged PVP-capped AgNWs and the positively charged active amine groups of the PLL, which enhances the anchoring of the AgNWs onto the surface during the alignment process. To confirm the interaction between the AgNWs and the pretreated surfaces, X-ray photoelectron spectroscopy (XPS) is performed for AgNW-coated PLL/Si substrates and PLL/Si substrates (Figure 5.6). The high-resolution N 1s spectra of the pristine AgNW is composed of two fitted peaks at 400.1 and 399.5 eV, which can be attributed to pyrrolic N and N-C due to the N atom of the PVP on the AgNW surface.¹⁹³ The N 1s spectra of the pristine PLL shows two deconvoluted peaks, with one arising from protonated amine ($-\text{NH}_3^+$) at 401.3 eV and the other from N-C at 399.3 eV.¹⁹⁴ After the deposition of the AgNW on the PLL-treated substrate, the high-resolution N 1s spectrum shows two fitted peaks at 400.2 and 399.3 eV, as is the case of pristine AgNW; however, the peak at 400.2 eV has broadened, which we believe is due to the involvement of pyrrolic N from PVP and $-\text{NH}_3^+$ from PLL. The large downward shift of the binding energy (~ 1.1 eV) in the $-\text{NH}_3^+$ peak of PLL is attributed to the charge transfer from the negatively charged PVP to the positively charged protonated amine groups in the PLL, which confirms the strong ionic interaction between the PLL and the AgNW (Figure 5.6a).¹⁹⁵

In contrast to PLL-modified surface, the surfaces modified using hexamethyldisilazane (HMDS) to produce the methyl group ($-\text{CH}_3$) and the surface modified by oxygen (O_2) plasma treatment to give the hydroxyl group ($-\text{OH}$) lead to a low density and poor alignment of the AgNWs (Figure 5.5b,c), which we attribute to the weak molecular interaction between the AgNWs and the methyl and hydroxyl groups, as shown by the XPS analysis. The XPS analysis of the high-resolution N 1s and C 1s spectra of the HMDS-treated and O_2 plasma-treated surfaces do not show any significant changes in the peak positions before and after the AgNW alignments (Figure 5.6a,b). Note that the high-resolution Ag spectra of none of the samples show any significant differences in the peak positions (Ag $3d_{3/2}$ and Ag $3d_{5/2}$ peaks at 374.3 and 368.3 eV in pristine AgNW), which suggests that Ag surface is intact to any kind of oxidation¹⁹⁶ and ionic interactions exist between the different functional groups ($-\text{NH}_2$, $-\text{CH}_3$, and $-\text{OH}$) and PVP rather than with the AgNW (Figure 5.6c).

Figure 5.2c shows a dark-field optical micrograph of a unidirectionally aligned AgNW array. The fast Fourier transform (FFT) image of the optical micrograph in the inset of the figure exhibits a clear line pattern, which indicates that the AgNW array has a highly aligned unidirectional structure. The advantage of our bar-coating assembly is that it allows for a multilayer AgNW arrays with precisely controllable interlayer orientations to be produced; this leads to cross-aligned AgNW arrays with user-defined internanowire angles (Figure 5.3). When a second bar-coating process is performed in a perpendicular direction on top of the pre-aligned AgNW array, cross-aligned AgNW arrays are observed in the FFT image with a clear crossed-line pattern (Figure 5.2d), which indicates a 90° orientation between the first and second AgNW arrays. These cross-aligned AgNW networks, in contrast to the random AgNW networks, have several advantages for the fabrication of high-performance transparent

electrodes, including highly uniform conductive networks, a lower percolation threshold, and excellent transparency at similar surface resistivity.¹⁹⁷

To quantitatively investigate the degree of alignment, radial summations of the pixel intensities of the FFT analysis are plotted as a function of the radial angle (0-360°) (Figure 5.7). The unidirectional AgNW array shows a clear and strong peak at 90°, which indicates a vertical alignment. The cross-aligned AgNW arrays show clear peaks at 0°, 90°, and 180° which indicate that the two aligned AgNW layers cross over at 90°. However, the random AgNW network does not provide any noticeable peaks, which is due to the lack of any particular orientation of the AgNWs, as indicated by the isotropic pattern of the FFT image in Figure 5.8. The AgNW alignment is also directly analyzed by measuring the distribution of the degree of alignment of 150 NWs from an aligned AgNW array in Figure 5.2c, which results in a full width at half maximum (FWHM) value of 21.4 (Figure 5.2e), confirming that most of the AgNWs are highly aligned along the direction of the coating.

One of the advantages of bar-coating assembly of the aligned AgNW networks is its scalability, as it can be used to produce films with large areas. Our bar-coating assembly can readily create uniformly aligned AgNW arrays on PET substrates over a 20 × 20 cm² area. The uniformity of the alignment over such an area is evaluated through an analysis of the distribution of FWHM values of aligned AgNW arrays in 16 local regions in a 20 × 20 cm² area (Figure 5.9). The FWHM values of AgNW arrays in all 16 local regions confirm the high uniformity and the scalability of the bar-coating assembly process (Figure 5.2f). Although the sample size is limited by the size of the equipment used in this study, we anticipate that the size of the aligned AgNW films can be further scaled up by using a longer Meyer rod or a roll-to-roll bar-coating process.

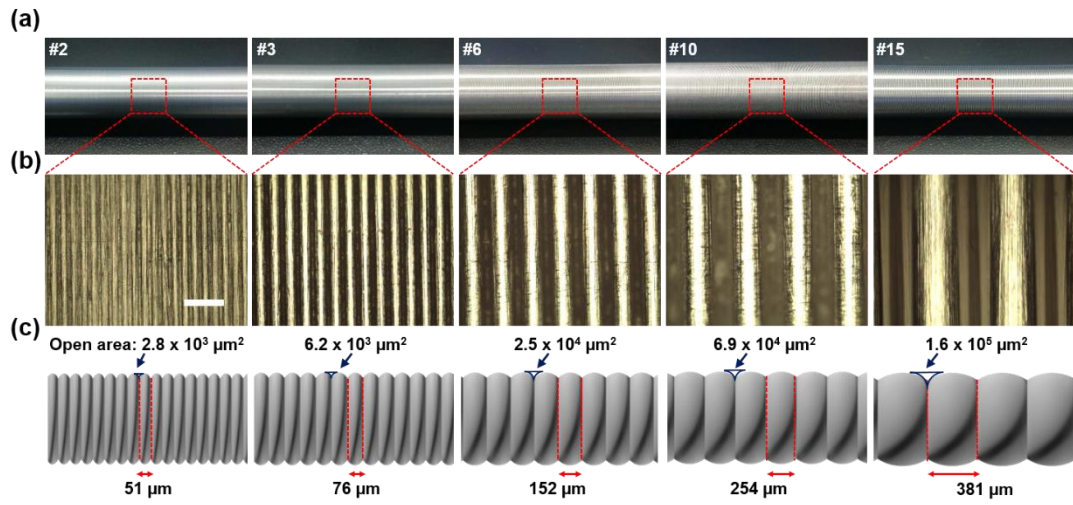


Figure 5.1. (a) Photographs of various kinds of Meyer rods (#2, #3, #6, #10, and #15) and (b) corresponding optical microscope images. The scale bar is 200 μm . (c) Schematic illustration of the specifications of various Meyer rods. The rod number determines the diameter of wrapped wires and the open area.

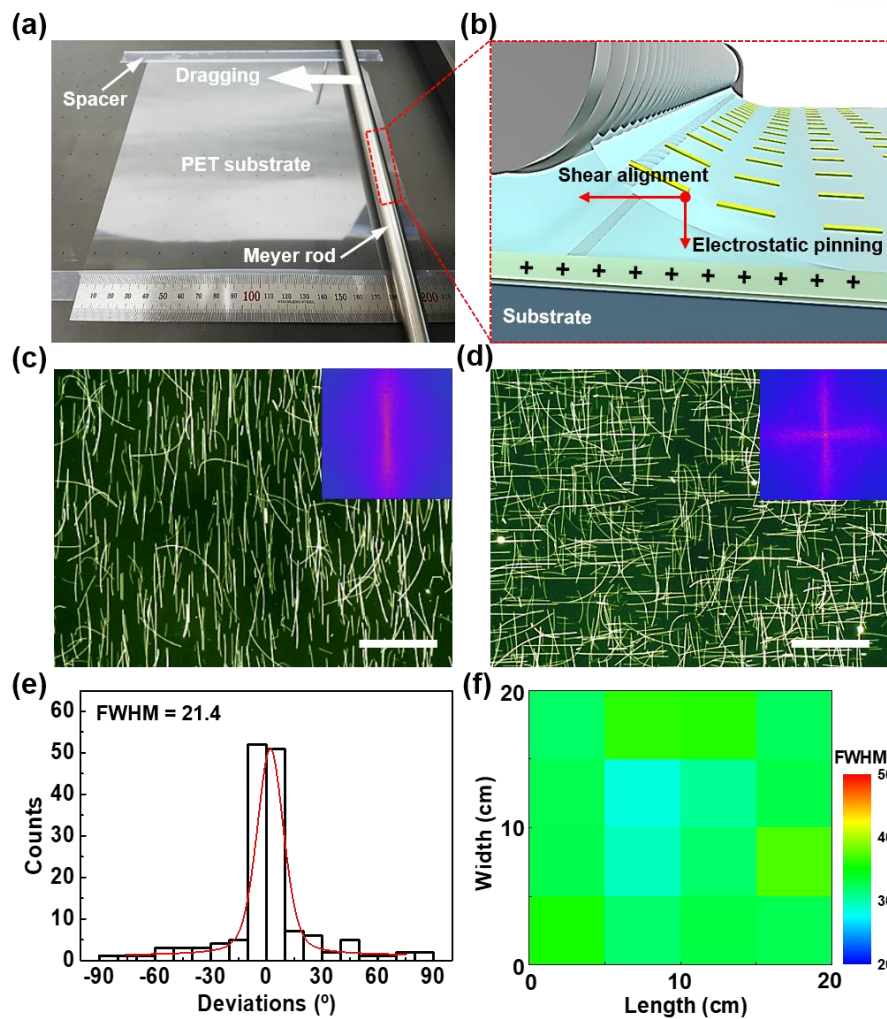


Figure 5.2. Large-scale bar-coating alignment of unidirectional and cross-aligned AgNW arrays. (a) A photograph of the solution-processed bar-coating alignment of the AgNWs on a $20 \times 20 \text{ cm}^2$ PET substrate and (b) a schematic showing the alignment process of AgNWs during the bar-coating assembly of the AgNW solution. The combined interaction between shear stress alignment and the electrostatic pinning produced highly aligned and uniform AgNW arrays during the dragging of a confined meniscus between the rod and substrate. (c) Dark-field optical microscope images of the unidirectionally aligned and (d) cross-aligned AgNW arrays. Insets are the fast Fourier transform (FFT) analyses of the optical micrographs indicating the direction and uniformity of the aligned AgNW structures. The scale bars are $40 \mu\text{m}$. (e) Distribution of the alignment degrees of 150 NWs in Fig. 5.2c with a full width at half maximum (FWHM) value of 21.4. (f) Mapping image showing the highly uniform distribution of FWHM values of each pixel in a 4×4 array over a large-area ($20 \times 20 \text{ cm}^2$) of aligned AgNWs. The FWHM values were calculated by fitting the radial summation of the pixel intensities of the FFT analysis.

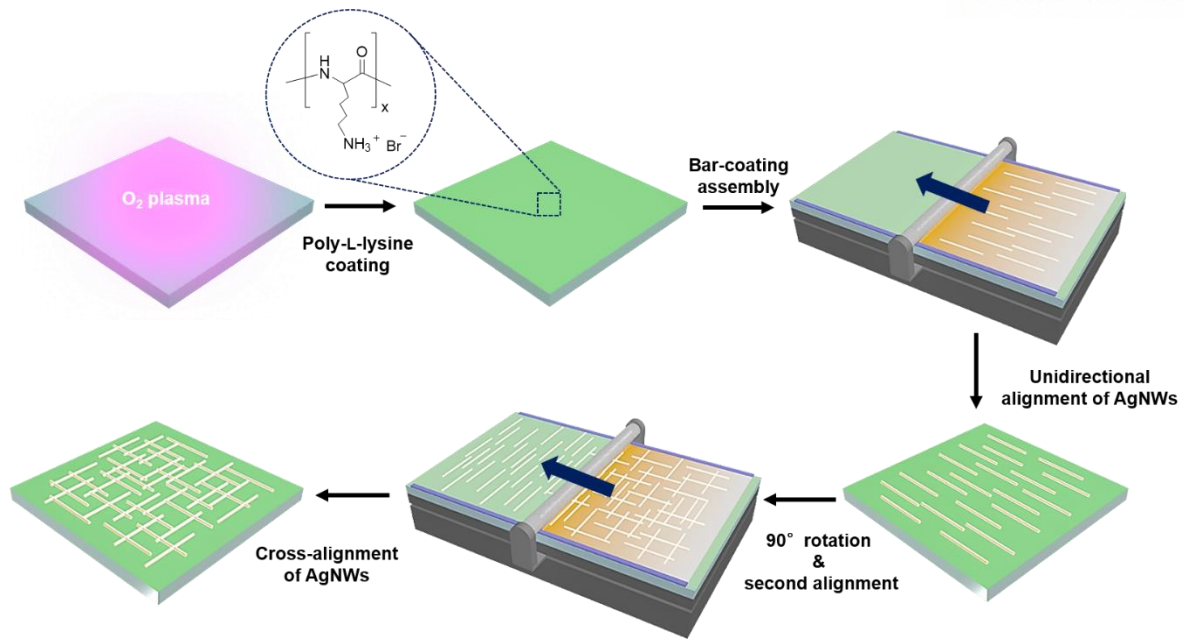


Figure 5.3. Schematic of an overall procedure for the solution-processed bar-coating assembly to fabricate unidirectionally and cross-aligned AgNW arrays. Before the bar-coating assembly, poly-L-lysine (PLL) solution is coated on O₂ plasma-treated target substrate to form amine groups on the surface. Consecutively, the meniscus dragging produces highly aligned AgNW arrays. The cross-aligned AgNW array is formed by repeating the bar-coating assembly in a perpendicular direction to that of the pre-aligned AgNW arrays.

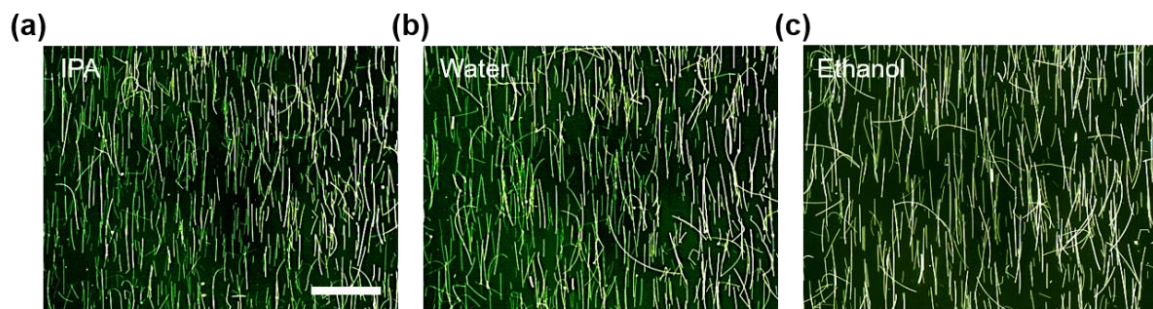


Figure 5.4. Dark-field optical micrographs of the unidirectionally aligned AgNWs coated with AgNW ink dispersed in different kinds of solvents; (a) isopropyl alcohol (IPA), (b) water, and (c) ethanol. During the bar-coating assembly, #2 bar, 3 μl of volume, and 10 mm s⁻¹ of coating speed were used in all experiments. The scale bar is 40 μm .



Figure 5.5. Dark-field optical micrographs of the aligned AgNW networks coated on substrates modified with different types of functional groups; (a) PLL (-NH₂), (b) hexamethyldisilazane (HMDS) (-CH₃), and (c) O₂ plasma (-OH). During the bar-coating assembly, #2 bar, 3 μl of volume, and 10 mm s⁻¹ of coating speed were used in all experiments. The scale bar is 40 μm.

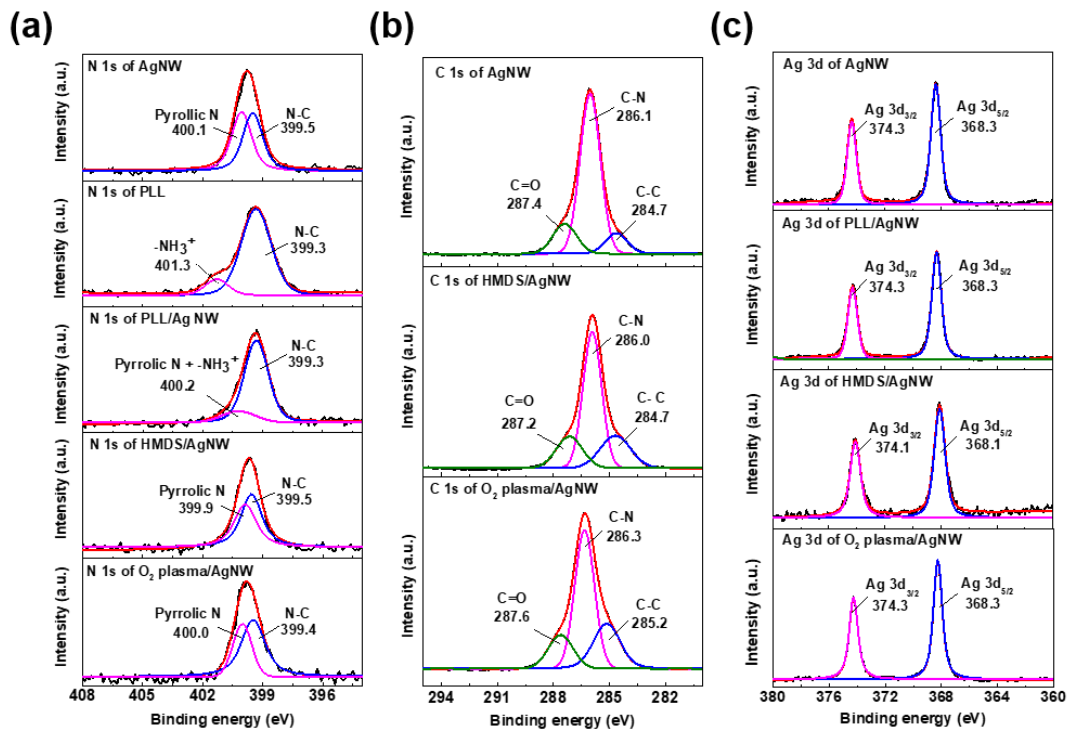


Figure 5.6. X-ray photoelectron spectroscopy (XPS) survey to investigate the interactions between AgNWs and the substrate surface pretreated with different functional groups with PLL, HMDS, and O₂ plasma. (a) High resolution N 1s spectra of the pristine AgNW, PLL, PLL/AgNW, HMDS/AgNW, and O₂ plasma/AgNW. (b) High resolution C 1s spectra of the pristine AgNW, HMDS/AgNW, and O₂

plasma/AgNW. (c) High resolution Ag 3d spectra of the pristine AgNW, PLL/AgNW, HMDS/AgNW, and O₂ plasma/AgNW.

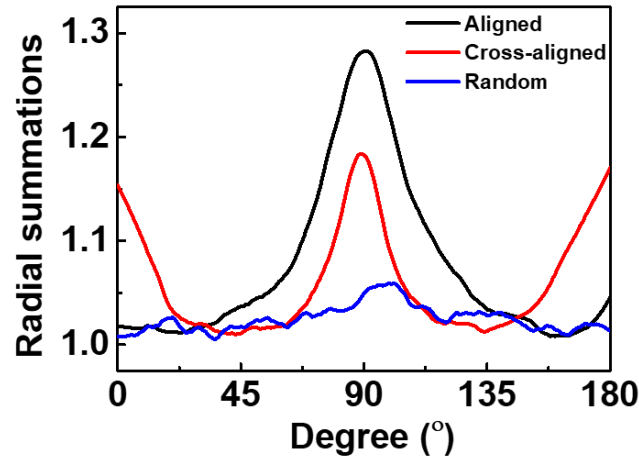


Figure 5.7. The radial summations of the pixel intensities of the fast Fourier transform (FFT) analysis data as a function of radial angle (0-180°) of the unidirectional AgNW array, cross-aligned AgNW arrays, and random AgNW network. Contrary to aligned and cross-aligned AgNWs networks which show clear Gaussian peaks, random AgNW network shows uncertain spectra of radial summations due to the lack of directionality.

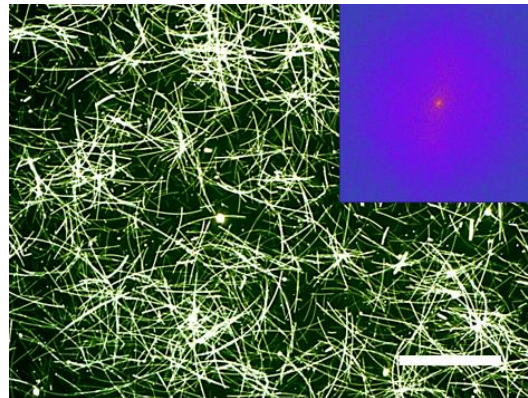


Figure 5.8. Dark-field optical micrograph of the random AgNW networks fabricated by conventional bar-coating process. Inset shows the corresponding FFT analysis data. The scale bar is 40 μm.

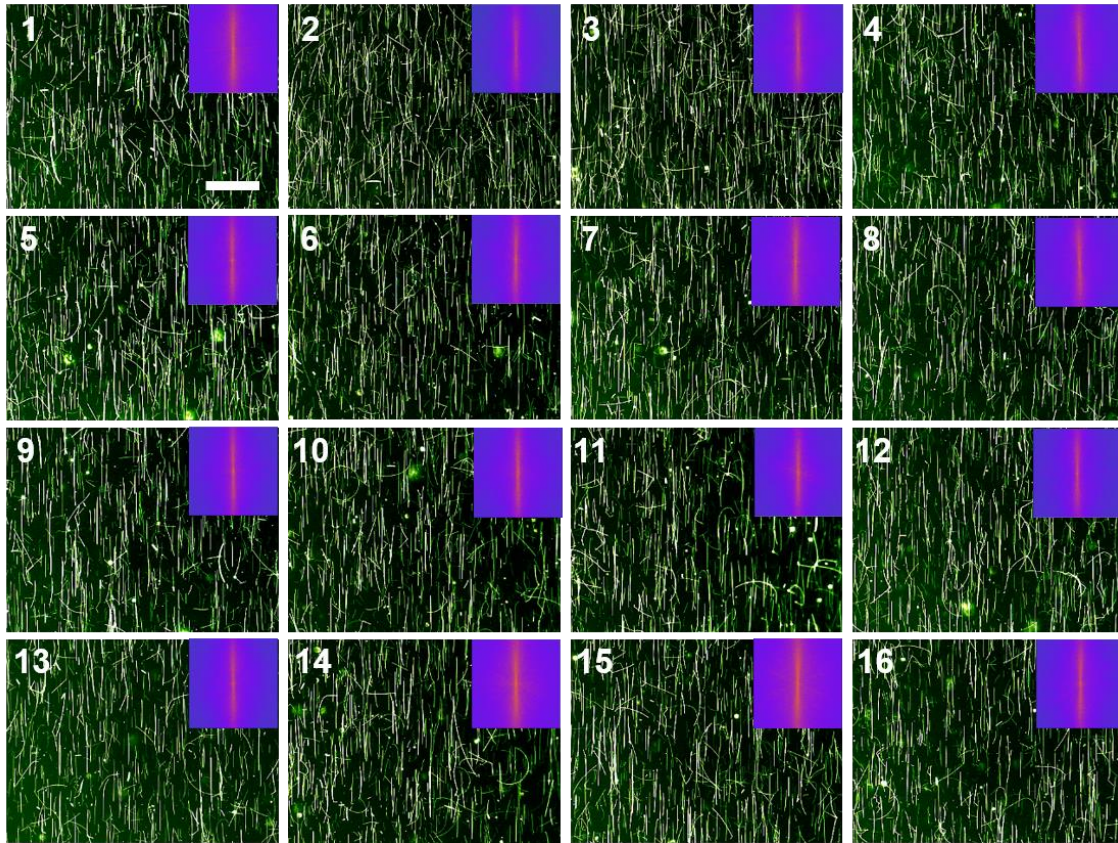


Figure 5.9. Large-area ($20 \times 20 \text{ cm}^2$) alignment of the AgNWs by bar-coating assembly. 16 dark-field optical micrographs of the aligned large-area AgNW arrays in a large-area PET film and the corresponding FFT analysis images in the insets. For the bar-coating assembly, #2 bar, $100 \mu\text{l}$ of volume, and 10 mm s^{-1} of coating speed were used in the experiment. The FWHM values of 16 AgNW arrays confirm the high uniformity and the scalability of the bar-coating assembly process as shown in Figure 5.2f. The scale bar is $40 \mu\text{m}$.

To further understand the mechanism behind the NW alignment, a number of parameters, including the amount of AgNW dispersion between the rod and substrate, the coating speed, and the substrate temperature, are investigated to monitor the alignment degree. We observed that the degree of alignment increases as the amount of AgNW dispersion, coating speed, and substrate temperature decrease (Figure 5.10a-c and Figure 5.11). As can be seen in Figure 5.10a, the FWHM value increases with the amount of AgNW dispersion, indicating that the degree of alignment of the NWs decreases. This behavior can be attributed to the increased meniscus thickness and contact area between the bar and the substrate, which increases the likelihood of misalignment of the AgNWs located far from the dragging bar (Figure 5.12). During the meniscus dragging, the shear force gradient is generated as a function of the height of the meniscus in a Couette flow.^{198, 199} Therefore, the AgNWs located far from the dragging bar have a high probability of misalignment due to a reduced shear force (Figure 5.13).²⁰⁰ This relationship between the NW alignment and the meniscus thickness (or the shear force gradient) is also confirmed through the direct control of the gap distance between the Meyer rod and the substrate. Figure 5.14 shows that the degree of NW alignment decreases as the gap between the Meyer rod and the substrate increases, which indicates that the AgNWs located far from the dragging bar are likely to be misaligned due to the decreased shear force.

A decrease in the coating speed results in a decrease in the FWHM value, which indicates that the degree of NW alignment increases (Figure 5.10b). In our alignment system, the coating speed affects the shear force and the thickness of the confined meniscus film. The lowest coating speed used in our bar-coating assembly ($= 10 \text{ mm s}^{-1}$) is well above the minimum coating speed ($\approx 1 \text{ mm s}^{-1}$) required for a shear-stress-induced alignment of the AgNWs, which is still significantly faster than that of conventional evaporation-induced assembly ($\approx 10\text{-}100 \mu\text{m s}^{-1}$).²⁰¹ The lower coating speed decreases the thickness of the wet meniscus film,²⁰² which enhances the shear-induced hydrodynamic dragging force used to align the AgNWs. A higher coating speed, however, leads to a thicker meniscus film and hinders the formation of a uniform meniscus during the coating process. The degree of NW alignment is also affected by the substrate temperature. As the substrate temperature increases, the FWHM value increases (and the degree of NW alignment decreases) (Figure 5.10c). The reduced alignment of the AgNWs is attributed to decreased viscosity resulting from the increase in the substrate temperature,²⁰³ which in turn results in a decreased shear force.

Our bar-coating process for NW alignment is different from conventional evaporation-induced assembly processes. In an evaporation-induced assembly process, NWs are aligned at the meniscus contact line due to the surface tension of the moving meniscus line during solvent evaporation;²⁰⁴ however, the surface tension of the moving meniscus line has minimal effects on NW alignment in our process. Before the solvent completely evaporates (which takes 0-7 s), most of the AgNWs are aligned by the shear-induced hydrodynamic force. After complete drying of the solvent (7-9 s), the aligned

AgNWs show negligible movement, which confirms the minimal effect of the surface tension of meniscus line on the prealigned NWs.

Highly aligned AgNW arrays produced by the bar-coating assembly exhibit the anisotropic optical properties. We investigate the polarized absorption spectra of the aligned AgNW arrays as a function of the polarization angle, θ , from 0 to 90°, where θ is the angle between the polarization direction of incident light and the alignment direction of the AgNW arrays (Figure 5.10d). Note that the absorption peak at 365 nm increases with θ , which is attributed to the greater effect of the transverse surface plasmon resonances of the AgNWs; meanwhile, the absorption peak at longer wavelength (> 500 nm) decreases, which is attributed to the longitudinal surface plasmon resonances of the AgNWs having less of an effect (Figure 5.10e).⁸⁷ Random AgNW networks without any anisotropic optical properties, however, do not show any noticeable change in their absorption peaks as the polarization angle increases (Figure 5.15). The strong anisotropic optical properties of the highly aligned AgNW array exhibit an optical dichroic characteristic; Figure 5.10f shows that the aligned AgNW arrays inside the “UNIST” letters become invisible or visible when the polarized light is parallel ($\theta = 0^\circ$) or perpendicular ($\theta = 90^\circ$) to the direction of the AgNW alignment, respectively; because the aligned AgNW arrays can act as a polarizing filter (Figure 5.16). These polarized absorption and dichroic properties clearly indicate the strong anisotropic optical properties of the aligned AgNW films.

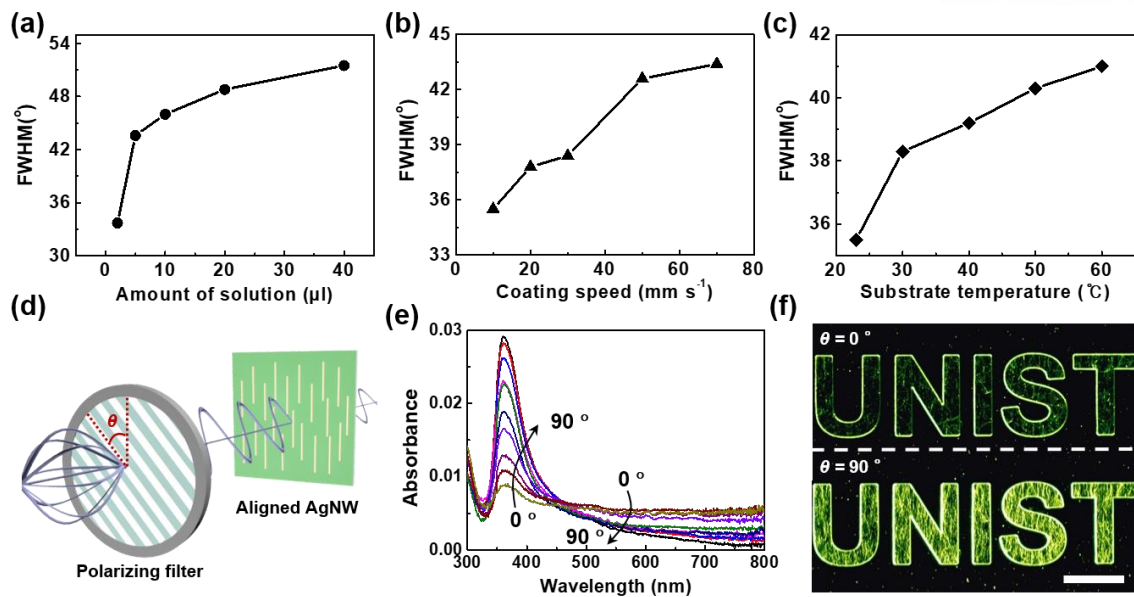


Figure 5.10. Unidirectional bar-coating alignment of the AgNW arrays and the anisotropic optical properties. (a-c) FWHM values according to the variation in the bar-coating parameters, including the amount of solution (2-40 μl), coating speed (10-70 mm s^{-1}), and substrate temperature (23-60 $^\circ\text{C}$). (d-f) Anisotropic optical properties of the unidirectional AgNW arrays. (d) Schematic showing the polarized absorption test as a function of the angle θ between the direction of the polarized incident light and the NW alignment. (e) Polarized UV-vis absorption spectra of unidirectionally aligned AgNW arrays as a function of polarization angle (0-90 $^\circ$). (f) Optical dichroic property of unidirectionally aligned AgNW array. Polarized optical microscope images of “UNIST” patterns with different AgNW alignment directions exhibits invisible AgNW arrays when the light was polarized parallel to the direction of AgNW alignment ($\theta = 0^\circ$) and clearly visible AgNW array when the light was polarized perpendicular to the direction of AgNW alignment ($\theta = 90^\circ$). The scale bar is 100 μm .

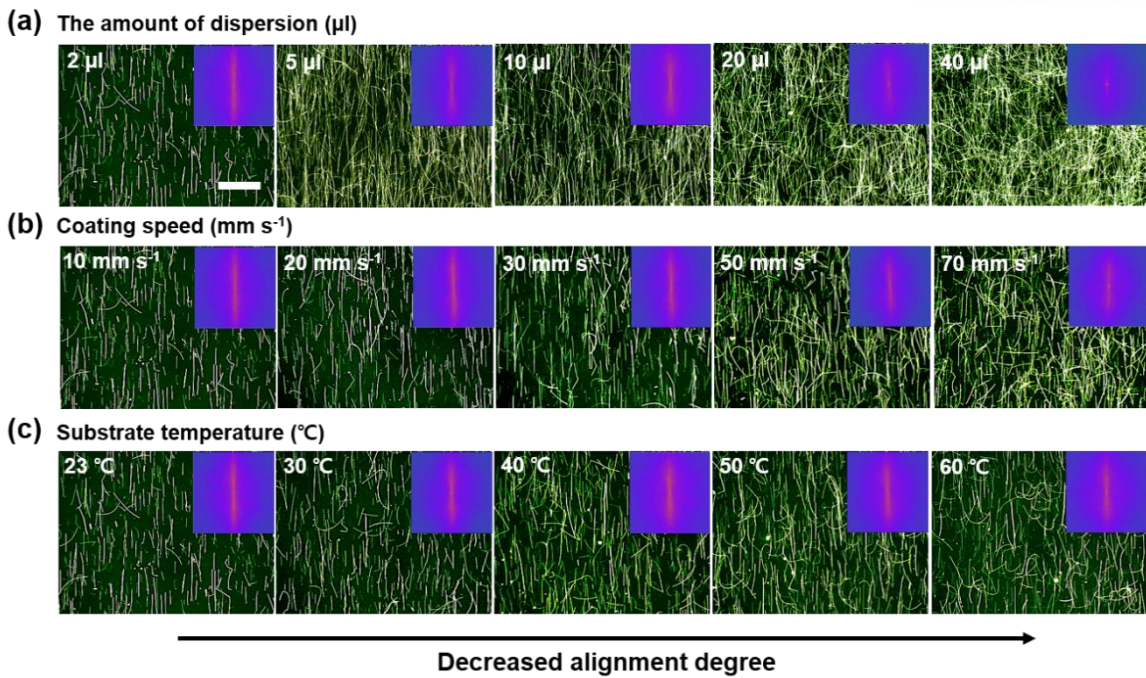


Figure 5.11. Dark-field optical micrographs of the aligned AgNW networks fabricated by the bar-coating assembly with different coating conditions; (a) volume of solution (2-40 μl), (b) coating speed (10-70 mm s^{-1}), and (c) substrate temperature (23-60 $^{\circ}\text{C}$). All insets show the corresponding FFT analysis images. The scale bar is 40 μm .

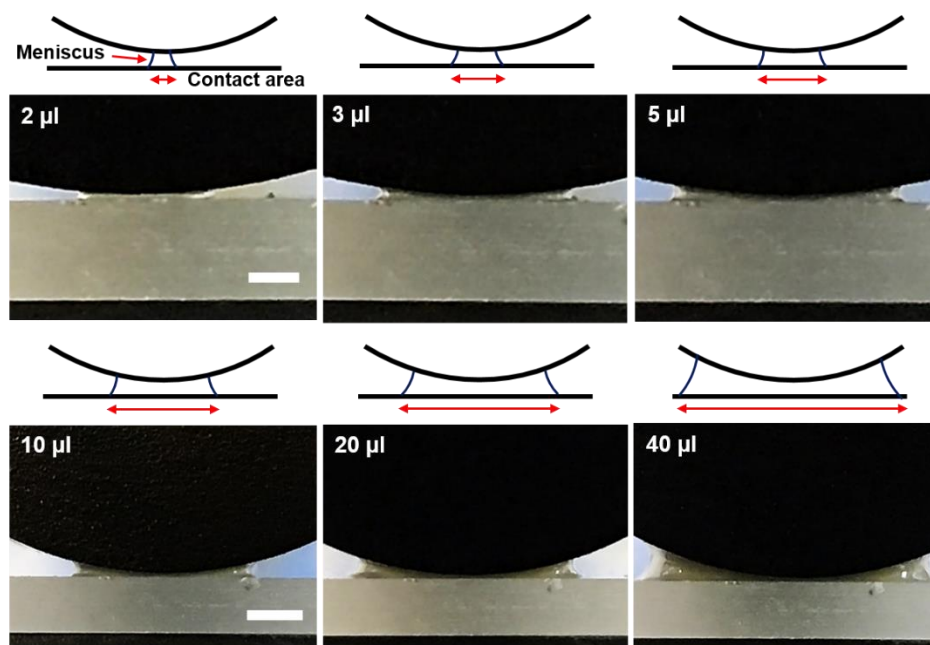


Figure 5.12. The effect of the amount of AgNW dispersion on the formation of contact area between the meniscus and the substrate. Schematics and close-up photographs show the meniscus between the rod and substrate with a different volume of dispersion (2-40 μl). As the volume of dispersion increases, the contact area becomes broader. The scale bars are 500 μm (top) and 1000 μm (bottom).

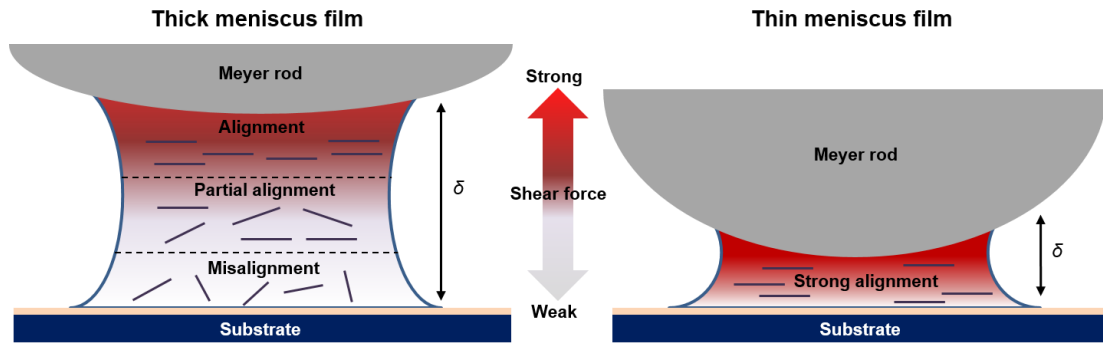


Figure 5.13. Schematic showing the intensity distribution of shear force according to the variation of the height (δ) of meniscus. In the meniscus dragging process, the shear force gradient is generated as a function of the height of the meniscus in a Couette flow. Therefore, the AgNWs located far from the dragging bar have a high probability of misalignment due to a reduced shear force. In thick meniscus film, many of AgNWs are located far from the dragging bar and thus have a high probability of misalignment. In thin meniscus film, most of AgNWs are near the dragging bar, which results in the high probability of alignment.

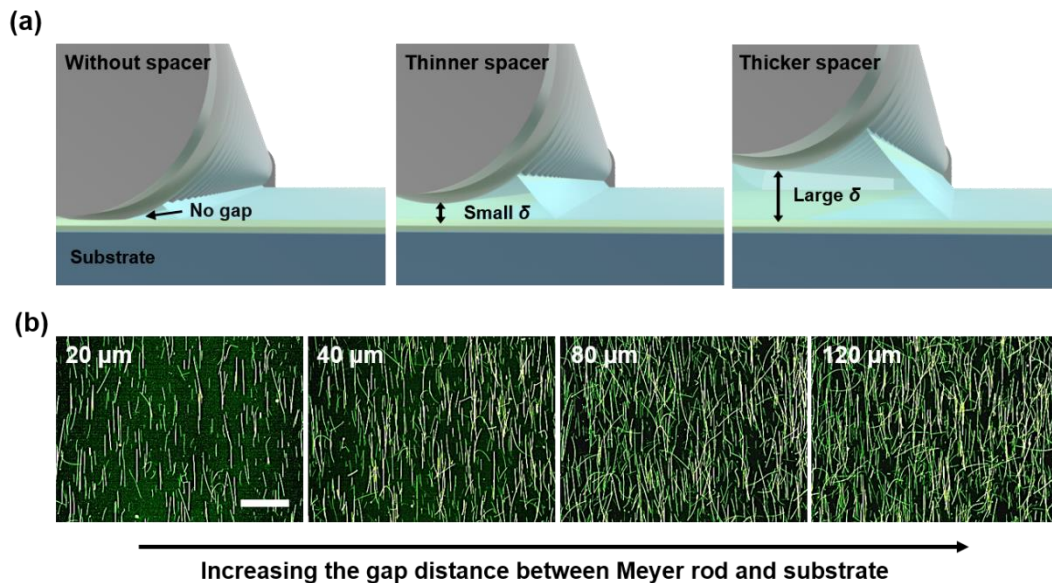


Figure 5.14. The effect of spacer thickness for the alignment of AgNWs. (a) Schematics showing the different height of the meniscus between the rod and the substrate depending on the thickness of spacer. As the thickness of spacer increases, the height of meniscus increases. (b) Dark-field optical micrographs showing the alignment of AgNWs depending on the variation of spacer thickness (20-120 μm). During the bar-coating assembly, #2 bar and 10 mm s^{-1} of coating speed were used in all experiments. The scale bar is $40 \mu\text{m}$.

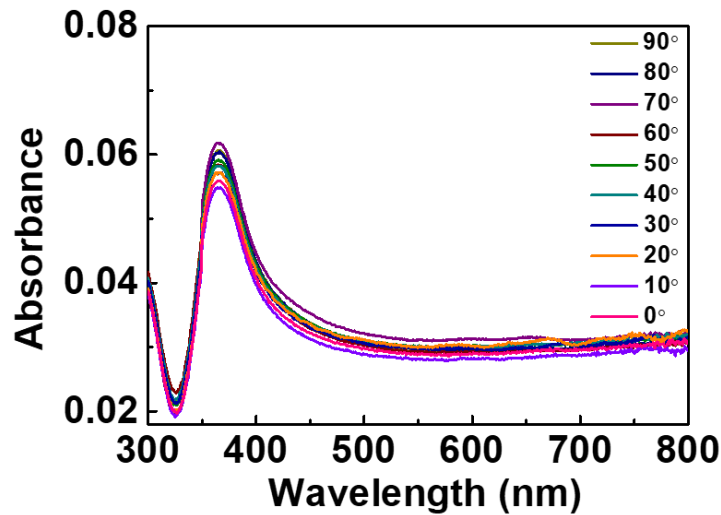


Figure 5.15. Polarized UV-Vis absorption spectra of the random AgNW networks as a function of polarization angle (θ) from 0 to 90°. As compared to aligned AgNW arrays, random AgNW networks without any anisotropic optical properties do not show any noticeable change in their absorption peaks as the polarization angle increases.

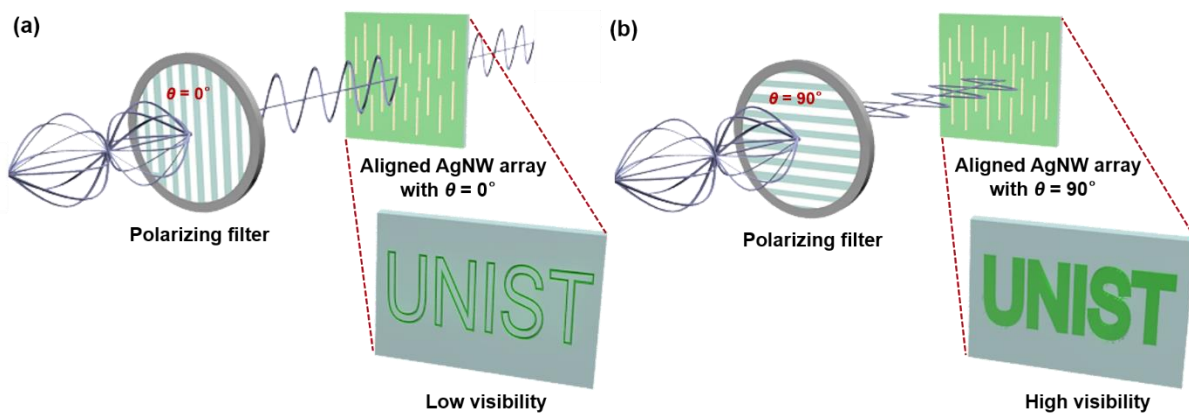


Figure 5.16. Schematics showing the polarized optical microscope modes according to the direction between the polarizing filter and the AgNW alignment direction; (a) $\theta = 0^\circ$, (b) $\theta = 90^\circ$. When the polarizing filter and the aligned AgNW array have the same vertical polarization direction ($\theta = 0^\circ$), vertically polarized light passes through the aligned AgNW film. However, when the polarizing filter and aligned AgNW array have the perpendicular polarization direction ($\theta = 90^\circ$), polarized light cannot penetrate the aligned AgNW film.

For TCE applications, aligned AgNW networks are more advantageous than random ones in terms of their higher network uniformity, lower percolation threshold, and better transparency.¹⁹⁷ We fabricated cross-aligned AgNW arrays with precisely controlled surface densities *via* a repeated multistep process, which provides highly uniform conductive networks (Figure 5.17). As seen in Figure 5.18a, cross-aligned AgNW arrays exhibit high optical transmittance (T of 87.6-97.2 % at 550 nm) and low sheet resistance (R_s of 10.4-69.7 Ω sq⁻¹) as a function of the number of cross-aligned coatings. Here, the increase in the number of coatings results in a dense and thick conducting film with lower optical transparency and higher electrical conductivity. To compare the tradeoff performance between R_s and T for the cross-aligned and random AgNW networks, a FoM for the electrical to optical conductivity ratio, defined as $T = \left[1 + \frac{1}{\Pi} \left\{ \left(\frac{Z_0}{R_s} \right) \right\}^{1/(n+1)} \right]^{-2}$, is used, where Z_0 is the impedance of free space ($Z_0 = 377 \Omega$), n is the percolation exponent describing the power law relationship between R_s and the film thickness, and Π is the percolative FoM.²⁰⁵ A high FoM value indicates low and high value of R_s and T , respectively. In addition, a low n value is preferred to obtain a high value of Π , which means the reduced NW-NW junction resistances over the thin film. In Figure 5.18b, the Π and n values can be calculated by fitting R_s and T data for cross-aligned (T of 93.5-96.5 % at 550 nm with R_s of 18.8-42.3 Ω sq⁻¹) and random (T of 88.2-97.0 % at 550 nm with R_s of 15.9-88.62 Ω sq⁻¹) AgNW networks. The Π value of the cross-aligned AgNW arrays (FoM = 479) is much higher than that of random AgNW networks (FoM = 254), which confirms the superior optical and electrical properties of the cross-aligned AgNW arrays. Meanwhile, the lower n value of the cross-aligned AgNW arrays ($n = 0.12$) than that of random AgNW networks ($n = 0.14$) confirms the high uniformity and reduced interwire junction resistances of the cross-aligned AgNW arrays. The higher Π and lower n values of the cross-aligned AgNW arrays indicate that the cross-aligned AgNW TCE is better suited for overcoming the issue of the tradeoff between the electrical conductivity and optical transparency of conventional random AgNW networks.

Figure 5.18c compares the R_s to T performance of various AgNW based TCEs. The R_s - T performance of the cross-aligned AgNW arrays (18.8-42.3 Ω sq⁻¹ at 88.2-97.0 %) surpasses those of other random AgNW networks. The best R_s - T performance of the cross-aligned AgNW arrays ($R_s = 21.0 \Omega$ sq⁻¹, $T = 95.0$ %) is superior to that of the previously reported random AgNW networks, such as purified AgNWs (32.0-130 Ω sq⁻¹ at 95.1-99.1 %),²⁰⁶ spray-coated long AgNWs (20.0 Ω sq⁻¹ at 92.1 %),⁴⁴ graphene-AgNWs hybrids (33.0 Ω sq⁻¹ at 94.0 %),⁹⁹ dry-transferred AgNWs (10.0 Ω sq⁻¹ at 85.0 %),⁸⁴ graphene oxide-soldered AgNWs (12.0-26.0 Ω sq⁻¹ at 86.0-92.1 %),³⁷ polymer-soldered AgNWs (25.0 Ω sq⁻¹ at 85.0 %),⁶⁴ multilength scaled AgNWs (28.0 Ω sq⁻¹ at 91.8 %),²⁰⁷ very long AgNWs (9-69 Ω sq⁻¹ at 89-95 %),⁸⁵ and hybrid of meso- and nanoscale metal NWs (0.36 Ω sq⁻¹ at 92 %).⁴⁸ In addition, our bar-coating assembly can produce large-area ($> 20 \times 20$ cm²) cross-aligned AgNW arrays with a highly uniform spatial distribution of the AgNW networks without any additives, transferring or lithography

processes, which cannot be achievable by most of the previously reported random AgNW networks.⁹⁹

²⁰⁷ To verify the spatial uniformity over such a large area, we fabricate TCEs based on cross-aligned AgNW arrays on large-area ($20 \times 20 \text{ cm}^2$) flexible substrates (Figure 5.18d). The R_s and T values of each pixel in a 4×4 array are then investigated. Figure 5.18e,f show mapping images of the R_s distribution of cross-aligned and random AgNW networks with similar average R_s values. The cross-aligned AgNW arrays show a uniform distribution of R_s with a small standard deviation of 1.2, which compares favorably with that of the random networks having large standard deviation of 6.5 (Figure 5.18e,f). Likewise, the T distribution of the cross-aligned AgNW arrays show a better uniformity across the entire area, having a standard deviation of 0.3, which is small compared to that of the random AgNW network, which has a standard deviation of 0.8 (Figure 5.18g,h). These large-scale uniformities of cross-aligned AgNW arrays can be attributed to the ordered surface geometry of the conductive AgNW network as well as the uniform NW-NW junctions that didn't exist in randomly-entangled NWs. We also note that the cross-aligned sizable AgNW arrays exhibit a higher optical transparency (95.9 %) than that of the random AgNW arrays (91.9 %) for similar average R_s values. Besides, the cross-aligned AgNW networks possess an outstanding mechanical stability. Those films show a negligible variation in resistance under the bending radius as small as 1.5 mm (Figure 5.19a). In addition, there is no significant change in resistance even after repetitive bending of 1000 times at 1.5 mm of bending radius (Figure 5.19b). Furthermore, the cross-aligned AgNW arrays can be fabricated in several minutes, which is better than the previous slow and complicated processes requiring additional transfer process and post-treatment. All of these characteristics are critical factors for practical applications of AgNW based TCEs in large-area optoelectronic devices.

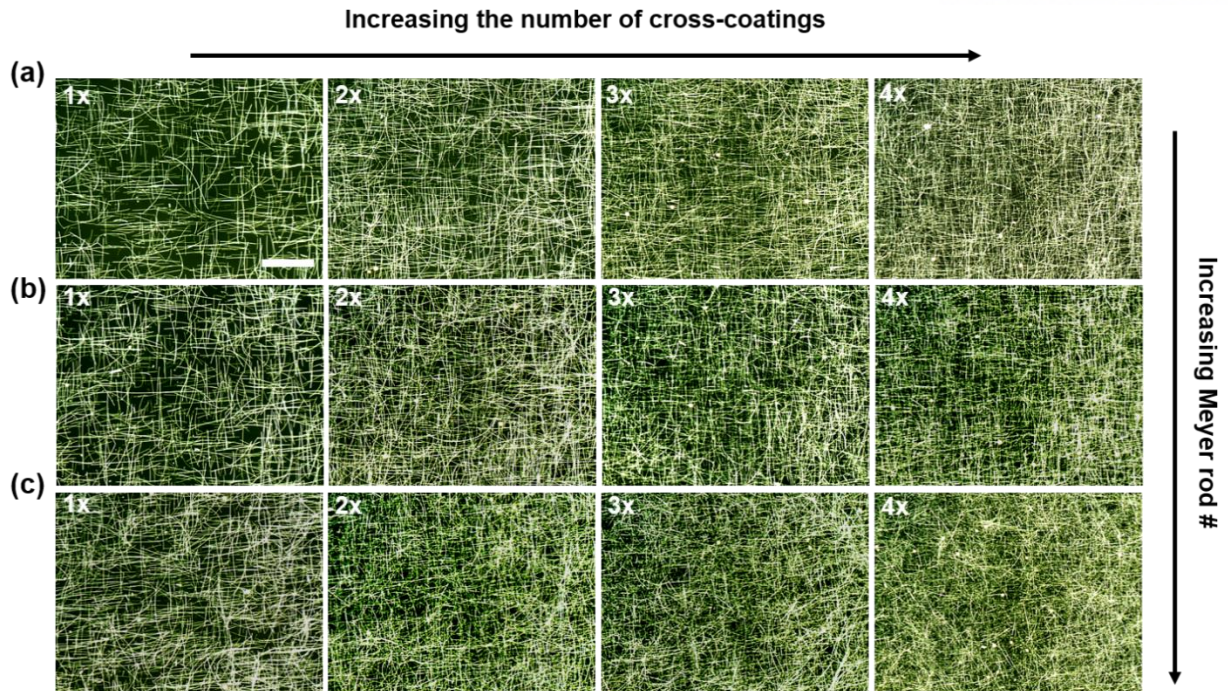


Figure 5.17. Dark-field optical micrographs of cross-aligned AgNW arrays by varying the number of cross-coatings for bar-coating conditions of (a) #2 bar and 3 μl , (b) #3 bar and 4 μl , and (c) #6 bar and 8 μl . All of the cross-aligned AgNW arrays were fabricated at the coating speed of 10 mm s^{-1} . The scale bar is 40 μm .

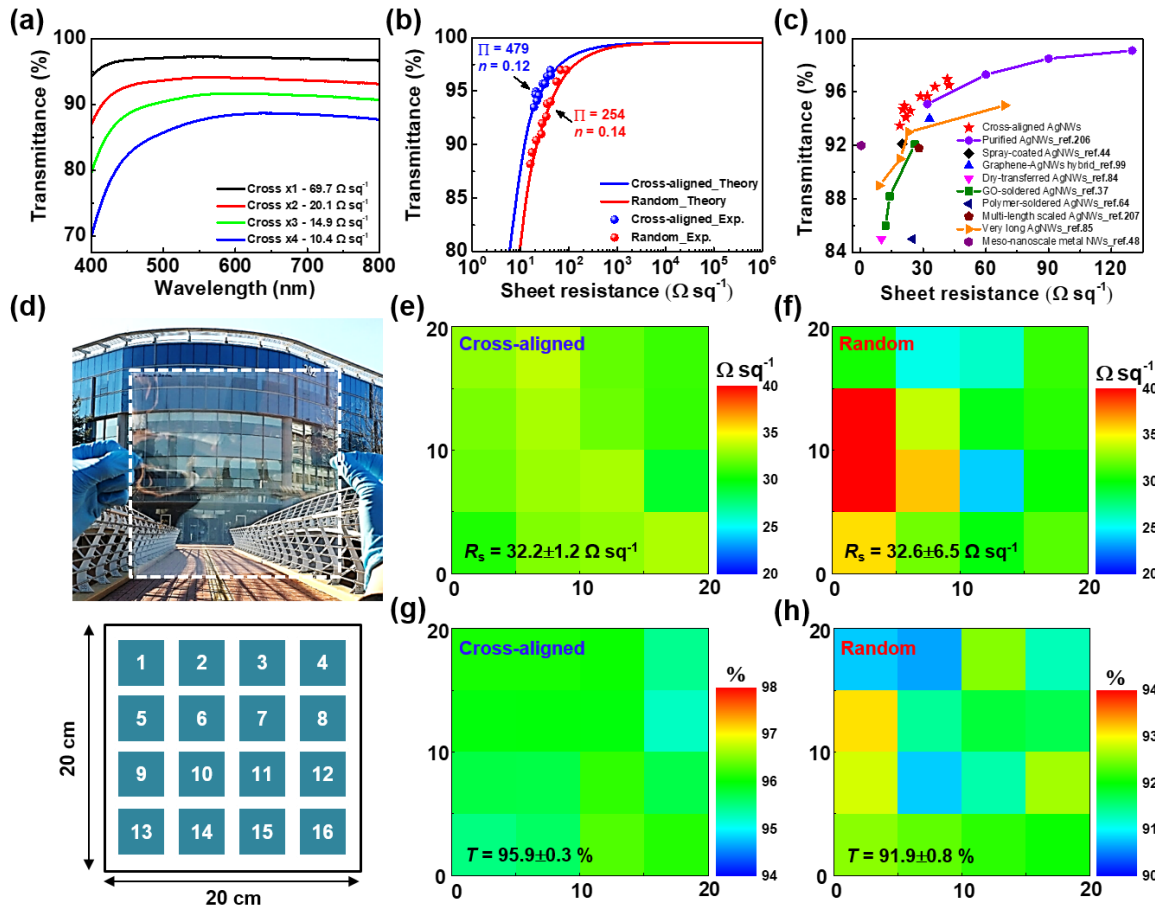


Figure 5.18. Optical and electrical performance of the large-area transparent conductive electrodes (TCEs) using the cross-aligned AgNW networks. (a) UV-vis spectra and corresponding sheet resistance, R_s , of cross-aligned AgNW arrays with different numbers of cross-coatings. The substrate was used as a reference in all UV-vis experiments. (b) R_s versus optical transmittance, T , at 550 nm for the cross-aligned and random AgNW networks fitted by percolative regime. (c) R_s versus T performance of various AgNW TCEs. (d) A photograph of large-scale ($20 \times 20 \text{ cm}^2$) TCE coated with uninform cross-aligned AgNW arrays (top), and schematic showing its 4×4 pixels for analysis (bottom). (e) 4×4 pixels mapping images showing the R_s distribution of cross-aligned and (f) random AgNW networks over a large substrate area ($20 \times 20 \text{ cm}^2$). The average R_s was set so as to be similar in both films. (g) 4×4 pixels mapping images showing the T distribution of cross-aligned and (h) random AgNW networks over a large substrate area ($20 \times 20 \text{ cm}^2$).

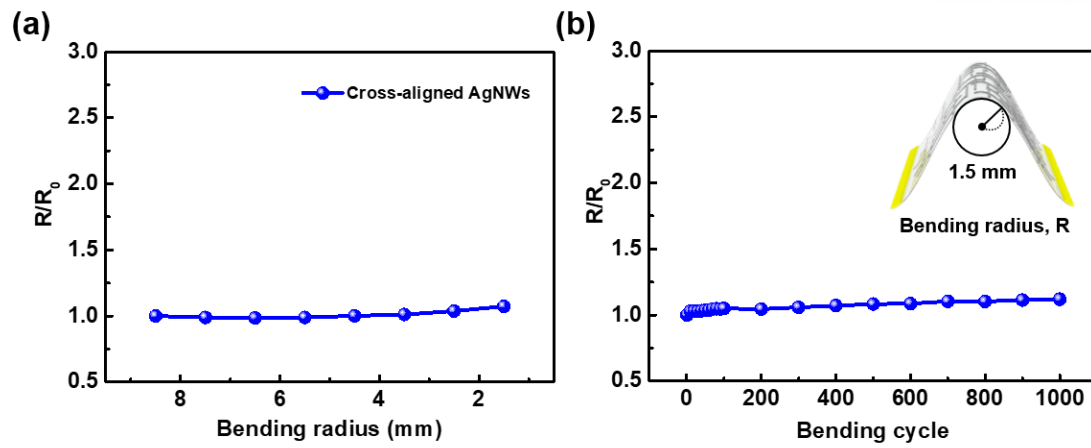


Figure 5.19. Mechanical stability of cross-aligned AgNW based TCEs on PET substrate. (a) Variation in resistance of cross-aligned AgNW TCEs as a function of bending radius. (b) Resistance change of cross-aligned AgNW TCEs during 1000 bending cycles at the bending radius of 1.5 mm.

For the proof of concept application of large-area TCEs, we demonstrated a large-area, flexible, and transparent touch screen based on a four-wire resistive-type touch sensor that uses cross-aligned AgNW TCEs as the top and bottom transparent electrodes without any protective layers or dot spacers (Figure 5.20a). Here, when the top electrode is depressed by an external force, the two resistive layers meet. When a voltage is applied across X or Y layers between X1-X2 or Y1-Y2 busbars, the other touching layer divides the applied voltage at the touch position and thus the controller circuit board captures the voltage change at the touch position along the X-Y coordinates. Figure 5.20b shows the flexible and transparent touch screen using a cross-aligned AgNW network that has an active area of $20 \times 20 \text{ cm}^2$. Figure 5.20c demonstrates the application of the large-scale touch screen for writing letters of the alphabet; we can write over the entire area of the touch screen without any disconnected lines or defects in the letters, which thereby demonstrates the outstanding touch sensitivity and uniformity of the device. Those writing performance can be attributed to the fine resolution of our touch screen. We investigate the resolution of touch screen by measuring the smallest distance between two adjacent touch lines that can be distinguished by our touch screen (Figure 5.21). The estimated resolution of touch screen is around $100 \mu\text{m}$ (Figure 5.21c), which is the smallest distance distinguishable by the touch controller board used in our study.

Note that the optical transparency of our touch screen allows for tracing and drawing underneath pictures. Figure 5.20d demonstrate the tracing of a picture of a butterfly below the transparent touch screen, where precise and continuous line drawing is possible without any defects. These results demonstrate the potential of our bar-coating assembly for fabricating cross-aligned AgNW arrays for large-area transparent electrodes that can be used in transparent and flexible touch screens. One advantage of our touch screen compared to previous ones is the optical transparency and flexibility, which enables the electronic tracing of underneath surface textures, graphics, and writings even on the curved surfaces, indicating bending-insensitive capability of our touch screens (Figure 5.22).

In addition to the tracing of touch location on the transparent touch screen, simultaneous detection of an applied force is beneficial in discriminating the pressure between gentle and hard touches on the screen during writing and tracing tasks. To create touch screens that recognize writing force as well as location, we incorporated a mechanochromic SP-PDMS composite film into the touch screen. The SP-PDMS film allows the visualization of applied force through a color change in response to the dynamic writing pressure. Spiropyran mechanophore (force-sensitive molecule) can be covalently coupled into PDMS network, so that local tension in the PDMS triggers a reversible color change in the spiropyran through a force-induced ring opening reaction,^{208, 209} that has been used previously for stress or strain sensing.²¹⁰⁻²¹² Figure 5.23a shows the schematic illustration of mechanochromic touch screens, which comprises cross-aligned AgNW TCE layers and over-coated mechanochromic SP-PDMS composite film. The mechanochromic touch screen enables the detection of location of dynamic touch that is

monitored by the resistive touch sensor; meanwhile, the intensity of force during the writing is detected by the change in color of mechanochromic force sensor, which is analyzed by the spectroradiometer (Figure 5.23b).

The applied writing force can be quantified by analyzing the intensity of visible color spectra as a function of dynamic writing force in horizontal lines that are drawn by a stylus (Figure 5.24). As can be seen in Figure 5.23c, the intensity of blue color obtained from the normalized luminance at 448 nm increases linearly with the writing force (luminance $\sim 0.37 \times F_{\text{write}}$). As seen in Figure 5.23d, the blue color intensity of the handwritten letters “FNL” gradually increases in response to increasing writing force (F_{write}) applied to a mechanochromic touch screen. This behavior can be attributed to the varying local deformation of the SP-PDMS film in response to different writing forces. Figure 5.23e shows the average intensities of blue color for handwritten letters “FNL”, which increases with the increase of dynamic writing force. Based on the linear calibration curve in Figure 5.23c, the applied forces can be determined to be from $F_1 = 4.3 \pm 0.2$ N to $F_5 = 14.9 \pm 3.4$ N. The degree of color change as a function of writing force can be further analyzed by standard colorimetric system called CIE 1931. Figure 5.23f shows the average color coordinates of letters “FNL” with different applied forces from 4.3 N to 14.9 N, where X-Y coordinates move to the deep blue region with increasing force. While the line width of writing letters in Figure 5.23d is ~ 1 mm, the resolution of dynamic writing on the SP-PDMS film can be further improved by decreasing the contact area of applied force. In our study, the line width of dynamic writing can be decreased down to ~ 79 μm by using a sharp stylus pen (Figure 5.25).

Combining the two detection mechanisms enables the simultaneous detection of location and intensity of force during the writing. When four different writing forces are applied for the handwritten letter “A”, the intensity of writing force can be discriminated by the different intensity of blue color on the mechanochromic touch screen (Figure 5.26a). At the same time, the corresponding location of writing signals of letter “A” can be precisely tracked on the monitor (Figure 5.26b). Moreover, writing touch signals and the color change can be clearly observed even under the bending state, indicating that the force-sensitive touch screen is insensitive to film bending. The real time visualization of writing force on the mechanochromic touch screen can be used to distinguish, for example, personal handwriting patterns with locally varying writing forces.²¹³ Figure 5.23g shows the spatial force mapping analysis (10×10 pixels array) of local writing force applied to the handwritten letter “A”. The locally different writing forces can be clearly observed along the letter “A”, indicating the potential application of mechanochromic touch screens for the enhanced security of personal identity based on the handwritten electronic signatures.

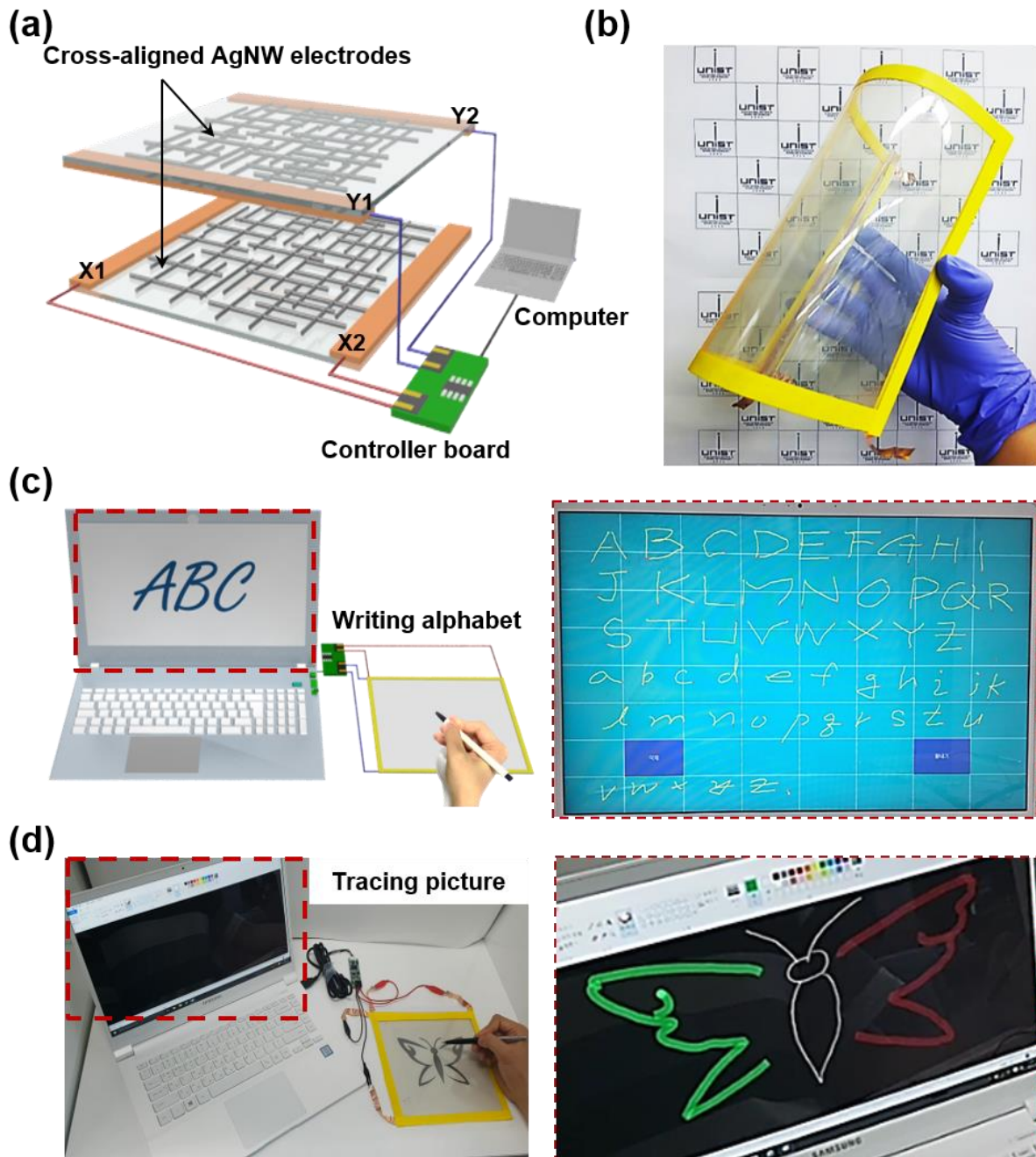


Figure 5.20. Large-scale, flexible, and transparent touch screens using cross-aligned AgNW TCEs. (a) Schematic showing the structure of the large-scale, flexible, and transparent touch screen using the cross-aligned AgNW arrays on a PET substrate connected to a laptop computer through a controller board. (b) A photograph of the large-scale, flexible, and transparent touch screen ($20 \times 20 \text{ cm}^2$) using cross-aligned AgNW TCEs. (c) Demonstration of writing alphabet letters on the transparent touch screen, which have been recorded on the computer monitor. (d) Demonstration of tracing a picture of a butterfly placed under the transparent touch screen.

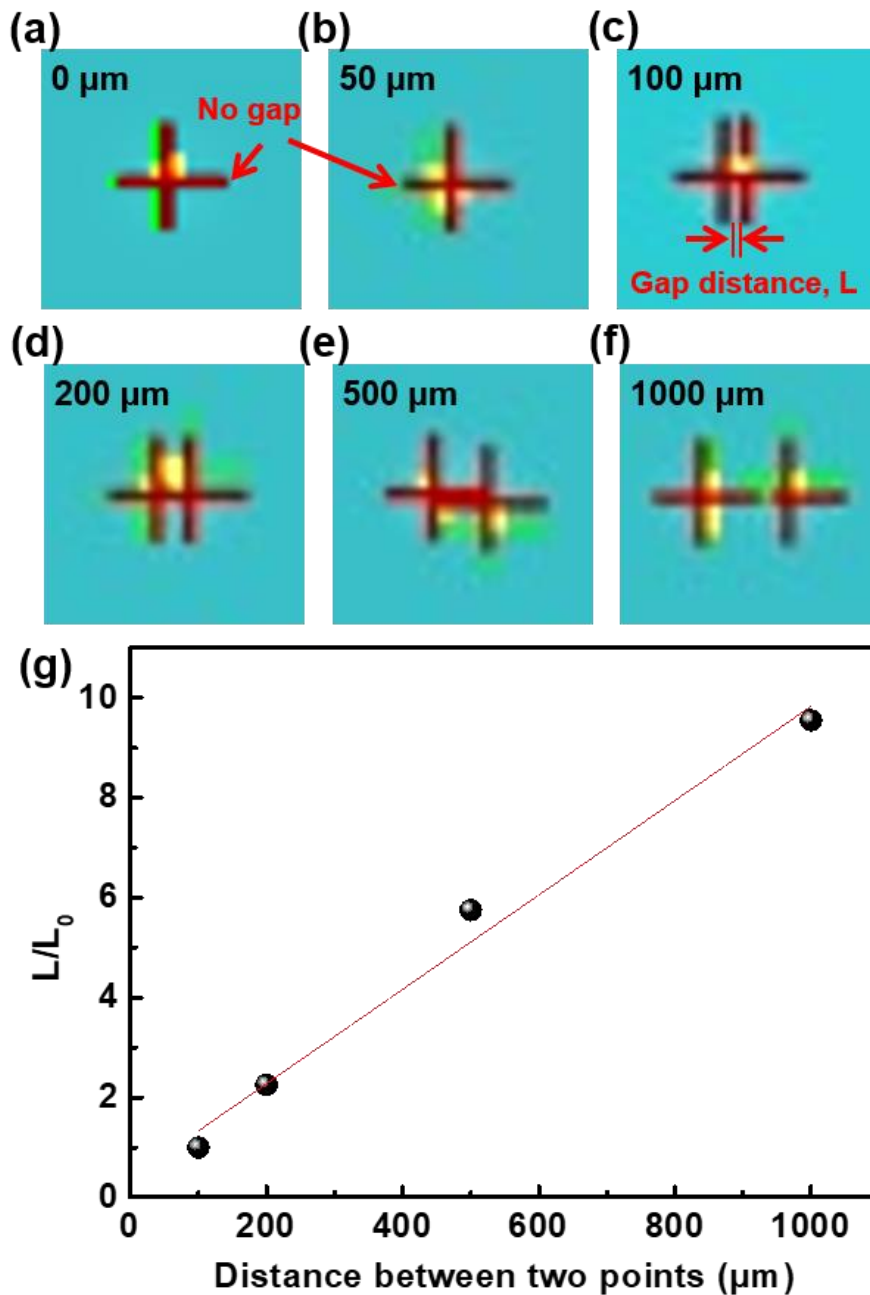


Figure 5.21. (a-f) Output images of touch signal and (g) normalized gap distance between adjacent touch signals, generated by two touch points pressed with different gap distance of (a) 0 μm, (b) 50 μm, (c) 100 μm, (d) 200 μm, (e) 500 μm, and (f) 1000 μm on touch screen based on cross-aligned AgNW TCEs. Our touch screen can detect touch location with the resolution of 100 μm, which corresponds to the resolution of touch controller board. L_0 is defined as minimum gap distance between two touch signals that can be distinguished by touch screen.

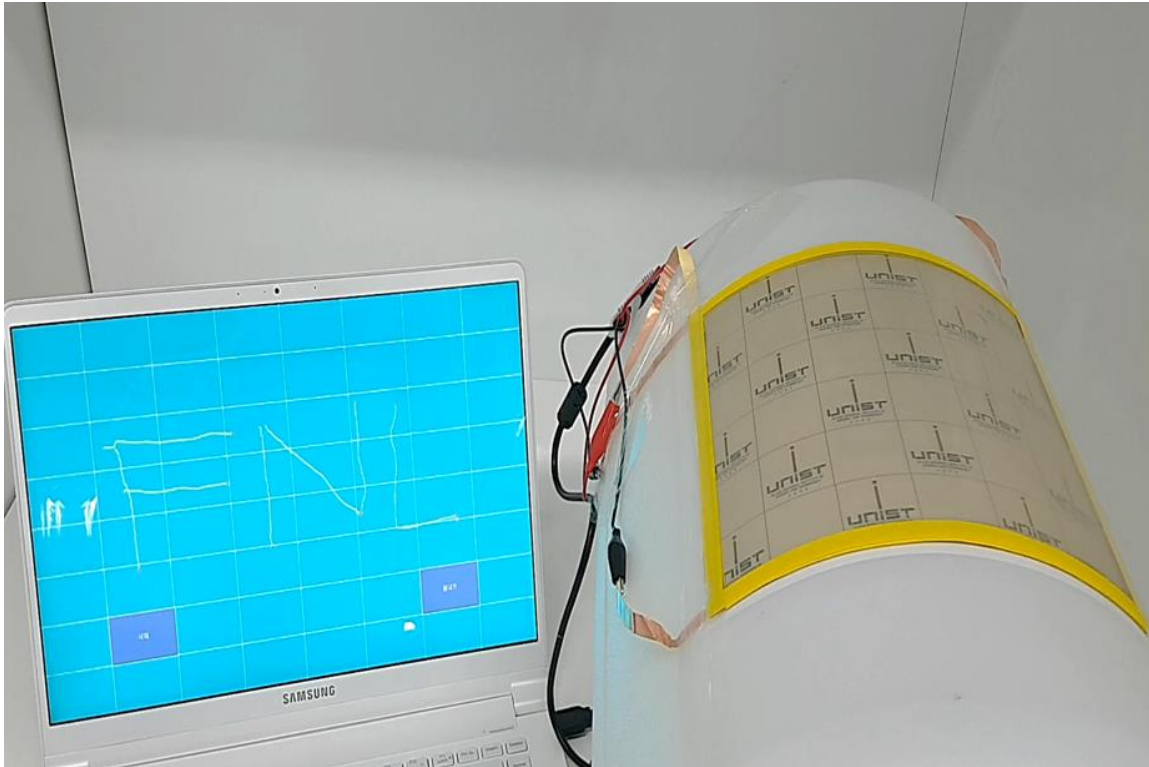


Figure 5.22. Demonstration of large scale, flexible touch screen fabricated by cross-aligned AgNW based TCEs. Handwritten letters “FNL” was precisely written on top of curved surface.

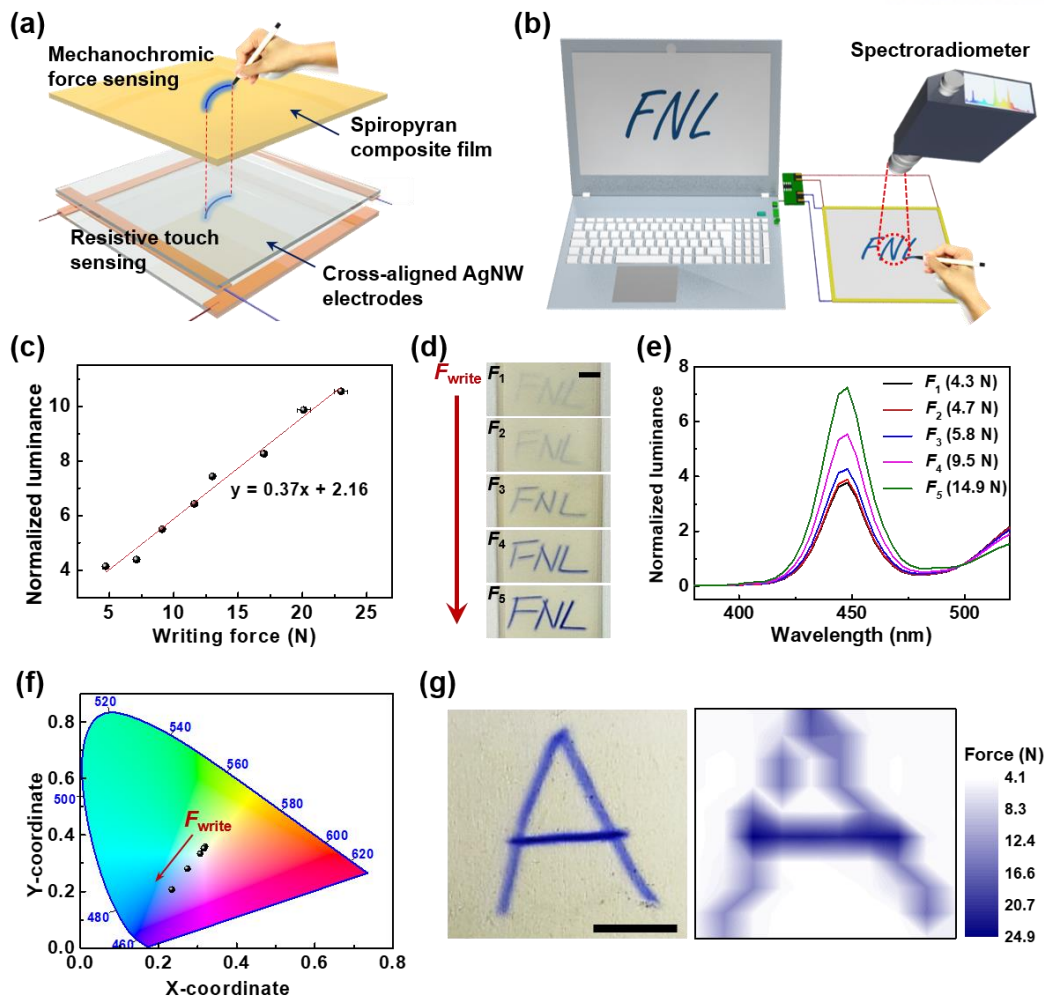


Figure 5.23. Flexible, transparent, and force-sensitive touch screens. (a) Schematic illustration of the device structure of a force-sensitive touch screen showing simultaneous force and touch sensing in response to dynamic writings. (b) Schematic illustration of the mechanochromic touch screen system with the color analysis using a spectroradiometer. (c) Normalized luminance at 448 nm wavelength as a function of the writing force. A fitted line shows a linear relationship between the normalized luminance and the writing force. (d) Photographs of mechanochromic color changes on the touch screen as a function of different dynamic writing force. The blue color intensity of the written letters “FNL” on the touch screen increases with the writing force. The scale bar is 1 cm. (e) Normalized luminance spectra of blue color letters “FNL” in visible range (380-520 nm). Based on the linear curve in Figure 5.23c, the applied forces can be determined to be from $F_1 = 4.3 \pm 0.2$ N to $F_5 = 14.9 \pm 3.4$ N. (f) Representation of the color coordinates on the CIE 1931 color space according to the different writing force. The X-Y coordinates move to the deep blue region with the increase of applied force. (g) A photograph of the written letter “A” on the mechanochromic touch screen (left) and its 10×10 pixels array of applied force mapping data showing the local force distribution (right). The scale bar is 1 cm.

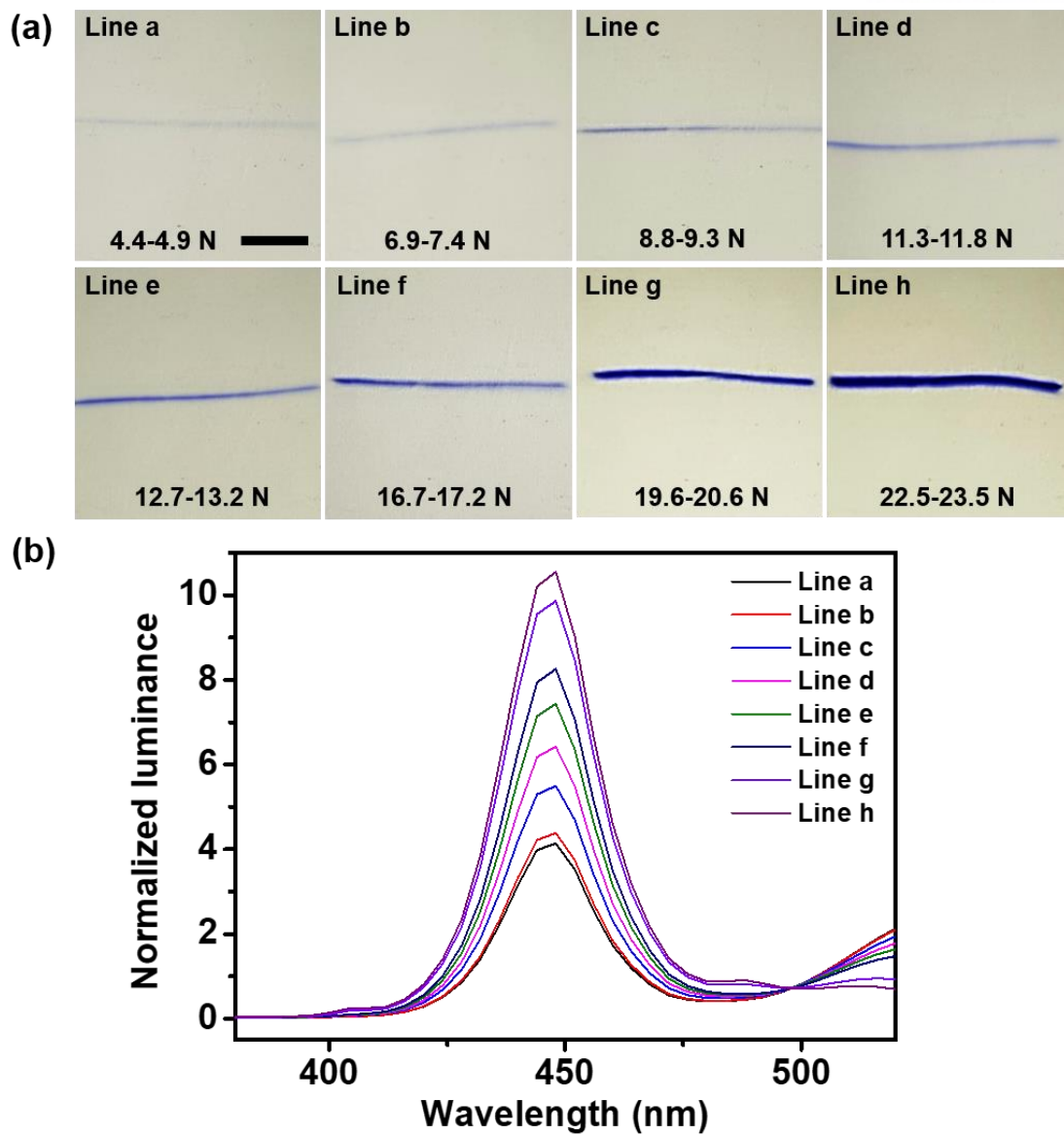


Figure 5.24. The investigation of the relationship between the color intensity and the applied writing force using a spectroradiometer. (a) The photographs of the different lines on the mechanochromic touch screen as a function of writing force and (b) its normalized luminance spectra in visible range (380-520 nm). The horizontal lines are drawn by a stylus as a function of dynamic writing force.

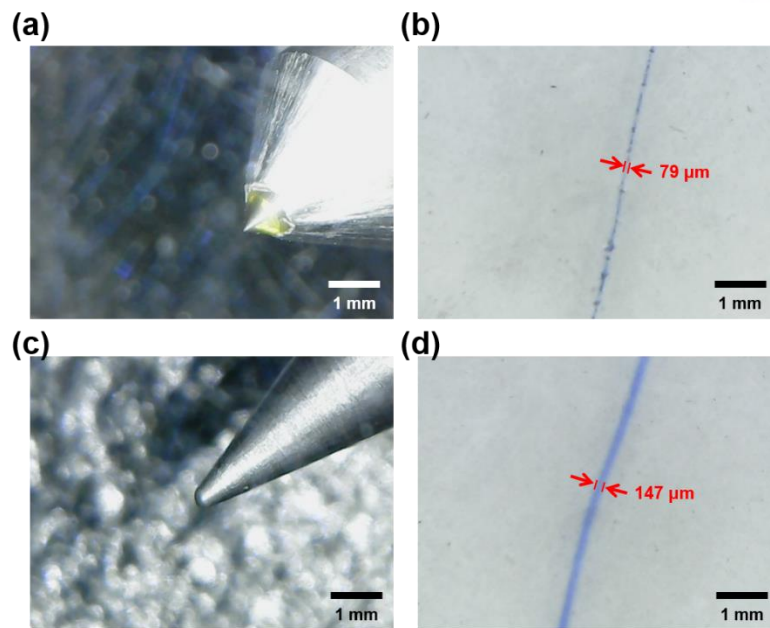


Figure 5.25. The resolution of line width drawn by using different tip size of stylus on mechanochromic SP-PDMS film. (a,b) The stylus with small size of tip can generate very thin blue line with the thickness of $\sim 79 \mu\text{m}$. (c,d) Stylus with large size of tip generates blue line with the thickness of $\sim 147 \mu\text{m}$.

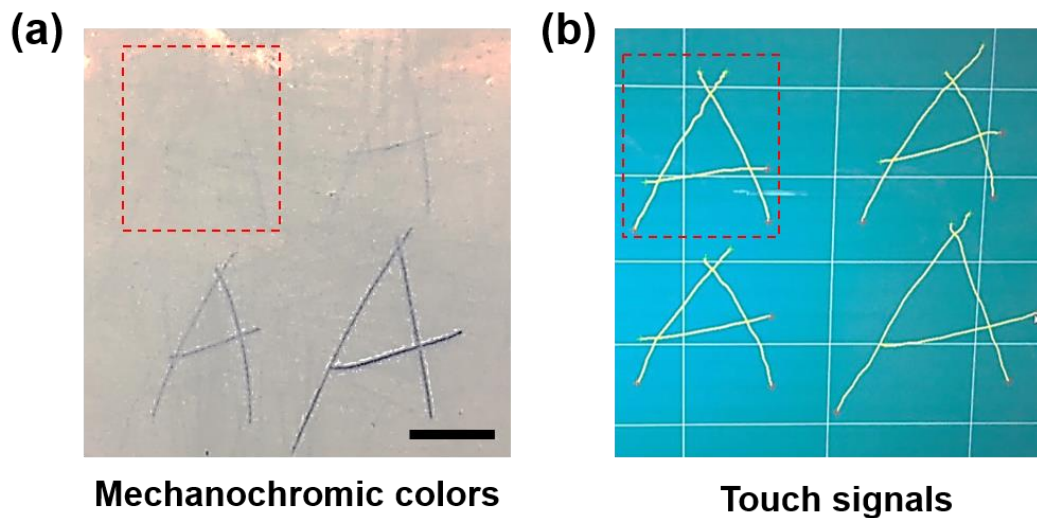


Figure 5.26. Real time monitoring images of mechanochromic colors on the touch screen (a) and its touch signals on the laptop monitor (b). The red dotted squares show the alphabet “A” written by the smallest force during the writing on the mechanochromic touch screen. The scale bar is 2 cm.

5.4 Conclusions

In conclusion, we developed a simple and efficient assembly strategy for the large-area, highly cross-aligned AgNW arrays for TCE applications through a modified bar-coating assembly. As opposed to conventional solvent-evaporation-induced assemblies, which are slow and produce nonuniform conductive networks, our modified bar-coating strategy enables fast, efficient, and uniform alignment of NWs in a large area by simply dragging the Meyer rod over AgNW solution on the target substrates. The cross-aligned AgNW arrays exhibited excellent electrical conductivity as well as optical transmittance over large area of film (R_s of $21.0 \Omega \text{ sq}^{-1}$ at 95.0 % of T over $20 \times 20 \text{ cm}^2$ area) with a FoM value of 479, which is much higher than that of the random AgNW networks (FoM = 254). For the potential applications of large-area cross-aligned AgNW transparent electrodes, we demonstrated large-scale, flexible, and transparent touch screens using resistive touch sensor based on cross-aligned AgNW electrodes, which exhibited highly uniform and precise touch sensing performance across the entire region. In addition, the combination of the force-sensitive touch screens and a mechanochromic SP-PDMS composite film has been developed to simultaneously detect human writing force and location. Our modified bar-coating assembly is not limited to AgNWs, but can be extended to align other types of metallic and semiconducting one-dimensional nanomaterials (copper, silicon, indium phosphide, *etc.*), as long as the NWs are formed in a solution state. Therefore, we anticipate that the suggested technique provides a robust and powerful platform for the controllable assembly of NWs beyond the scale of the conventional fabrication techniques, which can find diverse applications in multifunctional flexible electronic and optoelectronic devices.

Chapter 6. Transparent and conductive nano-membrane (NM) with orthogonal AgNW arrays for wearable acoustic device applications.

6.1 Introduction

Recently, various electronic devices have been developed to mimic the comprehensive capabilities of the human senses for a wide range of potential applications, such as electronic skin (E-skin) for tactile sensing,²¹⁴⁻²¹⁶ artificial basilar membranes for hearing,^{217, 218} and an artificial throat for speaking.²¹⁹ The human voice has been an important bio-signal for realizing user interfaces with the rapid growth of the “Internet of Things (IoT)” interconnecting humans and machines. In addition, acoustic hearing and speaking devices have attracted great interest as essential technologies for many potential human-machine interactive applications, such as voice security, the control of drones and robots, communication with artificial intelligence (AI), and many kinds of voice recognition system.^{220, 221} For these applications, personal wearable acoustic devices require advanced flexible, portable, and miniaturized appliances capable of detecting or producing the human voice, as well as sounds.^{219, 222-227} Previously, Fan et al. demonstrated an ultrathin, self-powered, and paper-like microphone for recording the human voice. This microphone generated a triboelectric voltage in response to sound pressure.²²³ In addition, Tao et al. developed a graphene-based artificial throat, which can function as both loudspeaker and microphone.²¹⁹ Despite the high-level of performance and functionality available from these flexible acoustic devices, they remain rigid, which prevents their intimate integration with the human skin or other electronic devices intended for a wearable device platform. Furthermore, wearable electronics are nowadays required to be ultrathin, lightweight, and transparent to offer better convenience and appearance,²²⁸ which may yield emerging technologies, such as imperceptible electronics, skin-attachable E-skin, and conformal electronics.²²⁹⁻²³⁵ Based on these concepts, highly conformal device/skin contact has become an essential feature because such devices can be directly attached to an uneven surface or even human skin, which can be characterized as a curvilinear and non-flat surface with a complex topology.²³⁶ To achieve conformal device/skin contact, various approaches have been suggested, including decreasing the substrate thickness, using bio-inspired structures, and adopting a micro-hair architecture, thus enabling the realization of a conformal interaction with the skin.²³⁵⁻²³⁷

Free-standing nano-membranes (NMs) with a nanoscale thickness of less than a few hundred nanometers can provide a powerful platform for conformal electronics that offers many features such as lightness, excellent flexibility, optical transparency, and conformability,^{238, 239} which are not available with bulk materials. Graphene-based conformal devices formed on ultrathin polymer NM substrates have been developed for skin-attachable devices.²³⁵ In addition, conformal tactile sensors fabricated by

forming MoS₂ semiconductors on NM substrates have demonstrated good optical transparency and mechanical flexibility for high sensitivity E-skin applications.²³⁴ Although such NM-based electronics are characterized by an extremely low bending stiffness, making them capable of achieving conformal contact with an uneven surface, the mechanical properties of such polymeric NMs are still limited by their low fracture toughness, which can result in mechanical failures, such as cracks or voids caused by the application of an externally applied strain.

Hybrid NMs differ from polymeric NMs, in that the electrical, optical, and mechanical properties of the NMs are determined by the type of the loading material, which can be metal nanoparticles (NPs), metal nanowires (NWs), carbon nanotubes (CNTs), or graphene.^{238, 240-242} In this respect, silver nanowire (AgNW)/polymer composite NMs are attractive candidates because they possess excellent mechanical and electrical/optical properties due to the large aspect ratio of the AgNWs used as reinforcement.^{240, 243} In addition, AgNW networks can be easily prepared by cost-effective and large-scale solution-based processes, such as spin-coating, drop-casting, rod-coating, and spray-coating.^{56, 70, 244} A few studies have addressed the mechanical properties of free-standing AgNW/polymer composite NMs formed using a layer-by-layer (LbL) assembly technique.^{240, 245} Gunawidjaja et al. investigated the mechanical properties of unidirectionally oriented AgNW embedded in polymeric NMs, which results in a significant enhancement of the mechanical strength along the NW orientation²⁴⁰. However, the scalability and fabrication process are not suitable for commercial applications. Furthermore, to the best of our knowledge, there have been no attempts to exploit hybrid NMs with an AgNW network to fabricate NM-based wearable electronic devices.

Herein, we introduce ultrathin, conductive, and transparent hybrid NMs that can be applied to the fabrication of skin-attachable NM loudspeakers and microphones, which would be unobtrusive in appearance due to their excellent transparency and conformal contact capability. Our hybrid NMs consist of an orthogonal AgNW array embedded in a polymer matrix, which substantially enhances the electrical and mechanical properties of ultrathin polymer NMs without any significant loss in the optical transparency due to the orthogonal array structure.

6.2 Experimental Details

Sample preparation. Si substrates were cleaned with isopropyl alcohol and D. I. water using ultrasonication for 5 min, respectively. ZnO films were deposited on Si substrates by a RF sputtering process to act as a sacrificial layer. The ZnO layer was treated with O₂ plasma for 5 min to produce the surface wettability and hydrophilicity. Poly-L-lysine (PLL) with amine functional groups was applied to the ZnO films by spin-coating at 4000 rpm for 60 s. Orthogonal AgNW arrays were fabricated on the PLL-treated ZnO films by using a modified bar-coating technique, in which AgNW ink (Nanopyxis Corp.) containing 0.15 wt.% AgNWs in ethanol with an average length of 20 μm and a diameter of 35 nm was used. Parylene-C films were deposited by a CVD method using a parylene coater (Alpha plus Corp.) on the orthogonal AgNW array to fabricate the hybrid NMs. The as-fabricated hybrid NMs on the ZnO film/Si substrate were placed in an etchant solution (citric acid 10 wt.% dispersed in D. I. water) to remove the ZnO sacrificial layer, which enables the production of free-standing hybrid NMs. The hybrid NM loudspeaker was fabricated by connecting two Cu wires and pasting liquid metal (Eutectic Gallium-Indium) to the two edges of hybrid NM. For the fabrication of microstructure-patterned PDMS film, PDMS films were prepared by mixing silicone elastomer base (Sylgard 184, Dow Corning) and a curing agent in the ratio of 10:1. The well-mixed liquid PDMS prepolymer was stored in a vacuum desiccator for 30 min to eliminate air bubbles. Subsequently, the liquid PDMS prepolymer was poured onto Si micromolds with different micropatterns (i. e. line, pyramid, pillar, and dome) and thermally annealed at 90°C for 3 hours.

Characterization. The surface morphology of orthogonal AgNW array was examined by an optical microscope (PSM-1000, Olympus). The sheet resistance of the orthogonal AgNW array was measured using a four-point probe method (Keithley 2400). The optical transmittance in the visible range was determined using UV-vis spectroscopy (JASCO 620). The total thickness of the NMs was measured by using atomic force microscopy (DI-3100, Veeco). The applied AC voltage was generated by a function generator (AFG 3011C, Tektronix). The surface temperature of hybrid NM under the application of AC voltage was monitored by an IR camera (Therm-App TH, Therm-App). A dynamic signal analyzer (National Instruments Corp.), integrated with a commercial microphone (40PH, G.R.A.S.) was used to collect the sound emitted by the loudspeaker and analyze the SPL and frequency. The output voltage of the NM microphone was measured using an oscilloscope (DPO 2022B, Tektronix). The adhesion force of micropatterned PDMS films was measured by a texture analyzer (TXA, YEONJIN S-Tech). The voice-based security system was built by using LabVIEW software with the analysis of FFT.

6.3 Results and Discussion

Ultrathin, transparent, and conductive AgNW nano-membranes. Figure 6.1a is a schematic of the fabrication procedure for transparent and conductive hybrid NMs using orthogonal AgNW arrays as the nano-reinforcement, as well as a polymer matrix. Zinc oxide (ZnO) films (thickness: ~200 nm) deposited on silicon (Si) substrates are prepared as a sacrificial layer, such that the NMs can be released from the Si substrate after the fabrication process. Here, ZnO films were chosen to ensure the alignment of AgNW arrays, in which the sacrificial films should not be dissolved in both deionized (D. I.) water and ethanol solvent. The orthogonal AgNW arrays were fabricated onto the ZnO layer by using a solution-based bar-coating assembly technique. Subsequently, parylene-C films are deposited on the orthogonal AgNW arrays by a chemical vapor deposition (CVD) method to form a polymer matrix of nanometer thickness. This material was chosen because of its good bio-compatibility and chemical stability.²⁴⁶ The as-fabricated hybrid NMs on Si substrates were placed in an etchant solution (citric acid 10 wt.% dispersed in D. I. water) to dissolve the ZnO layer and release the hybrid NMs. Figure 6.1b shows a hybrid NM suspended on the surface of the etchant solution. Here, suspended hybrid NMs can be easily transferred without any damage by using anodic aluminum oxide (AAO) templates as a carrier, due to their low friction originated from the nanoporous surface structure (Figure 6.2). Figure 6.1c shows dark-field optical micrographs of an orthogonal AgNW array produced by the bar-coating process. The fast Fourier transform (FFT) image in the inset indicates that the geometry clearly exhibits a cross configuration. The orthogonal AgNW arrays are tightly embedded in the polymer matrix, giving a total thickness of 100 nm, as shown in both the cross-sectional scanning electron microscopy (SEM) and atomic force microscopy (Fig. 6.1d and 6.3).

The optical and electrical properties of the hybrid NMs are determined from the density of the orthogonal AgNW array produced via a multi-step assembly process, in which the density of orthogonal AgNW arrays was controlled by varying the number of coatings (Figure 6.4). For 3 times of multi-step coatings, the pure orthogonal AgNW array shows a high transmittance of 97.4% at the wavelength of 550 nm and a low sheet resistance of 47.4 Ω /sq (Figure 6.4). The pure polymer NM exhibits a high transmittance of 98.2% at the same wavelength. In particular, the hybrid NMs composed of orthogonal AgNW arrays embedded in polymer matrix exhibit an excellent transmittance of 93.1% at wavelength of 550 nm without any significant optical loss, which is comparable to those of other conventional transparent substrates such as polyethylene terephthalate (PET) (92.9%) and glass (93.5%) (Figure 6.1e). Our hybrid NMs differ from other types of hybrid NMs integrated with nanomaterials, such as NPs, NWs, CNTs, and graphene,^{238, 240-242} in that the orthogonal AgNW arrays provide not only excellent electrical conductivity and optical transparency but also a significant improvement to the overall mechanical properties of the polymer matrix due to the effective interfacial interaction between the AgNW and the polymer matrix, resulting in efficient load transfer within the polymer matrix.^{247, 248}

Consequently, hybrid NMs suspended on the water surface maintain their original shape without any damage, such as cracking or fracturing when struck with a glass rod, or when lifted and lowered with a plastic pipette (Figure 6.1f). Furthermore, our transparent and free-standing hybrid NMs can be transferred on any three-dimensional (3D) surface with a curvilinear and complex morphology due to the low film thickness, which enables to be an imperceptible in appearance (Figure 6.1g-i). Note that hybrid NMs, placed on the back of a person's hand, maintain their electrical conductivity without breaking when subjected to a compression or stretching force.

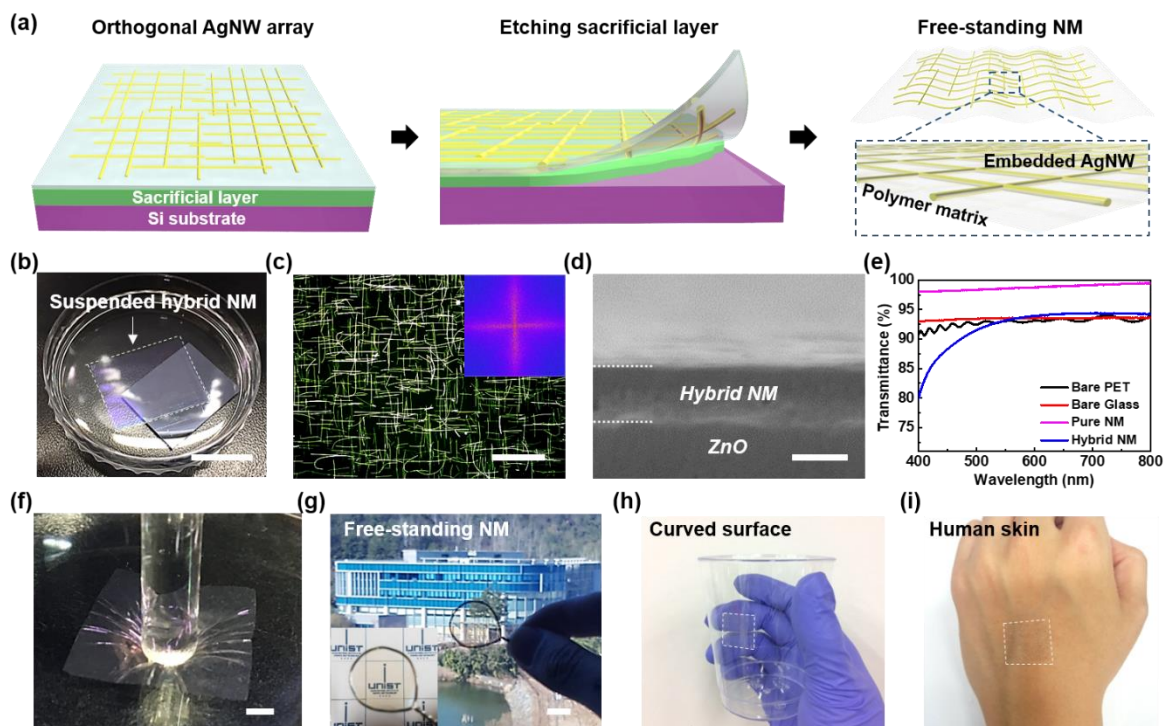


Figure 6.1. Fabrication of free-standing hybrid NMs with orthogonal AgNW array. (a) Schematic of fabrication procedure for free-standing hybrid NMs with orthogonal AgNW array embedded in polymer matrix. (b) Free-standing AgNW composite NMs floating on a surface of water. The scale bar indicates 1 cm. (c) Dark-field optical microscope image of orthogonal AgNW arrays. The inset shows a fast Fourier transform (FFT) image of the optical micrograph, corresponding to its surface geometric structure. The scale bar indicates 40 μm . (d) Cross-sectional SEM image of hybrid NM as-fabricated on a ZnO/Si substrate. The scale bar indicates 100 nm. (e) Optical transmittance of polymer NMs, hybrid NM, bare PET, and bare glass in visible range of 400-800 nm. The glass is used as a reference. (f) Photograph of hybrid NM on surface of water under compressive force applied by a glass rod. The scale bar indicates 3 mm. (g) Free-standing hybrid NM supported by a wire loop. Inset shows the high transparency of the hybrid NM. The scale bar indicates 1 cm. (h) Hybrid NMs transferred onto curvilinear surface and (i) onto human skin.

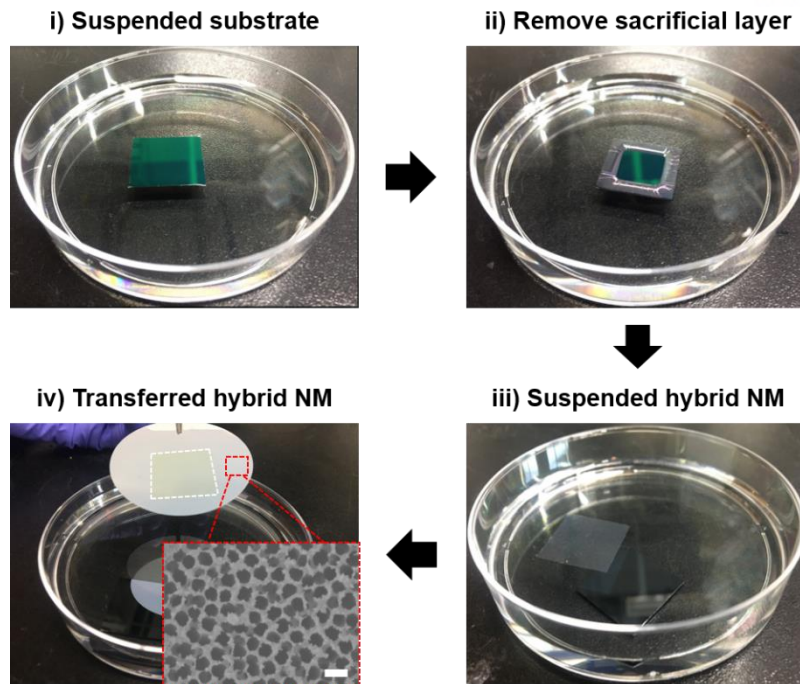


Figure 6.2. Fabrication of free-standing hybrid NM with orthogonal AgNW array by removing the sacrificial layer.

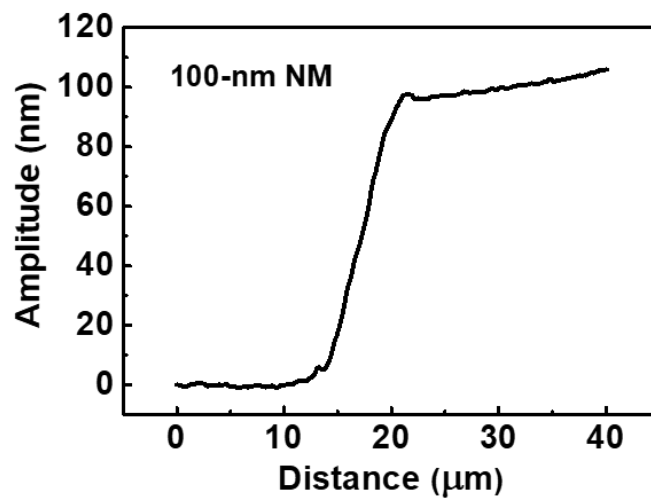


Figure 6.3. Total thickness of hybrid NMs measured by atomic force microscopy.

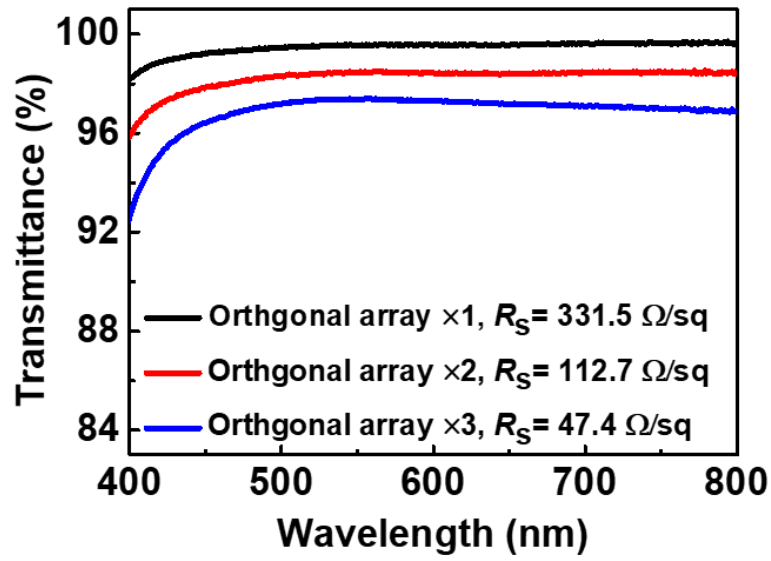


Figure 6.4. Transmittance in visible range of 400–800 nm and corresponding sheet resistance, R_s , of the orthogonal AgNW array with different numbers of orthogonal coatings.

Conformal contact capabilities of skin-attachable hybrid NMs. To quantitatively evaluate the conformal contact capabilities of hybrid NMs, we calculated the bending stiffness (EI) of hybrid NMs. For the calculation of bending stiffness of hybrid nanomembranes, a representative cross-sectional geometry of the thin film is illustrated in Figure 6.5. In this structure, there are n AgNWs with a radius of r and Young's modulus of 83 GPa, which were wrapped by a parylene film with the size of $b \times h$ and Young's modulus of 3.2 GPa. The distance between the neutral axis and bottom of the thin film is

$$y_0 = \frac{h}{2} * \frac{1 + \frac{2h' + 2r}{h} \left(\frac{E_{Ag}}{E_{Pa}} - 1 \right) n\pi r^2 / bh}{1 + \left(\frac{E_{Ag}}{E_{Pa}} - 1 \right) n\pi r^2 / bh} \quad (1)$$

where y_0 is the distance between the neutral axis and bottom of the thin film, h is the thickness of film, h' is the distance between bottom of AgNWs and thin film, r is the radius of AgNWs, b is the width of parylene film, and E_{Ag} and E_{Pa} are the Young's modulus of silver and parylene, respectively. From the value of y_0 , we can calculate the bending stiffness (EI) using the Eq (2) as below:

$$EI = E_{Pa}bh \left(\frac{1}{3}h^2 - hy_0 + y_0^2 \right) + (E_{Ag} - E_{Pa})n\pi r^2 \left[\frac{4}{3}r^2 + 2r(h' - y_0) + (h' - y_0)^2 \right] \quad (2)$$

As a result, hybrid NMs produced a bending stiffness of $5.51 \text{ GPa} \cdot \mu\text{m}^4$ which is comparable with previously reported values. Therefore, our hybrid NMs offer a high degree of bendability with a small bending radius of $\sim 2.2 \mu\text{m}$ due to their low bending stiffness caused by their nanoscale thickness, which facilitates the intimate contact even with 3D surfaces (Figure 6.6). Figure 6.7a is a schematic of the conformal contact property of a hybrid NM attached to human skin, the epidermis of which has a curvilinear and uneven surface with a complex topography. To prove the conformal contact capability of our NMs, we transferred hybrid NMs to the epidermis of human skin by using an AAO template as a carrier. Figure 6.7b shows a hybrid NM after being transferred to human finger, conformably contacting against fine ridges of the fingertip having a few hundred microns of surface roughness. To further investigate the conformal bendability, the hybrid NMs were transferred to polydimethylsiloxane (PDMS) that had been patterned with lines of widths of 20 and 120 μm . The transferred hybrid NMs were intimately adhered to the line-patterned PDMS surface and even along the edges of the line patterns, implying that the hybrid NMs have an excellent bendability (Figure 6.7c,d and 6.8). To show the conformal contact on the 3D surface, hybrid NMs with different film thicknesses (40, 100, and 200 nm) were transferred on micropyramid-patterned PDMS substrates (diameter of $\sim 10 \mu\text{m}$ and height of $\sim 7 \mu\text{m}$) (Figure 6.7e-g). As a result, 40 and 100 nm-thick hybrid NMs can form a conformal contact on

the surface of micropyramid-patterned PDMS with the step surface coverage (ratio of film-covered height to the total height of 3D structure) of $\sim 92\%$ and $\sim 73\%$ while 200 nm-thick hybrid NMs cannot conformably cover the surface with the lowest step surface coverage of $\sim 15\%$ (Figure 6.9).

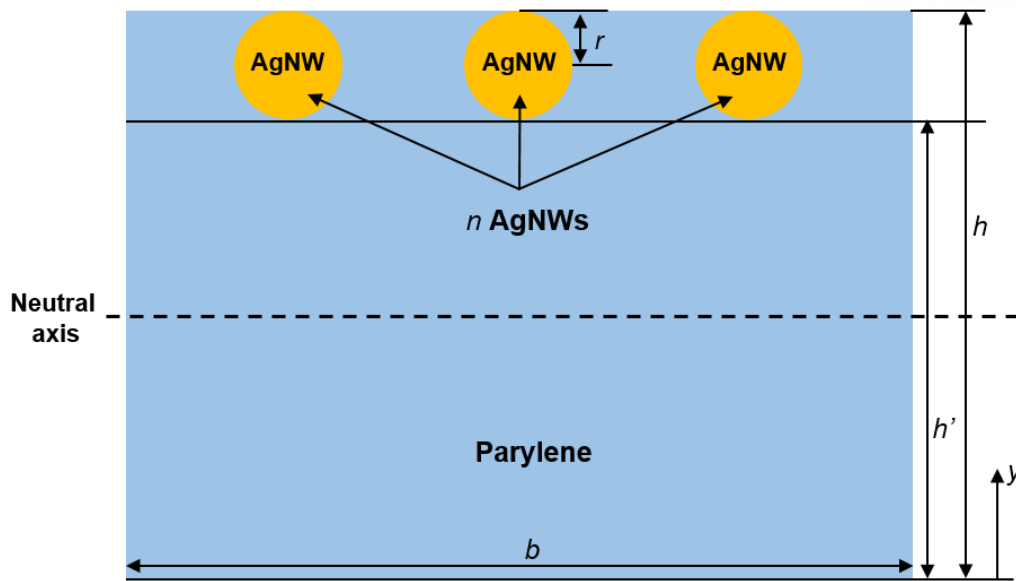


Figure 6.5. The structural design of the hybrid NM for the calculation of the bending stiffness with geometrical parameters illustrated.

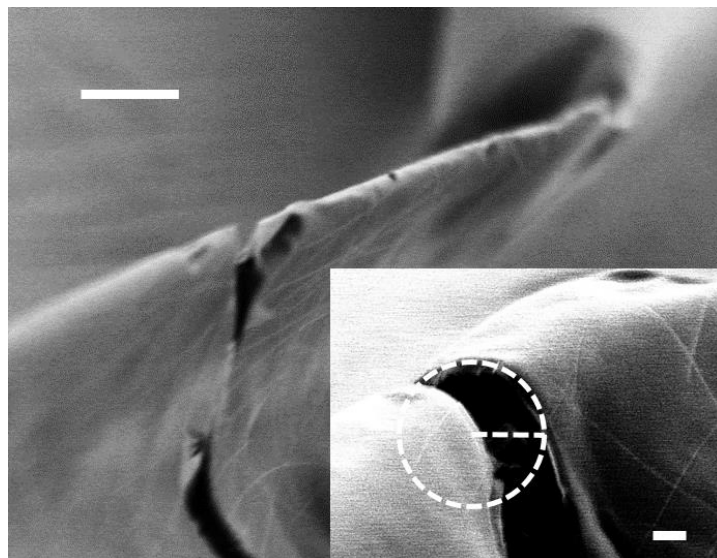


Figure 6.6. SEM images of the hybrid NM folded in half.

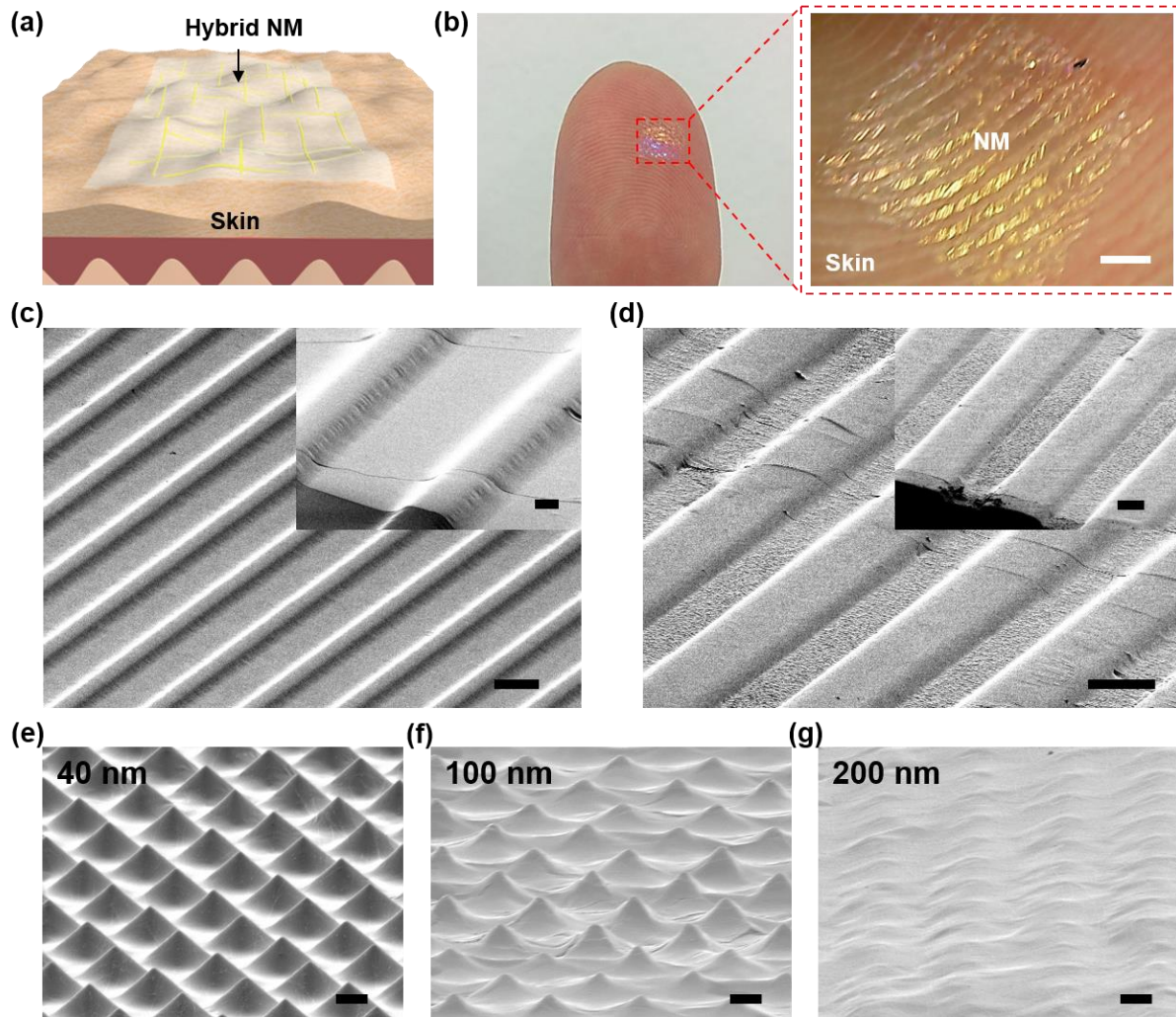


Figure 6.7. Conformal contact of AgNW composite hybrid NMs on 3D microstructures. (a) Schematic of conformal contact of NMs on the skin surface. (b) Hybrid NMs attached to a thumb. The inset shows a micrograph of a hybrid NM on the skin of a fingertip. The scale bar indicates 1 mm. (c) and (d) SEM images of the hybrid NMs transferred on line-patterned 3D PDMS microstructures with a line width of (c) 20 and (d) 120 μm . The scale bars indicate 10 and 20 μm , respectively. The insets show a magnification images with the scale bars indicating (c) 10 and (D) 50 μm . SEM images of the hybrid NMs with different thickness of (e) 40, (f) 100, and (g) 200 nm transferred on micropyramid-patterned 3D PDMS microstructures with diameter of 10 μm and height of 7 μm . All scale bars indicate 5 μm .

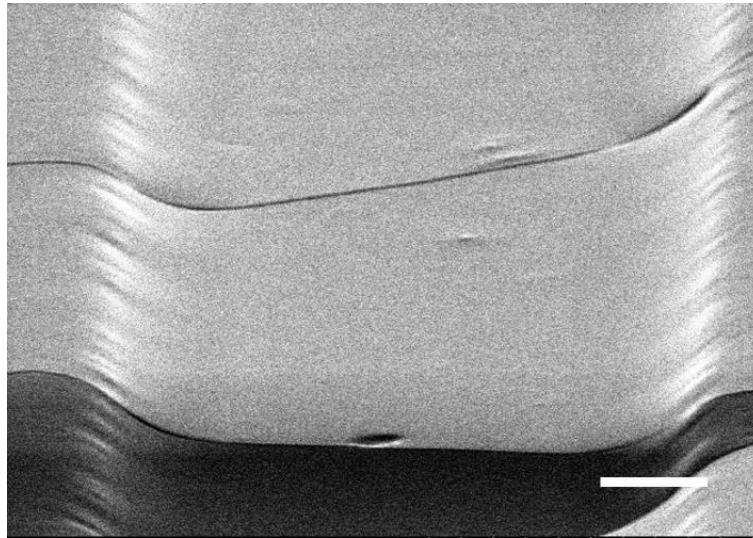


Figure 6.8. High magnitude SEM images of the hybrid NM transferred on the line-patterned PDMS with a line width of 20 μm .

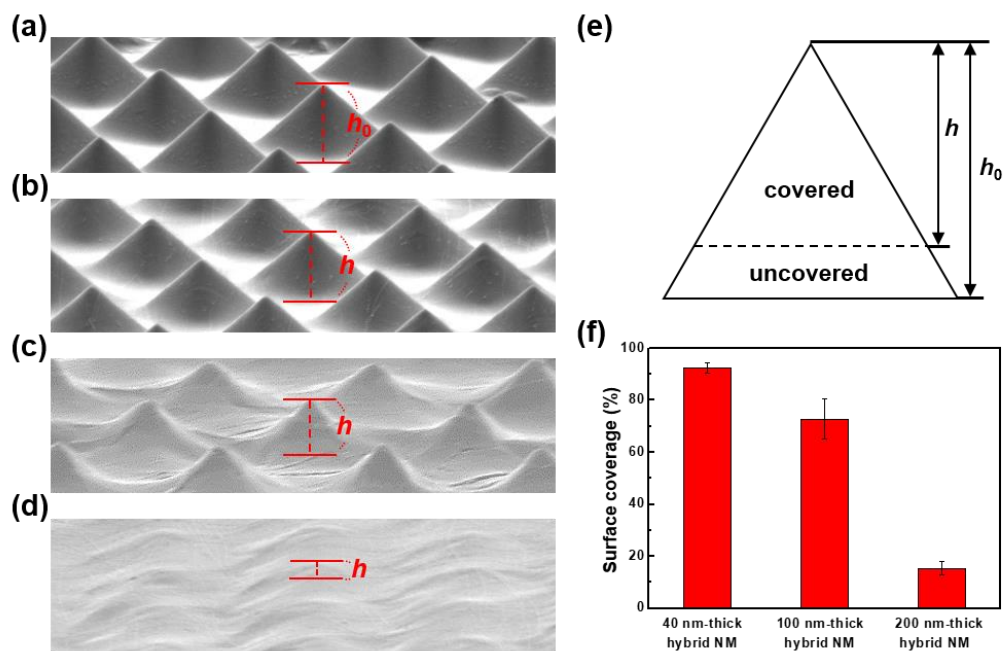


Figure 6.9. Estimated step surface coverage of the hybrid NMs with different thickness placed on a micropyramid-patterned PDMS substrate.

Mechanical properties of hybrid NMs. In general, conventional hybrid NMs containing nanomaterials exhibit enhanced mechanical properties relative to pure polymer NMs due to the reinforcing effect of fillers in the nanocomposite.²⁴⁰ To evaluate the mechanical properties of hybrid NMs, we performed a mechanical test to measure the Young's modulus (E), as obtained from wrinkles formed by the capillary force generated by placing a droplet of water in the center of a floating NM, using an optical microscope (Figure 6.10a). We observed that the number of wrinkles (N), as induced by the surface tension of the water droplet, decreased as the density of the orthogonal AgNW array increased (Figure 6.11). Hybrid NMs generate fewer wrinkles ($N < 39$) than pure polymer NMs ($N > 49$) without AgNWs. To further investigate the effect of an orthogonal AgNW array as a loading material on the Young's modulus, we plotted the number of wrinkles in the NM as a function of the combined dependence on the radius of the water droplet (a) and the thickness of the NM (h), captured by scaling $N \sim a^{1/2}h^{-3/4}$, as shown in Figure 6.12. Thus, the Young's modulus of the hybrid NMs was calculated using Eq.(3)²⁴⁹;

$$N = C_N \left[\frac{12(1-A^2)\gamma}{E} \right]^{1/4} a^{1/2} h^{-3/4} \quad (3)$$

where C_N is the numerical constant, A is the Poisson ratio, and γ is the surface tension of the droplet. We obtained $C_N=3.2$ from the experimental results with the slope of the fit line shown in figure 6.12. The Young's modulus of the hybrid NMs increases linearly with an increase in the density of the orthogonal AgNW arrays (Figure 6.10b). We also acquired the bending stiffness of hybrid NMs from the experimentally measured Young's modulus in Figure 6.10b. We compared the calculated and measured bending stiffness of hybrid NMs in Figure 6.10c. To investigate the measured bending stiffness of hybrid nanomembranes as a function of the density of orthogonal AgNW arrays, we assumed the hybrid NM as a single film and calculated the bending stiffness using the Eq (4);

$$EI = E_{Hybrid} bh \left(\frac{1}{3}h^2 - hy_0 + y_0^2 \right) \quad (4)$$

Here, E_{Hybrid} is the Young's modulus of hybrid NM with orthogonal AgNW arrays, which was experimentally obtained from the capillary wrinkling test. The measured bending stiffness (5.18 to 9.62 GPa· μm^4) increases with the density of orthogonal AgNW arrays, which is similar with the tendency of the calculated bending stiffness (5.33 to 6.88 GPa· μm^4). The slight difference in the calculated and measured values is attributed to the presence of random NW-NW junctions, which were not considered in the bending stiffness calculation in Figure 6.5.

We also performed an indentation test to measure the mechanical strength and ductility of the hybrid NMs while varying the density of the orthogonal AgNW array. In this test, free-standing hybrid NMs, placed over a hole in the supporting plate, were deformed by the application of a compressive force and then fractured when the force exceeded the maximum load that could be applied to the NMs (Figure

6.13). Figure 6.10d shows typical force vs indentation displacement ($F-d$) curves obtained by increasing the density of the orthogonal nanowire arrays. The $F-d$ curves shown in Figure 6.10d clearly show the increase in the tensile strength of the parylene as the density of the stiff nanowire array increases. Generally, adding NPs increases the stiffness and strength of a composite film. On the other hand, however, this reduces the ductility of the composite film. Contrary to this behavior, our hybrid NM exhibits a progressive increase in the indentation displacement as the AgNW density increases due to the high ductility of nano-sized AgNWs with a large aspect ratio and stretchability of AgNW networks, which is advantageous for flexible device applications.

The complete loading and unloading curves for polymer NMs and hybrid NMs are shown in Figure 6.14. For the cyclic test, a predefined indentation load was repeatedly applied on the NMs at a loading/unloading rate of 0.1 mm/sec. For an indentation load of ~ 27 mN, $F-d$ curves exhibit hysteresis behaviors for both hybrid and polymer NMs, indicating the inelastic deformation of AgNW networks and parylene polymer chains in the NMs during the indentation. The larger hysteresis of hybrid NMs than that of polymer NMs can be attributed to the larger inelastic deformation of hybrid NMs, in which the breakdown of interfacial bonding between AgNW and polymer matrix causes the larger energy dissipation than those by the polymer chain rearrangement.²⁵⁰ During the repeated loading-unloading cycles, the hysteresis gradually decreases. In particular, the hysteresis of hybrid NMs is greatly suppressed due to the permanent failure of AgNW and polymer interface. At a lower indentation load (~ 11 mN), both hybrid and polymer NMs exhibit weak hysteresis behaviors due to the elastic deformations. The maximum load and displacement that can be applied to the hybrid NMs until the failure gradually increases with the density of the orthogonal AgNW array (Figure 6.10e). The maximum load-displacement of the hybrid NMs with orthogonal AgNW arrays (load: 84.3 ± 3.03 mN, displacement: 2.85 ± 0.05 mm) is much higher compared with that of the pure polymer NMs (load: 44.8 ± 7.05 mN, displacement: 1.12 ± 0.06 mm). This could be attributed to the efficient load transfer between the orthogonal AgNW array and the polymer matrix in a nanocomposite system.²⁴⁷ These results suggest that the orthogonal AgNW array is an excellent loading material for enhancing the overall mechanical properties of a hybrid NM system.

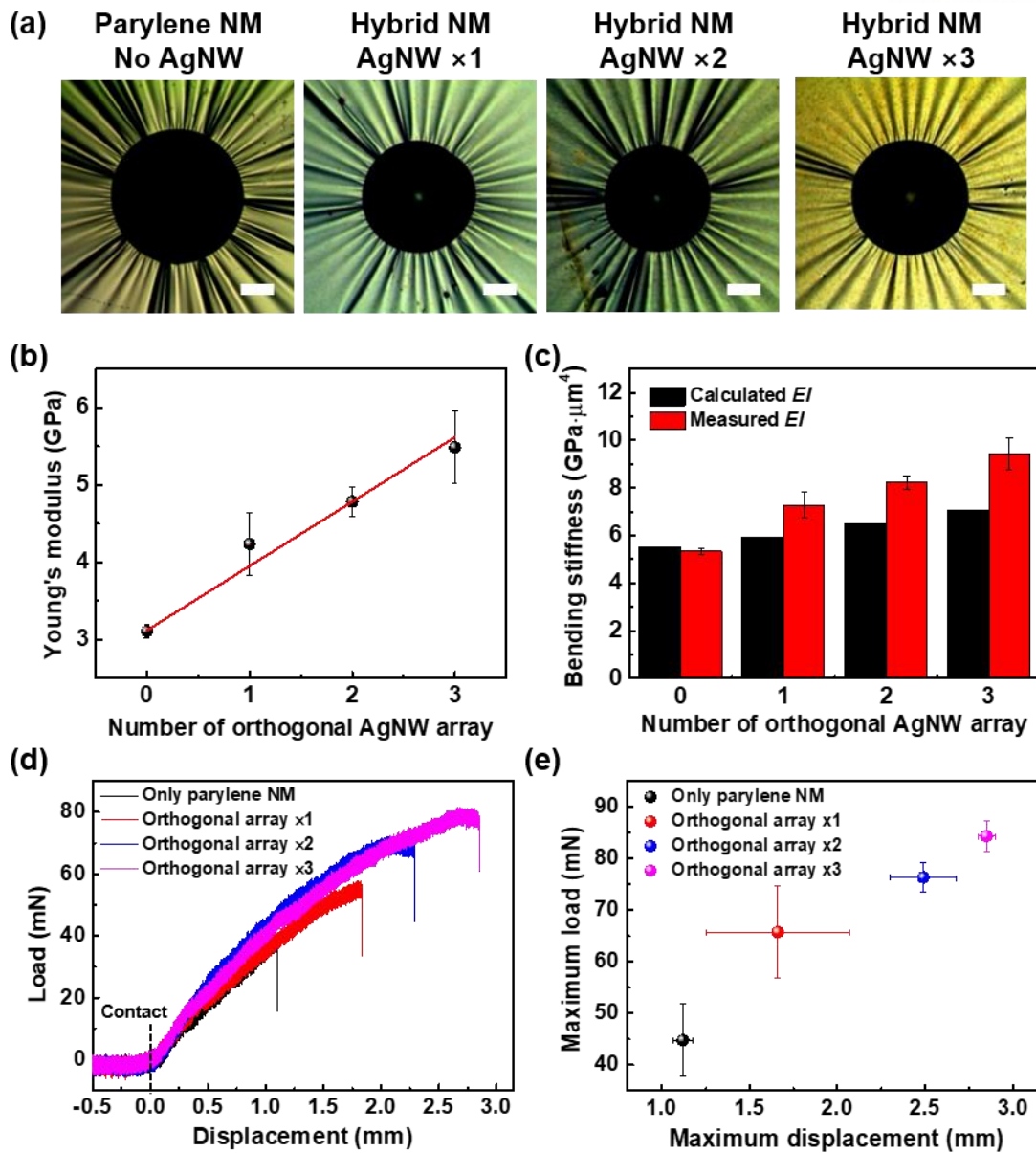


Figure 6.10. Mechanical properties of hybrid NMs with orthogonal AgNW array. (a) Free-standing hybrid NMs with different densities of orthogonal AgNW arrays floating on the water surface. NMs are wrinkled by a water droplet of radius $a \approx 0.3$ mm. The number of wrinkles decreases as the density of AgNWs increases. All scale bars indicate $200 \mu\text{m}$. (b) Young's modulus (E) of NMs as calculated from the wrinkle tests. (c) Comparison of calculated and experimental bending stiffness of hybrid NMs with different density of orthogonal AgNW arrays. Measured bending stiffness was calculated by using Young's modulus experimentally obtained from capillary wrinkling method. (d) Applied indentation load versus displacement of free-standing hybrid NMs as a function of density of orthogonal AgNW array. (e) Maximum indentation load versus displacement of hybrid NMs as a function of orthogonal AgNW arrays.

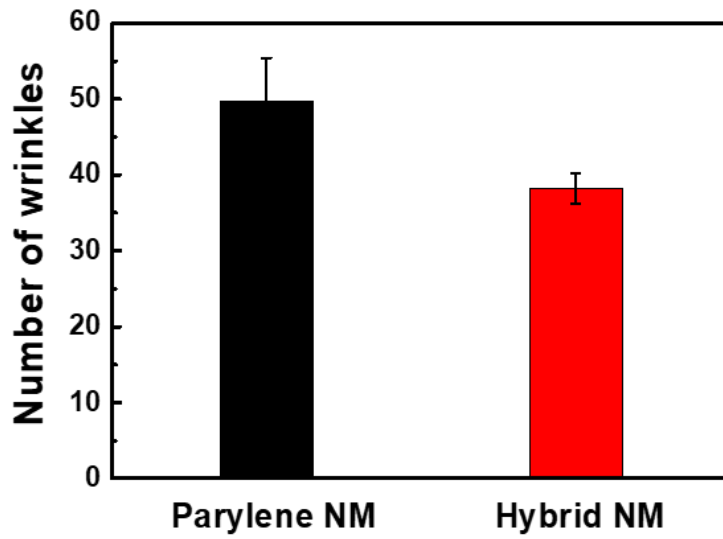


Figure 6.11. Number of wrinkles generated from a pure parylene NM and hybrid NMs.

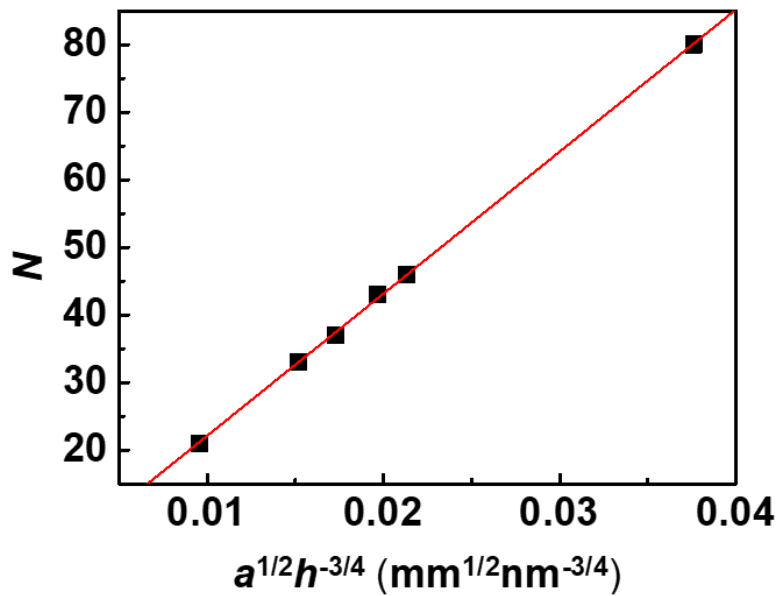


Figure 6.12. Variation in the number of wrinkles N as a function of $N \sim a^{1/2}h^{-3/4}$.

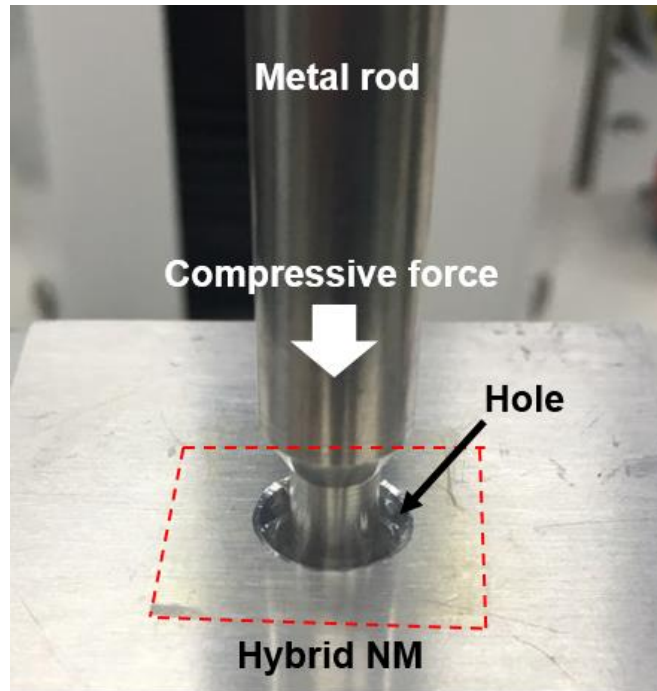


Figure 6.13. Indentation test for measuring the mechanical properties of NMs.

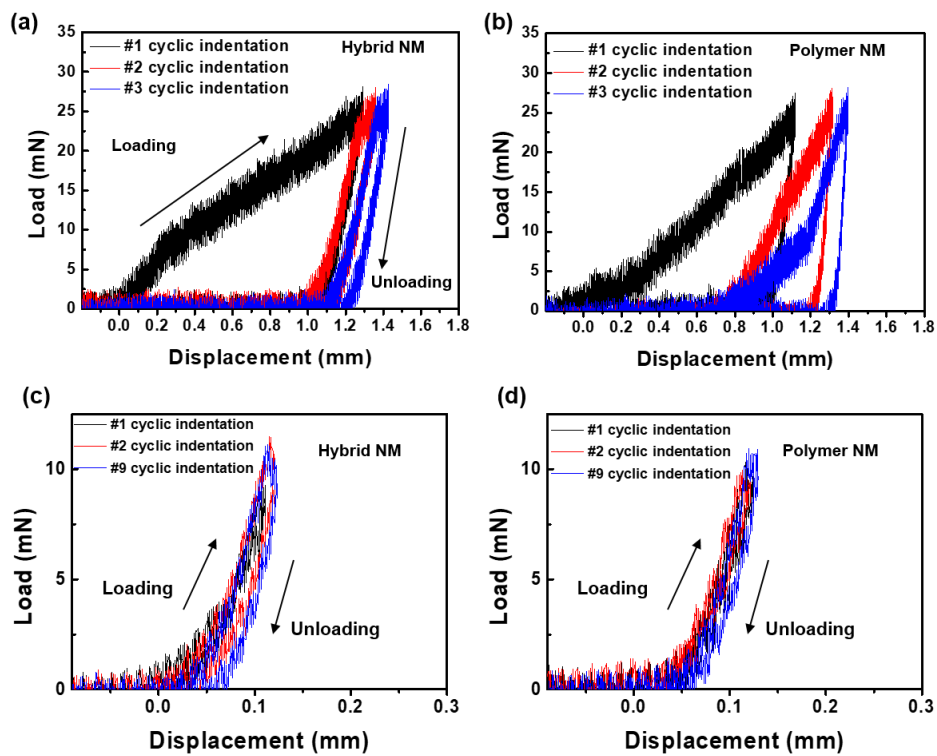


Figure 6.14. Loading-unloading indentation test.

Skin-attachable and transparent NM loudspeaker. For a proof-of-concept demonstration, we fabricated a skin-attachable loudspeaker using hybrid NMs. The speaker can emit thermoacoustic sound by the temperature-induced oscillation of the surrounding air. Here, the temperature oscillation is caused by Joule-heating of the orthogonal AgNW array upon the application of an AC voltage. Figure 6.15a is a schematic of the skin-attachable NM loudspeaker emitting thermoacoustic sound, where periodic Joule-heating generates a temperature oscillation, which then propagates into the surrounding medium, causing an air pressure oscillation (i.e., a sound wave). An infrared image of the loudspeaker with an orthogonal AgNW array reveals highly uniform Joule-heating performance with a slight increase in the surface temperature during a flow of AC 10 V at 10 kHz (Figure 6.16). Figure 6.15b shows the acoustic measurement system used to analyze the sound, as emitted from the NM loudspeaker upon the application of a voltage with a sinusoidal waveform, produced by a function generator. A commercial microphone was used to collect and record the sound produced by the loudspeaker. To characterize the sound generation of loudspeaker, we confirmed that sound pressure level (SPL) of the output sound increases linearly as the distance between the microphone and loudspeaker decreases (Figure 6.17). Figure 6.15c shows the sound pressure for a hybrid NM-based loudspeaker and a thick PET film-based loudspeaker (with a PET thickness of around 220 μm) with an orthogonal AgNW array as a function of the input power at a frequency of 10 kHz and a fixed measurement distance of 3 cm. The output sound pressure from both loudspeakers increases linearly as the input power is increased. Notably, the loudspeaker based on a hybrid NM produces a much larger sound pressure than that using thick PET film with an orthogonal AgNW array at the same input power. Figure 6.15d shows the SPL spectrum as the sound frequency is varied over a range of 1–20 kHz. We confirmed that the SPL of both thick-film and the NM loudspeakers gradually increases with an increase of sound frequency. These results can be explained by the following theoretical formula:²⁵¹

$$P_{\text{rms}} = \frac{\sqrt{\alpha}\rho_0}{2\sqrt{\pi}T_0} \cdot \frac{1}{r} \cdot P_{\text{input}} \cdot \frac{\sqrt{f}}{C_s} \quad (5)$$

where, P_{rms} is the root-mean-square sound pressure, α is the thermal diffusivity of the ambient gas, ρ_0 is the density, T_0 is the temperature, r is the distance between the loudspeaker and the microphone, P_{input} is the input power, f is the sound frequency, and C_s is the heat capacity per unit area. Our experimental results are well matched with the theoretical prediction in equation (5), where the generated sound pressure increases as a function of input power and sound frequency. Notably, NM loudspeakers produce a massive enhancement in the SPL across the entire measured frequency range compared to thick-film loudspeakers, attributed to a reduction in heat loss caused by substrates.^{252, 253} In general, a lower thermal effusivity of the substrate is preferred to facilitate the effective exchange of thermal energy with the surrounding air to efficiently generate sound.²⁵³ The thermal effusivity (e) can be calculated using the equation $e = (\kappa \cdot \rho \cdot C_p)^{1/2}$ where κ is the thermal conductivity, ρ is the density, and C_p is the heat capacity. We obtained $e = 262 \text{ W} \cdot \text{s}^{1/2}/\text{m}^2 \cdot \text{K}$ for the parylene NMs using literature values of κ

= 0.08 W/mK, $\rho = 1230 \text{ kg/m}^3$, and $C_p = 700 \text{ J/kg}\cdot\text{K}$, which is a small value compared with other materials.²⁵² In the NM loudspeakers, however, the low film thickness is a more crucial factor to minimize the heat dissipation for the enhanced sound pressure than the thermal effusivity.²⁵³ To further validate the effect of heat loss for the low NM thickness, we calculated the theoretical SPL for both thick PET film and hybrid NM loudspeakers as a function of frequency using the Eq.(6),²⁵³

$$\Delta P = \frac{3}{4\pi} \frac{P_{input} f}{v_{air}^2 r} \frac{e_{air}}{2e_{air} + (d_{sub}\rho_{sub}C_{p,sub} + d_{film}\rho_{film}C_{p,film})\sqrt{2\pi f}} \quad (6)$$

where ΔP is the sound pressure, v_{air} is the speed of sound in the air, e_{air} is the thermal effusivity of air, ρ_{sub} and ρ_{film} are the density of substrate and film, $C_{p,sub}$ and $C_{p,film}$ are the heat capacity of substrate and film, and d_{sub} and d_{film} are the thickness of a substrate and film, respectively. We obtained SPL of both loudspeakers by converting the sound pressure to SPL. As a result, the change of theoretical SPL as a function of frequency for both loudspeakers exhibited a good agreement with our experimental results (Figure 6.15d). Note that the huge enhancement in SPL is not mainly attributed to the discrepancy in thermal effusivity between parylene NMs and PET films. From the theoretical calculation of SPL, the influence of thermal effusivity on the SPL is negligible for films with the nanoscale thickness while the low thermal effusivity enhances the SPL in the case of thick-film loudspeaker system (Figure 6.18). Therefore, the considerable enhancement in the SPL of the NM loudspeaker could be attributed to the efficient heat transfer to the surroundings resulting from the reduction in the heat loss to the very thin substrate.²⁵² To demonstrate wearable and skin-attachable applications, the NM loudspeaker was mounted to the back of a subject's hand and connected by two copper-wire electrodes. This loudspeaker is unobtrusive in appearance due to the high transmittance and intimate contact with the human skin (Figure 6.15e). We were able to play and recognize Paganini's well-known "La Campanella" violin concerto when played through the NM loudspeaker attached to the skin.

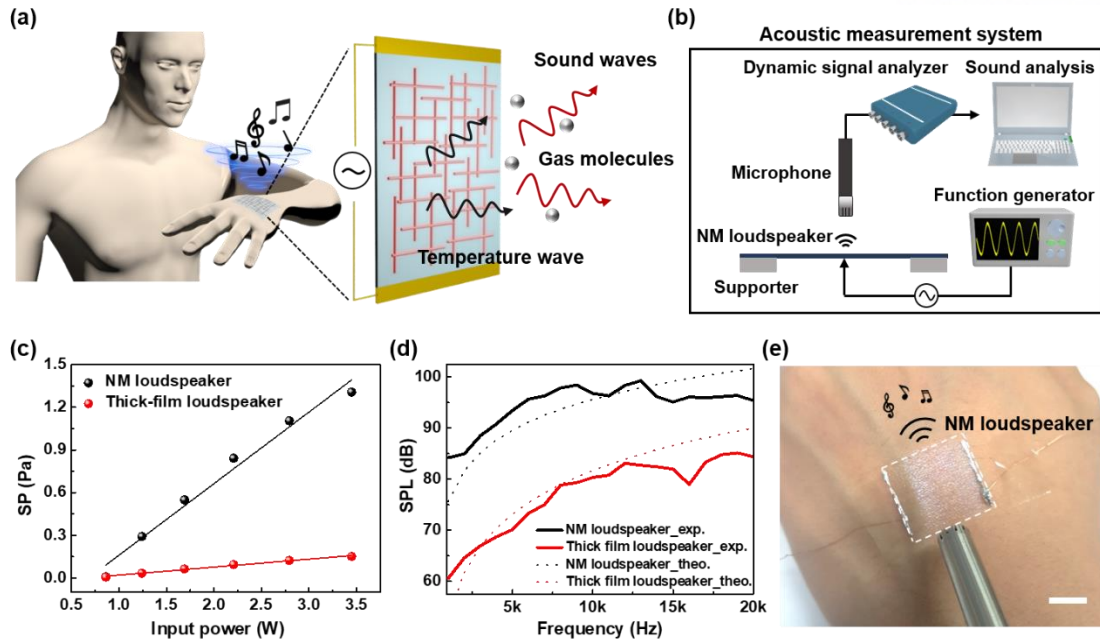


Figure 6.15. Skin-attachable NM loudspeaker. (a) Schematic of skin-attachable NM loudspeaker with orthogonal AgNW array. Sound is generated by temperature oscillation produced by applying an AC voltage. (b) Acoustic measurement system where sound emitted from NM loudspeaker is collected by a commercial microphone with a dynamic signal analyzer. (c) Variation in sound pressure (SP) generated from NM loudspeaker and thick film loudspeaker as a function of the input power at 10 kHz. (d) Experimental and theoretical values of sound pressure level (SPL) versus sound frequency for NM and thick PET film loudspeakers. (e) Skin-attachable NM loudspeaker mounted on the back of a hand. The scale bar indicates 1 cm.

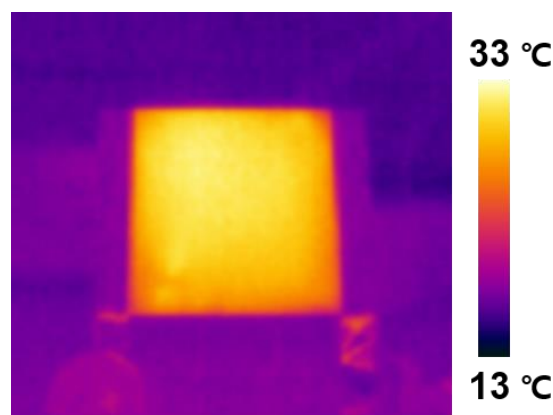


Figure 6.16. Infrared (IR) images of the orthogonal AgNW array with AC 10 V applied at a frequency of 10 kHz.

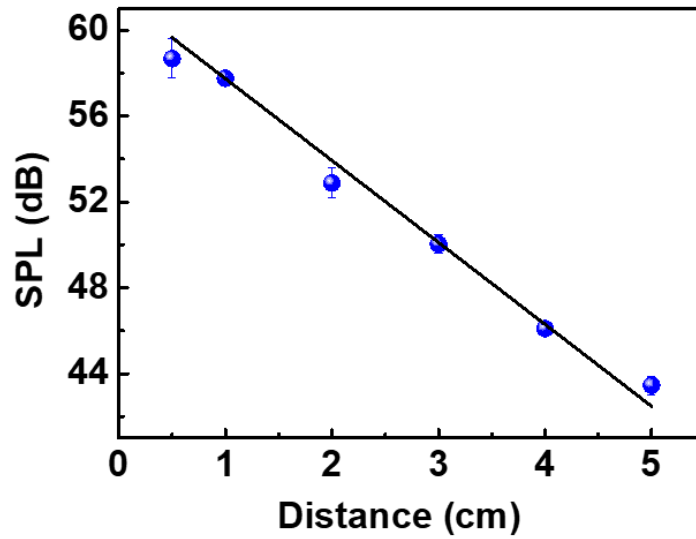


Figure 6.17. SPL versus distance between the commercial microphone and thermoacoustic loudspeaker using an orthogonal AgNW array on a PET substrate.

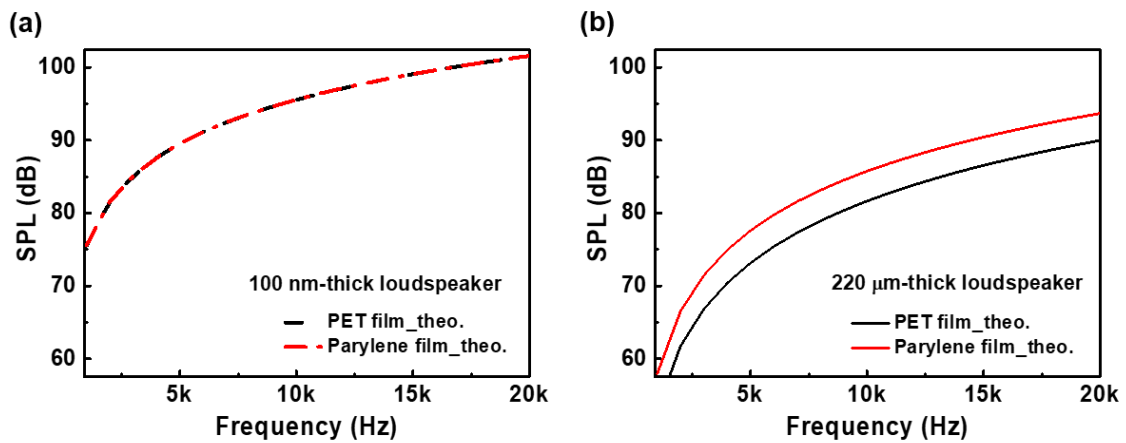


Figure 6.18. Theoretical values of SPL as a function of sound frequency for (a) 100 nm-thick and (b) 220 μm-thick loudspeakers with different substrates.

Wearable and transparent NM microphone. To further demonstrate the applicability of hybrid NMs, we designed a wearable and transparent microphone using hybrid NMs combined with micro-patterned PDMS (NM microphone). The resulting device was able to detect sound and recognize a human voice. Figure 6.19 illustrates the structure of the skin-attachable NM microphone, consisting of a hybrid NM mounted to a holey PDMS film and micropyramid-patterned PDMS film. This sandwich-like structure can precisely detect the sound as well as the vibration of the vocal cords by the generation of a triboelectric voltage resulting from the coupling effect of the contact electrification and electrostatic induction.²⁵⁴ Figure 6.19b shows the NM microphone, which is highly transparent. The holey PDMS film was used to receive a sound wave and to support free-standing NMs. A micropyramid-patterned PDMS film is selected because it provides the smallest adhesive force with a hybrid NM, in comparison with those of the microdome or micropillar-patterned PDMS films, which can facilitate the contact-separation mode of the NMs (Figure 6.20). To evaluate the sensitivity of the NM microphone in response to sound emissions, we fabricated two different device structures, namely, a free-standing hybrid NM, integrated with a holey PDMS film (NM microphone), and another which was fully adhered to a planar PDMS film without a hole (the so-called “thin-film microphone”, Figure 6.21). In addition, we monitored the voltage waveforms emitted by both microphones in response to sound emitted from a speaker, as schematically illustrated in Figure 6.19c. Both microphones exhibit narrow and sharp output voltage peak across a frequency range of 100 Hz–10 kHz, with the maximum voltage being obtained at 400 Hz, after which it gradually decreases (Figure 6.19d). Notably, the NM microphone produces a much higher output voltage than the thin-film microphone across the overall frequency range. Furthermore, the variations in the output voltage of both microphones were monitored with a decreasing SPL at a frequency of 400 Hz to determine their minimum sound-detection capability (Figure 6.19e). For the same SPL, the output voltage of the NM microphone was higher than that of the thin-film microphone. These results can be attributed to the excellent vibrational sensitivity of the free-standing NM, which enhance the coupling of triboelectric effect with an increase in the gap between the micropyramid-patterned PDMS and free-standing hybrid NM.²⁵⁵ We monitored the time-dependent variation in the voltage waveforms produced by a human voice. A speech entitled “There’s plenty of room at the bottom” by R. Feynman was played to both the NM microphone and thin-film microphone to demonstrate their ability to monitor acoustic waveforms (Figure 6.19f). The time-dependent waveform of the output voltage and the corresponding spectrograms from the NM microphone (middle) are in good agreement with the original sound waveform and spectrograms (left) of the sentence. On the other hand, the thin-film microphone (right) cannot precisely detect a human voice in that there are some discrepancies in the acoustic waveforms and spectrograms. Moreover, our NM microphone exhibits an excellent acoustic sensing capability, which is comparable to the commercial microphone (Figure 6.22). We also attempted to detect the vibrations produced by the vocal cords while speaking.

We observed that a NM microphone attached to a person’s neck can clearly detect the phonation of different words. This result indicates the applicability of the NM microphone to wearable or skin-attachable electronics, providing them outstanding acoustic sensing capabilities.

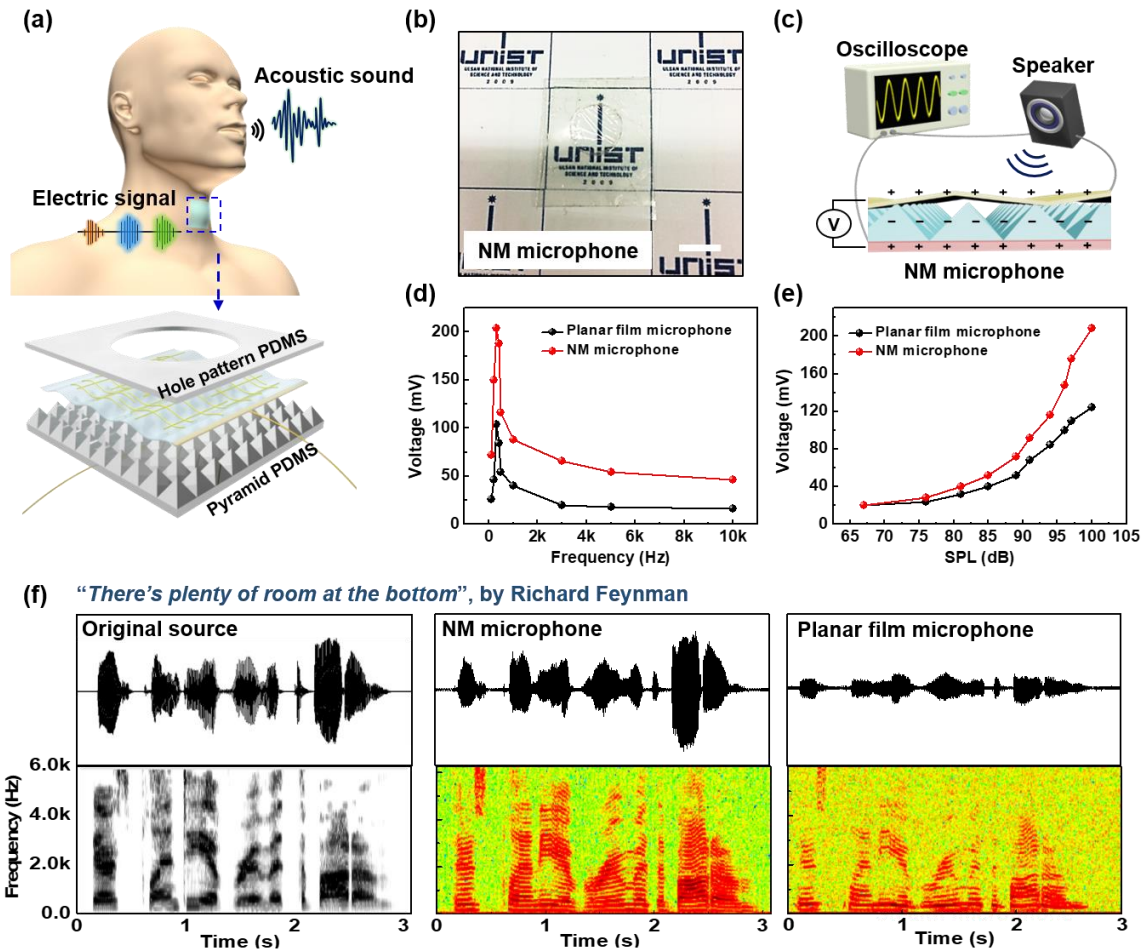


Figure 6.19. Wearable and transparent NM microphone. (a) Schematic of wearable NM microphone device. (b) Transparent NM microphone placed over “UNIST” logo, illustrating its transparent and unobtrusive appearance. The scale bar indicates 1 cm. (c) Sensing measurement system for NM microphone. Variation in the output voltages as a function of (d) sound frequency and (e) SPL for NM microphone and thin-film microphone. (f) Waveform and short-time Fourier transform (STFT) signals of original sound (“There’s plenty of room at the bottom”, left) extracted by the sound wave analyzer, the signal read from the NM-based microphone (middle), and thin-film microphone (right)

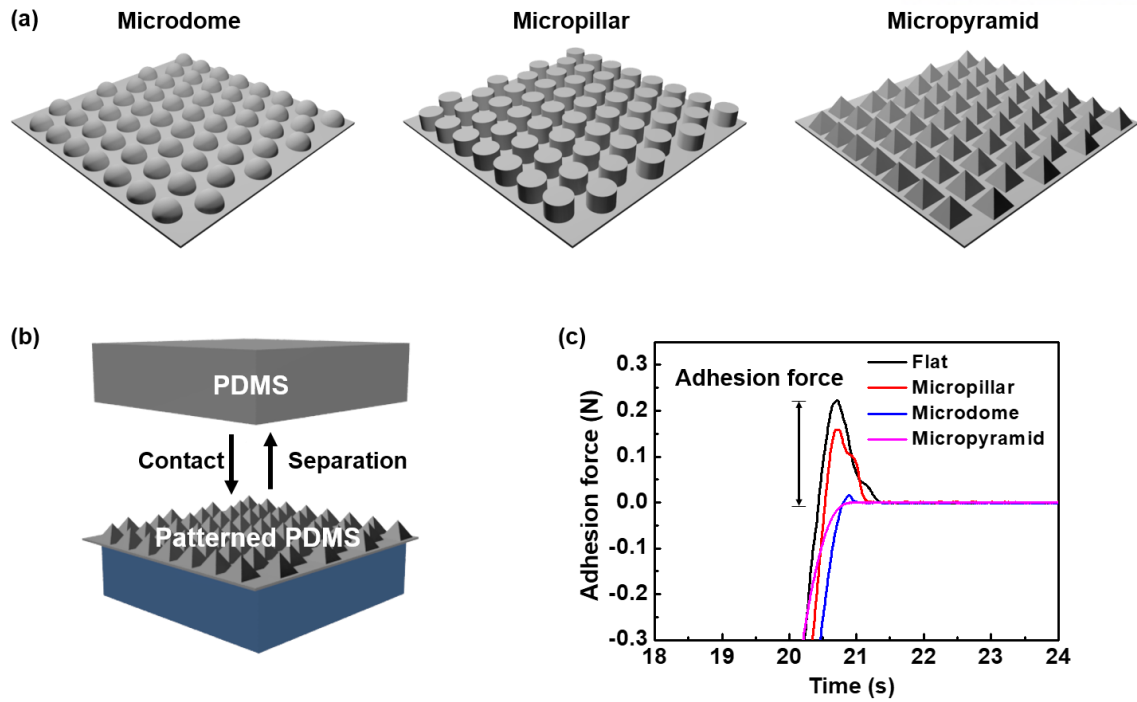


Figure 6.20. Comparison of adhesion force of various micro-patterned PDMS films.

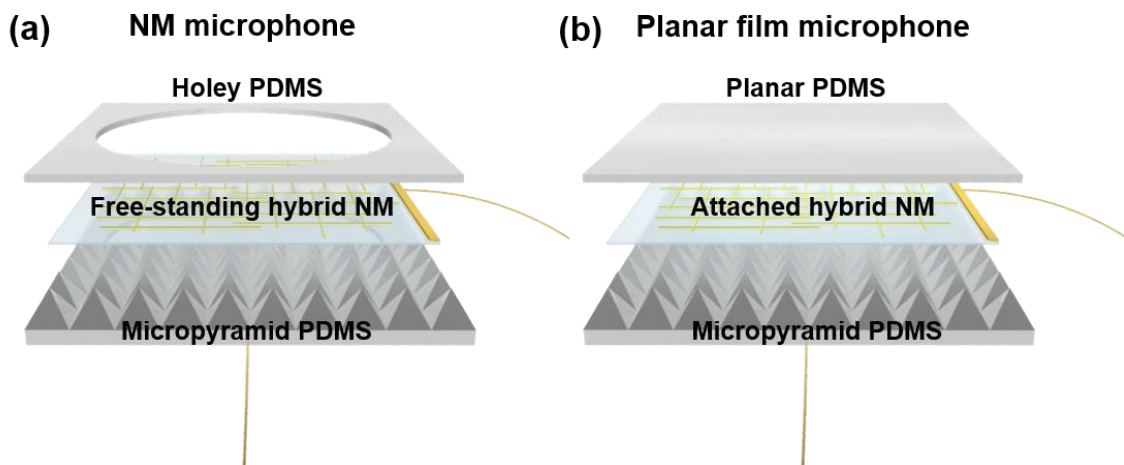


Figure 6.21. Schematic of (a) NM and (b) thin-film microphone devices. In the NM microphone, NMs are mounted to the “holey” PDMS film as a free-standing geometry. In the thin-film microphone, a hybrid NM mounted to a planar PDMS film without a hole is fully laminated with the surface of PDMS film, where NMs cannot be free-standing.

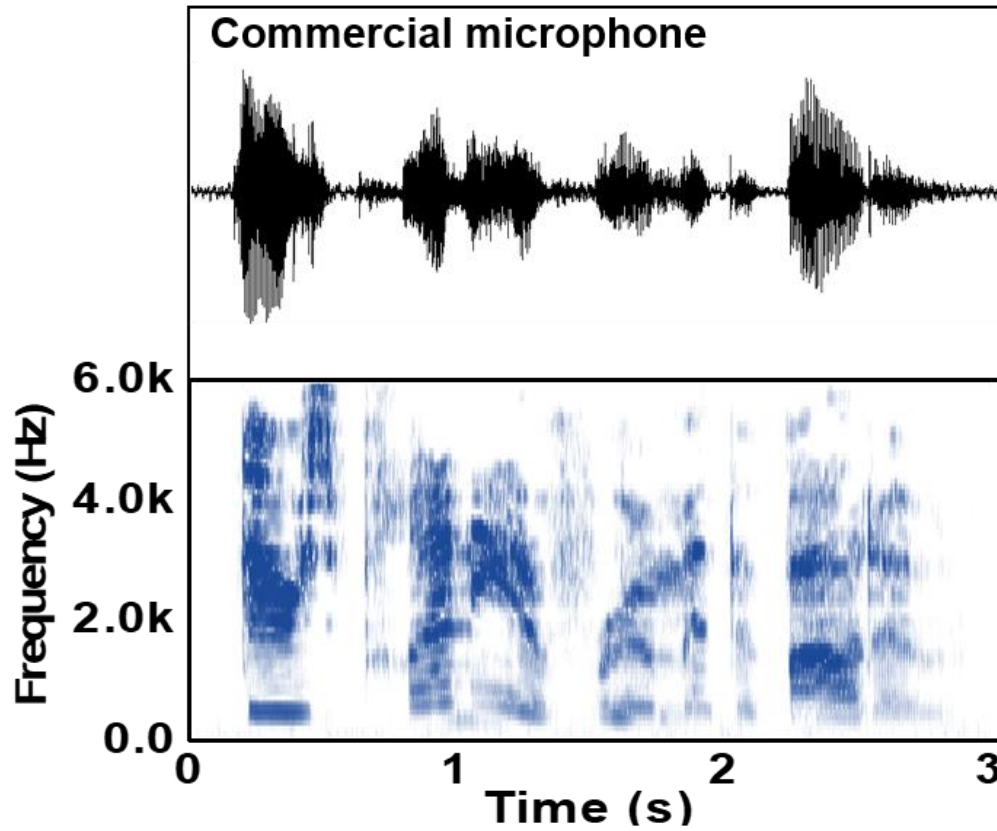


Figure 6.22. Waveform and short-time Fourier transform (STFT) signals of original sound (“There’s plenty of room at the bottom”, left) extracted by the sound wave analyzer, where the signal was read from a commercial microphone.

Personal voice security system. As personal information and security became more important, voice recognition has become essential to IoT sensors, voice security, and acoustic interaction with AI. To validate the acoustic sensing capability of the NM microphone and its applicability to human-machine interfaces, we designed a personal voice security system based on the NM microphone, which can recognize a registrant by perceiving the user's voiceprint. Figure 6.23a shows the voice-based security system with a free-standing NM microphone, which prevents unauthorized users from accessing the system by analyzing the user's voiceprint, as obtained from a recording of the user's voice. In the personal voice security system, we obtained user's voiceprint using LabVIEW software, where the sound waveform signal of user's voice was first recorded by a microphone and then the frequency-domain analysis was performed using FFT with noise filtering. From the FFT spectrum, the frequency of user's voiceprint is arranged according to the amplitude to quantitatively determine the probability of matching with the frequency ordering of authorized voiceprint by using a customized LabVIEW software (S.C.V Corp.). When the user says "hello" using the NM microphone, the computer analyzes the frequency pattern of the user's voiceprint based on the matching probability, relative to the registered voiceprint. If the matching probability is more than 98%, the computer authorizes the user to access the system, which issues a greeting.

Figure 6.23b shows the sound waveforms produced in response to the sound of the word "nanomembrane", recorded by a registrant, authorized user, and denied user using the NM microphone. The time-dependent acoustic information of the sound waveform of the authorized user corresponds closely to that of the registrant whereas that of the sound waveform of denied user is not matched. Figure 6.23c shows the voiceprints obtained for the original sound waveform produced by the registrant, authorized user, and denied user, all of which exhibit a frequency-dependent spectrum. The voiceprints of both the registrant and authorized user are well matched with a 99.3% matching probability in the frequency domain. In the analysis of FFTs, they also exhibit similar frequency patterns across the entire range with a higher pitch than that of a denied user (Figure 6.24). In addition, we could confirm that the overall frequency patterns of FFT obtained from the NM microphone are similar with those from a commercial microphone although there is a slight discrepancy of frequency domain in the same voice (Figure 6.25). To further certify whether the NM microphone could be applied to voice recognition, we compared the matching probabilities obtained using the NM and conventional microphones in response to the voice of a registrant for repeated test of 10 times, respectively (Figure 6.23d). It is worth noting that the matching probability using the NM microphone showed an average reliability of $98.6 \pm 0.8\%$ and a small error variance, which is comparable to that of a commercial microphone ($99.1 \pm 0.6\%$), implying that our NM microphone can accurately recognize registrant's voice with high accuracy and precision. To further validate the precision and selectivity of the NM microphone, we measured the matching probability using the NM microphone in response to voice sounds generated by different persons

including the registrant, a man, and two women (Figure 6.23e). As a result, our NM microphone can selectively recognize registrant's voices among different voices, in which all voices show different and reproducible frequency patterns (Figure 6.26).

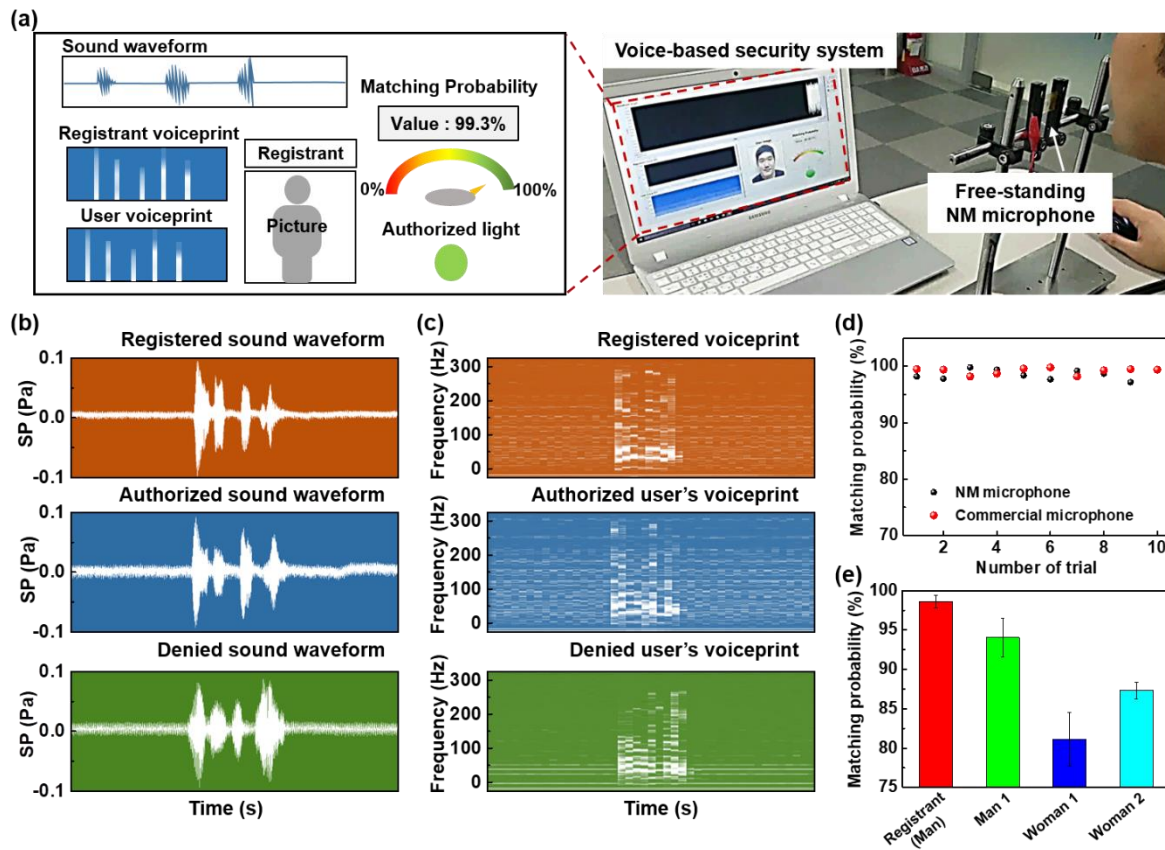


Figure 6.23. Personal voice-based security system. (a) Schematic of voice security system (left) and photograph of authorization process using free-standing NM microphone (right). (b) Sound waveforms and (c) voiceprints collected from registrant, authorized user, and denied user using NM microphone. (d) Matching probability of voiceprint for authorized user using NM microphone and commercial microphone. (e) Matching probability of voiceprints obtained from different users including registrant, man, and two women.

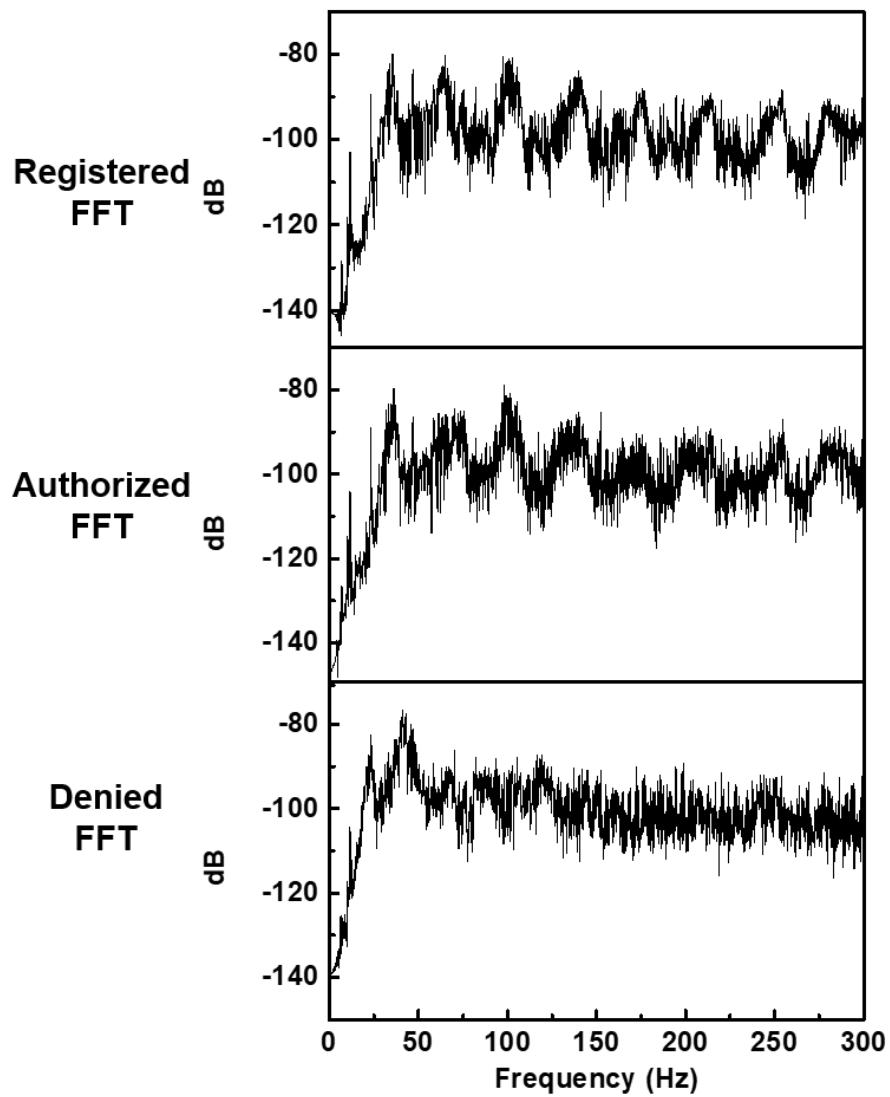


Figure 6.24. FFTs extracted from the sound wave of the word “Nanomembrane” obtained from voices of different subjects including the registrant, authorized user and denied users.

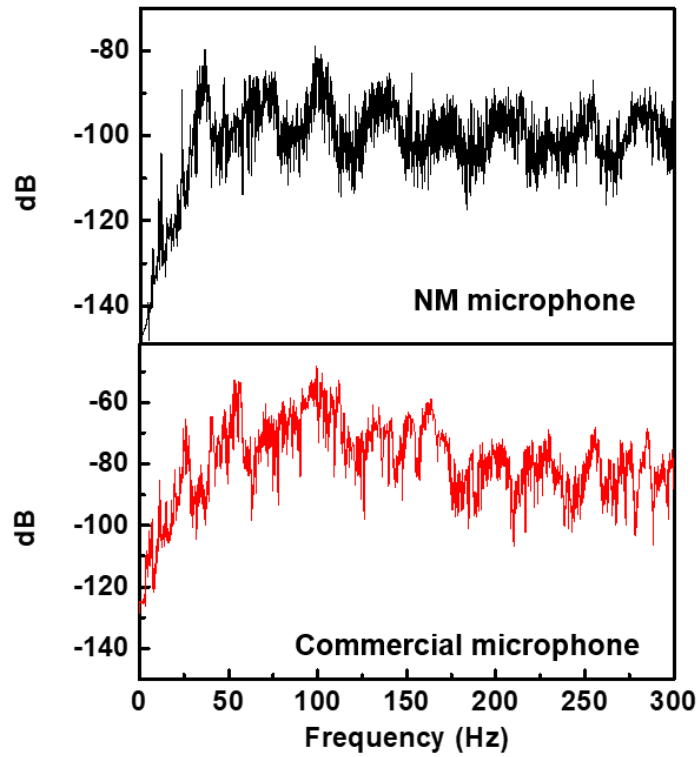


Figure 6.25. FFTs extracted from the sound wave, obtained from the voice of a registrant by using (upper) NM microphone and (bottom) commercial microphone (40PH, G.R.A.S.).

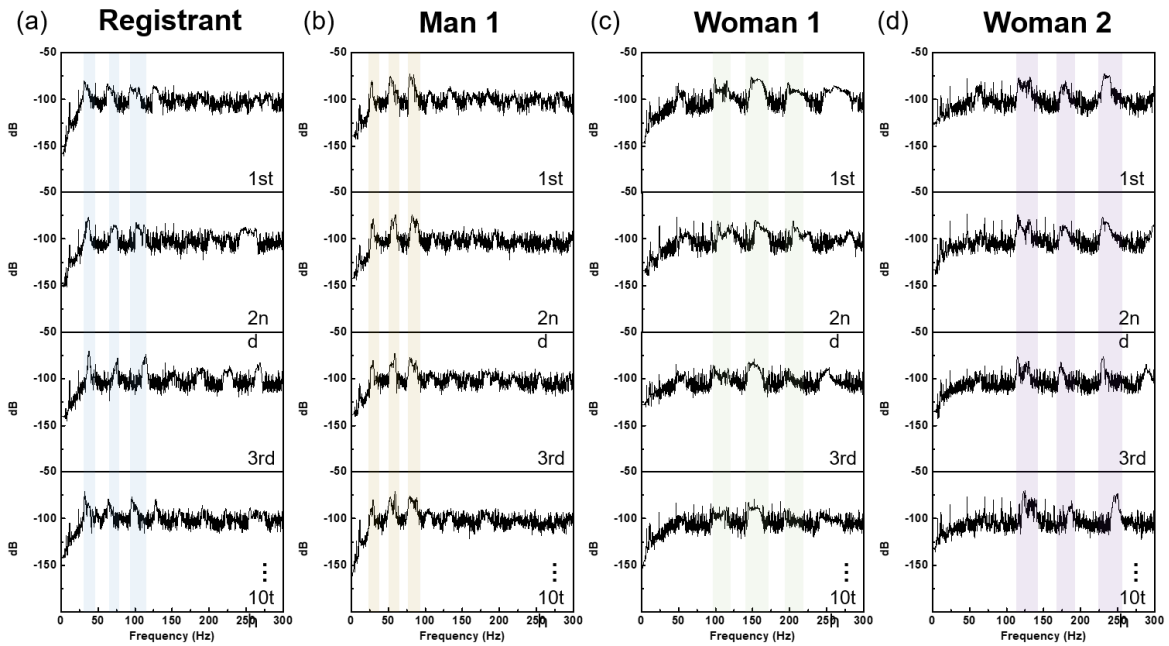


Figure 6.26. FFTs for repeated test of 10 times, extracted from the sound wave of the word “hello” obtained from various voices of different subjects including the registrant, a man, and two women.

6.4 Conclusions

In conclusion, we demonstrated a highly conductive and transparent hybrid NM, consisting of an orthogonal AgNW array embedded into a polymer matrix, which provides excellent electrical and mechanical properties compared to pure polymer NMs. Our hybrid NMs facilitate conformal contact with curvilinear and dynamic surfaces without any cracking or rupture. As a conformal/skin-attachable device application, a skin-attachable thermoacoustic NM loudspeaker is presented, enabling intimate contact with human skin, resulting in an imperceptible and transparent appearance. We have also presented a wearable and transparent NM microphone integrated with a micropyramid-patterned PDMS film for precisely detecting sounds as well as vocal vibrations produced by the triboelectric voltage signals corresponding to sounds. As a proof-of-concept demonstration, our NM microphone was applied to a personal voice security system requiring voice-based identification applications. The NM microphone was able to accurately recognize a user's voice and authorize access to the system by the registrant only. These NM-based acoustic devices can be further explored for various potential applications, such as wearable IoT sensors and conformal healthcare devices.

Chapter 7. Summary and Future Perspective

7.1 Summary

In this thesis, we suggest high-performance transparent electrodes with aligned AgNW networks for the fabrication of optoelectronic and functional electronic devices. To achieve research goals, we firstly developed solution-based capillary printing technique to fabricate aligned AgNW networks, which provide large improvement in electrical and optical properties for high-performance transparent electrodes due to lower percolation threshold compared to random AgNW network. Secondly, we further developed scalable and simple alignment technique using conventional bar-coating process in which large-area transparent electrodes with cross-aligned AgNW networks are successfully fabricated that provide highly uniform and excellent electrical and optical properties.

Based on these alignment techniques, we have fabricated various optoelectronic and electronic devices integrated with aligned AgNW transparent electrodes. Here, we have considered additional materials and structural designs corresponding to each target device, such as OSC, OLED, lightweight and flexible PSC, skin-attachable loudspeaker, and wearable microphone. As a result, we have demonstrated an improvement of device performance in several optoelectronic and electronic devices with aligned AgNW transparent electrodes.

In chapter 2, we demonstrated a capillary printing technique to highly align AgNWs for the fabrication of high-performance transparent electrodes. In this process, the dragging of AgNW solutions by PDMS stamp with nano-patterned channels produces highly aligned AgNW arrays. By tuning the degree of NW alignment, we demonstrated that the degree of NW alignment could be optimized for the fabrication of high-performance TCEs. Thus, aligned AgNW networks showed lower electrical percolation thresholds than random AgNW networks, resulting in an improvement in an electrical conductivity and optical transmittance. The aligned AgNW transparent electrodes exhibited excellent performances of $19.5 \Omega/\text{sq}$ at 96.7% transmittance and a high FoM value of 571.3. In addition, we have reported improved device performance for PCE of 8.57% in PSCs and the luminance efficiency of 14.25 cd/A and power efficiency of 10.62 lm/W in PLEDs integrated with aligned AgNW transparent electrodes, respectively. This study suggests that aligned Ag NW transparent electrodes are promising candidates for low-cost ITO-free TCEs used in optoelectronic devices and future flexible electronics.

In chapter 3, we introduced NP-enhanced plasmonic AgNW electrodes, consisting of aligned AgNW networks decorated by core-shell Ag@SiO₂NPs, which serve as outstanding transparent electrodes and powerful plasmonic structures, simultaneously. Here, NP-NW hybrid plasmonic system generates gap-plasmon couplings at NP-NW interfaces, which provide large near-field enhancement, resulting in an improvement of device efficiency for both OSC and OLED devices. Simulation results for near-field

distributions of the NP-NW system showed a large local E-field enhancement at NP-NW junctions due to strong gap-plasmon coupling between LSPs of AgNPs and propagating SPPs of AgNWs. In addition, we certified gap plasmon effects in NP-NW system by using various measurements including SERS, CLSM, UV-vis, PL and EL measurements. As a result, results obtained from those measurements showed good agreements with simulation results. Finally, we have reported high EL efficiencies of 25.33 cd/A and power efficiency of 25.14 lm/W in OLEDs as well as high PCEs of 9.19% in OSCs integrated with NP-enhanced plasmonic AgNW electrodes. In this study, we expect that NP-enhanced plasmonic AgNW films will be a multifunctional platform which may provide great utility in a wide variety of optoelectronic devices and other plasmonic applications.

In chapter 4, we demonstrate ultrathin orthogonal AgNW transparent electrodes fabricated on 1.3 μm -thick PEN foils for the fabrication of lightweight PSCs. Orthogonal AgNW electrodes provide better capability to effectively prevent non-conducting silver-halide formation generated by chemical reaction between AgNW and iodine of active layer, due to its smooth surface morphologies, resulting in significant improvement of device performance, achieving higher PCE of 15.19% for PSC with orthogonal AgNW electrode on glass substrate than that with random AgNW network of 10.3%. Moreover, ultrathin and lightweight PSC foils with orthogonal AgNW electrodes exhibited an excellent power-per-weight of 34.4 W g^{-1} . These lightweight energy harvesting platforms can be further expanded for various wearable optoelectronic devices.

In chapter 5, we introduced scalable and simple alignment technique for the fabrication of large-area and aligned AgNW arrays through a modified bar-coating assembly. Simple dragging of the Meyer rod over AgNW solution on the target substrates enables fast, efficient, and uniform alignment of NWs in a large area. Cross-aligned AgNW transparent electrodes fabricated by multiple alignment process showed outstanding electrical conductivity as well as optical transmittance (R_s of 21.0 $\Omega \text{ sq}^{-1}$ at 95.0 % of T over $20 \times 20 \text{ cm}^2$ area) with higher large-area uniformity than that of the random AgNW transparent electrodes. For the proof-of-concept demonstrates, we demonstrated large-scale, flexible, and transparent touch screen incorporated with cross-aligned AgNW electrodes, which provided uniform and accurate sensing capability across the entire region. In addition, we introduced flexible force-sensitive touch screen combined with mechanochromic SP-PDMS composite film, which can detect human writing force and location, simultaneously. In this work, we anticipate that large-scale alignment technique provides a robust and powerful platform for the controllable assembly of NWs beyond the scale of the conventional fabrication techniques, which can find diverse applications in flexible electronic and optoelectronic devices.

In chapter 6, we introduce ultrathin, transparent, and conductive hybrid NMs, consisting of an orthogonal AgNW array embedded in a polymer matrix. Hybrid NMs significantly enhance the electrical and mechanical properties of the ultrathin polymer NMs that can be intimately attached to

human skin. As a proof-of-concept, we present a skin-attachable NM loudspeaker, which exhibits a significant enhancement in thermoacoustic capabilities without any significant heat loss from the substrate. We also present a wearable transparent NM microphone combined with a micropatterned polydimethylsiloxane film, which provides excellent acoustic sensing capabilities based on a triboelectric voltage signal. Furthermore, the NM microphone can be used to provide a user interface for a personal voice-based security system in that it can accurately recognize a user's voice. This study addressed NM-based conformal electronics for acoustic device platforms, which could be further expanded for application to conformal wearable sensors and healthcare devices.

In summary, this thesis presents novel approaches for the fabrication of high-performance transparent electrodes with aligned AgNW network for the development of high-efficient optoelectronic and functional electronic devices. Here, we certify that aligned AgNW network provides an improved electrical and optical properties compared than random AgNW network due to lower percolation threshold. Moreover, we confirmed that aligned AgNW networks have smoother surface morphologies as well as high uniformity of electrical and optical properties. For the proof-of-concept, we designed and fabricated several kinds of optoelectronic and electronic devices integrated with aligned AgNW transparent electrodes corresponding to each device, such as OSCs, OLEDs, flexible touch screen, flexible PSCs, and wearable acoustic devices. As a result, we have reported an improvement of these device performances in the comparison with control devices, indicating the possibility of the fabrication of various flexible/wearable optoelectronic and electronic devices with simple, fast, cost-effective approaches. This study will be powerful platform for realizing high-performance NW-based devices beyond the scale of conventional fabrication techniques, which can be further extended for diverse applications in multifunctional wearable electronic and optoelectronic devices.

7.2 Future perspective

While significant progress of the alignment technique has been made to assemble various types of semi-conducting or metallic NWs, large-scale and high-throughput assembly techniques with accurate positioning have not yet been developed, which could overcome the limitation of conventional photolithography fabrication for realizing flexible/wearable NW-based FET devices. In terms of this, our alignment techniques including capillary printing and bar-coating assembly are beneficial to be compatible with large-scale and mass-productive commercial fabrication process. Our alignment techniques may be further explored and applied to the alignment and assembly of other NW types. In addition, it may be newly designed in the development and mass production of NW-based optoelectronic and electronic devices. Specifically, we suggest that the combination with large-scale assembly technique for NWs and self-assembly monolayer for nano-patterning of functional molecules could offer the possibility for achieving the controllable NW assembly including the positioning, NW density, and multi-stacking to realize the fabrication of large-scale NW-based lithography techniques beyond the scale of the conventional fabrication techniques. Therefore, we anticipate that the suggested future works may be of great utility in the development of wearable NW-based electronic devices in various applications, such as FET, photodetector, bio-sensors, and e-skin devices. Furthermore, it will provide the powerful platform for NW-based device integration in the next-generation flexible/wearable optoelectronic and electronic applications.

References

1. Sekitani, T.; Nakajima, H.; Maeda, H.; Fukushima, T.; Aida, T.; Hata, K.; Someya, T., Stretchable active-matrix organic light-emitting diode display using printable elastic conductors. *Nat. Mater.* **2009**, *8*, 494.
2. Gaynor, W.; Hofmann, S.; Christoforo, M. G.; Sachse, C.; Mehra, S.; Salleo, A.; McGehee, M. D.; Gather, M. C.; Lüssem, B.; Müller-Meskamp, L., Color in the Corners: ITO-Free White OLEDs with Angular Color Stability. *Adv. Mater.* **2013**, *25*, 4006-4013.
3. Muth, J. T.; Vogt, D. M.; Truby, R. L.; Mengüç, Y.; Kolesky, D. B.; Wood, R. J.; Lewis, J. A., Embedded 3D printing of strain sensors within highly stretchable elastomers. *Adv. Mater.* **2014**, *26*, 6307-6312.
4. Miyamoto, A.; Lee, S.; Cooray, N. F.; Lee, S.; Mori, M.; Matsuhisa, N.; Jin, H.; Yoda, L.; Yokota, T.; Itoh, A., Inflammation-free, gas-permeable, lightweight, stretchable on-skin electronics with nanomeshes. *Nat. Nanotechnol.* **2017**, *12*, 907.
5. Lipomi, D. J.; Vosgueritchian, M.; Tee, B. C.; Hellstrom, S. L.; Lee, J. A.; Fox, C. H.; Bao, Z., Skin-like pressure and strain sensors based on transparent elastic films of carbon nanotubes. *Nat. Nanotechnol.* **2011**, *6*, 788.
6. Liang, J.; Li, L.; Niu, X.; Yu, Z.; Pei, Q., Elastomeric polymer light-emitting devices and displays. *Nat. Photonics* **2013**, *7*, 817.
7. Lee, S.; Reuveny, A.; Reeder, J.; Lee, S.; Jin, H.; Liu, Q.; Yokota, T.; Sekitani, T.; Isoyama, T.; Abe, Y., A transparent bending-insensitive pressure sensor. *Nat. Nanotechnol.* **2016**, *11*, 472.
8. Trung, T. Q.; Lee, N.-E., Materials and devices for transparent stretchable electronics. *J. Mater. Chem. C* **2017**, *5*, 2202-2222.
9. Ye, S. R.; Rathmell, A. R.; Chen, Z. F.; Stewart, I. E.; Wiley, B. J., Metal Nanowire Networks: The Next Generation of Transparent Conductors. *Adv. Mater.* **2014**, *26* (39), 6670-6687.
10. Ellmer, K., Past achievements and future challenges in the development of optically transparent electrodes. *Nat. Photonics* **2012**, *6*, 809.
11. Hecht, D. S.; Hu, L.; Irvin, G., Emerging Transparent Electrodes Based on Thin Films of Carbon Nanotubes, Graphene, and Metallic Nanostructures. *Adv. Mater.* **2011**, *23* (13), 1482-1513.
12. Bae, S.; Kim, S. J.; Shin, D.; Ahn, J.-H.; Hong, B. H., Towards industrial applications of graphene electrodes. *Phys. Scr.* **2012**, *2012*, 014024.
13. Kuang, P.; Park, J. M.; Leung, W.; Mahadevapuram, R. C.; Nalwa, K. S.; Kim, T. G.; Chaudhary, S.; Ho, K. M.; Constant, K., A New Architecture for Transparent Electrodes: Relieving the Trade-Off Between Electrical Conductivity and Optical Transmittance. *Adv. Mater.* **2011**, *23*, 2469-2473.
14. De, S.; Higgins, T. M.; Lyons, P. E.; Doherty, E. M.; Nirmalraj, P. N.; Blau, W. J.; Boland, J. J.;

- Coleman, J. N., Silver nanowire networks as flexible, transparent, conducting films: extremely high DC to optical conductivity ratios. *ACS nano* **2009**, *3*, 1767-1774.
15. Wu, Z.; Chen, Z.; Du, X.; Logan, J. M.; Sippel, J.; Nikolou, M.; Kamaras, K.; Reynolds, J. R.; Tanner, D. B.; Hebard, A. F.; Rinzler, A. G., Transparent, Conductive Carbon Nanotube Films. *Science* **2004**, *305*, 1273-1276.
 16. Kim, K. S.; Zhao, Y.; Jang, H.; Lee, S. Y.; Kim, J. M.; Kim, K. S.; Ahn, J.-H.; Kim, P.; Choi, J.-Y.; Hong, B. H., Large-scale pattern growth of graphene films for stretchable transparent electrodes. *Nature* **2009**, *457*, 706.
 17. Schneider, J.; Rohner, P.; Thureja, D.; Schmid, M.; Galliker, P.; Poulikakos, D., Electrohydrodynamic nanodrip printing of high aspect ratio metal grid transparent electrodes. *Adv. Funct. Mater.* **2016**, *26*, 833-840.
 18. Kirchmeyer, S.; Reuter, K., Scientific importance, properties and growing applications of poly(3, 4-ethylenedioxythiophene). *J. Mater. Chem.* **2005**, *15*, 2077-2088.
 19. Allen, B. L.; Kichambare, P. D.; Star, A., Carbon nanotube field-effect-transistor-based biosensors. *Adv. Mater.* **2007**, *19*, 1439-1451.
 20. Fuhrer, M.; Nygård, J.; Shih, L.; Forero, M.; Yoon, Y.-G.; Choi, H. J.; Ihm, J.; Louie, S. G.; Zettl, A.; McEuen, P. L., Crossed nanotube junctions. *Science* **2000**, *288*, 494-497.
 21. Yu, L.; Shearer, C.; Shapter, J., Recent development of carbon nanotube transparent conductive films. *Chem. Rev.* **2016**, *116*, 13413-13453.
 22. Wu, H.; Kong, D.; Ruan, Z.; Hsu, P.-C.; Wang, S.; Yu, Z.; Carney, T. J.; Hu, L.; Fan, S.; Cui, Y., A transparent electrode based on a metal nanotrough network. *Nat. Nanotechnol.* **2013**, *8*, 421.
 23. Han, B.; Pei, K.; Huang, Y.; Zhang, X.; Rong, Q.; Lin, Q.; Guo, Y.; Sun, T.; Guo, C.; Carnahan, D.; Giersig, M.; Wang, Y.; Gao, J.; Ren, Z.; Kempa, K., Uniform Self-Forming Metallic Network as a High-Performance Transparent Conductive Electrode. *Adv. Mater.* **2014**, *26*, 873-877.
 24. Kang, M. G.; Guo, L. J., Nanoimprinted semitransparent metal electrodes and their application in organic light-emitting diodes. *Adv. Mater.* **2007**, *19*, 1391-1396.
 25. Hu, L.; Kim, H. S.; Lee, J.-Y.; Peumans, P.; Cui, Y., Scalable coating and properties of transparent, flexible, silver nanowire electrodes. *ACS nano* **2010**, *4*, 2955-2963.
 26. Yim, J. H.; Joe, S.-y.; Pang, C.; Lee, K. M.; Jeong, H.; Park, J.-Y.; Ahn, Y. H.; de Mello, J. C.; Lee, S., Fully Solution-Processed Semitransparent Organic Solar Cells with a Silver Nanowire Cathode and a Conducting Polymer Anode. *ACS nano* **2014**, *8*, 2857-2863.
 27. Lee, J.-Y.; Connor, S. T.; Cui, Y.; Peumans, P., Solution-processed metal nanowire mesh transparent electrodes. *Nano Lett.* **2008**, *8*, 689-692.
 28. Liu, C. H.; Yu, X., Silver nanowire-based transparent, flexible, and conductive thin film. *Nanoscale Res. Lett.* **2011**, *6*, 75.

29. Scardaci, V.; Coull, R.; Lyons, P. E.; Rickard, D.; Coleman, J. N., Spray deposition of highly transparent, low-resistance networks of silver nanowires over large areas. *Small* **2011**, *7*, 2621-2628.
30. Lim, J.-W.; Cho, D.-Y.; Na, S.-I.; Kim, H.-K., Simple brush-painting of flexible and transparent Ag nanowire network electrodes as an alternative ITO anode for cost-efficient flexible organic solar cells. *Sol. Energy Mater. Sol. Cells* **2012**, *107*, 348-354.
31. Krantz, J.; Richter, M.; Spallek, S.; Spiecker, E.; Brabec, C. J., Solution-processed metallic nanowire electrodes as indium tin oxide replacement for thin-film solar cells. *Adv. Funct. Mater.* **2011**, *21*, 4784-4787.
32. Lee, P.; Lee, J.; Lee, H.; Yeo, J.; Hong, S.; Nam, K. H.; Lee, D.; Lee, S. S.; Ko, S. H., Highly stretchable and highly conductive metal electrode by very long metal nanowire percolation network. *Adv. Mater.* **2012**, *24*, 3326-3332.
33. Sun, Y.; Mayers, B.; Herricks, T.; Xia, Y., Polyol synthesis of uniform silver nanowires: a plausible growth mechanism and the supporting evidence. *Nano Lett.* **2003**, *3*, 955-960.
34. Hu, L.; Hecht, D. S.; Grüner, G., Percolation in Transparent and Conducting Carbon Nanotube Networks. *Nano Lett.* **2004**, *4*, 2513-2517.
35. Mutiso, R. M.; Sherrott, M. C.; Rathmell, A. R.; Wiley, B. J.; Winey, K. I., Integrating Simulations and Experiments To Predict Sheet Resistance and Optical Transmittance in Nanowire Films for Transparent Conductors. *ACS Nano* **2013**, *7*, 7654-7663.
36. Tokuno, T.; Nogi, M.; Karakawa, M.; Jiu, J.; Nge, T. T.; Aso, Y.; Suganuma, K., Fabrication of silver nanowire transparent electrodes at room temperature. *Nano Res.* **2011**, *4*, 1215-1222.
37. Liang, J.; Li, L.; Tong, K.; Ren, Z.; Hu, W.; Niu, X.; Chen, Y.; Pei, Q., Silver Nanowire Percolation Network Soldered with Graphene Oxide at Room Temperature and Its Application for Fully Stretchable Polymer Light-Emitting Diodes. *ACS Nano* **2014**, *8*, 1590-1600.
38. Garnett, E. C.; Cai, W.; Cha, J. J.; Mahmood, F.; Connor, S. T.; Greyson Christoforo, M.; Cui, Y.; McGehee, M. D.; Brongersma, M. L., Self-limited plasmonic welding of silver nanowire junctions. *Nat. Mater.* **2012**, *11*, 241.
39. Khaligh, H. H.; Goldthorpe, I. A., Hot-rolling nanowire transparent electrodes for surface roughness minimization. *Nanoscale Res. Lett.* **2014**, *9*, 310.
40. Gaynor, W.; Burkhard, G. F.; McGehee, M. D.; Peumans, P., Smooth nanowire/polymer composite transparent electrodes. *Adv. Mater.* **2011**, *23*, 2905-10.
41. Chung, C.-H.; Song, T.-B.; Bob, B.; Zhu, R.; Yang, Y., Solution-processed flexible transparent conductors composed of silver nanowire networks embedded in indium tin oxide nanoparticle matrices. *Nano Res.* **2012**, *5*, 805-814.
42. Nam, S.; Song, M.; Kim, D.-H.; Cho, B.; Lee, H. M.; Kwon, J.-D.; Park, S.-G.; Nam, K.-S.;

- Jeong, Y.; Kwon, S.-H., Ultrasoother, extremely deformable and shape recoverable Ag nanowire embedded transparent electrode. *Sci. Rep.* **2014**, *4*, 4788.
43. Araki, T.; Jiu, J.; Nogi, M.; Koga, H.; Nagao, S.; Sugahara, T.; Sugauma, K., Low haze transparent electrodes and highly conducting air dried films with ultra-long silver nanowires synthesized by one-step polyol method. *Nano Res.* **2014**, *7*, 236-245.
 44. Kim, T.; Canlier, A.; Kim, G. H.; Choi, J.; Park, M.; Han, S. M., Electrostatic Spray Deposition of Highly Transparent Silver Nanowire Electrode on Flexible Substrate. *ACS Applied Materials & Interfaces* **2013**, *5*, 788-794.
 45. Rycenga, M.; Cobley, C. M.; Zeng, J.; Li, W.; Moran, C. H.; Zhang, Q.; Qin, D.; Xia, Y., Controlling the synthesis and assembly of silver nanostructures for plasmonic applications. *Chem Rev.* **2011**, *111*, 3669-712.
 46. Wang, B.-Y.; Yoo, T.-H.; Lim, J. W.; Sang, B.-I.; Lim, D.-S.; Choi, W. K.; Hwang, D. K.; Oh, Y.-J., Enhanced Light Scattering and Trapping Effect of Ag Nanowire Mesh Electrode for High Efficient Flexible Organic Solar Cell. *Small* **2015**, *11*, 1905-1911.
 47. Li, L.; Yu, Z.; Chang, C.-h.; Hu, W.; Niu, X.; Chen, Q.; Pei, Q., Efficient white polymer light-emitting diodes employing a silver nanowire-polymer composite electrode. *Phys. Chem. Chem. Phys.* **2012**, *14*, 14249-14254.
 48. Hsu, P.-C.; Wang, S.; Wu, H.; Narasimhan, V. K.; Kong, D.; Ryoung Lee, H.; Cui, Y., Performance enhancement of metal nanowire transparent conducting electrodes by mesoscale metal wires. *Nat. Commun.* **2013**, *4*, 2522.
 49. Guo, C. F.; Sun, T.; Liu, Q.; Suo, Z.; Ren, Z., Highly stretchable and transparent nanomesh electrodes made by grain boundary lithography. *Nat. Commun.* **2014**, *5*, 3121.
 50. Gao, T.; Wang, B.; Ding, B.; Lee, J.-k.; Leu, P. W., Uniform and Ordered Copper Nanomeshes by Microsphere Lithography for Transparent Electrodes. *Nano Lett.* **2014**, *14*, 2105-2110.
 51. He, T.; Xie, A.; Reneker, D. H.; Zhu, Y., A Tough and High-Performance Transparent Electrode from a Scalable and Transfer-Free Method. *ACS Nano* **2014**, *8*, 4782-4789.
 52. Hsu, P.-C.; Kong, D.; Wang, S.; Wang, H.; Welch, A. J.; Wu, H.; Cui, Y., Electrolessly Deposited Electrospun Metal Nanowire Transparent Electrodes. *J. Am. Chem. Soc.* **2014**, *136*, 10593-10596.
 53. Cai, B.; Xing, Y.; Yang, Z.; Zhang, W.-H.; Qiu, J., High performance hybrid solar cells sensitized by organolead halide perovskites. *Energy Environ. Sci.* **2013**, *6*, 1480-1485.
 54. Yang, L.; Zhang, T.; Zhou, H.; Price, S. C.; Wiley, B. J.; You, W., Solution-Processed Flexible Polymer Solar Cells with Silver Nanowire Electrodes. *ACS Appl. Mater. Interfaces* **2011**, *3*, 4075-4084.
 55. Song, M.; Park, J. H.; Kim, C. S.; Kim, D.-H.; Kang, Y.-C.; Jin, S.-H.; Jin, W.-Y.; Kang, J.-W.,

- Highly flexible and transparent conducting silver nanowire/ZnO composite film for organic solar cells. *Nano Res.* **2014**, *7*, 1370-1379.
56. Song, M.; You, D. S.; Lim, K.; Park, S.; Jung, S.; Kim, C. S.; Kim, D. H.; Kim, D. G.; Kim, J. K.; Park, J., Highly efficient and bendable organic solar cells with solution-processed silver nanowire electrodes. *Adv. Funct. Mater.* **2013**, *23*, 4177-4184.
 57. Lee, S. J.; Kim, Y.-H.; Kim, J. K.; Baik, H.; Park, J. H.; Lee, J.; Nam, J.; Park, J. H.; Lee, T.-W.; Yi, G.-R.; Cho, J. H., A roll-to-roll welding process for planarized silver nanowire electrodes. *Nanoscale* **2014**, *6*, 11828-11834.
 58. Seo, J. H.; Hwang, I.; Um, H. D.; Lee, S.; Lee, K.; Park, J.; Shin, H.; Kwon, T. H.; Kang, S. J.; Seo, K., Cold Isostatic-Pressured Silver Nanowire Electrodes for Flexible Organic Solar Cells via Room-Temperature Processes. *Adv. Mater.* **2017**, *29*, 1701479.
 59. Leem, D. S.; Edwards, A.; Faist, M.; Nelson, J.; Bradley, D. D.; de Mello, J. C., Efficient organic solar cells with solution-processed silver nanowire electrodes. *Adv. Mater.* **2011**, *23*, 4371-4375.
 60. Zeng, X.-Y.; Zhang, Q.-K.; Yu, R.-M.; Lu, C.-Z., A New Transparent Conductor: Silver Nanowire Film Buried at the Surface of a Transparent Polymer. *Adv. Mater.* **2010**, *22*, 4484-4488.
 61. Yu, Z.; Zhang, Q.; Li, L.; Chen, Q.; Niu, X.; Liu, J.; Pei, Q., Highly Flexible Silver Nanowire Electrodes for Shape-Memory Polymer Light-Emitting Diodes. *Adv. Mater.* **2011**, *23*, 664-668.
 62. Li, L.; Yu, Z.; Hu, W.; Chang, C.-h.; Chen, Q.; Pei, Q., Efficient Flexible Phosphorescent Polymer Light-Emitting Diodes Based on Silver Nanowire-Polymer Composite Electrode. *Adv. Mater.* **2011**, *23*, 5563-5567.
 63. Lee, H.; Lee, K.; Park, J. T.; Kim, W. C.; Lee, H., Well-Ordered and High Density Coordination-Type Bonding to Strengthen Contact of Silver Nanowires on Highly Stretchable Polydimethylsiloxane. *Adv. Funct. Mater.* **2014**, *24*, 3276-3283.
 64. Lee, J.; Lee, P.; Lee, H. B.; Hong, S.; Lee, I.; Yeo, J.; Lee, S. S.; Kim, T.-S.; Lee, D.; Ko, S. H., Room-Temperature Nanosoldering of a Very Long Metal Nanowire Network by Conducting-Polymer-Assisted Joining for a Flexible Touch-Panel Application. *Adv. Funct. Mater.* **2013**, *23*, 4171-4176.
 65. Li, J.; Liang, J.; Li, L.; Ren, F.; Hu, W.; Li, J.; Qi, S.; Pei, Q., Healable capacitive touch screen sensors based on transparent composite electrodes comprising silver nanowires and a furan/maleimide diels-alder cycloaddition polymer. *ACS Nano* **2014**, *8*, 12874-12882.
 66. Du, J.; Pei, S.; Ma, L.; Cheng, H.-M., 25th Anniversary Article: Carbon Nanotube- and Graphene-Based Transparent Conductive Films for Optoelectronic Devices. *Adv. Mater.* **2014**, *26*, 1958-1991.
 67. Kumar, A.; Zhou, C., The race to replace tin-doped indium oxide: which material will win? *ACS*

- nano* **2010**, *4*, 11-14.
68. Hu, L.; Wu, H.; Cui, Y., Metal nanogrids, nanowires, and nanofibers for transparent electrodes. *MRS Bull.* **2011**, *36*, 760-765.
 69. Kuang, P.; Park, J.-M.; Leung, W.; Mahadevapuram, R. C.; Nalwa, K. S.; Kim, T.-G.; Chaudhary, S.; Ho, K.-M.; Constant, K., A New Architecture for Transparent Electrodes: Relieving the Trade-Off Between Electrical Conductivity and Optical Transmittance. *Adv. Mater.* **2011**, *23*, 2469-2473.
 70. Daniel, L.; Gaël, G.; Céline, M.; Caroline, C.; Daniel, B.; Jean-Pierre, S., Flexible transparent conductive materials based on silver nanowire networks: a review. *Nanotechnology* **2013**, *24*, 452001.
 71. Van De Groep, J.; Spinelli, P.; Polman, A., Transparent conducting silver nanowire networks. *Nano Lett.* **2012**, *12*, 3138-3144.
 72. Zhang, D.; Ryu, K.; Liu, X.; Polikarpov, E.; Ly, J.; Tompson, M. E.; Zhou, C., Transparent, Conductive, and Flexible Carbon Nanotube Films and Their Application in Organic Light-Emitting Diodes. *Nano Lett.* **2006**, *6*, 1880-1886.
 73. Bae, S.; Kim, H.; Lee, Y.; Xu, X.; Park, J.-S.; Zheng, Y.; Balakrishnan, J.; Lei, T.; Ri Kim, H.; Song, Y. I.; Kim, Y.-J.; Kim, K. S.; Özyilmaz, B.; Ahn, J.-H.; Hong, B. H.; Iijima, S., Roll-to-roll production of 30-inch graphene films for transparent electrodes. *Nat. Nanotechnol.* **2010**, *5*, 574.
 74. Bonaccorso, F.; Sun, Z.; Hasan, T.; Ferrari, A. C., Graphene photonics and optoelectronics. *Nat. Photonics* **2010**, *4*, 611.
 75. Gomez De Arco, L.; Zhang, Y.; Schlenker, C. W.; Ryu, K.; Thompson, M. E.; Zhou, C., Continuous, Highly Flexible, and Transparent Graphene Films by Chemical Vapor Deposition for Organic Photovoltaics. *ACS Nano* **2010**, *4*, 2865-2873.
 76. Wang, X.; Zhi, L.; Müllen, K., Transparent, Conductive Graphene Electrodes for Dye-Sensitized Solar Cells. *Nano Lett.* **2008**, *8*, 323-327.
 77. Kiruthika, S.; Gupta, R.; Rao, K. D. M.; Chakraborty, S.; Padmavathy, N.; Kulkarni, G. U., Large area solution processed transparent conducting electrode based on highly interconnected Cu wire network. *J. Mater. Chem. C* **2014**, *2*, 2089-2094.
 78. Zhu, R.; Chung, C.-H.; Cha, K. C.; Yang, W.; Zheng, Y. B.; Zhou, H.; Song, T.-B.; Chen, C.-C.; Weiss, P. S.; Li, G., Fused silver nanowires with metal oxide nanoparticles and organic polymers for highly transparent conductors. *ACS nano* **2011**, *5*, 9877-9882.
 79. Madaria, A. R.; Kumar, A.; Zhou, C., Large scale, highly conductive and patterned transparent films of silver nanowires on arbitrary substrates and their application in touch screens. *Nanotechnology* **2011**, *22*, 245201.

80. Lee, Y.; Suh, M.; Kim, D.; Lee, D.; Chang, H.; Lee, H. S.; Kim, Y. W.; Kim, T.; Suh, K. S.; Jeon, D. Y., Improved Operational Stability of Polymer Light-Emitting Diodes Based on Silver Nanowire Electrode Through Pre-Bias Conditioning Treatment. *Adv. Funct. Mater.* **2014**, *24*, 6465-6472.
81. Liu, Y.; Chang, Q.; Huang, L., Transparent, flexible conducting graphene hybrid films with a subpercolating network of silver nanowires. *J. Mater. Chem. C* **2013**, *1*, 2970-2974.
82. De, S.; Coleman, J. N., The effects of percolation in nanostructured transparent conductors. *MRS Bull.* **2011**, *36*, 774-781.
83. White, S. I.; Mutiso, R. M.; Vora, P. M.; Jahnke, D.; Hsu, S.; Kikkawa, J. M.; Li, J.; Fischer, J. E.; Winey, K. I., Electrical Percolation Behavior in Silver Nanowire–Polystyrene Composites: Simulation and Experiment. *Adv. Funct. Mater.* **2010**, *20*, 2709-2716.
84. Madaria, A. R.; Kumar, A.; Ishikawa, F. N.; Zhou, C., Uniform, highly conductive, and patterned transparent films of a percolating silver nanowire network on rigid and flexible substrates using a dry transfer technique. *Nano Res.* **2010**, *3*, 564-573.
85. Lee, J.; Lee, P.; Lee, H.; Lee, D.; Lee, S. S.; Ko, S. H., Very long Ag nanowire synthesis and its application in a highly transparent, conductive and flexible metal electrode touch panel. *Nanoscale* **2012**, *4*, 6408-6414.
86. Wu, H.; Kong, D.; Ruan, Z.; Hsu, P.-C.; Wang, S.; Yu, Z.; Carney, T. J.; Hu, L.; Fan, S.; Cui, Y., A transparent electrode based on a metal nanotrough network. *Nat. Nanotechnol.* **2013**, *8*, 421.
87. Tao, A.; Kim, F.; Hess, C.; Goldberger, J.; He, R.; Sun, Y.; Xia, Y.; Yang, P., Langmuir–Blodgett Silver Nanowire Monolayers for Molecular Sensing Using Surface-Enhanced Raman Spectroscopy. *Nano Lett.* **2003**, *3*, 1229-1233.
88. Fan, Z.; Ho, J. C.; Jacobson, Z. A.; Yerushalmi, R.; Alley, R. L.; Razavi, H.; Javey, A., Wafer-Scale Assembly of Highly Ordered Semiconductor Nanowire Arrays by Contact Printing. *Nano Lett.* **2008**, *8*, 20-25.
89. Bang, J.; Choi, J.; Xia, F.; Kwon, S. S.; Ashraf, A.; Park, W. I.; Nam, S., Assembly and Densification of Nanowire Arrays via Shrinkage. *Nano Lett.* **2014**, *14*, 3304-3308.
90. Yao, J.; Yan, H.; Lieber, C. M., A nanoscale combing technique for the large-scale assembly of highly aligned nanowires. *Nat. Nanotechnol.* **2013**, *8*, 329.
91. Zhou, X.; Zhou, Y.; Ku, J. C.; Zhang, C.; Mirkin, C. A., Capillary Force-Driven, Large-Area Alignment of Multi-segmented Nanowires. *ACS Nano* **2014**, *8*, 1511-1516.
92. Huang, Y.; Duan, X.; Wei, Q.; Lieber, C. M., Directed Assembly of One-Dimensional Nanostructures into Functional Networks. *Science* **2001**, *291*, 630-633.
93. Gerdes, S.; Ondarçuhu, T.; Cholet, S.; Joachim, C., Combing a carbon nanotube on a flat metal-insulator-metal nanojunction. *EPL (Europhys. Lett.)* **1999**, *48*, 292.

94. Noy, A.; Frisbie, C. D.; Rozsnyai, L. F.; Wrighton, M. S.; Lieber, C. M., Chemical Force Microscopy: Exploiting Chemically-Modified Tips To Quantify Adhesion, Friction, and Functional Group Distributions in Molecular Assemblies. *J. Am. Chem. Soc.* **1995**, *117*, 7943-7951.
95. Arianna, L. W.; Giuseppe, R. P., Ultralow percolation threshold of single walled carbon nanotube-epoxy composites synthesized via an ionic liquid dispersant/initiator. *Mater. Res. Express* **2014**, *1*, 035013.
96. Du, F.; Fischer, J. E.; Winey, K. I., Effect of nanotube alignment on percolation conductivity in carbon nanotube/polymer composites. *Phys. Rev. B* **2005**, *72*, 121404.
97. Kocabas, C.; Pimparkar, N.; Yesilyurt, O.; Kang, S. J.; Alam, M. A.; Rogers, J. A., Experimental and Theoretical Studies of Transport through Large Scale, Partially Aligned Arrays of Single-Walled Carbon Nanotubes in Thin Film Type Transistors. *Nano Lett.* **2007**, *7*, 1195-1202.
98. White, S. I.; DiDonna, B. A.; Mu, M.; Lubensky, T. C.; Winey, K. I., Simulations and electrical conductivity of percolated networks of finite rods with various degrees of axial alignment. *Phys. Rev. B* **2009**, *79*, 024301.
99. Lee, M. S.; Lee, K.; Kim, S. Y.; Lee, H.; Park, J.; Choi, K. H.; Kim, H. K.; Kim, D. G.; Lee, D. Y.; Nam, S.; Park, J. U., High-Performance, Transparent, and Stretchable Electrodes Using Graphene-Metal Nanowire Hybrid Structures. *Nano Lett.* **2013**, *13*, 2814-2821.
100. Ko, S.-J.; Choi, H.; Lee, W.; Kim, T.; Lee, B. R.; Jung, J.-W.; Jeong, J.-R.; Song, M. H.; Lee, J. C.; Woo, H. Y.; Kim, J. Y., Highly efficient plasmonic organic optoelectronic devices based on a conducting polymer electrode incorporated with silver nanoparticles. *Energy Environ. Sci.* **2013**, *6*, 1949-1955.
101. Kim, A.; Won, Y.; Woo, K.; Kim, C.-H.; Moon, J., Highly Transparent Low Resistance ZnO/Ag Nanowire/ZnO Composite Electrode for Thin Film Solar Cells. *ACS Nano* **2013**, *7*, 1081-1091.
102. Kang, H.; Jung, S.; Jeong, S.; Kim, G.; Lee, K., Polymer-metal hybrid transparent electrodes for flexible electronics. *Nat. Commun.* **2015**, *6*, 6503.
103. Liao, S. H.; Jhuo, H. J.; Cheng, Y. S.; Chen, S. A., Fullerene derivative-doped zinc oxide nanofilm as the cathode of inverted polymer solar cells with low-bandgap polymer (PTB7-Th) for high performance. *Adv Mater* **2013**, *25*, 4766-71.
104. Kim, Y.; Ryu, T. I.; Ok, K.-H.; Kwak, M.-G.; Park, S.; Park, N.-G.; Han, C. J.; Kim, B. S.; Ko, M. J.; Son, H. J.; Kim, J.-W., Inverted Layer-By-Layer Fabrication of an Ultraflexible and Transparent Ag Nanowire/Conductive Polymer Composite Electrode for Use in High-Performance Organic Solar Cells. *Adv. Funct. Mater.* **2015**, *25*, 4580-4589.
105. Bundgaard, E.; Livi, F.; Hagemann, O.; Carlé, J. E.; Helgesen, M.; Heckler, I. M.; Zawacka, N. K.; Angmo, D.; Larsen-Olsen, T. T.; dos Reis Benatto, G. A.; Roth, B.; Madsen, M. V.;

- Andersson, M. R.; Jørgensen, M.; Søndergaard, R. R.; Krebs, F. C., Matrix Organization and Merit Factor Evaluation as a Method to Address the Challenge of Finding a Polymer Material for Roll Coated Polymer Solar Cells. *Adv. Energy Mater* **2015**, *5*, 1402186-n/a.
106. Søndergaard, R.; Hösel, M.; Angmo, D.; Larsen-Olsen, T. T.; Krebs, F. C., Roll-to-roll fabrication of polymer solar cells. *Mater. Today* **2012**, *15*, 36-49.
107. Chen, H.-Y.; Hou, J.; Zhang, S.; Liang, Y.; Yang, G.; Yang, Y.; Yu, L.; Wu, Y.; Li, G., Polymer solar cells with enhanced open-circuit voltage and efficiency. *Nat. Photonics* **2009**, *3*, 649-653.
108. Choi, H.; Ko, S. J.; Kim, T.; Morin, P. O.; Walker, B.; Lee, B. H.; Leclerc, M.; Kim, J. Y.; Heeger, A. J., Small-bandgap polymer solar cells with unprecedented short-circuit current density and high fill factor. *Adv. Mater.* **2015**, *27*, 3318-24.
109. Dou, L.; You, J.; Yang, J.; Chen, C.-C.; He, Y.; Murase, S.; Moriarty, T.; Emery, K.; Li, G.; Yang, Y., Tandem polymer solar cells featuring a spectrally matched low-bandgap polymer. *Nat. Photonics* **2012**, *6*, 180-185.
110. Yang, Y.; Chen, W.; Dou, L.; Chang, W.-H.; Duan, H.-S.; Bob, B.; Li, G.; Yang, Y., High-performance multiple-donor bulk heterojunction solar cells. *Nat. Photonics* **2015**, *9*, 190-198.
111. Kim, J. Y.; Lee, K.; Coates, N. E.; Moses, D.; Nguyen, T.-Q.; Dante, M.; Heeger, A. J., Efficient Tandem Polymer Solar Cells Fabricated by All-Solution Processing. *Science* **2007**, *317*, 222-225.
112. Heo, M.; Cho, H.; Jung, J.-W.; Jeong, J.-R.; Park, S.; Kim, J. Y., High-Performance Organic Optoelectronic Devices Enhanced by Surface Plasmon Resonance. *Adv. Mat.* **2011**, *23*, 5689-5693.
113. Kim, J. Y.; Kim, S. H.; Lee, H. H.; Lee, K.; Ma, W.; Gong, X.; Heeger, A. J., New Architecture for High-Efficiency Polymer Photovoltaic Cells Using Solution-Based Titanium Oxide as an Optical Spacer. *Adv. Mat.* **2006**, *18*, 572-576.
114. Atwater, H. A.; Polman, A., Plasmonics for improved photovoltaic devices. *Nat. Mater.* **2010**, *9*, 205-13.
115. Niesen, B.; Rand, B. P.; Van Dorpe, P.; Cheyns, D.; Tong, L.; Dmitriev, A.; Heremans, P., Plasmonic Efficiency Enhancement of High Performance Organic Solar Cells with a Nanostructured Rear Electrode. *Adv. Energy Mat.* **2013**, *3*, 145-150.
116. Jung, K.; Song, H.-J.; Lee, G.; Ko, Y.; Ahn, K.; Choi, H.; Kim, J. Y.; Ha, K.; Song, J.; Lee, J.-K.; Lee, C.; Choi, M., Plasmonic Organic Solar Cells Employing Nanobump Assembly via Aerosol-Derived Nanoparticles. *ACS Nano* **2014**, *8*, 2590-2601.
117. Lin, L.; Xie, Y.; Wang, S.; Wu, W.; Niu, S.; Wen, X.; Wang, Z. L., Triboelectric active sensor array for self-powered static and dynamic pressure detection and tactile imaging. *ACS nano* **2013**, *7*, 8266-8274.

118. Choi, H.; Ko, S.-J.; Choi, Y.; Joo, P.; Kim, T.; Lee, B. R.; Jung, J.-W.; Choi, H. J.; Cha, M.; Jeong, J.-R.; Hwang, I.-W.; Song, M. H.; Kim, B.-S.; Kim, J. Y., Versatile surface plasmon resonance of carbon-dot-supported silver nanoparticles in polymer optoelectronic devices. *Nat. Photonics* **2013**, *7*, 732-738.
119. Kim, C.-H.; Cha, S.-H.; Kim, S. C.; Song, M.; Lee, J.; Shin, W. S.; Moon, S.-J.; Bahng, J. H.; Kotov, N. A.; Jin, S.-H., Silver Nanowire Embedded in P3HT:PCBM for High-Efficiency Hybrid Photovoltaic Device Applications. *ACS Nano* **2011**, *5*, 3319-3325.
120. Wang, D. H.; Park, K. H.; Seo, J. H.; Seifter, J.; Jeon, J. H.; Kim, J. K.; Park, J. H.; Park, O. O.; Heeger, A. J., Enhanced Power Conversion Efficiency in PCDTBT/PC70BM Bulk Heterojunction Photovoltaic Devices with Embedded Silver Nanoparticle Clusters. *Adv. Energy Mat.* **2011**, *1*, 766-770.
121. Li, X.; Choy, W. C. H.; Lu, H.; Sha, W. E. I.; Ho, A. H. P., Efficiency Enhancement of Organic Solar Cells by Using Shape-Dependent Broadband Plasmonic Absorption in Metallic Nanoparticles. *Adv. Funct. Mat.* **2013**, *23*, 2728-2735.
122. Erwin, W. R.; Zarick, H. F.; Talbert, E. M.; Bardhan, R., Light trapping in mesoporous solar cells with plasmonic nanostructures. *Energy Environ. Sci.* **2016**, *9*, 1577-1601.
123. Lu, L.; Luo, Z.; Xu, T.; Yu, L., Cooperative plasmonic effect of Ag and Au nanoparticles on enhancing performance of polymer solar cells. *Nano Lett.* **2013**, *13*, 59-64.
124. Choi, H.; Lee, J.-P.; Ko, S.-J.; Jung, J.-W.; Park, H.; Yoo, S.; Park, O.; Jeong, J.-R.; Park, S.; Kim, J. Y., Multipositional Silica-Coated Silver Nanoparticles for High-Performance Polymer Solar Cells. *Nano Lett.* **2013**, *13*, 2204-2208.
125. Jeong, S.-H.; Choi, H.; Kim, J. Y.; Lee, T.-W., Silver-Based Nanoparticles for Surface Plasmon Resonance in Organic Optoelectronics. *Part. Part. Syst. Charact.* **2015**, *32* (2), 164-175.
126. Li, X.; Choy, W. C.; Huo, L.; Xie, F.; Sha, W. E.; Ding, B.; Guo, X.; Li, Y.; Hou, J.; You, J.; Yang, Y., Dual plasmonic nanostructures for high performance inverted organic solar cells. *Adv. Mater.* **2012**, *24*, 3046-52.
127. Krantz, J.; Richter, M.; Spallek, S.; Spiecker, E.; Brabec, C. J., Solution-Processed Metallic Nanowire Electrodes as Indium Tin Oxide Replacement for Thin-Film Solar Cells. *Adv. Funct. Mater.* **2011**, *21*, 4784-4787.
128. Knight, M. W.; Grady, N. K.; Bardhan, R.; Hao, F.; Nordlander, P.; Halas, N. J., Nanoparticle-Mediated Coupling of Light into a Nanowire. *Nano Lett.* **2007**, *7*, 2346-2350.
129. Pan, D.; Wei, H.; Jia, Z.; Xu, H., Mode Conversion of Propagating Surface Plasmons in Nanophotonic Networks Induced by Structural Symmetry Breaking. *Sci. Rep.* **2014**, *4*.
130. Hao, F.; Nordlander, P., Plasmonic coupling between a metallic nanosphere and a thin metallic wire. *Appl. Phys. Lett.* **2006**, *89*, 103101.

131. Kang, S.; Kim, T.; Cho, S.; Lee, Y.; Choe, A.; Walker, B.; Ko, S. J.; Kim, J. Y.; Ko, H., Capillary Printing of Highly Aligned Silver Nanowire Transparent Electrodes for High-Performance Optoelectronic Devices. *Nano Lett.* **2015**, *15*, 7933-7942.
132. Mock, J. J.; Hill, R. T.; Degiron, A.; Zauscher, S.; Chilkoti, A.; Smith, D. R., Distance-Dependent Plasmon Resonant Coupling between a Gold Nanoparticle and Gold Film. *Nano Lett.* **2008**, *8*, 2245-2252.
133. Park, B.; Bae, I. G.; Huh, Y. H., Aligned silver nanowire-based transparent electrodes for engineering polarisation-selective optoelectronics. *Sci. Rep.* **2016**, *6*, 19485.
134. Akimov, A. V.; Mukherjee, A.; Yu, C. L.; Chang, D. E.; Zibrov, A. S.; Hemmer, P. R.; Park, H.; Lukin, M. D., Generation of single optical plasmons in metallic nanowires coupled to quantum dots. *Nature* **2007**, *450*, 402-6.
135. Hutchison, J. A.; Centeno, S. P.; Odaka, H.; Fukumura, H.; Hofkens, J.; Uji-i, H., Subdiffraction Limited, Remote Excitation of Surface Enhanced Raman Scattering. *Nano Lett.* **2009**, *9*, 995-1001.
136. Wei, H.; Hao, F.; Huang, Y.; Wang, W.; Nordlander, P.; Xu, H., Polarization Dependence of Surface-Enhanced Raman Scattering in Gold Nanoparticle–Nanowire Systems. *Nano Lett.* **2008**, *8*, 2497-2502.
137. Sun, Y.; Yin, Y.; Mayers, B. T.; Herricks, T.; Xia, Y., Uniform Silver Nanowires Synthesis by Reducing AgNO₃ with Ethylene Glycol in the Presence of Seeds and Poly(Vinyl Pyrrolidone). *Chem. Mater.* **2002**, *14*, 4736-4745.
138. Ko, S.-J.; Choi, H.; Lee, W.; Kim, T.; Lee, B. R.; Jung, J.-W.; Jeong, J.-R.; Song, M. H.; Lee, J. C.; Woo, H. Y.; Kim, J. Y., Highly efficient plasmonic organic optoelectronic devices based on a conducting polymer electrode incorporated with silver nanoparticles. *Energy Environ. Sci.* **2013**, *6*, 1949-1955.
139. Mat Teridi, M. A.; Sookhakian, M.; Basirun, W. J.; Zakaria, R.; Schneider, F. K.; da Silva, W. J.; Kim, J.; Lee, S. J.; Kim, H. P.; Mohd Yusoff, A. R. b.; Jang, J., Plasmon enhanced organic devices utilizing highly ordered nanoimprinted gold nanodisks and nitrogen doped graphene. *Nanoscale* **2015**, *7*, 7091-7100.
140. Kaltenbrunner, M.; Adam, G.; Glowacki, E. D.; Drack, M.; Schwodiauer, R.; Leonat, L.; Apaydin, D. H.; Groiss, H.; Scharber, M. C.; White, M. S.; Sariciftci, N. S.; Bauer, S., Flexible high power-per-weight perovskite solar cells with chromium oxide-metal contacts for improved stability in air. *Nat. Mater.* **2015**, *14*, 1032-9.
141. Schubert, M. B.; Werner, J. H., Flexible solar cells for clothing. *Mater. today* **2006**, *9*, 42-50.
142. Pan, S.; Yang, Z.; Chen, P.; Deng, J.; Li, H.; Peng, H., Wearable solar cells by stacking textile electrodes. *Angew. Chem.* **2014**, *126*, 6224-6228.

143. Liu, Z.; You, P.; Xie, C.; Tang, G.; Yan, F., Ultrathin and flexible perovskite solar cells with graphene transparent electrodes. *Nano Energy* **2016**, *28*, 151-157.
144. Zhang, X.; Öberg, V. A.; Du, J.; Liu, J.; Johansson, E. M., Extremely lightweight and ultra-flexible infrared light-converting quantum dot solar cells with high power-per-weight output using a solution-processed bending durable silver nanowire-based electrode. *Energy Environ. Sci.* **2018**, *11*, 354-364..
145. Kaltenbrunner, M.; White, M. S.; Glowacki, E. D.; Sekitani, T.; Someya, T.; Sariciftci, N. S.; Bauer, S., Ultrathin and lightweight organic solar cells with high flexibility. *Nat. Commun.* **2012**, *3*, 770.
146. Li, Y.; Meng, L.; Yang, Y. M.; Xu, G.; Hong, Z.; Chen, Q.; You, J.; Li, G.; Yang, Y.; Li, Y., High-efficiency robust perovskite solar cells on ultrathin flexible substrates. *Nat. Commun.* **2016**, *7*, 10214.
147. Kojima, A.; Teshima, K.; Shirai, Y.; Miyasaka, T., Organometal Halide Perovskites as Visible-Light Sensitizers for Photovoltaic Cells. *J. Am. Chem. Soc.* **2009**, *131*, 6050-6051.
148. Lee, M. M.; Teuscher, J.; Miyasaka, T.; Murakami, T. N.; Snaith, H. J., Efficient Hybrid Solar Cells Based on Meso-Superstructured Organometal Halide Perovskites. *Science* **2012**, *338*, 643-647.
149. Johnston, M. B.; Herz, L. M., Hybrid Perovskites for Photovoltaics: Charge-Carrier Recombination, Diffusion, and Radiative Efficiencies. *Acc. Chem. Res.* **2016**, *49*, 146-154.
150. Liu, T.; Chen, K.; Hu, Q.; Zhu, R.; Gong, Q., Inverted Perovskite Solar Cells: Progresses and Perspectives. *Adv. Energy Mater.* **2016**, *6*, 1600457.
151. Bai, Y.; Meng, X.; Yang, S., Interface Engineering for Highly Efficient and Stable Planar p-i-n Perovskite Solar Cells. *Adv. Energy Mater.* **2017**, *8*, 1701883.
152. Guo, F.; Azimi, H.; Hou, Y.; Przybilla, T.; Hu, M.; Bronnbauer, C.; Langner, S.; Spiecker, E.; Forberich, K.; Brabec, C. J., High-performance semitransparent perovskite solar cells with solution-processed silver nanowires as top electrodes. *Nanoscale* **2015**, *7*, 1642-1649.
153. Kim, A.; Lee, H.; Kwon, H.-C.; Jung, H. S.; Park, N.-G.; Jeong, S.; Moon, J., Fully solution-processed transparent electrodes based on silver nanowire composites for perovskite solar cells. *Nanoscale* **2016**, *8*, 6308-6316.
154. Lee, E.; Ahn, J.; Kwon, H. C.; Ma, S.; Kim, K.; Yun, S.; Moon, J., All-Solution-Processed Silver Nanowire Window Electrode-Based Flexible Perovskite Solar Cells Enabled with Amorphous Metal Oxide Protection. *Adv. Energy Mater.* **2018**, *8*, 1702182.
155. Jeon, I.; Seo, S.; Sato, Y.; Delacou, C.; Anisimov, A.; Suenaga, K.; Kauppinen, E. I.; Maruyama, S.; Matsuo, Y. Perovskite Solar Cells using Carbon Nanotubes both as Cathode and Anode. *J. Phys. Chem. C* **2017**, *121*, 25743-25749.

156. Li, Z.; Kulkarni, S. A.; Boix, P. P.; Shi, E.; Cao, A.; Fu, K.; Batabyal, S. K.; Zhang, J.; Xiong, Q.; Wong, L. H., Laminated carbon nanotube networks for metal electrode-free efficient perovskite solar cells. *ACS nano* **2014**, *8*, 6797-6804.
157. Luo, Q.; Ma, H.; Hou, Q.; Li, Y.; Ren, J.; Dai, X.; Yao, Z.; Zhou, Y.; Xiang, L.; Du, H., All-Carbon-Electrode-Based Endurable Flexible Perovskite Solar Cells. *Adv. Funct. Mater.* **2018**, *28*, 1706777 .
158. Bryant, D.; Greenwood, P.; Troughton, J.; Wijdekop, M.; Carnie, M.; Davies, M.; Wojciechowski, K.; Snaith, H. J.; Watson, T.; Worsley, D., A transparent conductive adhesive laminate electrode for high-efficiency organic-inorganic lead halide perovskite solar cells. *Adv. Mater.* **2014**, *26*, 7499-7504.
159. Cho, S.; Kang, S.; Pandya, A.; Shanker, R.; Khan, Z.; Lee, Y.; Park, J.; Craig, S. L.; Ko, H., Large-area cross-aligned silver nanowire electrodes for flexible, transparent, and force-sensitive mechanochromic touch screens. *ACS nano* **2017**, *11*, 4346-4357.
160. Xiong, W.; Liu, H.; Chen, Y.; Zheng, M.; Zhao, Y.; Kong, X.; Wang, Y.; Zhang, X.; Kong, X.; Wang, P., Highly Conductive, Air-Stable Silver Nanowire@ Ionogel Composite Films toward Flexible Transparent Electrodes. *Adv. Mater.* **2016**, *28*, 7167-7172.
161. Burschka, J.; Pellet, N.; Moon, S.-J.; Humphry-Baker, R.; Gao, P.; Nazeeruddin, M. K.; Grätzel, M., Sequential deposition as a route to high-performance perovskite-sensitized solar cells. *Nature* **2013**, *499*, 316.
162. Xiao, Z.; Dong, Q.; Bi, C.; Shao, Y.; Yuan, Y.; Huang, J., Solvent annealing of perovskite-induced crystal growth for photovoltaic-device efficiency enhancement. *Adv. Mater.* **2014**, *26*, 6503-6509.
163. Back, H.; Kim, J.; Kim, G.; Kim, T. K.; Kang, H.; Kong, J.; Lee, S. H.; Lee, K., Interfacial modification of hole transport layers for efficient large-area perovskite solar cells achieved via blade-coating. *Sol. Energy Mater. Sol. Cells* **2016**, *144*, 309-315.
164. Crist, B. V., A review of XPS data-banks. *XPS Rep.* **2007**, *1* (1).
165. Xue, Q.; Liu, M.; Li, Z.; Yan, L.; Hu, Z.; Zhou, J.; Li, W.; Jiang, X. F.; Xu, B.; Huang, F., Efficient and Stable Perovskite Solar Cells via Dual Functionalization of Dopamine Semiquinone Radical with Improved Trap Passivation Capabilities. *Adv. Funct. Mater.* **2018**, *28*, 1707444.
166. Kim, H.-B.; Choi, H.; Jeong, J.; Kim, S.; Walker, B.; Song, S.; Kim, J. Y., Mixed solvents for the optimization of morphology in solution-processed, inverted-type perovskite/fullerene hybrid solar cells. *Nanoscale* **2014**, *6*, 6679-6683.
167. Eunsong, L.; Jihoon, A.; Hyeok-Chan, K.; Sunihl, M.; Kyungmi, K.; Seongcheol, Y.; Joocho, M., All-Solution-Processed Silver Nanowire Window Electrode-Based Flexible Perovskite Solar

- Cells Enabled with Amorphous Metal Oxide Protection. *Adv. Energy Mater.* **2018**, 8 (9), 1702182.
168. Yunsheng, F.; Zhicong, W.; Jia, L.; Fangyuan, J.; Kui, Z.; Yanli, Z.; Yinhua, Z.; Jun, Z.; Bin, H., High-Performance Hazy Silver Nanowire Transparent Electrodes through Diameter Tailoring for Semitransparent Photovoltaics. *Adv. Funct. Mater.* **2018**, 28, 1705409.
169. Li, Y.; Meng, L.; Yang, Y.; Xu, G.; Hong, Z.; Chen, Q.; You, J.; Li, G.; Yang, Y.; Li, Y., High-efficiency robust perovskite solar cells on ultrathin flexible substrates. *Nat. Commun.* **2016**, 7, 10214.
170. Han, J.; Yuan, S.; Liu, L.; Qiu, X.; Gong, H.; Yang, X.; Li, C.; Hao, Y.; Cao, B., Fully indium-free flexible Ag nanowires/ZnO:F composite transparent conductive electrodes with high haze. *J. Mater. Chem. A* **2015**, 3, 5375-5384.
171. Liu, T.; Liu, W.; Zhu, Y.; Wang, S.; Wu, G.; Chen, H., All solution processed perovskite solar cells with Ag@Au nanowires as top electrode. *Sol. Energy Mater. Sol. Cells* **2017**, 171, 43-49.
172. Han, T. H.; Lee, Y.; Choi, M. R.; Woo, S. H.; Bae, S. H.; Hong, B. H.; Ahn, J. H.; Lee, T. W., Extremely efficient flexible organic light-emitting diodes with modified graphene anode. *Nat. Photonics* **2012**, 6, 105-110.
173. Li, N.; Oida, S.; Tulevski, G. S.; Han, S. J.; Hannon, J. B.; Sadana, D. K.; Chen, T. C., Efficient and bright organic light-emitting diodes on single-layer graphene electrodes. *Nat Commun* **2013**, 4, 2294.
174. Guo, C. F.; Ren, Z. F., Flexible transparent conductors based on metal nanowire networks. *Mater. Today* **2015**, 18, 143-154.
175. Mayousse, C.; Celle, C.; Fraczkiewicz, A.; Simonato, J.-P., Stability of silver nanowire based electrodes under environmental and electrical stresses. *Nanoscale* **2015**, 7, 2107-2115.
176. Selzer, F.; Weiß, N.; Kneppe, D.; Bormann, L.; Sachse, C.; Gaponik, N.; Eychmüller, A.; Leo, K.; Müller-Meskamp, L., A spray-coating process for highly conductive silver nanowire networks as the transparent top-electrode for small molecule organic photovoltaics. *Nanoscale* **2015**, 7, 2777-2783.
177. Kim, T.; Kim, Y. W.; Lee, H. S.; Kim, H.; Yang, W. S.; Suh, K. S., Uniformly Interconnected Silver-Nanowire Networks for Transparent Film Heaters. *Adv. Funct. Mater.* **2013**, 23, 1250-1255.
178. Lee, Y.; Min, S. Y.; Kim, T. S.; Jeong, S. H.; Won, J. Y.; Kim, H.; Xu, W.; Jeong, J. K.; Lee, T. W., Versatile Metal Nanowiring Platform for Large-Scale Nano-and Opto-Electronic Devices. *Adv. Mater.* **2016**, 28, 9109-9116.
179. Rathmell, A. R.; Bergin, S. M.; Hua, Y. L.; Li, Z. Y.; Wiley, B. J., The Growth Mechanism of Copper Nanowires and Their Properties in Flexible, Transparent Conducting Films. *Adv. Mater.*

- 2010**, 22, 3558.
180. Koga, H.; Nogi, M.; Komoda, N.; Nge, T. T.; Sugahara, T.; Suganuma, K., Uniformly connected conductive networks on cellulose nanofiber paper for transparent paper electronics. *NPG Asia Mater.* **2014**, 6, e93.
 181. Bergin, S. M.; Chen, Y. H.; Rathmell, A. R.; Charbonneau, P.; Li, Z. Y.; Wiley, B. J., The effect of nanowire length and diameter on the properties of transparent, conducting nanowire films. *Nanoscale* **2012**, 4, 1996-2004.
 182. Huang, J. X.; Fan, R.; Connor, S.; Yang, P. D., One-step patterning of aligned nanowire arrays by programmed dip coating. *Angew. Chem. Int. Edit.* **2007**, 46, 2414-2417.
 183. Smith, P. A.; Nordquist, C. D.; Jackson, T. N.; Mayer, T. S.; Martin, B. R.; Mbindyo, J.; Mallouk, T. E., Electric-field assisted assembly and alignment of metallic nanowires. *Appl Phys Lett.* **2000**, 77, 1399-1401.
 184. Shi, H. Y.; Hu, B.; Yu, X. C.; Zhao, R. L.; Ren, X. F.; Liu, S. L.; Liu, J. W.; Feng, M.; Xu, A. W.; Yu, S. H., Ordering of Disordered Nanowires: Spontaneous Formation of Highly Aligned, Ultralong Ag Nanowire Films at Oil-Water-Air Interface. *Adv. Funct. Mater.* **2010**, 20, 958-964.
 185. Duan, S. K.; Niu, Q. L.; Wei, J. F.; He, J. B.; Yin, Y. A.; Zhang, Y., Water-bath assisted convective assembly of aligned silver nanowire films for transparent electrodes. *Phys. Chem. Chem. Phys.* **2015**, 17, 8106-8112.
 186. Lee, H.; Seong, B.; Kim, J.; Jang, Y.; Byun, D., Direct Alignment and Patterning of Silver Nanowires by Electrohydrodynamic Jet Printing. *Small* **2014**, 10, 3918-3922.
 187. Ko, Y.; Song, S. K.; Kim, N. H.; Chang, S. T., Highly Transparent and Stretchable Conductors Based on a Directional Arrangement of Silver Nanowires by a Microliter-Scale Solution Process. *Langmuir* **2016**, 32, 366-373.
 188. Le Berre, M.; Chen, Y.; Baigl, D., From Convective Assembly to Landau-Levich Deposition of Multilayered Phospholipid Films of Controlled Thickness. *Langmuir* **2009**, 25, 2554-2557.
 189. Freer, E. M.; Grachev, O.; Duan, X.; Martin, S.; Stumbo, D. P., High-yield self-limiting single-nanowire assembly with dielectrophoresis. *Nat. Nanotechnol.* **2010**, 5, 525-530.
 190. Ko, H.; Peleshanko, S.; Tsukruk, V. V., Combing and bending of carbon nanotube arrays with confined microfluidic flow on patterned surfaces. *J. Phys. Chem. B* **2004**, 108, 4385-4393.
 191. Luu, Q. N.; Doorn, J. M.; Berry, M. T.; Jiang, C. Y.; Lin, C. K.; May, P. S., Preparation and optical properties of silver nanowires and silver-nanowire thin films. *J. Colloid. Interf. Sci.* **2011**, 356, 151-158.
 192. Badoga, S.; Pattanayek, S. K.; Kumar, A.; Pandey, L. M., Effect of polymer-surfactant structure on its solution viscosity. *Asia-Pac J. Chem. Eng.* **2011**, 6, 78-84.
 193. Kowalski, D.; Schmuki, P., Polypyrrole self-organized nanopore arrays formed by controlled

- electropolymerization in TiO₂ nanotube template. *Chem. Commun.* **2010**, *46*, 8585-8587.
194. Huang, S. W.; Neoh, K. G.; Kang, E. T.; Han, H. S.; Tan, K. L., Palladium-containing polyaniline and polypyrrole microparticles. *J. Mater. Chem.* **1998**, *8*, 1743-1748.
195. Sun, Q.; Lee, S. J.; Kang, H.; Gim, Y.; Park, H. S.; Cho, J. H., Positively-charged reduced graphene oxide as an adhesion promoter for preparing a highly-stable silver nanowire film. *Nanoscale* **2015**, *7*, 6798-6804.
196. Jiang, P.; Li, S. Y.; Xie, S. S.; Gao, Y.; Song, L., Machinable long PVP-stabilized silver nanowires. *Chem.-Eur. J.* **2004**, *10*, 4817-4821.
197. Liu, J. W.; Wang, J. L.; Wang, Z. H.; Huang, W. R.; Yu, S. H., Manipulating Nanowire Assembly for Flexible Transparent Electrodes. *Angew. Chem. Int. Edit.* **2014**, *53*, 13477-13482.
198. Choi, C. H.; Kim, C. J., Large slip of aqueous liquid flow over a nanoengineered superhydrophobic surface. *Phys. Rev. Lett.* **2006**, *96*, 066001.
199. Yu, H. J.; Zhang, P. W., A kinetic-hydrodynamic simulation of microstructure of liquid crystal polymers in plane shear flow. *J. Non-Newton. Fluid.* **2007**, *141*, 116-127.
200. Kuncicky, D. M.; Naik, R. R.; Velev, O. D., Rapid deposition and long-range alignment of nanocoatings and arrays of electrically conductive wires from tobacco mosaic virus. *Small* **2006**, *2*, 1462-1466.
201. Janneck, R.; Vercesi, F.; Heremans, P.; Genoe, J.; Rolin, C., Predictive Model for the Meniscus-Guided Coating of High-Quality Organic Single-Crystalline Thin Films. *Adv. Mater.* **2016**, *28*, 8007-8013.
202. Khim, D. Y.; Han, H.; Baeg, K. J.; Kim, J. W.; Kwak, S. W.; Kim, D. Y.; Noh, Y. Y., Simple Bar-Coating Process for Large-Area, High-Performance Organic Field-Effect Transistors and Ambipolar Complementary Integrated Circuits. *Adv. Mater.* **2013**, *25*, 4302-4308.
203. Doolittle, A. K., Studies in Newtonian Flow .1. The Dependence of the Viscosity of Liquids on Temperature. *J. Appl. Phys.* **1951**, *22*, 1031-1035.
204. Zhang, C. Y.; Zhang, X. J.; Zhang, X. H.; Fan, X.; Jie, J. S.; Chang, J. C.; Lee, C. S.; Zhang, W. J.; Lee, S. T., Facile one-step growth and patterning of aligned squaraine nanowires via evaporation-induced self-assembly. *Adv. Mater.* **2008**, *20*, 1716-+.
205. De, S.; King, P. J.; Lyons, P. E.; Khan, U.; Coleman, J. N., Size Effects and the Problem with Percolation in Nanostructured Transparent Conductors. *ACS Nano* **2010**, *4*, 7064-7072.
206. Li, B.; Ye, S. R.; Stewart, I. E.; Alvarez, S.; Wiley, B. J., Synthesis and Purification of Silver Nanowires To Make Conducting Films with a Transmittance of 99%. *Nano Lett.* **2015**, *1*, 6722-6726.
207. Wu, J.; Que, X. L.; Hu, Q.; Luo, D. Y.; Liu, T. H.; Liu, F.; Russell, T. P.; Zhu, R.; Gong, Q. H., Multi-Length Scaled Silver Nanowire Grid for Application in Efficient Organic Solar Cells. *Adv.*

- Funct. Mater.* **2016**, *26*, 4822-4828.
208. Davis, D. A.; Hamilton, A.; Yang, J. L.; Cremar, L. D.; Van Gough, D.; Potisek, S. L.; Ong, M. T.; Braun, P. V.; Martinez, T. J.; White, S. R.; Moore, J. S.; Sottos, N. R., Force-induced activation of covalent bonds in mechanoresponsive polymeric materials. *Nature* **2009**, *459*, 68-72.
 209. Gossweiler, G. R.; Hewage, G. B.; Soriano, G.; Wang, Q. M.; Welshofer, G. W.; Zhao, X. H.; Craig, S. L., Mechanochemical Activation of Covalent Bonds in Polymers with Full and Repeatable Macroscopic Shape Recovery. *ACS Macro Lett.* **2014**, *3*, 216-219.
 210. Wang, Q. M.; Gossweiler, G. R.; Craig, S. L.; Zhao, X. H., Cephalopod-inspired design of electro-mechano-chemically responsive elastomers for on-demand fluorescent patterning. *Nat. Commun.* **2014**, *5*, 4899.
 211. Gossweiler, G. R.; Brown, C. L.; Hewage, G. B.; Sapiro-Gheiler, E.; Trautman, W. J.; Welshofer, G. W.; Craig, S. L., Mechanochemically Active Soft Robots. *ACS Appl. Mater. Interfaces* **2015**, *7*, 22431-22435.
 212. Fang, X. L.; Zhang, H.; Chen, Y. J.; Lin, Y. J.; Xu, Y. Z.; Weng, W. G., Biomimetic Modular Polymer with Tough and Stress Sensing Properties. *Macromolecules* **2013**, *46*, 6566-6574.
 213. Wang, X.; Zhang, H.; Yu, R.; Dong, L.; Peng, D.; Zhang, A.; Zhang, Y.; Liu, H.; Pan, C.; Wang, Z. L., Dynamic pressure mapping of personalized handwriting by a flexible sensor matrix based on the mechanoluminescence process. *Adv. Mater.* **2015**, *27*, 2324-2331.
 214. Pan, L. J.; Chortos, A.; Yu, G. H.; Wang, Y. Q.; Isaacson, S.; Allen, R.; Shi, Y.; Dauskardt, R.; Bao, Z. N., An ultra-sensitive resistive pressure sensor based on hollow-sphere microstructure induced elasticity in conducting polymer film. *Nat. Commun.* **2014**, *5*, 3002.
 215. Park, J.; Kim, M.; Lee, Y.; Lee, H. S.; Ko, H., Fingertip skin-inspired microstructured ferroelectric skins discriminate static/dynamic pressure and temperature stimuli. *Sci. Adv.* **2015**, *1*, 1500661.
 216. Park, J.; Lee, Y.; Hong, J.; Ha, M.; Jung, Y. D.; Lim, H.; Kim, S. Y.; Ko, H., Giant Tunneling Piezoresistance of Composite Elastomers with Interlocked Microdome Arrays for Ultrasensitive and Multimodal Electronic Skins. *ACS Nano* **2014**, *8*, 4689-4697.
 217. Lee, H. S.; Chung, J.; Hwang, G. T.; Jeong, C. K.; Jung, Y.; Kwak, J. H.; Kang, H.; Byun, M.; Kim, W. D.; Hur, S.; Oh, S. H.; Lee, K. J., Flexible Inorganic Piezoelectric Acoustic Nanosensors for Biomimetic Artificial Hair Cells. *Adv. Funct. Mater.* **2014**, *24*, 6914-6921.
 218. Jang, J.; Lee, J.; Jang, J. H.; Choi, H., A Triboelectric-Based Artificial Basilar Membrane to Mimic Cochlear Tonotopy. *Adv. Healthc. Mater.* **2016**, *5*, 2481-2487.
 219. Tao, L. Q.; Tian, H.; Liu, Y.; Ju, Z. Y.; Pang, Y.; Chen, Y. Q.; Wang, D. Y.; Tian, X. G.; Yan, J. C.; Deng, N. Q.; Yang, Y.; Ren, T. L., An intelligent artificial throat with sound-sensing ability

- based on laser induced graphene. *Nat. Commun.* **2017**, *8*, 14579.
220. Bertrand, A. In *Applications and trends in wireless acoustic sensor networks: A signal processing perspective*, Communications and Vehicular Technology in the Benelux (SCVT), 2011 18th IEEE Symposium on, IEEE: 2011; pp 1-6.
221. Sidner, C. L.; Kidd, C. D.; Lee, C.; Lesh, N. In *Where to look: a study of human-robot engagement*, Proceedings of the 9th international conference on Intelligent user interfaces, ACM: 2004; pp 78-84.
222. Yang, J.; Chen, J.; Liu, Y.; Yang, W. Q.; Su, Y. J.; Wang, Z. L., Triboelectrification-Based Organic Film Nanogenerator for Acoustic Energy Harvesting and Self-Powered Active Acoustic Sensing. *ACS Nano* **2014**, *8*, 2649-2657.
223. Fan, X.; Chen, J.; Yang, J.; Bai, P.; Li, Z. L.; Wang, Z. L., Ultrathin, Rollable, Paper-Based Triboelectric Nanogenerator for Acoustic Energy Harvesting and Self-Powered Sound Recording. *ACS Nano* **2015**, *9*, 4236-4243.
224. Lang, C. H.; Fang, J.; Shao, H.; Ding, X.; Lin, T., High-sensitivity acoustic sensors from nanofibre webs. *Nat. Commun.* **2016**, *7*, 11108.
225. Park, B.; Kim, J.; Kang, D.; Jeong, C.; Kim, K. S.; Kim, J. U.; Yoo, P. J.; Kim, T. I., Dramatically Enhanced Mechanosensitivity and Signal-to-Noise Ratio of Nanoscale Crack-Based Sensors: Effect of Crack Depth. *Adv. Mater.* **2016**, *28*, 8130-8137.
226. Cheong, O. J.; Lee, J. S.; Kim, J. H.; Jang, J., High Performance Flexible Actuator of Urchin-Like ZnO Nanostructure/Polyvinylene fluoride Hybrid Thin Film with Graphene Electrodes for Acoustic Generator and Analyzer. *Small* **2016**, *12*, 2567-2574.
227. Li, W.; Torres, D.; Diaz, R.; Wang, Z. J.; Wu, C. S.; Wang, C.; Wang, Z. L.; Sepulveda, N., Nanogenerator-based dual-functional and self-powered thin patch loudspeaker or microphone for flexible electronics. *Nat. Commun.* **2017**, *8*, 15310.
228. Trung, T. Q.; Lee, N. E., Flexible and Stretchable Physical Sensor Integrated Platforms for Wearable Human-Activity Monitoring and Personal Healthcare. *Adv. Mater.* **2016**, *28*, 4338-4372.
229. Kaltenbrunner, M.; Sekitani, T.; Reeder, J.; Yokota, T.; Kuribara, K.; Tokuhara, T.; Drack, M.; Schwodiauer, R.; Graz, I.; Bauer-Gogonea, S.; Bauer, S.; Someya, T., An ultra-lightweight design for imperceptible plastic electronics. *Nature* **2013**, *499*, 458.
230. Melzer, M.; Kaltenbrunner, M.; Makarov, D.; Karnaushenko, D.; Karnaushenko, D.; Sekitani, T.; Someya, T.; Schmidt, O. G., Imperceptible magnetoelectronics. *Nat. Commun.* **2015**, *6*, 6080.
231. Yokota, T.; Zalar, P.; Kaltenbrunner, M.; Jinno, H.; Matsuhisa, N.; Kitanosako, H.; Tachibana, Y.; Yukita, W.; Koizumi, M.; Someya, T., Ultraflexible organic photonic skin. *Sci. Adv.* **2016**, *2*, 1501856.

232. White, M. S.; Kaltenbrunner, M.; Glowacki, E. D.; Gutnichenko, K.; Kettlgruber, G.; Graz, I.; Aazou, S.; Ulbricht, C.; Egbe, D. A. M.; Miron, M. C.; Major, Z.; Scharber, M. C.; Sekitani, T.; Someya, T.; Bauer, S.; Sariciftci, N. S., Ultrathin, highly flexible and stretchable PLEDs. *Nat. Photonics* **2013**, *7*, 811-816.
233. Kim, D. H.; Viventi, J.; Amsden, J. J.; Xiao, J. L.; Vigeland, L.; Kim, Y. S.; Blanco, J. A.; Panilaitis, B.; Frechette, E. S.; Contreras, D.; Kaplan, D. L.; Omenetto, F. G.; Huang, Y. G.; Hwang, K. C.; Zakin, M. R.; Litt, B.; Rogers, J. A., Dissolvable films of silk fibroin for ultrathin conformal bio-integrated electronics. *Nat. Mater.* **2010**, *9*, 511-517.
234. Park, Y. J.; Lee, S. K.; Kim, M. S.; Kim, H.; Ahn, J. H. *ACS Nano* **2014**, *8*, 7655-7662.
235. Park, Y. J.; Lee, S. K.; Kim, M. S.; Kim, H.; Ahn, J. H., Graphene-Based Conformal Devices. *ACS Nano* **2014**, *8* (8), 7655-7662.
236. Pang, C.; Koo, J. H.; Nguyen, A.; Caves, J. M.; Kim, M. G.; Chortos, A.; Kim, K.; Wang, P. J.; Tok, J. B. H.; Bao, Z. A., Highly Skin-Conformal Microhairy Sensor for Pulse Signal Amplification. *Adv. Mater.* **2015**, *27*, 634-640.
237. Kwak, M. K.; Jeong, H. E.; Suh, K. Y., Rational Design and Enhanced Biocompatibility of a Dry Adhesive Medical Skin Patch. *Adv. Mater.* **2011**, *23*, 3949-+.
238. Jiang, C. Y.; Markutsya, S.; Pikus, Y.; Tsukruk, V. V., Freely suspended nanocomposite membranes as highly sensitive sensors. *Nat. Mater.* **2004**, *3*, 721-728.
239. Rogers, J. A.; Lagally, M. G.; Nuzzo, R. G., Synthesis, assembly and applications of semiconductor nanomembranes. *Nature* **2011**, *477*, 45-53.
240. Gunawidjaja, R.; Jiang, C. Y.; Peleshanko, S.; Ornatska, M.; Singamaneni, S.; Tsukruk, V. V., Flexible and robust 2D arrays of silver nanowires encapsulated within freestanding layer-by-layer films. *Adv. Funct. Mater.* **2006**, *16*, 2024-2034.
241. Kulkarni, D. D.; Choi, I.; Singamaneni, S.; Tsukruk, V. V., Graphene Oxide-Polyelectrolyte Nanomembranes. *ACS Nano* **2010**, *4*, 4667-4676.
242. Mamedov, A. A.; Kotov, N. A.; Prato, M.; Guldi, D. M.; Wicksted, J. P.; Hirsch, A., Molecular design of strong single-wall carbon nanotube/polyelectrolyte multilayer composites. *Nat. Mater.* **2002**, *1*, 190-194.
243. Lee, S.; Shin, S.; Lee, S.; Seo, J.; Lee, J.; Son, S.; Cho, H. J.; Algadi, H.; Al-Sayari, S.; Kim, D. E.; Lee, T., Ag Nanowire Reinforced Highly Stretchable Conductive Fibers for Wearable Electronics. *Adv. Funct. Mater.* **2015**, *25*, 3114-3121.
244. Sim, H.; Bok, S.; Kim, B.; Kim, M.; Lim, G. H.; Cho, S. M.; Lim, B., Organic-Stabilizer-Free Polyol Synthesis of Silver Nanowires for Electrode Applications. *Angew. Chem. Int. Edit.* **2016**, *55*, 11814-11818.
245. Gunawidjaja, R.; Jiang, C. Y.; Ko, H. H.; Tsukruk, V. V., Freestanding 2D arrays of silver

- nanorods. *Adv. Mater.* **2006**, *18*, 2895.
246. Hassler, C.; Boretius, T.; Stieglitz, T., Polymers for Neural Implants. *J. Polym. Sci. Pol. Phys.* **2011**, *49*, 18-33.
247. Qian, D.; Dickey, E. C.; Andrews, R.; Rantell, T., Load transfer and deformation mechanisms in carbon nanotube-polystyrene composites. *Appl. Phys. Lett.* **2000**, *76*, 2868-2870.
248. Podsiadlo, P.; Kaushik, A. K.; Arruda, E. M.; Waas, A. M.; Shim, B. S.; Xu, J. D.; Nandivada, H.; Pumphlin, B. G.; Lahann, J.; Ramamoorthy, A.; Kotov, N. A., Ultrastrong and stiff layered polymer nanocomposites. *Science* **2007**, *318*, 80-83.
249. Huang, J.; Juszkiwicz, M.; De Jeu, W. H.; Cerda, E.; Emrick, T.; Menon, N.; Russell, T. P., Capillary wrinkling of floating thin polymer films. *Science* **2007**, *317*, 650-653.
250. Bokobza, L., Multiwall carbon nanotube elastomeric composites: A review. *Polymer* **2007**, *48*, 4907-4920.
251. Xiao, L.; Chen, Z.; Feng, C.; Liu, L.; Bai, Z.-Q.; Wang, Y.; Qian, L.; Zhang, Y.; Li, Q.; Jiang, K., Flexible, stretchable, transparent carbon nanotube thin film loudspeakers. *Nano Lett.* **2008**, *8*, 4539-4545.
252. Suk, J. W.; Kirk, K.; Hao, Y.; Hall, N. A.; Ruoff, R. S., Thermoacoustic sound generation from monolayer graphene for transparent and flexible sound sources. *Adv. Mater.* **2012**, *24*, 6342-6347.
253. Kim, C. S.; Hong, S. K.; Lee, J. M.; Kang, D. S.; Cho, B. J.; Choi, J. W., Free-Standing Graphene Thermophone on a Polymer-Mesh Substrate. *Small* **2016**, *12*, 185-189.
254. Lin, L.; Xie, Y.; Wang, S.; Wu, W.; Niu, S.; Wen, X.; Wang, Z. L., Triboelectric active sensor array for self-powered static and dynamic pressure detection and tactile imaging. *ACS nano* **2013**, *7*, 8266-8274.
255. Niu, S.; Wang, S.; Lin, L.; Liu, Y.; Zhou, Y. S.; Hu, Y.; Wang, Z. L., Theoretical study of contact-mode triboelectric nanogenerators as an effective power source. *Energy Environ. Sci.* **2013**, *6*, 3576-3583.

*Chapter 2 is reproduced in part with permission of “Capillary Printing of Highly Aligned Silver Nanowire Transparent Electrodes for High-Performance Optoelectronic Devices, *Nano Lett.* 2015, 15, 7933”. Copyright 2015 American Chemical Society

*Chapter 3 is reproduced in part with permission of “Nanoparticle-Enhanced Silver Nanowire Plasmonic Electrodes for High-Performance Organic Optoelectronic Devices, *Adv. Mater.* 2018 (DOI: 10.1002/adma.201800659)”. Copyright 2018 John Wiley & Sons, Inc.

*Chapter 5 is reproduced in part with permission of “Large-Area Cross-aligned Silver Nanowire Electrodes for Flexible, Transparent, and Force-Sensitive Mechanochromic Touch Screens, *ACS Nano*, 2017, 11, 4346.”. Copyright 2017 American Chemical Society

*Chapter 6 is reproduced in part with permission of “Ultrathin, Transparent, and Conductive Nanomembrane with Orthogonal Silver Nanowire Array for Skin-Attachable Loudspeakers and Microphones, *Sci. Adv.* 2018”.

Appendix A: List of Achievements

The results of this dissertation have been published in: (†: equal contribution)

1. **Saewon Kang**†, Seungse Cho†, Ravi Shanker, Hochan Lee, Jonghwa Park, Doo-Seung Um, Youngoh Lee, Hyunhyub Ko*, “Ultrathin, Transparent, and Conductive Nano-membrane with Orthogonal Silver Nanowire Array for Skin-Attachable Loudspeakers and Microphones”, *Sci. Adv.* **2018**
2. Taehyo Kim†, **Sewon Kang**†, Jungwoo Heo, Seungse Cho, Jae Won Kim, Ayoung Choi, Bright Walker, Ravi Shanker, Hyunhyub Ko* and Jin Young Kim*, “Nanoparticle-Enhanced Silver Nanowire Plasmonic Electrodes for High-Performance Organic Optoelectronic Devices”, *Adv. Mater.* **2018 (DOI: 10.1002/adma.201800659)**
3. Seungse Cho†, **Saewon Kang**†, Ashish Pandya, Ravi Shanker, Ziyauddin Khan, Youngsu Lee, Jonghwa Park, Stephen L. Craig, and Hyunhyub Ko*, “Large-Area Cross-aligned Silver Nanowire Electrodes for Flexible, Transparent, and Force-Sensitive Mechanochromic Touch Screens” *ACS Nano*, **2017, 11, 4346.**
4. **Saewon Kang**†, Taehyo Kim†, Seungse Cho, Youngoh Lee, Ayoung Choe, Bright Walker, Seo-Jin Ko, Jin Young Kim, and Hyunhyub Ko*, “Capillary Printing of Highly Aligned Silver Nanowire Transparent Electrodes for High-Performance Optoelectronic Devices”, *Nano lett.*, **2015, 15, 7933**

The other related results have been published in:

1. Yoon Ho Lee, Tae Kyung Lee, Hongki Kim, Inho Song, Jiwon Lee, **Saewon Kang**, Hyunhyub Ko, Sang Kyu Kwak and Joon Hak Oh*, “A Flexible High-Performance Photoimaging Device Based on Bio-Inspired Hierarchical Multiple-Patterned Plasmonic Nanostructures”, *Small*. **2018, 14, 1703890**
2. Youngoh Lee, Jonghwa Park, Soowon Cho, Young-Eun Shin, Hochan Lee, Jinyoung Kim, Jinyoung Myoung, **Saewon Kang**, hyunhyub Ko*, “Flexible Ferroelectric Sensors with Ultrahigh Pressure Sensitivity and Linear Response over Exceptionally Broad Pressure Range”, *ACS Nano* **2018, 12, 4045**

Conference Presentation:

1. **Saewon Kang**, Seungse Cho and Hyunhyub Ko, “Aligned silver nanowire transparent electrodes for flexible electronic devices” *ACS spring 2017*, San Francisco, USA.
2. **Saewon Kang**, Taehyo Kim, Seungse Cho, Youngoh Lee, Ayoung Choe, Bright Walker, Seo-Jin Ko, Jin Young Kim, and Hyunhyub Ko, “Aligned Silver Nanowire Transparent Electrodes for High Performance Solar cells and Light Emitting Diodes” *MRS spring 2016*, Phoenix, USA
3. **Saewon Kang**, Seungse Cho, Youngoh Lee, Ayoung Choe and Hyunhyub Ko, “Solution printed, aligned silver nanowire arrays for high performance transparent electrodes” *MRS spring 2015*, San Francisco, USA. (Best Poster Nominee)
4. **Saewon Kang**, Taehyo Kim, Seungse Cho, Youngoh Lee, Ayoung Choe, Bright Walker, Seo-Jin Ko, Jin Young Kim, and Hyunhyub Ko, “Solution printed, highly aligned silver nanowire transparent electrodes for high performance photovoltaic devices” *ICAE 2015*, Jeju, South Korea

Honors and Awards:

1. The Outstanding Graduate Student Award presented by the Energy and Chemical Engineering Department of UNIST. December 2017
2. The Outstanding Graduate Student Award presented by the Energy and Chemical Engineering Department of UNIST. December 2015

Acknowledgements

First of all, I would like to thank my appreciations to Prof. Hyunhyub Ko. It is a great honor and fortune in my life to work under his guidance during my doctoral course. I have learned a lot of things from him, such as research ability, logic, writing skill, and research ethics. In addition, he gave me great support, such as many opportunities for novel research idea and kind advice. My thesis works would not have been possible without his support.

And, I would like to thank my committee members, Prof. Jin Young Kim, Prof. Sang Kyu Kwak, Prof. Myoung Hoon Song and Prof. Kwanyong Seo, *Ulsan National Institute of Science and Technology (UNIST)*, for their kind encouragement and constructive reviews.

I would like to thank lab leaders, Dr. Jiwon Lee, *first Ph.D. and lab leader in our lab*, Jonghwa Park and Seungyoung Park, *past and current lab leaders*, for their dedication and efforts to the lab. Also, I would like to thank lab members, Dr. Minsoo Kim, Dr. Ziyauddin Khan, Dr. Ravi Shanker, Dr. Doo-Seung Um, Young-Eun Shin, Young-Ryul Kim, Seongdong Lim, Minjeong Ha, Hochan Lee, Youngsu Lee, Youngoh Lee, Ayoung Choe, Seungse Cho, Jeonghee Yeom, Jinyoung Kim, Jinyoung Myoung, Yoojeong Park, Sangyun Na, and Donghee Kang for their consideration and research assistance. Especially, I would like to thank Seungse Cho, *my colleague and team member*, for his devoted help during my Ph.D. course. Due to his support, I could complete my achievements and research papers.

In addition, I would like to express my appreciations to special members, Dr. Doo-Seung Um, *my troubleshooter*, Jonghwa Park and Youngoh Lee, *my spiritual mentors and roommates*, Dr. Ziyauddin Khan, Dr. Ravi Shanker, Seungyoung Park, Seongdong Lim, Hochan Lee, Youngsu Lee, and Ayoung Choe, *my research collaborators*, for their devotion to my researches.

Lastly, I would like to appreciate my parents and brother, my beautiful wife and lovely daughter and my parents-in-law, for big encouragement and long waiting. Especially, I dedicate this thesis to the health of my wife who is fighting cancer.

Thanks

